Presented to

the faculty of the School of Engineering and Applied Science

University of Virginia

in partial fulfillment

of the requirements for the degree

by

APPROVAL SHEET

is submitted in partial fulfillment of the requirements
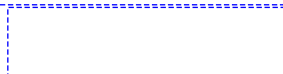
for the degree of

Marshall Tabetah

AUTHOR

Advisor

Accepted for the School of Engineering and Applied Science:

Dean, School of Engineering and Applied Science

ACKNOWLEDGEMENTS

I wish to thank my native family for patiently waiting to see me achieve this major academic milestone.

I am gratefully thankful to my Supervisor, Pr. Leonid Zhigilei, for providing the guidance, in the form of useful criticisms and suggestions, that enabled the accomplishment of this work.

I am thankful to Dr. Jorgen Schou in the Technical University of Denmark for the discussions that led to the computational investigations on lysozyme targets in this work.

I am highly appreciative of the members of the research group, the 'Computational Materials Group' at the University of Virginia, in which I accomplished this work. Through their collaboration, a working computing machine has been maintained in the group. They made useful criticisms to my ideas when I presented them. Particularly, I wish to mention Dr. Alexey Volkov, a former postdoctoral researcher in the group, who was helpful beyond the academic milieu.

I wish to thank my Committee Members for helping me see through what it takes to make a thesis statement out of the tremendous amount of work I did.

TABLE OF CONTENTS

LIST OF SYMBOLS

A_c constant that controls the rate of exchange between the heat bath and the breathing mode.

A_m molar mass of material.

a refers to lattice parameter, unless otherwise stated.

a_{mol} is the molar absorption coefficient of metalorganic precursor.

B bulk modulus

b the summed molar absorption coefficient of the products of decomposition of palladium acetate, unless otherwise stated.

C generally refers to molar concentration of metalorganic precursor, unless otherwise stated.

C^{exp} experimental specific heat capacity of group of atoms or molecules.

C^{int} heat capacity of heat bath per breathing sphere unit.

C^R heat capacity due to breathing motion of breathing sphere unit.

C^{tr} heat capacity due to translational motion of breathing sphere unit.

c_P material heat capacity at constant pressure

C_S speed of sound.

    diffusion coefficient of single atom.

$_e$ parameter of Morse potential: the well depth.

$_T$ material thermal diffusivity.

d diameter of cluster of metal atoms.

E generally refers to energy variable.

E_a generally denotes activation energy.

E_a adsorption energy of H_2O molecule above metal surface in SPC model

E_p the energy of an Einstein (a mole of photons).

F laser irradiation fluence.

F*   threshold fluence for material ejection.

H generally refers to thermodynamic enthalpy.

H_m enthalpy of melting

I generally refers to light intensity.

K referring to the kinetic energy of system.

k_0 rate constant for thermal decomposition of palladium acetate

k_1 constant of breathing potential; the other constants, k_2 and k_3, are related to k_1.

L generally refers to thickness of sample.

L_D^P distance over which laser-deposited energy diffuses during pulsed-irradiation.

L_{NP} average spacing between NPs.

L_p penetration depth.

L_∞ mean free path of electron.

M generally refers to mass of breathing sphere unit.

m generally refers to material or system mass, or to the mass of atom or molecule when indexed.

M_I inertia parameter of breathing motion.

N generally describes the number atoms, molecules or units.

n unless otherwise stated, generally refers to number density.

P unless otherwise stated, refers to pressure variable.

Q refers to thermodynamic heat variable.

R unless otherwise stated, refers to radius of breathing sphere unit, radius of cluster of atoms.

r_C potential cut-off: range over which potential is described.

r_e parameter of Morse potential – the equilibrium separation.

S_k scaling parameter that controls strength of breathing potential.

S_k scaling parameter that controls inertia parameter of breathing motion.

T unless otherwise stated, refers to temperature variable.

T_b^* temperature of explosive boiling.

T_c critical temperature.

T_m temperature of melting.

$\langle T^{BS} \rangle$ temperature of breathing motion per breathing sphere unit.

$\langle T^{int} \rangle$ temperature of heat bath per breathing sphere unit.

$\langle T^{TR} \rangle$ temperature of translational motion per breathing sphere unit.

U generally refers to potential energy.

V generally refers to volume, unless otherwise stated.

v generally refers to velocity of a particle

Y generally refers to yield of ejected molecules from irradiated target, unless otherwise stated.

Greek Symbols

α unless otherwise stated, is the absorption coefficient

β unless otherwise stated, is the parameter of the Morse potential that describes the range of interaction.

γ electron collision rate in metallic nanoparticles.

ε dielectric permittivity.

ε_m water dielectric constant.

ε_{coh} cohesive energy per molecule.

ϵ energy density.

Θ_{HOH} H-O-H bond angle in water.

λ wavelength of light.

μ reduced mass of two interacting units.

ν frequency of periodic motion.

ρ density

σ absorption cross-section.

T   period of vibrational or oscillatory motion.

τ generally describes a decay time constant, e.g. time it takes for difference between heat bath and breathing mode temperatures to decay by $1/e$.

τ_p laser pulse duration.

τ_{th} characteristic time of thermal relaxation.

τ_S characteristic time of mechanical relaxation.

χ^{ib} interband susceptibility.

ω_p plasma frequency of conduction electrons.

LIST OF FIGURES

LIST OF TABLES

1. INTRODUCTION

This dissertation is the result of a comprehensive computational investigation of laser interactions with molecular targets in thin film deposition approaches that have a common root in the matrix-assisted pulsed laser evaporation (MAPLE) technique. The investigations carried out in this dissertation work are listed below.

i. Computational investigations are done to determine the minimum amount of solvent matrix needed for laser ablation of a polymer target. The investigations reveal a new phenomenon in material ejection from an irradiated biopolymer target of the protein lysozyme: the ejection of intact biomolecules (or macromolecules) from a target having low water concentration. Based on the observed phenomenon, a new non-destructive approach for the deposition of polymer and biomolecular films can be developed. Because the solvent content in the target is low, unlike MAPLE targets that usually have more than 90 wt% of solvent, this approach, dubbed an 'inverse MAPLE' technique, provides dry deposition conditions that can be beneficial for applications that require minimization of the solvent-related effects.

ii. The fundamental mechanisms responsible for the generation of metallic nanoparticles in an experimental approach based on the laser irradiation of aqueous solutions of metalorganic precursors are explored in a computational investigation. In this approach, the irradiated target is frozen, and it consists of low concentration solute (typically less than or equal to 5 wt%) suspended or dissolved in a solvent (the matrix), like in the MAPLE technique. It however differs from MAPLE in that the solute is the light-absorbing material instead of the solvent. This approach has a promise of providing an efficient method for dry synthesis and deposition of clean

nanoparticles with narrow size distributions and compositions tailored to the requirements of applications. In the process of determining the most likely scenario of ejection of nanoparticles (NPs) from the target, a new mechanism in which material is ejected from the target without being entrained by the matrix is revealed. This mechanism may have implications for the development of techniques enabling size-selective generation and ejection of clean solvent-free nanoparticles.

In this introductory section, a review of laser interactions with molecular materials is provided, and popular methods that have been developed based on these interactions are discussed. Background material providing the motivation for the development of the laser deposition approaches considered in this work is provided on (1) the formation of metallic nanoparticles for thin film deposition and (2) the deposition of polymer and biomolecular films. The research objectives of this work are stated at the end of this section, after providing a background review on the modeling of molecular materials.

A description of the coarse-grained molecular model used for studying the laser targets investigated in this work is provided in section 2. The computational investigation of laser irradiation of the lysozyme material system is presented and discussed in section 3. The computational investigation of nanoparticle formation from aqueous solutions of metalorganic precursors is presented and discussed in section 4. A summary of the contributions of the author and the main findings reported in the dissertation is provided in section 5.

1.1   Laser Interactions with Molecular Materials

A laser, first invented in 1960 [1], is a device that emits light through optical amplification based on the stimulated emission of electromagnetic radiation. The term "laser" originated as an abbreviation for *Light Amplification by Stimulated Emission of Radiation*. A laser differs from other light sources because it emits light that is both temporally coherent and spatially coherent.

Temporal coherence is a measure of the correlation of the amplitude or phase of a wave over time, in the direction of propagation. The time delay over which the amplitude or phase of the wave is predictable is called the coherence time τ_C, and the distance over which the wave travels during τ_C is called the coherence length L_C [2,3]. The faster a wave decorrelates (the smaller τ_C) the broader the range of frequencies Δf the wave contains, i.e. $\tau_C \Delta f \approx 1$. According to this relation, a wave containing a single frequency (monochromatic wave) is perfectly correlated at all times, as its coherence time is infinitely long. Lasers are the most monochromatic sources, having coherence lengths up to hundreds of meters, for example a helium-neon laser can produce light with coherence lengths in excess of 5 m. The property of monochromaticity enables chemical and physical sensing techniques based on high-resolution spectroscopy.

Spatial coherence is a measure of the phase correlation in two spatial points transverse to the direction of propagation of the wave. It is indicative of how uniform the phase of a wavefront is; if the phase difference at any two points on the wavefront is constant at all times, then the wave is said to be perfectly spatially coherent. In practice, spatial coherence occurs only in a limited area of the wavefront, and spatial coherence is, therefore, ordinarily characterized by the area of coherence A_{coh}, or by a transverse coherence length $_C$ [2]. Laser beams have a small angle of divergence that is determined through the diameter of the aperture $_A$ in the diffraction limit as

$\theta_D \cong \lambda/D_A$, but due to partial spatial coherence the divergence is determined as $\theta_D \cong \lambda/\sqrt{A_{Coh}}$ or $\theta_D \cong \lambda/D_C$. The laser beam comes from the resonant cavity, and only light waves that propagate along the optical axis are sustained in the cavity. This, in addition to the small divergence, enables high directionality of the laser beam. The directionality and spatial coherence of the laser beam keep a laser beam collimated over long distances and allow a laser to be focused to a tight spot. Collimation, easily evidenced in laser pointers, has enabled applications like remote sensing, range-finding, and target designation applications [2]. The ability to focus a laser beam to a tight spot has enabled applications like laser cutting, laser drilling and laser lithography.

Owing to its high intensity, early applications of the laser on materials were those that required brute force, such as cutting, drilling and welding, in the early 1960s. It was later, in the mid-sixties, that more delicate applications, like "laser erasing" (which involved removal of print without damaging the underlying paper) [4] and plasma generation at the surface of a solid – for the resulting spectral emission to be used for elemental analysis, arose [5]. However, it was still not used for thin film processing as early films deposited by laser irradiation [6] were poor in quality in relation to films produced by established techniques, and it wasn't until two decades later, in the 1980s, that laser-produced films became competitive. The initial poor film quality can be attributed to limited control of the quality and tunability of the laser output. Firstly, an irregular pattern of lasing pulses, termed 'spiking', can be generated due to temperature fluctuations or pump-light instabilities (arising from fluctuations about the excited state population threshold). Spiking was observed in many early lasers including the first to be demonstrated experimentally, the ruby laser. Secondly, in the first thin-film deposition experiment, the pulse duration was 1 ms for a pulse energy of 3 J, and the radiation frequency

was 1 pulse per minute, providing low tunability in the output. Today, with the relatively high tunability of lasers, quality thin film deposition has been attained with pulse durations ranging from a few femtoseconds to several nanoseconds, while pulse repetition rates can get as low as 5 Hz.

In pulsed laser interactions with materials, the duration of the pulse (or the pulse width) is an important control parameter since it determines the heat dissipation in the material from deposited laser energy: if the laser pulse is shorter than a certain time, the heat deposited in the material does not spread beyond the designated material volume; otherwise, heat dissipates beyond the designated volume, causing heat effects in parts of material that are not to be effected, or causing an unpredictable amount of energy density to be deposited in the target volume. Examples of applications that make use of a controlled pulse duration are (1) in laser surgery – where the deposited heat from the laser only has to affect the target tissue, and (2) in laser irradiation of target materials for deposition of films – where the right amounts of energy density are needed for the evaporation or vaporization of target material that is only a few to several nanometers thick.

Control of the laser pulse output, to do away with spiking, and to have shorter pulse durations, has been achieved using three different methods: pulsed pump excitation, Q-switching, and mode locking [2]. In pulsed pump excitation, the laser output approximately follows the pump pulse in situations where the lifetime of the excited state is long enough to avoid spiking. For shorter pulses, of nanosecond duration or sub-nanosecond duration, Q-switching or mode locking is used in combination with the pump. In Q-switching, the resonator quality factor (Q) is switched to alter the inversion threshold to a lower value, to induce lasing. This happens within a few nanoseconds, a characteristic time delay between the switching and the laser pulse. In mode

locking, the laser is run continuously above threshold, with a large number of simultaneous lasing modes, the superposition of which leads to pulsations having widths in the order of picoseconds, or even lower [2].

Another parameter of a laser pulse that is considered key to laser-material interactions is the fluence F. This is the total amount of energy irradiated on a unit area of the material surface, during a single pulse. It is equivalent to the integral value of the laser intensity over the time, $I_S = I_S(t)$, of the pulse duration τ_p:

$$F = \int_0^{\tau_p} dt\, I_S(t) \tag{1.1}$$

The variation in intensity over time can be described by the equation

$$I_S(t) = I_S^0 f(t) \tag{1.2}$$

where I_S^0 is a constant parameter with the dimension of intensity, and $f(t)$ is a dimensionless function that describes the shape of the pulse, and is defined by the normalization procedure (see appendix A1 for a more detailed description of Gaussian function):

$$\frac{1}{\tau_p} \int_0^{\tau_p} f(t)\, dt = 1 \tag{1.3}$$

In laser-material interactions, there are two kinds of pulse shapes commonly met: the rectangular (or square) pulse, and the Gaussian pulse. For a rectangular pulse, $f(t) = 1$, so that $I_S(t) = I_S^0$. For a Gaussian pulse, $f(t) = \tau_p g(t)$, where $g(t)$ is a normalized Gaussian function, described by Eq. (1.4).

$$g(t) = \frac{1}{\tau_w\sqrt{2\pi}} \exp\left[-\frac{(t - t_c)}{2\tau_w^2}\right] \tag{1.4}$$

In Eq. (4), t_c is the centre of the pulse, and τ_w determines the full width at half-maximum (FWHM) of the Gaussian pulse. In our computational investigations, for simplicity, a rectangular pulse will be used rather than the Gaussian pulse shape used in experiment: in this approximation, the fluence is maintained to be the same, and the pulse duration of the rectangular pulse is assumed to be the FWHM of the Gaussian pulse.

For a fundamental understanding of how the irradiation of a laser pulse eventually leads to the ejection of material for subsequent thin film deposition, we provide in the following subsections an overview to describe how laser light excites material, the material response to the excitation, and how the initiated response leads to the collective ejection of molecules and/or atoms in different ways.

1.1.1   Laser Excitation Mechanisms

When light interfaces with matter, it can be scattered or absorbed, and the amount of incident light that is scattered or absorbed depends on the optical properties of the material. We describe commonly met scattering and absorption mechanisms.

1.1.1.1 Scattering mechanisms

Scattering of light is a process which involves a change in the direction of propagation as it interfaces with material. If scattering from the material medium can be described by the law of reflection, then this form of scattering is known as reflection, and is usually encountered on the surface of macroscopic media. Scattering from particles of sizes in the microscopic and

mesoscopic range, e.g. molecules, dust particles, nanoparticles, can be more complex, and is usually classified as elastic or inelastic scattering. In elastic scattering the loss in energy of the scattering electromagnetic wave is negligible; typical elastic scattering theories include Rayleigh scattering and Mie scattering. In inelastic scattering, the loss in energy of the scattering wave is significant; a typical inelastic scattering mechanism is Raman scattering. The fraction of the power of incident light that is reflected off a medium, the reflection coefficient R, is determined by the Fresnel's equations [7]; in the case when the light is normally incident, the reflection coefficient is easily defined through the index of refraction of the medium of incidence, n_1, and the index of refraction of the reflecting medium, n_2:

$$R = \left(\frac{n_1 - n_2}{n_1 + n_2} \right)^2 \tag{1.5}$$

The reflectivity of a medium is dependent on the wavelength (or frequency), since the refractive index is wavelength-dependent through the dispersion relation.

  Rayleigh scattering is a process in which light is scattered by a particle that is much smaller than the wavelength and has variable refractive index or density fluctuations. The scattering particle could be a bubble, droplet, or a cluster of gas molecules, and its size is typically about one-tenth of the wavelength; in this size range its shape is not significant and the particle can be treated as a sphere. Rayleigh scattering is primarily responsible for the pale blue color of the Earth's sky, as shorter wavelengths from the Sun are more strongly scattered according to Rayleigh's $1/\lambda^4$ relation, and the solar spectrum peaks around blue.

  Unlike in Rayleigh scattering, in Raman scattering an incident photon scatters off a molecule or a particle whilst transferring part of its energy to a rotational or vibrational excitation of the scatterer.

Mie scattering is the scattering from spheres that are comparable in size to the wavelength. In this size range, the shape of the scattering object is significant and the model (Mie theory) only well describes objects of spherical shape.

Only some of the scattering mechanisms described can be encountered in the systems studied in this work, and are thus worthy of consideration. Reflection of laser radiation is expected to occur from the surface of the material targets. In the irradiated targets of the computational investigations, the light-absorbing material has negligible fractions of gaseous particles, and so Rayleigh scattering (relates to such particles) can be neglected. For the same reason, Raman scattering is not considered in this work. In the metalorganic solution target, metallic nanoparticles mostly of spherical shape are formed; these particles are expected to be in the ~ 1-10 nm size range, and because of their relatively small size in comparison to the laser wavelength (248 nm), they can be treated by Mie theory in the dipolar approximation (quasi-static approximation). A more detailed description of the use of Mie theory to determine the absorption of metallic nanoparticles will be provided in the section (section 4) relating to the computational study of the laser irradiation of the metalorganic solution target.

1.1.1.2 Absorption mechanisms

Once unscattered or unreflected light is inside the material, due to absorption the intensity may decay in the direction of light propagation at a rate determined by the material's absorption coefficient α. The absorption coefficient is a function of wavelength, $\alpha = \alpha(\lambda)$. In the investigations, irradiation is done normal to the target surface, and the laser beam sizes are much smaller than the surface area of the irradiated targets, so that the attenuation of light can be described as a function of depth z from the surface, in accordance with Beer's law:

$$I(z) = I(0)e^{-\alpha z} \tag{1.6}$$

where $I(0)$ is the intensity of light inside the surface after reflection losses, and is related to the incident intensity I_s as $I(0) = (1 - R)I_s$.

Optical absorption can be due to vibrational excitation by a photon (typically infrared (IR) wavelength) of energy equal to the difference in energy between the ground state and an excited vibrational state, resulting in the exertion of the corresponding vibrational mode(s), e.g. bending or stretching in a molecule. Absorption of light energy can be due to the transfer of electrons from the ground state to an excited state upon the absorption of a photon of energy (e.g. excitation of conduction band electrons in metals, creation of electron-hole pairs in semiconductors, or the creation of excited electronic states in molecules), resulting in the relaxation and transfer of the photon energy to phonons and/or vibrational modes. When the photon energy is larger than the energy of the chemical bond in a molecule, the absorption can lead to bond breaking.

The rate of deposited irradiation energy per unit volume in a single pulse, through absorption, can be determined, by taking the magnitude of the gradient of intensity in Beer's law, as $\alpha I(0)e^{-\alpha z}$. Assuming that energy does not dissipate from the absorbed regions during the time of irradiation τ, the energy density at variable depth, $\epsilon(z, \tau)$, can be written in terms of the integral flux over time through through z, $\Phi(z, \tau)$:

$$\epsilon(z, \tau) = \lim_{\Delta z \to 0} \frac{\Phi(z, \tau) - \Phi(z + \Delta z, \tau)}{\Delta z} = -\frac{\partial \Phi(z, \tau)}{\partial z} \tag{1.7}$$

The penetration depth (or absorption length), which is the inverse of the absorption coefficient $L_p = 1/\alpha$, is more frequently met in literature, and will be mostly referred to in this work.

1.1.2   Material Response to Laser Irradiation

The material response depends on the nature (metallic, metalorganic, or polymeric) of the material system, the properties of the material (e.g., penetration depth, thermal diffusivity, heat capacity, phase transition temperatures), and the laser processing conditions including the parameters of the pulse. Energy densities deposited by the laser pulse can be sufficiently high, leading to material removal or ejection through a number of response mechanisms or processes. Most of the frequently met response processes can be classified as photochemical, photothermal and photomechanical. The process of material removal from the irradiated target can be classified into a number of mechanisms or models – those commonly met are desorption, explosive boiling or phase explosion, hydrodynamic sputtering and spallation. The latter three are collectively referred to as ablation in literature.

1.1.2.1 Photochemical processes

Photolysis occurs when the energy of the absorbed photon is high enough to compensate the energy of chemical bonding leading to fragmentation of the molecule. The products of fragmentation can be atoms, ions, ligands, radicals, and molecules, depending on the chemical composition of the fragmenting molecule and the source of decomposition. Reactions with radicals can be highly reactive, leading to a chain of abstraction reactions (extraction of an ion from the parent molecule) and recombination reactions that make significant contributions to heating and pressure build-up in the material. A rise in temperature, due to laser irradiation, above the thermal decomposition temperature of the material can also lead to molecular fragmentation. In this work, the metalorganic target which is studied for the formation of metallic nanoparticles has metalorganic molecules which can photolytically or thermally

decompose to release metal atoms. The photochemical processes associated with the decomposition will be accounted for in the computational investigations.

1.1.2.2 Photothermal processes

If laser induced excitation is slow compared to the thermalization time, then a photothermal response ensues, in which the absorbed laser energy is transformed to heat through thermal relaxation of the absorbed photons. In this case, the material response will be a function of the local heating and cooling rates, temperature gradients, and maximum temperatures attained, most of which can be estimated from the solution to the heat equation for the given irradiation conditions. The timescale used to characterize the photothermal regime depends on the thermal diffusion coefficient and the penetration depth of the material. The thermal relaxation time is evaluated as $\tau_{th} = L_p^2/K_1 \ _T$, where $_T$ is the thermal diffusivity of the material, L_p is the laser penetration depth, and K_1 is a constant defined by the geometry of the absorbing region — K_1 is close to unity and will be assumed to be so in this work. Thermal relaxation corresponds to the diffusion of heat out of the absorbing volume, and occurs when the pulse duration is longer than the thermal relaxation time, $\tau_p > \tau_{th}$. A regime closely associated with photothermal processes is the *thermal confinement* regime [8, 9, 10]. In the regime of thermal confinement, heat conduction does not contribute to energy redistribution during the laser pulse, so that the thermal energy is largely confined within the absorbing region. This condition is generally satisfied when the pulse duration is less than the thermal relaxation time, $\tau_p < \tau_{th}$.

At low fluences, heating of the target leads to evaporation of individual molecules from the surface; this is usually referred to as desorption. At larger fluences, typically in the thermal confinement regime, fast overheating of the surface region can trigger a rapid transition of the material from a superheated liquid to a mixture of vapour and liquid droplets.

1.1.2.3 Photomechanical processes

When the laser pulse duration is so short that heating of the material takes place at constant volume conditions, it results in the build-up of thermoelastic stresses. The resulting irradiation regime is one of *stress confinement* [8, 9, 10]. This regime is defined by a timescale that depends on the speed of sound in the target material C_s, and the penetration depth. To be in the stress confinement, the condition to be satisfied is $\tau_p < \tau_s$, where τ_s is the mechanical relaxation time, and is approximated as $\tau_s \sim L_p/C_s$. At the limit of the stress confinement regime, the combination of transient melting and relaxation of laser-induced stresses can induce hydrodynamic motions of the melted surface which can yield large droplets of liquid material. Mechanical relaxation of laser-induced stresses typically proceeds by material expansion, and results in a partial or complete relaxation of the thermoelastic stresses.

1.1.3   Analytical Models for Material Ejection from Laser Targets

Material may be removed from the target in the form of vapor, liquid droplets and solid flakes. A combination of different material responses may account for one or more of these forms of material ejection. Various model definitions are used to describe the different forms of the material ejection process.

Evaporation – escape of atoms or molecules from a liquid surface to the ambient when the vapor pressure in the ambient is less than the saturation pressure of the liquid at the liquid temperature [11, 12].

Sublimation - In a solid, lattice vibrational energy releases individual atoms or molecules from the bulk surface by bond breaking.

Evaporation and sublimation can be collectively referred to as *desorption*, and the rate of material removal can be described by the desorption model. Laser-induced desorption is defined as particle ejection without any detectable mesoscopic modification of surface composition or structure, and with a particle yield that is a linear function of the density of electronic or vibrational excitation [13]. The rate of molecular desorption, at low fluences, can be described by an Arrhenius-type equation:

$$Y = A\exp\left[-\frac{E_a}{k_B T_0 + BF}\right] \text{ for } F < F_{th}, \tag{1.8}$$

where E_a is an activation energy for molecular desorption from the surface, A is a pre-exponential or frequency factor, and B is a factor that describes the conversion of the deposited energy into the temperature increase, k_B is Boltzmann's constant, T_0 the initial temperature of the system, and F_{th} is a threshold fluence that corresponds to the transition from desorption to ablation.

Explosive boiling (or *phase explosion*) − This is a commonly occurring process leading to material ejection from laser ablated targets. A liquid is heated beyond its boiling point if the heating rate is fast enough. The resultant superheated liquid is in a metastable state. The metastable liquid seeks equilibrium that results in its return to the binodal through explosive boiling, and never attains the spinodal; see Figure 1.1 for illustration of phase diagram. This involves rapid and spontaneous homogeneous creation of vapor nuclei in the liquid. The nuclei grow in size or coalesce to form larger bubbles. Beyond a critical size, the bubble will burst propelling liquid droplets from the target [11, 12]. Heterogeneous boiling may also occur due to vapor bubble formation at nucleation sites (foreign bubble or container wall scratch) but the low

rate of this event coupled with the relatively slow growth of the bubble makes it an unimportant process of material ejection.

Hydrodynamic sputtering – Collective motion of melted material leads to ejection of droplets as a result of transient melting and motion of liquid caused by steep thermal gradients and relaxation of the laser induced pressure [14, 15, 16].

Exfoliation – Material is removed in solid flakes from the surface. This could be due to energy absorbing defects on the target surface [14].

Spallation – Spallation is a process in which material removal occurs due to the generation of high thermoelastic stresses. Spallation arises from the photomechanical response of the target material, and for it to occur, the system must be in the regime of stress confinement. Strong pressure build-up due to the generated thermoelastic stresses drives a compressive pressure wave that travels towards and away from the free surface of the material to become a tensile wave. If the resulting tensile stress exceeds the dynamic tensile strength of the material, it can cause mechanical fracture (spallation) through the formation of voids or cavities.

Laser ablation is a sputtering process in which material removal rates typically exceed one-tenth monolayer per pulse; the surface is structurally or compositionally modified at mesoscopic length scales; and particle yields are superlinear functions of the density of excitation [13]. The formation of an ablation plume—a weakly ionized, low-to-moderate density expanding gas cloud—adds to laser ablation the complications of plasma-surface interactions, gas dynamics, and laser-induced photochemistry [13]. Material removal through explosive boiling, hydrodynamic instabilities, exfoliation, and spallation, are all different forms of ablation. The formation of a plume may occur only in some of these forms, e.g. in material ejection through

explosive boiling. Due to phase explosion, which is the main mode of ablation in the targets investigated in this work, the number of ejected molecules can be described by Eq. (1.9).

$$N = n_m L_p \ln \left[\frac{F}{L_p(\epsilon^* - c_p T_0)} \right] \text{ for } F > F_{th} \qquad (1.9)$$

where L_p is the penetration depth, n_m is the molecular density, c_p is the specific heat capacity, and ϵ^* is energy density at the ablation threshold.
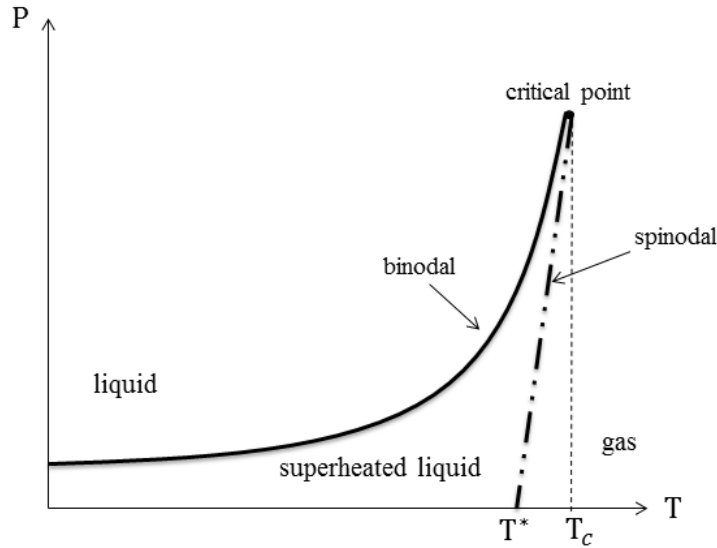
Figure 1.1: Schematic illustration of the temperature-pressure phase diagram at temperatures close to the temperature of phase explosion, illustrated on the diagram as T*. The critical temperature is illustrated as T_c.

1.1.4 Summary on Laser Interactions with Molecular Materials

Laser interaction with materials results in a complexity of processes and phenomena that are governed both by the laser irradiation parameters and the physical and chemical properties of the material. In this dissertation, given the laser irradiation conditions and the target materials

investigated, only certain mechanisms will be accountable to the resultant ejection of material: energy deposition will occur by thermal relaxation of the absorbed photons; in addition to this, in the metalorganic solution target, photochemical and thermal decomposition of the metalorganic precursor molecule will be modeled. The laser irradiation regime of the system under investigation will be considered in order to explain specific aspects of material removal, if need be.

1.2   Molecular Transport and Thin Film Deposition by Laser Interactions

The range of research and industrial applications based on laser interactions is broad. There is a myriad of applications focused on the surface modification of laser targets: micromachining of electronic chips, circuits, and other nanodevices is successfully performed by short laser pulses due to the precision involved in targeting the laser energy [17]; tensile stresses induced at surfaces of laser targets can be used for the ejection of surface contaminants in a process called dry laser cleaning [18]. Although fewer, techniques that are dedicated to molecular entrainment or transport from targets through laser-induced desorption and ablation have been on the rise. A survey of three techniques, that are commonly utilized and are of high relevance to understanding the investigations in this work, is provided – the techniques are pulsed laser deposition, matrix-assisted laser desorption/ionization, and matrix-assisted pulsed laser evaporation.

1.2.1   Pulsed Laser Deposition

Pulsed laser deposition (PLD) is a thin film growth method that proceeds by pulsed laser irradiation of a solid target, in vacuum or gaseous environment, for the ejection of material and

its subsequent deposition onto a substrate. [See diagrammatic representation of technique in Fig. 1.2, for polymer thin film deposition]. The surface region of the target is rapidly heated leading to ejection of material in an ablation plume for transfer onto the substrate. Entrainment is sometimes done in a gaseous environment for the formation of composite structures, made of the ejected material and the gas, on the substrate. This technique has been used on a wide variety of solid targets, ranging from inorganic materials, such as metals and semiconductors, to molecular and organic materials. Although it has been implemented successfully for the ablation of metal and semiconductor targets [14, 15, 19, 20], it shall be seen later, in section 1.3, that PLD is not suitable for the deposition of a vast majority of polymer films due to a number of reasons related to the functionality of the films.

1.2.2   Matrix-assisted Laser Desorption/Ionization

Matrix-assisted laser desorption/ionization (MALDI) is a technique that utilizes the ability of laser ablation of a volatile matrix to entrain, eject, and, if needed, gently deliver large macromolecules or other nano-objects to a substrate. In MALDI, the molecules of interest (the analytes) are incorporated into a matrix of solvent molecules. The system is irradiated by a laser pulse, the matrix molecules absorb the light and ablate, sweeping the analytes along into the plume. Some of the analyte molecules are ionized and the ions can be extracted from the plume and mass analyzed, e.g. see reviews [21, 22, 23, 24]. This technique has become a major tool for analysis of non-volatile organic and biological molecules such as proteins, nucleic acids, polymers, etc. [25, 26, 27].

1.2.3 Matrix-assisted Pulsed Laser Evaporation

Matrix assisted pulsed laser evaporation (MAPLE), a method related to MALDI, was developed in the mid to late 90's [28, 29, 30, 31, 32]. Sharing many of its attributes with MALDI, MAPLE utilizes a volatile solvent to sofly eject intact macromolecules or nano-scale elements from the frozen solvent target; the entraining solvent, being lighter, is pumped away as the ejecta travel towards the substrate. [See diagrammatic representation of MAPLE technique in Fig. 1.2, for polymer thin film deposition]. There are also some differences between the typical experimental set-ups used in the two methods, particularly in the amounts of macromolecules present in target, laser fluences used in experiments, and the emphasis on the ionization process in MALDI but not in MAPLE. Significantly higher concentrations of macromolecules and energy densities are used in MAPLE in order to grow thin films in a reasonable timeframe. In both techniques, however, the selection of matrix has been shown to be a critical step in tailoring the characteristics of laser-target interactions for the requirements of each technique.

In the method of synthesis of nanoparticles on which part of the research work is focused, the role of the matrix will be different from both MAPLE and MALDI, though. Instead of absorbing laser irradiation and providing conditions for "soft" ejection of intact molecules, the transparent matrix used in this technique serves as a medium for diffusion of the metal atoms released from metalorganic precursors and allows for control over the growth of the nanoparticles during the irradiation process.

In the inverse MAPLE process for deposition of lysozyme films, water, in a low concentration, increases the volatility of the solid target, enhancing the ejection and subsequent deposition of intact biomolecules.

1.2.4   Summary on Laser-assisted Molecular Transport

Alternative to the recently described laser-based techniques for molecular transport are several non-laser traditional methods that have been used for the deposition of thin films. To make clear the importance of the techniques, rooted in MAPLE, that are investigated in this work, we provide a background, in section 1.3, on non-laser methods that have been commonly used for the deposition of thin films that are of similar composition to those that are a subject of this investigation.
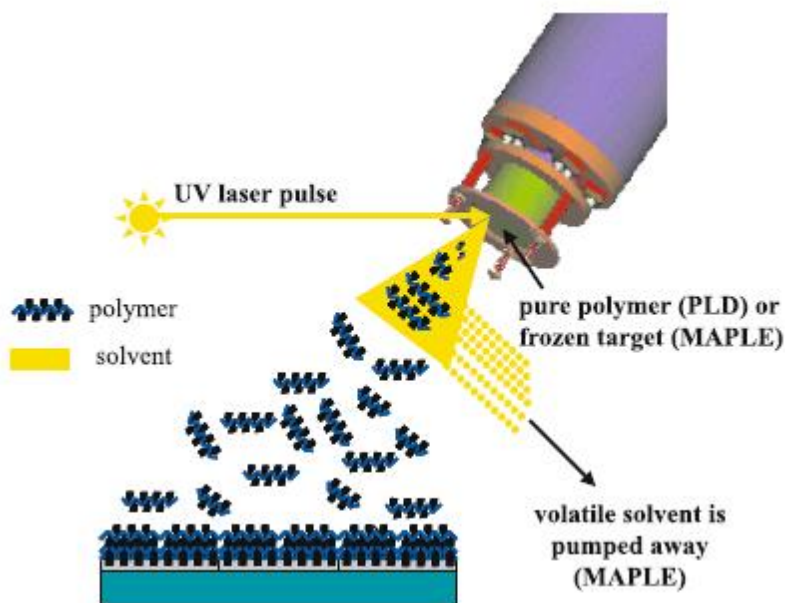
Figure 1.2: Diagram of experimental set-up for the deposition of polymer thin films by both PLD and MAPLE, obtained from Ref. [30].

1.3   Advantages of Investigated Techniques over Alternative and more Traditional Thin Film Deposition Methods

We provide reviews of techniques that have been employed for thin film depositions of nanoparticles and polymer or organic films. Their limitations and disadvantages in comparison to the investigated techniques in our work are elaborated.

1.3.1   Formation of Metallic Nanoparticles for Thin Film Deposition

The synthesis and analysis of nanoparticles (NPs) of various elements and compounds is of great interest both for technological applications and for fundamental research. Due to surface and quantum confinement effects, NPs possess unique properties that are often superior to those of the relative bulk material— structural, magnetic, optical, dielectric, thermal and other physico-chemical properties [33, 34]. NPs on a substrate may form a film of loosely aggregated NPs or may be organized to form an ordered structure. Metallic NPs and composite structures offer great perspectives in areas such as biomedical applications [35, 36, 37], sensing [35], information storage [38], microelectronics [38], and others.

Traditionally, several methods and techniques have been utilized to synthesize NPs. Some of the most used methods and techniques include mechanical milling, thermal evaporation, wet chemical processing, metalorganic chemical vapor deposition (MOCVD), molecular beam epitaxy (MBE) [33, 34, 39]. The above cited techniques have shortcomings that limit the use of NPs produced by them for several scientific applications.

In mechanical milling the required forces increase exponentially with decreasing particle size.

In thermal evaporation, in addition to difficulties preparing NPs of elements and compounds with high melting points, metal reaction with the crucibles during heating is possible.

Wet chemical processing techniques for NP production are toxic due to contamination with chemical precursors or additives during synthesis [35, 36].

Nanoparticles deposited with MBE and MOCVD, in addition to having a wider size distribution of ~ 10-20 %, are usually embedded in semiconductor or dielectric layers directly in their final position, thus preventing their growth on non-planar substrates, and their mixing with other materials [34].

In addition to unique advantages, synthesis techniques by pulsed laser ablation (PLA) can overcome many of the shortcomings of the above described techniques for the synthesis of NPs. Deposition with uniform substrate coverage can occur both on rough and clean substrates, whilst ensuring a good control of the film thickness [34]. There is the possibility of growing films with a complex stoichiometry [33, 39], as well as multilayered films of different NP sizes and NP materials [34]. Fabrication systems can be maintained at low temperatures (close to room temperature) while still maintaining high deposition rates. Pure NPs can be produced by PLA in liquids. Contrary to wet chemical techniques there is suppressed contamination [35, 39], and lesser need for surfactants. The ablation process can be easily controlled by tuning the laser parameters—the fluence, the wavelength, the pulse duration, etc. This means an easy control of NP characteristics—dimensions, size, quantity, etc. Any target can be ablated with a proper choice of laser parameters.

For the generation of metallic NPs, different PLA fabrication systems with differing effects on the ablation process have been used. PLD and MAPLE have already been discussed in the previous sub-section (section 1.2) as reliable methods for NP production. Another method of

metallic NP generation worth mentioning is the pulsed laser ablation of a bulk solid target immersed in a liquid solution (mostly water or pure organic solvents), [40, 41, 42] – it is known as laser ablation in a liquid (LAL) or Laser Ablation Synthesis in Solution (LASIS).

The laser beam spot sizes in pulsed laser ablation for NP generation are in the range of 10^{-4} cm^2 – 10^{-2} cm^2, and the pulse duration can be from 100–500 fs to tens of ns and longer.

The parameters of the laser pulse (particularly the pulse duration and the fluence), as well as the medium of ablation, significantly effect the ablation process.

Femtosecond laser pulses deposit energy to electrons in the target on a time-scale much faster than electron–phonon thermalization (~ 10 ps) processes, while longer pulses (picosecond and nanosecond laser pulses) deposit energy on a time-scale comparable with the thermal relaxation processes of the target. Femtosecond laser pulses, unlike nanosecond laser pulses, do not therefore interact with ejected material [42, 43, 44]. Some of these secondary laser-ejecta interactions can result in photofragmentation and collisional processes that contribute to the formation of vapor particles and/or alter the size distribution of particles [42, 43].

If the laser fluence on a target is gradually increased, the amount of ablated material may drastically increase at a certain threshold laser fluence. The threshold laser fluence is material dependent. At higher laser fluences, laser-induced fragmentations and hydrodynamic sputtering may significantly affect the size distribution and number of NPs [19, 36, 37, 42]. Larger size distributions are generally observed with higher fluences [35, 37, 38, 40, 42].

Ablation of a metal target in vacuum is characterized by the generation of a plume which consists of a fast component (electrons, ions, neutral atoms) and a slow component (NPs). The fast component separates from the target at ~ 10^6 cm^2/s, while the slow component has an ejection velocity of ~ 10^4 –10^5 cm^2/s [45] at fluences in the order of ~ 1 J/cm^2. By supplying

different background gases, multicomponent NPs with various structural forms and chemical compositions can be generated [38]. With increasing gas pressure, the ablated species are more likely to undergo collision-induced aggregation. By varying the background pressure, a large range of kinetic energies of the ablated species can be obtained. Pulsed laser ablation in a liquid medium confines the ablation plume near the target, suppressing diffusion of ablated species away from the plume region. This maintains the metal surface at ablation temperatures for long times, causing the ablation plume to persist for times longer than the laser pulse duration [41, 42]. Changing the liquid environment has an effect on the shape, mean size, size distribution and surface composition of the NPs [19, 36, 41, 42]. Functionalization and stabilization of NPs is possible by choosing a suitable solvent or using surfactants [19, 41, 42]. Whereas the ablation rate in air increases gradually with a growing fluence, the ablation rate in water reaches a maximum at a certain fluence and then decreases due to optical breakdown in liquid [35, 41].

NP synthesis after material ejection depends on possible condensation and agglomeration of vapor particles in gas [45], undercooling due to vacuum expansion [43], NP nucleation from metal atoms and further growth of nucleus in liquid solution [40, 42].

Pulsed laser ablation is a versatile and reliable technique for metallic NP production given its multiple advantages over other conventional techniques, including the fine and easy tuning of laser parameters.

In PLD, because of the solid nature of the target, ablation of the target material can be by hydrodynamic sputtering, phase explosion, exfoliation or spallation; in MAPLE, ablation is dominantly by phase explosion, and it is much gentler since it requires explosive boiling of a liquid (lower temperatures), making MAPLE a more controllable and predictable process for the

generation of NPs. In MAPLE, thin films of NPs with narrow size distributions have been deposited [34, 46, 47].

A reliable prediction of NP yield characteristics based solely on experimental observations and analysis is not usually achieved. This has necessitated the development of computational models for investigation of the mechanisms of NP formation, which provide guidance in exploration of experimental conditions and laser parameters for NP production [19, 39, 41, 43, 45].

1.3.2 Deposition of Polymer and Biomolecular Films

The control of deposition of proteins on surfaces is a current demand for many applications such as biosensors, medical implants, food packaging and marine and industrial equipment. In particular it is important to produce protein films that preserve biological activity (or functional properties) and resist biofouling. The experimentally related work investigates deposition of the protein lysozyme which is a bacteriocidal enzyme commonly found in human secretions such as saliva, tears, and sweat. Lysozyme is useful as a model protein for deposition in vacuum because its properties are well known, it is not heavy (~ 14 kDa), and its activity can be tested after deposition.

Numerous applications of protein films, as well as biomaterial and polymer films at large, demand preservation of their chemical structure during deposition. In addition, the physical qualities of the deposited films should be excellent. The inadequacies of popularly employed deposition techniques in fulfilling either of these demands founded the motivation leading to the development of the MAPLE technique; a discussion of this development, realized mostly from reviews made in Refs. [48, 49], is provided below.

Although functionality and chemical integrity are preserved in simple (and cheap) solution-based traditional techniques, such as spin coating, dip coating and spray coating, the deposited polymer films are usually non-uniform and inhomogeneous due to uneven wetting of the substrate and evaporation of solvent molecules. In addition, these techniques allow the treatment of a limited class of compounds; spin-coating is limited to the processing of soluble polymers [50], as an example. This led to the search for a technique that deposits a wide class of soft materials, while allowing for the control of several deposition parameters for the attainment of excellent film qualities. Important parameters and/or qualities are: the preservation of chemical integrity and physical properties, thickness, film adhesion to substrate, film uniformity and homogeneous coverage of substrate. Use of PLD for the deposition of both organic and inorganic films has presented advantages, such as monolayer thickness control, good film-to-substrate adhesion, minimum material consumption, low substrate temperatures, but it turned out to be unsuitable for the deposition of large delicate molecules like polymers and biomaterials, due to molecular bond breaking. This means the properties, or the activity in the case of proteins, of the deposited films cannot be retained. For several polymers that have been deposited by PLD, e.g. polyethylene, polycarbonate, polyimide, polymethyl methacrylate (PMMA), and PTFE (Teflon), a decrease in molecular weight has been frequently observed. In many of these cases, film deposition is supposed to occur via pyrolytic decomposition, followed by repolymerization. Repolymerization, however, can be incomplete, leading to a change in properties. PLD is therefore not a reliable technique for the deposition of soft or delicate materials if the retention of their properties or activity is to be accounted for. The MAPLE technique has proven to be reliable in the deposition of films that have shown little or no difference in properties from the bulk as indicated by characterization techniques such as FTIR and MALDI, while retaining the

advantages presented by PLD. Despite having met general satisfaction in the preservation of bulk functionality and excellence in film quality unlike techniques broadly employed prior to its development, the MAPLE technique has still shown a few drawbacks. Notable drawbacks are listed. i) Typical deposition rates are an order of magnitude lower than those for PLD – the concentration of the solute has to be very small to maximize photon interaction with the absorbing solvent. ii) Although the highly volatile solvent is pumped away during the flight to the substrate and the deposited film should be composed only of the solute material, large droplets are commonly found on the film surface. The presence of solvent may dissolve the underlying layers of a fragile substrate, e.g. in the application of the polymer film as a drug coating for controlled drug delivery [51]. Significant roughness or unexpected surface features (such as deflated balloon features) have been evidenced due to the generation of a mixture of liquid droplets and gas-phase matrix molecules when the limit of thermodynamic stability is attained [52]. iii) Depending on the type of solvent, the chemical structure and functionality of the deposited material may not be preserved, for example, deposited PEG films from chloroform matrices have shown decomposition of the starting material as opposed to water matrices [48]. The decomposition is due to photochemical reactions of the solvent molecules with the laser pulse, which results in the generation of highly reactive radicals that can alter the chemical structure and functionality of the solute material being deposited.

The drawbacks of the MAPLE technique have led the scientific community to develop variations of the technique with the purpose of overcoming the drawbacks. Notable variants of the MAPLE technique are listed below.

i)   In resonant infrared MAPLE (RIR-MAPLE) an infrared laser, instead of a UV laser, is used to irradiate the target in order to avoid decomposition of the solvent which

may lead to modification of the chemical structure of the solute molecules through the reactivity of generated radicals. For example, MEH-PPV films with properties identical to those of the bulk have been grown from chloroform matrix using IR radiation as opposed to UV radiation [48].

ii)   A variant that has been developed to reduce the quantity of droplets on films is called off-axis MAPLE, in which the substrate is placed parallel to the deposition axis rather than normal to it. This technique has shown promise in significantly eliminating the presence of droplets in chemoselective polymers, while suffering a lower deposition rate of about a third to half [48].

The RIR-MAPLE technique avoids the chemical modification of the solute molecules but evidently does not get rid of the solvent presence on the deposited film. Although the off-axis MAPLE technique significantly reduces solvent deposition on the substrate, it does not account for the deposition of solvent in a frozen state; depending on the regime of laser irradiation the ejection of frozen material from the target is possible. Because the MAPLE technique (and its variants) has been the most reliable for the dry deposition of films that preserve their structure and functionality, the exposed inadequacies of it as a dry technique bring the 'inverse MAPLE' method to light as 'unique' for the deposition of solvent-free films that preserve bulk structure and functionality. Since the solvent content is very low, the 'inverse MAPLE' method, as a technique, is expected to dramatically lower solvent presence on film surfaces, given that the same deposition apparatus in MAPLE will be employed. And because the same deposition apparatus will be employed, the technique will be accepting of developed variants of the MAPLE technique. The 'inverse MAPLE' technique will be 'void' of solvent effects on the quality of interfaces, and this will enable the realization of high quality polymer-based devices

with multilayer structures, as well as the deposition of polymer or protein coatings (or layers) without deterioration of the underlying layers.

1.3.3   Understanding Laser-assisted Molecular Transport Techniques

A reliable prediction of the mode of ejection of polymer molecules based solely on experimental observations is not usually achieved. In relation to the yield of nanoparticles, the mechanism of formation and ejection from the target cannot also be understood based only on experimental observations and analyses. This has necessitated the development of computational models for the investigation of molecular targets. These models will also provide guidance in exploration of experimental conditions and laser parameters for material yield.

1.4   Modeling of Laser Interactions with Materials

The complexity and multiplicity of the processes involved in pulsed laser–matter interaction and the wide range of the time- and space scales of their manifestation makes it impossible to create a model describing this phenomenon with all its features [53]. This has motivated the development of numerous models that treat different aspects of material behavior and evolution under differing conditions of pulsed laser irradiation. Despite the wide variety, one can easily identify those models that treat matter as a continuum, and those that relate to matter as a system of particles. A model that treats the irradiated material as a continuum is called a *continuum model*. Among models that treat matter as composed of particles are statistical models that are based on events probabilities and follow a Boltzmann distribution, and models based on *molecular dynamics* that use equations of motion to follow the evolution of particles. A typical particle-based statistical model is the *Monte Carlo*. Particle-based models based on classical

mechanics can be sub-classified into those that include into their study the atomic structure of the material, and those that have as particle representation a molecule or a grain of molecules; the former are called *atomistic models* and the latter are called *mesoscopic models*. The choice of the model depends on the behavior and phenomena to be studied, and the efficiency of the model to adequately carry out the relevant investigations. Atomic-level simulations can provide information on energy redistribution among different dynamic modes, but are very limited in the length and time scales that can be modeled – they cannot in reasonable times reproduce the collective motion of several tens of thousands of molecules. Mesoscopic-level simulations, although losing the precision of atomic-level calculations, increase dramatically the scale of the simulations (up to a few nanoseconds and a few or several nanometers). Data collected, from molecular dynamics simulations, on cluster formation, collision frequency, etc. can be used as input for a suitably larger scale technique such as the Monte Carlo. Continuum models and statistical models offer the opportunity of investigation on a much larger scale (several microns and several microseconds), but may be limited to addressing specific issues (or aspects). We briefly describe the different model types that are developed and used in this dissertation work.

1.4.1   Continuum Model

In the continuum model the material is treated as a homogeneous medium whose behavior is characterized by macroscopic properties and parameters such as density, thermal conductivity, diffusivity, absorption coefficient, and any others relevant to the study. This study, which is at a macroscopic level, enables the consideration of the behavior of large systems over long periods of time. The limitation to applying the continuum model is therefore connected to how well the studied material system can sustain its homogeneity over the time scale considered. Continuum models are suitable for systems involving a 'gentle' process of material removal.

Application of the continuum model to study laser interactions with a solid target has been done in Ref. [53]. Also, in this reference, the usefulness of the continuum model in describing the behavior of a given system is assessed.

1.4.2   Atomistic Models

The main strength of atomic-level simulations, over other model simulations, is the ability to provide detailed information on the rates and channels of energy redistribution among the translational, rotational, and other internal degrees of freedom of molecules. In laser irradiation, following the excitation of molecules by absorption of photons, the rate of energy transfer from the internal energy of the excited molecules to the thermal energy of the molecular solid or liquid is an important parameter that defines the character of the molecular ejection process. Atomistic simulations have been used to study processes of laser ablation in the picosecond and sub-picosecond regime, mostly in metals, where there are no molecular internal degrees of freedom, see Refs. [54,55,56]. The absence of internal dynamic modes allows simulations of up to ~ a hundred thousand atoms within a few nanoseconds. On the other hand, where internal degrees of freedom are present, as in atomistic simulations of the explosive boiling of water films adjacent to heated metal surfaces [57], only about a few thousand molecules were modeled within hundreds of picoseconds.

Due to the high computational cost, the applicability of atomic-level molecular dynamics (MD) has been limited to small systems and short simulation times, and so cannot be applied for simulation of the whole ablation process, from laser irradiation to collective molecular ejection, within a reasonable computing period (~ a few weeks). To overcome the limitations of atomistic

modeling, coarse-grained modeling for MD simulation of laser ablation of molecular materials has been developed.

1.4.3 Mesoscopic Molecular Dynamics

In atomic-level modeling, a molecule or monomer unit can include tens of atoms, and the timestep of integration of the equations of motion must be small enough, ~ 0.1 fs, to follow high-frequency rotational and vibrational motions of H, C, and N atoms. A coarse-grained representation of the molecules can be used to address collective processes leading to material ejection in laser ablation, while overcoming the limitations of the atomistic MD model. With the aim of simulating laser ablation of molecular solids, a coarse-grained "breathing sphere" MD model was developed, see Ref. [58]. To simulate molecular excitation by photon absorption and vibrational relaxation of the excited molecules, an additional internal degree of freedom – the breathing mode – was attributed to each molecule. More details of the breathing sphere computational model will be provided in section 2. The breathing sphere model has – since its inception – been used for simulating laser interactions with molecular targets.

The processes occurring during the first nanoseconds of laser ablation set an initial stage for further slower processes in the ablation plume. The processes occurring during the long-term plume expansion can include collisions among the ejected molecules, leading to cluster growth by condensation, ionization and chemical reactions. These processes, however, occur on the timescale of microseconds, and are rather lengthy to be considered for MD simulation. A larger-scale technique that can adequately describe the plume expansion, such as the Monte Carlo, is more useful.

1.4.4   Summary on Modeling of Laser Interactions with Materials

In application to laser interactions with materials, the continuum model is a macroscopic model that treats the irradiated material as a homogeneous medium, and is insufficient to the description of processes involving material discontinuities and inhomegeneities, such as the removal of layers, the formation and ejection of clusters. The continuum model alone cannot be used to study metal cluster formation and growth in a laser target; it cannot, for example, be used to explain the ejection of intact biomolecules from a biopolymer target. However, because of its relative immediacy in yielding simulation results, it will be used in this work to provide important estimates that will serve to guide the exploration of parameters in the coarse-grained modeling of the laser ablation of the metalorganic precursor solution target. Details of this will be covered in section 4.

Given the limitations, described earlier, of the atomistic model in simulating several tens of thousands of molecules, mesoscopic modeling will be adopted for the computational study and simulation of the phenomena and mechanisms investigated in this dissertation. However, material properties are governed by the structure at the atomic level; material representation by 'unreal' coarse-grained molecules requires adequate replication of atomic-level properties. In case, the atomic-level properties are not databased, they will first have to be determined using an atomistic representation. In this dissertation, an atomistic model will be used to determine those properties that are relevant to the parametrization of the coarse-grained model. This method of parametrization will be used to reproduce the interaction between metal atoms and coarse-grained molecules in the metalorganic precursor solution target: by first determining a property of metal-solvent interaction in the atomistic representation, which will be aimed at during the

parametrization of the coarse-grained model. More details will be provided in section 4. Also, it is worth noting that laser ablation simulations will not completely be void of atomic-level representation; metal clusters and nanoparticles are originally formed from single atoms that will be represented by a suitable atomistic model.

  As noted earlier in section 1.4.3, MD simulations are inadequately applicable to describing the latter stage of laser ablation (the processes accompanying plume expansion) given the time-limitations in simulating processes within the microsecond-scale. However, the mechanisms (or aspects) of laser ablation investigated in this work are in an earlier stage of the laser ablation process – lasting a few nanoseconds only, hence the adequacy of coarse-grained MD simulations in this research. For the same reason that we are not studying processes in the microsecond-scale, a Monte Carlo approach will not be used to satisfy our modeling requirements.

1.5   Molecular Dynamics Simulation Basics

  Apart from laser irradiation simulations, numerous simulations will be run to determine material properties, and also to prepare target samples by thermodynamic relaxation prior to their laser irradiation. These simulations will be run under differing thermodynamic conditions, and so to describe the thermodynamic state in which the material equilibrates to during the simulation, the material system will frequently be defined as an *ensemble* of particles of that state. The different thermodynamic ensembles in the material simulations, in this work, are listed below.

  i.   *NPT* ensemble: At equilibrium, the ensemble, of a fixed number (N) of particles, has a predefined pressure (P) at a given temperature (T).

ii. *NVT* ensemble: At equilibrium, the ensemble, of a fixed number (*N*) of particles, has a predefined volume (*V*) at a given temperature (*T*).

iii. *NVE* ensemble: At equilibrium, the ensemble, of a fixed number (*N*) of particles, maintains a constant energy (*E*) for a given volume (*V*).

iv. *NPH* ensemble: At equilibrium, the ensemble, of a fixed number (*N*) of particles, has constant enthalpy (*H*) at a predefined pressure (*P*).

Simulations of a *NPT* ensemble, with *P* = 0, will be most frequently run, to determine material physical properties at a given temperature, and to equilibrate target samples to the required temperature prior to laser irradiation. Simulations of *NVT* ensembles will be needed to determine important kinetic relations, e.g. the diffusivity of metal atoms in water as a function of variable temperature. Simulations of *NVE* ensembles will be needed to determine material properties, which are defined through a variation in pressure while the energy of the system stays unchanged, e.g. the bulk modulus is defined through a change in pressure at different volumes; the pressure is determined in a constant-energy simulation.

Unless otherwise stated, the simulations for the determination of material properties are mostly run with periodic boundary conditions (PBC) applied in all directions of a 3-D orthorgonal system. This means that the particle distribution is periodic across a vector $\vec{L}$ that is a linear combination of the lengths of the sides of the computational cell (C.C.) of the system of particles. A particle at position $\vec{r1}$ of the computational cell is reproduced at position $\vec{r2}$ across the vector $\vec{L}$:

$$\vec{r1} = \vec{r2} + \vec{L}; \; \vec{L} = n_1 L_x \hat{e}_x \; + n_2 L_y \hat{e}_y \; + n_3 L_z \hat{e}_z \tag{1.10}$$

where L_x, L_y, and L_z are side lengths of the computational cell; and n_1, n_2, and n_3 are integers. The application of periodic boundary conditions means that the particles close to the boundaries

of the computational cell interact in the same way as all the other particles – on average they see the same number of interacting particles. This may also be interpreted to imply that although there are a limited number of particles in the computational cell, material properties are computed over an infinite number of replicas of the computational cell particles.

In case periodicity is lacking in any orthogonal direction of the computational cell, then the simulation is said to be run with a free boundary condition (FBC) in that direction. This will be the case for simulations of laser irradiation, as there will be a FBC in the direction of propagation of irradiating light.

In order to control the thermodynamic variables, as needed in simulations of the described thermodynamic ensembles, relevant schemes have to be employed. We describe the schemes that are used to maintain a constant pressure, as well as a constant temperature, in this work. It will first be important to provide definitions of pressure and of temperature for a system of N particles.

The pressure is calculated in a computer simulation via the virial theorem of Clausius. The virial function is the sum of the dot products of the coordinates of particles and the forces acting on them:

$$W = \sum_{i=1}^{N} \vec{r_i} \cdot \vec{F_i} \tag{1.11}$$

The virial theorem states that the expectation value of the virial function is equal to twice the negative of the average kinetic energy ($K.E.$), as formulated in the following equation:

$$\langle W \rangle = -2\langle K.E. \rangle = -3Nk_B T \tag{1.12}$$

The force acting on a particle is made of an internal part, which is the sum of forces from all other particles on the particle, and an external part which is due to the pressure acting on the

system of the particles, i.e. $\vec{F_i} = \overrightarrow{F_i^{int}} + \overrightarrow{F_i^{ext}}$. Consequently, the virial is made of an external component and an internal component. The external part of the virial is $\langle W_{ext} \rangle = -3PV$. Expectedly, the internal part of the virial is described through only the internal forces acting on the particles:

$$\langle W_{int} \rangle = \langle \sum_{i=1}^{N} \vec{r_i} \cdot \overrightarrow{F_i^{int}} \rangle \tag{1.13}$$

Inserting the above definitions, the equation describing the virial theorem, Eq. (1.12), then becomes

$$\langle \sum_{i=1}^{N} \vec{r_i} \cdot \overrightarrow{F_i^{int}} \rangle - 3PV = -3Nk_BT \tag{1.14}$$

This equation is known as the virial equation, from which the pressure is retrieved as

$$P = \frac{Nk_BT}{V} + \frac{1}{3V} \langle \sum_{i=1}^{N} \vec{r_i} \cdot \overrightarrow{F_i^{int}} \rangle \tag{1.15}$$

In this work, the temperature is directly related to the kinetic energy of the system as follows:

$$\frac{3}{2} Nk_BT = \sum_{i=1}^{N} \frac{1}{2} m_i \left(\vec{v_i} - \overrightarrow{v^{CM}} \right)^2 \tag{1.16}$$

In this equation, m_i is the mass of the particle (or molecule), and $\overrightarrow{v^{CM}}$ is the velocity of the centre of mass of the system. In simulations with free boundary conditions in the z-direction, motion of the system on average is only in the direction in which the free boundary is imposed, and the centre of mass velocity therefore becomes $\overrightarrow{v^{CM}} = v^{CM} \hat{e}_z$.

Maintaining a constant pressure in simulations involves volume changes. The most straightforward way to adjust pressure is to scale the size of the computational cell and all the

interparticle distances during the simulation. The scheme used in this work is called Berendsen

barostat [59]. It scales the volume of the system at every time step by the scaling factor

$$\zeta = 1 - \beta_T \frac{\Delta t}{\tau}(P_0 - P) \tag{1.17}$$

where P_0 is the desired pressure, P is the instantaneous internal pressure, Δt is the timestep of

integration, β_T is the isothermal compressibility, and τ is the characteristic time of volume

relaxation. The particle coordinates are scaled correspondingly, in Eq.(1.18).

$$\vec{r}' = \zeta^{1/3}\vec{r} \tag{1.18}$$

The temperature is controlled by coupling the system to the Berendsen thermostat [59], so that

the velocities are scaled every timestep by the scaling factor

$$\xi = \left[1 + \frac{\Delta t}{\tau_T}\left(\frac{T_0}{T} - 1\right)\right]^{\frac{1}{2}} \tag{1.19}$$

where τ_T is the time constant of the coupling, and T and T_0 are the temperatures of the particle

system and thermostat, respectively.

The described schemes that maintain temperature and pressure directly relate to simulating a

NPT ensemble, as the pressure and temperature have to be controlled. In a simulation of a *NVT*

ensemble, only the scheme that controls temperature is implemented. In a simulation of a *NVE*

ensemble, the volume and energy are kept constant by neither implementing a pressure-control

scheme nor a temperature-control scheme. If the pressure is kept constant during a simulation,

and there is no heat flow into or out of the system, then the system is simulated as a *NPH*

ensemble. It would be clear, later on, how the enthalpy H is unchanged when the heat flow is

zero, in a simulation to determine the melting temperature of water through equilibration of a co-

existing liquid-solid interface, in section 2.2. In laser irradiation simulations, although the

external pressure may be maintained constant, the irradiated system of particles cannot be

described by any of the previously cited ensembles, given that there is energy gained, in the form of heat, from laser absorption, and there is no temperature control.

1.6   Research Objectives of the Dissertation

As discussed so far, due to the considerable time scale, mesoscopic molecular dynamics will be used to adequately describe laser-induced processes leading to the realization of the phenomena investigated in this work. We get more specific in revealing the investigations to be carried out, in order to study the proposed approaches outlined at the beginning of this introduction.

i.   Computational investigations are done to determine the minimum amount of solvent matrix needed for the laser ablation of a biopolymer target that leads to the ejection of intact biomolecules (or macromolecules). We expect that the ablation of pure lysozyme should lead to the ejection of only fragmented macromolecules, not intact macromolecules. Simulations of the ablation of lysozyme targets with varying water content, ranging from 5 wt% to 20 wt%, are done to determine the minimum concentration of water that is needed for the ejection of intact lysozyme molecules from a solid irradiated target. In relating this work to conventional MAPLE, in which the solvent is the major target constituent – responsible for providing a driving force for the ejection of solute molecules, we also aim at studying the effect of the increasing concentration of water on lowering the threshold fluence for the ejection of intact lysozyme molecules. Simulations of laser irradiation of lysozyme targets having different concentrations of water, up to 30 wt%, are run to study the effect of increasing water concentration on lowering the threshold fluence for the ejection of intact molecules.

ii. The fundamental mechanisms responsible for the generation of metallic nanoparticles in an experimental approach based on the laser irradiation of a frozen aqueous solution of metalorganic precursors (typically less than 5 wt% concentration) are computationally investigated. The approach slightly differs from conventional MAPLE in that the solute, ie. the metalorganic precursor, is the light-absorbing material instead of the solvent. Metallic nanoparticles, in the laser-irradiated material target, are formed from single atoms released in photo-induced fragmentation of MOP molecules. In the particular system investigated in this work, palladium acetate (PdAc or $Pd(OAc)_2$) is the metalorganic precursor to palladium (Pd) atom. As the main purpose of this work, the developed computational model is used to study the formation and growth of metallic clusters, and to determine the most likely scenario leading to the ejection of nanoparticles from the irradiated target. Because PdAc is insoluble in water at room temperature, it will be represented in solution both in a monomolecular phase and in a clustered phase. PdAc will be represented in the clustered phase as nanometer-sized (~ 1-3 nm) particles made of PdAc molecules. This would make it possible to study the effect of solubility of precursor molecules on the formation and growth of the metallic clusters during laser irradiation. MD simulations of a parametrized coarse-grained model of a computational system of the irradiated target will be performed. It shall be revealed that ejection of nanoparticles (NPs) from the target occurs without the NPs necessarily being entrained by the matrix, as most of the target matrix is not led to a state of phase explosion. Material ejection from the target in a MAPLE process without active evaporation of the solvent has not been encountered in experiment, and is thus deemed a novel process that is revealed by our computational investigations.

The sizes of the computational systems used for the coarse-grained simulations will be chosen so as to carry out the investigations within a reasonable time frame. In this regard, computational cell sizes will only be as big as ~ 100 nm so as to allow simulations to be accomplished within a few weeks.

2. COARSE-GRAINED MOLECULAR MODEL

As already discussed, molecular dynamics at the meso-scale, or coarse-grained molecular dynamics (CGMD), will be used for the description of laser interactions with the target materials. Within this approach, molecules are represented as coarse grains. In order to make a clear relation to a coarse-grained representation of the molecular structure of the targets, we provide a molecular description of the laser irradiated material systems, both lysozyme and metalorganic solution targets. In the coarse-grained approach employed in this work, the representation of the molecular structure and the description of molecular interactions are done within the *breathing sphere model*, introduced in section 1.4.3. A description of the breathing sphere model for the investigated systems is provided in this section.

2.1 Structural and Molecular Description of Investigated Target Systems

In this sub-section, a molecular description of the investigated targets, both lysozyme and metalorganic precursor (MOP) solution targets, is provided. In each case, the experimental target is first described. The experimental (or laboratory) description of the pulsed laser irradiation of the aqueous solution of MOP is based on the experimental set-up used in investigations on the generation of nanoparticles in the proposed technique. The experimental (or laboratory) description of the pulsed laser irradiation of lysozyme is based on the experimental set-up and observations obtained in investigations leading to the deposition of thin films with significant amounts of intact molecules.

2.1.1   Molecular Description of Lysozyme Targets

Both an experimental overview of the irradiated target, and a coarse-grained molecular representation are provided.

2.1.1.1 Experimental data on laser interaction with lysozyme

Lysozyme used in laser ablation experiments performed in the lab is chicken egg white lysozyme, which is obtained from Sigma Aldrich [60] and has molecular weight of 14307 Da. It is a single chain polypeptide of 129 amino acids cross-linked with four disulfide bridges [61]. The density of a pressed lysozyme pellet, prepared for laser irradiation is ~ 0.76 g/cm^3. In comparison, some densities of lysozyme crystals are: 1.38 g/cm^3 – determined from the fractional weight of protein in citrate/phosphate buffer solutions [62]; 1.2 g/cm^3 – determined from the velocities of sound of tetragonal lysozyme [63]; and ~ 1.4 g/cm^3 – determined for lysozyme with a solvent (water) content of 22% [64]. A molecule has a globular conformation, with dimensions of 4.5 nm x 3.0 nm x 3.0 nm [62], and its density is, therefore, 1.23 g/cm^3, calculated from the volume of a rectangular parallelepiped occupied by the molecule.

In experiments, a Nd:YAG laser is employed at a wavelength, λ, of 355 nm, with a pulse duration, τ_p, of 6 ns. The laser penetration depth measured for a dry pressed lysozyme target is $L_p \sim 30$ μm. Laser fluences used for ablation are ~1-2 J/cm^2. The target to substrate distance is about 60 mm, and a vacuum of base pressure 5x10^{-5} mbar is maintained during the deposition, at room temperature. Thin films of lysozyme were deposited on Si substrate, and analysed by MALDI.

2.1.1.2 Coarse-grained molecular representation of lysozyme targets.

Lysozyme derived from chicken egg white contains 129 amino acids, so in our computational model, a lysozyme molecule is represented by 129 monomers (or polymer units), each of mass 110.91 Da, in a bead-and-spring model [65], so that the total mass of the molecule sums up to 14307 Da, the laboratory mass. In the bead-and-spring model, linked monomers (represented by beads) are connected by anharmonic springs with strengths appropriate for chemical bonding while non-linked monomers interact by weak non-bonding interactions.

In this model, the laser irradiation of pure solid lysozyme targets, as well as lysozyme targets with impregnated water will be simulated. Both lysozyme and water are modeled as breathing spheres. The interaction between water and lysozyme molecules is weak (non-bonding), and due to the low concentrations of water, it is approximated to be the same interaction potential used for non-bonding interactions in lysozyme molecules.

The breathing sphere model has been combined with the bead-and-spring model for studying the ejection of polymer molecules in matrix-assisted pulsed laser evaporation [8]. The bead-and-spring model developed in this work for polymer lysozyme is a modified version, with the bead additionally exercising breathing motion, and so it differs from the conventional model of hard beads. This version can be called the "soft-bead-and-spring" model or the "breathing-bead-and-spring" model.

2.1.2   Molecular Description of Metalorganic Precursor Solution Target

Both an experimental overview of the irradiated target, and a coarse-grained molecular representation are provided.

2.1.2.1 Experimental overview of laser irradiation of metalorganic

precursor solution target

In the research nomenclature, the target is defined as the solid mass resulting from the flash-freezing of specific acetate systems in solvent. Material systems investigated by our experimental collaborators are chiefly made of single noble metal-acetate/solvent solution, e.g. [PdAc + H_2O], [AgAc + H_2O], [PdAc + acetone] for the formation of nanoparticles. The reasoning behind the selection of H_2O as a candidate solvent is based on the reduction of photochemical effects due to weak absorption and high freezing temperature. In addition, contamination from external moisture build-up during chamber transfers will not adversely affect the deposition characteristics. The target typically contains < 5 wt% of frozen solute material, the MOP.

The frozen composite target is positioned on a cold stage in a vacuum system, at a base pressure of 10^{-6} Torr. The nanoparticles generated in the ablation process are deposited on substrates of single crystal Si, electron microscopy grids, and on NaCl crystals. Fluencies employed for ablation of the target are typically less than 1 J/cm^2.

2.1.2.2 Coarse-grained molecular representation of metalorganic precursor solution target

Laser interactions with a MAPLE target loaded with metalorganic precursors are described in the proposed work by CGMD, combining the breathing sphere model for simulation of the molecular matrix and MOP molecules and the embedded-atom method (EAM) [66] for interactions among the metal atoms released in laser-induced decomposition of the precursors.

The EAM potential [67] provides a computationally simple but rather realistic description of bonding in metallic systems. A MOP molecule, containing a single metal atom, is represented in the CGMD by a breathing sphere. Due to direct photon absorption or local temperature increase, the MOP molecule can decompose to release the metal atom and the product molecules or radicals. The chemical energy released (or absorbed) is to be distributed among the reaction products and surrounding molecules. The coarse-grained representation of chemical reactions is an important feature of the model that allows us to not only reproduce the release of the metal atoms, but to account for the heats of the photochemical and thermally-activated reactions and corresponding contributions to the ablation process.

2.2 Breathing Sphere Model

The breathing sphere model has been actively used in investigations of laser interaction with molecular targets, e.g. in Refs. [9, 58, 68, 69, 70, 71]. Briefly, the model adapts a coarse-grained representation of the molecules by spherical particles with real translational degrees of freedom, but approximate representation of the internal vibrational modes by a single internal degree of freedom. The internal degree of freedom, or breathing mode, is implemented by allowing the particles to change their sizes or to "breathe". The breathing mode can be used for simulation of molecular excitation by photon absorption and vibrational relaxation of the excited molecules. The use of water as a matrix eliminates the necessity to consider the matrix as a recipient of the photon energy, as the absorption of water is negligible at laser wavelengths used in experiments [72]. At the same time, the parameters of a potential function attributed to the internal motion can be used to provide a realistic representation of the thermodynamic properties of water while

still keeping the computationally efficient coarse-grained representation of the material. In the model that is developed for this project, the breathing mode is connected to a "heat bath" representing the internal degrees of freedom of the matrix units that are active at a given temperature and contribute to the heat capacity of the matrix, but are missing in the breathing sphere model. An energy transfer algorithm is used to connect the breathing mode to the energy bath with a heat capacity chosen based on the real heat capacity of the group of atoms or molecules represented by each breathing sphere. The rate of the energy exchange between the breathing motion energy and the energy of translational motions of the breathing spheres, as well as the coupling strength between the breathing motion and the heat bath are parameters of the model that are chosen to bring the heat capacity of the model material close to experimental values.

In the breathing sphere (BS) model, the dynamic unit is a spherical particle that is void of any intramolecular structure, has mass M, and is assigned an equilibrium radius, R_0, about which it can expand or contract resulting in a variable radius, $R(t)$. Each coarse-grained particle is therefore a breathing sphere molecule that exercises breathing motion about its equilibrium radius in addition to its translational motion. For water, a breathing sphere represents a group of water molecules. For lysozyme, a breathing sphere is a monomer in a polymer chain, *i.e.*, a bead in the bead-and-spring model representation.

In the breathing sphere model, all intermolecular interactions are described by the Morse potential, originally developed for the description of diatomic molecules [73], and later adopted for describing intermolecular non-bonding interactions, *e.g.*, [8, 74, 75]. The functional form of the Morse potential is

$$U(r) = D_e \{\exp[-2\beta(r - r_e)] - 2\exp[-\beta(r - r_e)]\} \qquad (2.1)$$

where r is the distance between edges of any two BS molecules: $r = \left| \overline{r_i} - \overline{r_j} \right| - R_i - R_j$, r_e is the equilibrium separation, $\overline{r_i}$ and $\overline{r_j}$ are positions of molecules i and j, respectively, and R_i and R_j are their radii. The parameters of the Morse potential, $_e$, β, and r_e, along with the mass M and the equilibrium radius R_o of a breathing sphere particle, are defining the physical properties of the model material.

The breathing motion is controlled by an inertia parameter (or effective mass) M_I ascribed to the corresponding breathing degree of freedom and an anharmonic potential [58]:

$$U_R(R) = k_1(R_i - R_o)^2 + k_2(R_i - R_o)^3 + k_3(R_i - R_o)^4 \tag{2.2}$$

where R_i is the instantaneous radius of particle i and k_1, k_2, and k_3 are parameters of the potential. The parameters of this potential control the strength of coupling between the vibrational modes of translational motion of the particles and their breathing mode. The choice of the parameters, therefore, can be used to ensure that the rate of the energy equilibration between the optically-excited molecules and their surroundings matches the results of pump-probe experiments or atomistic simulations.

Water is the major constituent (the matrix) of targets containing the aqueous solutions of MOP, and is the minor constituent of lysozyme targets. Water is also abundant in nature, and its properties are well known. Therefore, significant effort is made to adequately represent properties of bulk water in the coarse-grained computational model. Unlike water (or in comparison to water), not so many physical properties of lysozyme are known. Given the variation in determined values of the density of lysozyme, ranging from ~ 0.76 g/cm^3 in the PLD experiment to $\sim 1.2 - 1.4$ g/cm^3 as lab grown samples, only an approximate value of the density of lysozyme will be aimed at in the fitting of the Morse potential: the density of a globule has been calculated to be 1.2 g/cm^3 (above, in sub-section 2.1.1), and we will aim at 1 g/cm^3.

In the aqueous solution of metalorganic precursor system, all other molecules are also represented as coarse-grained breathing sphere molecules. The physical state of solute MOP (PdAc) molecules in solution is of interest to us, and so the interaction between PdAc molecules is fitted to approximately describe some useful properties of solid PdAc. The remaining intermolecular interactions (i.e. exclusive of water-water and MOP-MOP interactions) are unknown, but because of their non-bonding nature, they can be approximately described by the same interaction potential used for water molecules. This includes the interactions (1) between water and all other molecules, be it MOP or a product molecule of its photolytic decomposition, (2) between MOP and product molecules, and (3) between product molecules. This approximation is adequate for a semi-quantitative description of the laser target, as the interactions considered are less than ~ 5 % of the total number of interactions. The laser target contains less than or equal to 5 wt% of PdAc and its decomposition products.

The breathing sphere (BS) model is adapted to adequately describe known material properties of water, lysozyme and palladium acetate. The same breathing sphere reference system is adopted to describe the intermolecular interactions (Morse potential) and the breathing potential in both water and lysozyme, so the determination of the Morse potential will be described first, followed by the determination of the internal potential. We start the description of the breathing sphere model with descriptions for the target matrix, i.e. water for the metalorganic precursor target, and lysozyme for the target made of lysozyme and water. This will be followed by a description of the model for energy transfer between the dynamic modes and the internal modes. Parametrization of the breathing sphere model for the metalorganic precursor will be lastly discussed.

2.2.1   Parametrization of Breathing Sphere Model for Target Matrices –

Water and Lysozyme

In this sub-section, for water and lysozyme, we discuss the determination of the intermolecular potential and its implementation, followed by fitting of the internal 'breathing' potential to adequately couple the breathing and translational degrees of freedom.

2.2.1.1 Determination of the intermolecular potential

The intermolecular interactions are calculated between every pair of molecules in the system, and the number of terms to be calculated in a system of N molecules is $N(N-1)/2$, and so its increase in relation to the increase in the number of molecules is of order N^2. However, pair potentials fall off rapidly with distance, e.g. at 2.5σ the Lennard-Jones potential has just 1% of its value at σ, $1/(2^{1/6})$ of the equilibrium separation [76] [The Morse potential behaves similarly]. To reduce the number of pair-wise calculations for a molecule, without significantly altering the total potential, a cut-off range is implemented within which pair-wise interactions are considered. Truncating the potential, however, introduces discontinuities both in the potential and its derivative. A discontinuity in the derivative means an abrupt change in the force field. Such a change is misrepresentative of actual dynamics, and may lead to failure in energy conservation. It is therefore necessary to implement a switching function at the cut-off, which renders the modified potential continuous. Discussion of the implementation of the switching function is done in the last part of this sub-section.

2.2.1.1.1   Determination of the intermolecular potential for water

The Morse potential parameters of the untermolecular potential, Eq. (2.1), for water are chosen to approximately reproduce the following properties of water: density (ρ), speed of sound (C_s) or bulk modulus (B), melting temperature (T_m), and the critical temperature (T_c) of water. These

are properties that are well known, and are of important consideration to laser ablation investigations. Ambient water density (ρ_0) of 1.0 g/cm^3 is primarily aimed at during fitting. The remaining properties – C_s, T_c, T_m – are fitted, within an accuracy of ~ 20 %, to experimental properties of water. This accuracy is satisfactory, as we aim only at a semi-quantitative description of the ablation phenomenon.

The parameters of the Morse potential are fitted, in comparison, to a parametrized breathing sphere model first used for a generic description of amorphous organic solids [55], and later on used for describing organic materials, having similar properties to water, such as chlorobenzene, toluene or chloroform, in laser ablation investigations [8, 9, 10]. The material properties of the model amorphous solid, not significantly differing from those of water, are: density (ρ) = 1.2 g/cm^3, bulk modulus (B) = 5 GPa, cohesive energy (ε_{coh}) = 0.6 eV. The parameters for the described BS organic model are: D_e= 0.1 eV, β = 1.0 Å, r_e = 3.0 Å^{-1}, M = 100 Da, and R_0 = 1.4 Å. A number of approximations, described in the next few paragraphs, will be useful to scaling these parameters to those that fit to water properties. In these approximations, the density, the bulk modulus, and the surface energy per unit area are properties that are compared for the reference model system and the fitting breathing sphere model for water, through parameters of the intermolecular potential. The properties of the fitting system, the density and the bulk modulus assume the values ρ' = 1.0 g/cm^3 and B' = 2.2 GPa, respectively, while the cohesive energy ε_{coh}' is made adjustable.

Two different BS molecule ensembles, material properties of which are to be compared, can be defined: an ensemble of BS molecules of mass M and radius R described by a set of Morse potential interaction parameters – $\{D_e, r_e, \beta\}$, and another ensemble of BS molecules of

mass, M', and radius, R', described by a set of Morse potential interaction parameters – $\{D_e', r_e', \beta'\}$.

The densities of the reference system and the fitting system can be related. Defining r_o, half the equilibrium separation of two BS molecules, through R and r_e as $r_o = R + r_e/2$, we obtain a relation between equilibrium separations of BS edges for two ensembles of differing densities, ρ and ρ':

$$\frac{\rho'}{\rho} = \frac{M'}{M}\left(\frac{2R + r_e}{2R' + r_e'}\right)^3 \tag{2.3}$$

For a given cohesive energy per molecule, ε_{coh}, the surface energy per unit area, ε_S, is proportional to the number density of molecules:

$$\varepsilon_S \propto \varepsilon_{coh} \cdot n_V{}^{2/3} \tag{2.4}$$

If one were to maintain the same energy per surface area for two systems with differing BS masses, the relation between cohesive energies per molecule for the systems with different masses is derived from Eq. (2.4) to be:

$$\frac{\varepsilon_{coh}'}{\varepsilon_{coh}} = \left(\frac{M'}{M} \cdot \frac{\rho}{\rho'}\right)^{2/3} \tag{2.5}$$

after employing a usual definition of the number density, $n_V = \rho/M$. Inserting the relation in Eq. (2.3) into Eq. (2.5) obtains

$$\frac{\varepsilon_{coh}'}{\varepsilon_{coh}} = \left(\frac{2R' + r_e'}{2R + r_e}\right)^2 \tag{2.6}$$

The Morse potential well depth $_e$ is deemed to be directly proportional to the cohesive energy per molecule in the new system, so that the well depth in the old and new system can be related in Eq. (2.7),

$$_e' = D_e(\varepsilon_{coh}'/\varepsilon_{coh}) \tag{2.7}$$

At separations close to the equilibrium separation r_e, a second order Taylor expansion of the Morse potential, $\Phi(r - r_e) \cong U(r)$, can be obtained:

$$\Phi(r - r_e) = -D_e + D_e\beta^2(r - r_e)^2 \tag{2.8}$$

Eq. (2.8) can be observed to be simple harmonic in displacements from equilibrium, $x = r - r_e$, about the well depth, $-D_e$, so that making a comparison to the simple harmonic potential form about the well depth,

$$U = \frac{1}{2}kx^2 \tag{2.9}$$

we obtain the harmonic force constant,

$$k = 2D_e\beta^2 \tag{2.10}$$

The elastic properties of a material depend on the force constant: the higher the value of k, the higher the bulk modulus, B, is expected to be. The relation in Eq. (2.10) is used to modify the Morse parameters to the attainment of a desirable value of the bulk modulus.

In summary, in the process of determining parameters of the Morse potential that aim at describing material properties, the derived relations will be useful in modifying already known parameters to alter the material properties of the system to desired values: Eq. (2.3) relates the parameters r_e and R to the density; Eqs. (2.5) – (2.7) relate D_e to the cohesive energy; and (Eq. 2.10) relates D_e and β to the bulk modulus. The following steps are made to determine approximate parameters of the intermolecular potential, D_e', β', r_e', M', and R_0', for water.

i. Although a coarse grain is made of a number of molecules, the strength of the cohesive energy is mostly governed by interactions between molecules at its surface; the separation between BS edges r_e will therefore be chosen to equal an approximate value of intermolecular separation in experimental or atomistic water. The separation between O

atoms in water molecules is ~ 3 Å (see section 4 for atomistic model), and so $r_e = 3.0$ Å will be chosen, as it well approximates this value.

ii. Initially, one aims at reducing the bulk modulus from the value of the reference system, $B' = 5$ GPa, to $B = 2.2$ GPa, the value for water. Since the force constant is related to the bulk modulus, scaling it down by the same factor – which is $k'/k = B'/B = 2.2/5 = 0.44$ – the bulk modulus ought to be scaled leads to a down-scale in $_e$, according to Eq. (2.10) by the same factor: $D_e' = 0.44 D_e = 0.044$ eV.

iii. The relation in Eq. (2.8) is used to find an estimate for the cohesive energy per molecule $\varepsilon_{coh}' = 0.264$ eV. If the surface energy of the fitting system is the same as that of the reference system, then the equilibrium BS radius, according to Eq. (2.6), would be $R' = 0.42$ Å, and the mass of BS molecule, according to Eq. (2.3), would be $M' = 35$ Da. Although the estimated value for M' is approximately representative of the mass of two water molecules, in order to increase computational efficiency, we aim at having a higher mass without significantly deviating from the fitting material properties. Setting a mass of BS molecule to be $M' = 50$ Da in Eq. (2.3) then determines the value of the equilibrium BS radius to be $R' = 0.95$ Å.

The already approximated parameters of the fitting Morse potential are: $M' = 50$ Da, $R' = 0.95$ Å, $_e' = 0.044$ eV, $r_e' = 3.0$ Å. Fitting is done around these values, in addition to varying the value of β', to aim at experimental water properties.

The variation in β is mostly used to adjust to material properties in a compensatory fashion: making β higher is expected to increase the bulk modulus as already described before, but this makes the range of the potential shorter, reducing the attraction of molecules beyond the equilibrium distance from a molecule and effectively lowering the density.

Simulations are run – in which densities, bulk moduli, and phase transition temperatures are estimated – for a few trial values around the approximated parameters $M' = 50$ Da, $R' = 0.95$ Å, $_e' = 0.044$ eV, $r_e' = 3.0$ Å. A final set of parameters, that provide a satisfactory semi-quantitaive description of experimental properties of water relevant to the ablation phenomenon, are: $M = 50$ Da, $R = 0.8$ Å, $D_e = 0.045$ eV, $r_e = 3.0$ Å, $\beta = 1.3$ Å^{-1}, see Table 2.1.

Further investigations are then carried out, by MD simulations, to determine the properties of an equilibrated system of BS molecules that is described by the fitted parameters. Comparisons are then made to experimental properties, and summarized in Table 2.4. The properties of the parametrized and equilibrated NPT ($P = 0$, $T = 300$K) ensemble of 6912 BS molecules in a cubic computational cell, of side length 82.76 Å, with an equilibrated density of 1.0 g/cm^3, that are to be determined are: speed of sound (C_s), explosive boiling temperature (T_b^*), and melting temperature (T_m).

Table 2.1. Parameters of the coarse-grained breathing sphere model for water.

M, a.m.u	R, Å	$_e$, eV	β, 1/Å	r_e, Å
50	0.8	0.045	1.3	3.0

2.2.1.1.1.1 Determination of the speed of sound

The speed of sound C_s is related to the bulk modulus B, given the value of the density ρ_0, as described in Eq. (2.11).

$$C_s = \sqrt{B/\rho_o} \tag{2.11}$$

The bulk modulus can be determined through an equation of state, Eq. (2.12), that provides for easy determination of the speed of sound in the BS model, using Eq. (2.11).

$$B = -V\frac{\partial P}{\partial V} \tag{2.12}$$

The speed of sound of water in ambient conditions has been determined experimentally to be

1492 m/s [77], from which the bulk modulus can be determined as $B = 2.2$ GPa, implementing

Eq. (2.11).

Rewriting Eq. (2.12) in terms of the density ρ, obtains

$$B = \rho \frac{\partial P}{\partial \rho} \tag{2.13}$$

which is equivalent to

$$B = \tilde{\rho} \frac{\partial P}{\partial \tilde{\rho}} \tag{2.14}$$

where the relative density, $\tilde{\rho}$, is $\tilde{\rho} = \rho/\rho_0$. The bulk modulus B is determined in Eq. (2.14)

from a $\tilde{\rho}$ vs P dependence about the equilibrium ($\tilde{\rho} = 1$), for simulated *NVE* ensembles of the

parametrized system. This dependence is displayed in Table 2.2.

Table 2.2. Dependence of density on pressure for breathing sphere water.

$\tilde{\rho}$	P (MPa)	Uncertainty in P, ΔP (MPa)
0.98	-36	5
0.99	-16	3
1.01	19	4
1.02	35	4

A plot of $\tilde{\rho}$ vs. P is shown in Figure 2.1. The density – pressure relationship is quasi-linear, and

B can be found from the slope of the linear dependence at $\tilde{\rho} = 1.0$, according to Eq. (2.14), to be

$B = 1.8\ GPa$, erring from experimental value by 18 %. Given the value of B, the speed of sound

is calculated from Eq. (2.11) to be $C_s = 1340\ m/s$.

The relative error in C_s can be determined by Eq. (2.15), see appendix B1 for error propagation analysis,

$$\frac{\Delta C_s}{C_s} = \frac{1}{2}\left(\frac{\Delta B}{B} + \frac{\Delta \rho}{\rho}\right) \tag{2.15}$$

in which $\Delta\rho/\rho = 0$ %, and $\Delta B/B = 18$ %, yielding $\Delta C_s/C_s = 9$ %.
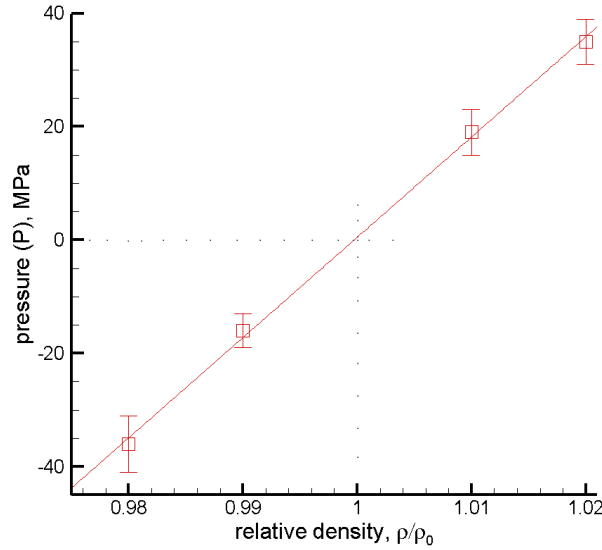
Figure 2.1 Pressure of BS water as a function of density in relation to the equilibrium density ρ_0. The dotted lines refer to the state of equilibrium $(P = 0)$

2.2.1.1.1.2 Determination of the critical temperature of water

The critical temperature of the model material is not rigorously calculated but estimated from the threshold temperature for the onset of explosive boiling.

The physical properties of superheated water have been studied at temperatures up to 220 ^{o}C, at one bar pressure [78]. In this study the thermal expansivity of water is determined, and it is noticed to rise significantly as it approaches the temperature upper-limit of the measurement (220 ^{o}C $\equiv$ 493 K). A significant or dramatic increase in volume is characteristic of a state that is approaching a state of phase explosion (or explosive boiling).

Similar to the observations on the dependence of expansivity on temperature in Ref. [78], we can determine the dependence of volume on temperature at constant pressure. The material system in a liquid state is heated at constant pressure, and the onset of phase explosion is determined from a sharp rise in the volume, as had been done earlier for the breathing sphere representation of Ar, in Ref. [147]. The threshold temperature of explosive boiling can be expected at ∼ 10-20 % below the critical temperature [12]. Thus, the critical temperature T_c is estimated from the approximated relation $T_b^* \approx 0.85\ T_c$.

The volume-temperature dependence of a *NPT* ($P = 0$) ensemble of the parametrized system is determined, displayed in Table 2.3 in the form of a ρ vs. T dependence, and plotted in Figure 2.2. Starting from 300 K, the temperature of the system is increased at intervals of (100 ps)/(20 K), until its temperature is 400 K when the interval rate is increased to (200 ps)/(10 K); the interval rate becomes (200 ps)/(5 K) at 480 K. At 495 K, the rate of temperature increase is more than (100 ps)/K, as it takes indefinitely long for the system to equilibrate at 496 K.

The temperature of BS water for the onset of a phase explosion at P = 0 is considered to be T_b^* = 495 K ± 1 K. At 495K, the ensemble of water molecules has a density of 0.57 g/cm^3. In comparison, the experimental explosive boiling of water at ∼ $0.8T_c - 0.9T_c$, where T_c = 647K [79] is the critical temperature at a critical density of 0.32 g/cm^3, is ∼ 518K – 582K. The experimental value is above the obtained simulated value by up to about 18 %.

Table 2.3 Dependence of density on temperature of paramterized breathing sphere (BS) water at P = 0.

T, K	300	320	340	360	380	400	410	420	430	440	450	460	470
ρ, g/cm^3	1.01	0.99	0.97	0.94	0.91	0.88	0.86	0.84	0.82	0.80	0.77	0.75	0.71
T, K	480	485	490	495									

ρ, g/cm^3	0.67	0.64	0.61	0.57									

Figure 2.2 Temperature vs. volume dependence of parametrized breathing sphere (BS) water.

2.2.1.1.1.3 Determination of melting temperature

The melting temperature of ice will not be determined from directly heating the solid until it is seen to melt, in *NPT* simulations. This is because, the absence of a nucleation region (impurity, defect, or interface) will lead to the solid being superheated, causing the solid to melt homogeneously at a temperature that is higher than its actual melting point. Introducing a liquid-solid interface will remove the need of avoiding superheating (or supercooling) in computer simulation.

The melting point of ice I_h has been determined from direct co-existence of the solid-liquid interface, using molecular dynamics simulations of computational cell boxes containing liquid

water and ice in contact, see Ref. [80]. In this Ref., the implementation is based on the analysis of the evolution of the total energy along *NPT* simulations at different temperatures about the melting point: at a temperature above the melting point, the energy is bound to rise (due to heat needed for melting) until it becomes constant when the whole box is melted; at a temperature below the melting point, the energy is bound to decrease (due to heat extracted during solidification) until it becomes constant when the whole box is solidified. In this work, rather than run several *NPT* simulations that differ by temperature, we adopt an approach similar to the molecular-dynamics based approach used in Ref. [81], in which co-existing solid and liquid phases of the modelled material system evolve toward the same melting temperature. In Ref. [81], the material system is simulated in a *NVE* ensemble, but in this work the pressure is maintained constant during simulations. It will also be demonstrated that the thermodynamic enthalpy is unchanged in the simulation, i.e. the thermodynamic ensemble is *NPH*.

Natural water is having a hexagonal close-packed (HCP) structure in the solid state (ice). In the BS model, to reproduce a closely packed but simpler structure, a face-centred cubic (FCC) structure for ice is generated. The period of the lattice spacing a_l is related to the density ρ through Eq. (2.16),

$$\rho = \frac{n_k . A_m}{N_A . a_l{}^3} \tag{2.16}$$

where n_k is the number of atoms in a unit cell, A_m is the molar mass, and N_A is the Avogadro number. For FCC, $n_k = 4$. A FCC structure of BS water at $T = 0$ K is displayed in Figure 2.3.
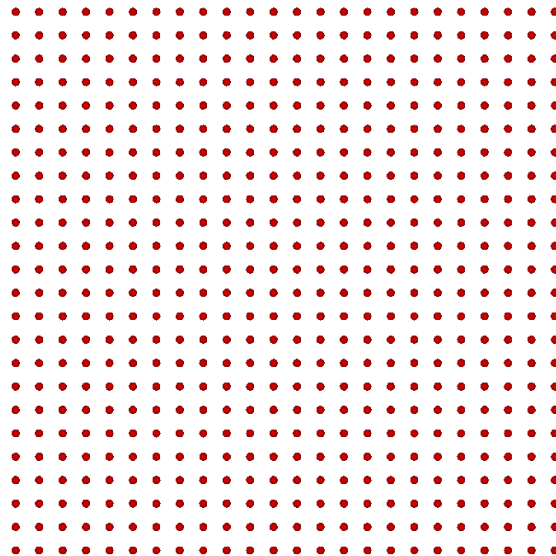
Figure 2.3   FCC breathing sphere ice at $T = 0$ K.

A solid FCC sample of 20736 molecules, with dimensions 80.65 Å $\times 80.65$ Å $\times 241.96$ Å, is equilibrated at $T = 260$ K, at $P = 0$. One third of the sample is quickly heated to 380 K, so that only the heated part is melted, obtaining a solid-liquid co-existing structure. The resultant structure is then relaxed at $P = 0$ in periodic boundary conditions; snapshots of the equilibrating structure are displayed in Figure 2.4. During equilibration, the liquid part, which is originally only a third of the sample, is seen to grow until its volume fraction becomes unchanged, at equilibrium. The temperature of the equilibrating sample is also observed – see Figure 2.5; it decreases, owing to heat loss due to melting, until it assumes a mildly fluctuating equilibrium temperature at ~ 1300 ps. This equilibrium temperature is determined here as the melting temperature (T_m), and it is $T_m = 329.8\pm1.5$ K. The uncertainty in the temperature is the standard deviation (*STD*) about the equilibrium, and is determined in appendix B2.

It is demonstrated that the simulated ensemble for the determination of melting temperature is a *NPH* ensemble, by showing that the enthalpy is unchanged ($dH = 0$). Defining enthalpy as $H = U + PV$, a change in enthalpy is defined as

$$dH = dU + PdV + VdP \tag{2.17}$$

which in the thermodynamic conditions of the simulation ($dP = 0$), becomes

$$dH = dQ \tag{2.18}$$

after implementing the first law of thermodynamics, $dU = dQ - PdV$, in which dQ is an infinitesimal amount of heat flow. In the simulation, there is no heat flow into or out of the system, and so $dQ = 0$ in Eq. (2.18). Hence,

$$dH = 0 \tag{2.19}$$

and the ensemble is *NPH*.
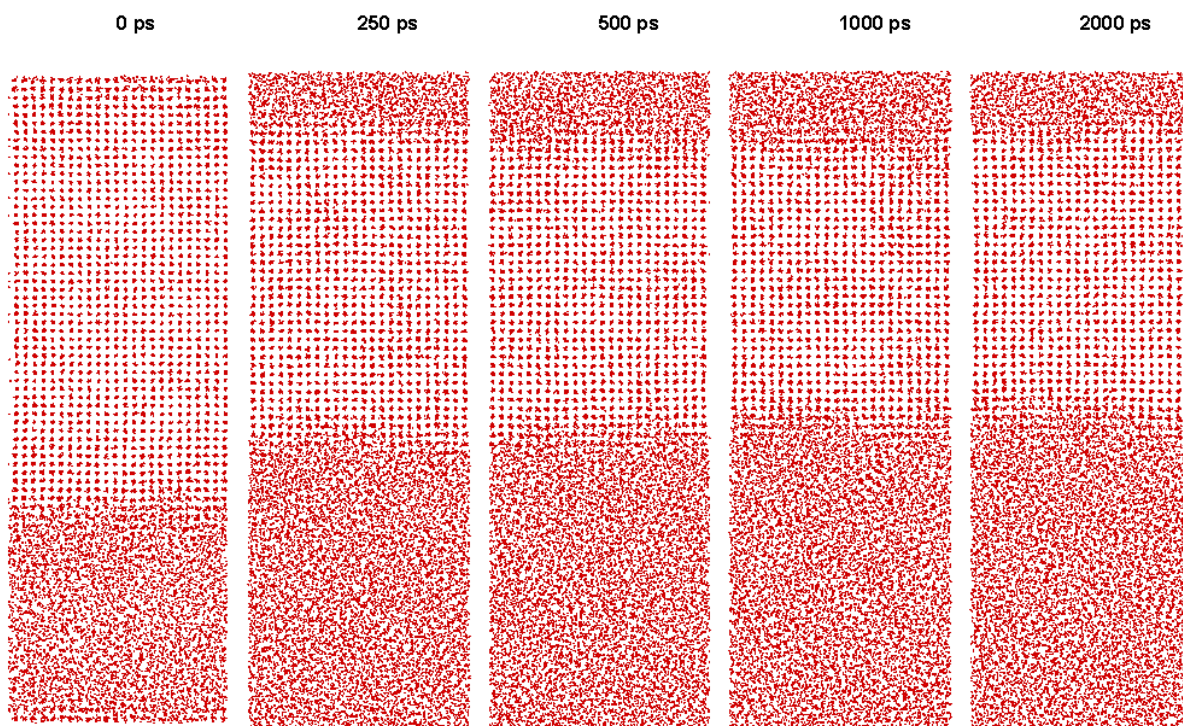
Figure 2.4   Snapshots of the co-existing solid-liquid BS water structure.
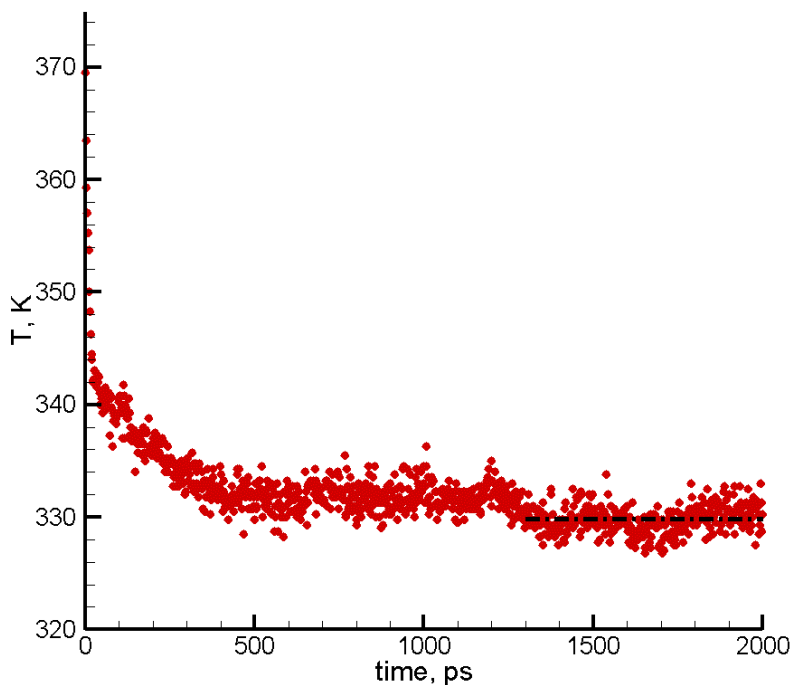
Figure 2.5 Temperature of the co-existing solid-liquid BS water structure during simulation. The black dash-dotted line is the average temperature (T_m) during the estimated equilibration time.

2.2.1.1.1.4 Summary on fitting of Morse potential for breathing sphere water

The determined properties of breathing sphere water described by the parametrized Morse potential are summarized in Table 2.4, alongside the experimental properties of water. The fitted properties deviate from the experimental properties up to about 20 %. The parametrization of the breathing sphere model for water is, however, not yet complete, since the parameters of the internal breathing potential still have to be determined, see sub-section 2.2.3

Table 2.4. Comparison of fitted BS water properties to experimental properties

properties of water	experiment	model	error, %
density, g/cm^3	1.0 [82]	1.0	0
speed of sound, m/s	1492 [77], 1497 [83]	1340	9
bulk modulus, GPa	2.2[1]	1.8	18
critical temperature, K	647 [82]	582	10
melting temperature, K	273 [82]	330	21

2.2.1.1.2   Fitting of Morse potential for lysozyme

The Morse potential parameters for chemical bonding between polymer units: D_e = 3.48 eV, β = 2.37 Å^{-1}, r_e = 1.54 Å, are those priorly fitted to the characteristics of a typical carbon-carbon bond in a polymer molecule [8]. The value of r_e is the length of the middle C-C bond in (C#)$_3$-C-CH$_2$-C# (where C# is any sp^3 carbon atom) [84], the depth of the potential well, D_e, approximately reproduces the value of the energy of dissociation, through the C-C backbone, of poly(methyl methacrylate) (PMMA) – 332 kJ/mol [85], and β is calculated from the value of the stretching force constant for C-C bond in polyethylene [86], $d^2U/dr^2|_{r_e}$ = $2\beta^2D_e$ = 39 eV/Å^2. The backbone strength is expected to insignificantly change from one polypeptide material to another.

The fitting of the Morse potential for non-bonding interactions between polymer units are fitted using the reference set of parameters used for a generic description of amorphous organic solids

---

[1] The value for bulk modulus is calculated from the experimental values of the speed of sound and the density.

[58], as was done for fitting the breathing sphere water potential. Most of the organic materials whose properties are aimed at in the parametrization of the reference potential have approximately the same mass of a molecule as that of a lysozyme polymer unit, and are of densities close to that of lysozyme, e.g., glycerol has density 1.25 g/cm^3 and molecular mass 92.1 Da [87], toluene has density 1.01 g/cm^3 and molecular mass 92.1 Da [88]. The parameters of the Morse potential in the reference BS organic model are: D_e= 0.1 eV, β = 1.0 Å, r_e = 3.0 Å^{-1}, M = 100 Da, and R_0 = 1.4 Å. In our model, a lysozyme polymer unit has mass M = 111 Da – this is close to the mass of BS molecule in the reference model, and so many of the Morse parameters are expected to be similar. The equilibrium radius of a polymer unit in the model of lysozyme is set to that of the reference model, R_0 = 1.4 Å, and Morse parameters are adjusted to approximately reproduce the experimental density of a thermally equilibrated lysozyme globule in MD simulation at constant temperature (T = 300 K) and constant pressure (P = 0). The density of the globule from simulation is determined in the same way as was done for determining the experimental density: the mass of the globule is divided by the volume defined by the dimensions of the globule. Because in a state of thermal equilibration the dimensions may mildly fluctuate over time, a precise value as that determined from experiment is not aimed at, but rather a close and adequate value is aimed at. A density of 1 g/cm^3 is aimed at. The resultant set of parameters that is consistent with obtaining a density of 1 g/cm^3 is D_e= 0.15 eV, β = 0.9 Å^{-1}, r_e = 2.8 Å.

  The parameters of the BS model for intermolecular interactions in lysozyme are summarized in Table 2.5.

Table 2.5. Parameters of the BS model for intermolecular interactions in lysozyme

Intermolecular potential	M, a.m.u	R_o, Å	$_e$, eV	β, 1/Å	r_e, Å

| Lysozyme bonding | 111 | 1.4 | 3.5 | 2.37 | 1.54 |
| Lysozyme non-bonding | 111 | 1.4 | 0.15 | 0.9 | 2.8 |

2.2.1.1.3   Implementation of intermolecular (Morse) potential

The Morse potential function, $U(r)$, truncated at some finite distance – the cut-off distance (r_C) – is having a non-zero value in the function and in the derivative at r_C. It is desired to smoothly bring both the implemented potential and its first derivative to zero at r_C. This can be done by applying a switching function, $S(r)$, which in addition to satisfying zero-value boundary conditions at r_C satisfies continuity conditions with the Morse potential and its derivative at the switching point, r_S. The boundary conditions are then:

$$\text{i. } S(r) = U(r) \text{ at } r = r_S$$

$$\text{ii. } S'(r) = U'(r) \text{ at } r = r_S$$

$$\text{iii. } S(r) = 0 \text{ at } r = r_C$$

$$\text{iv. } S'(r) = 0 \text{ at } r = r_C.$$

The switching function $S(r)$ can be suitably described by a cubic polynomial function,

$$S(r) = a_3(r - r_S)^3 + a_2(r - r_S)^2 + a_1(r - r_S) + a_0 \qquad (2.20)$$

having as first derivative

$$S'(r) = 3a_3(r - r_S)^2 + 2a_2(r - r_S) + a_1 \qquad (2.21)$$

Implementing condition i) in Eq. (2.20) yields the value of a_0 :

$$a_0 = U(r_S)$$

Implementing condition ii) in Eq. (2.21) yields the value of a_1:

$$a_1 = U'(r_S)$$

Using already obtained values of a_0 and a_1, implementation of boundary conditions (iii) and (iv) in Eqs. (2.20) and (2.21), respectively, yield equations in a_2 and a_3:

$$a_3(r_C - r_S)^3 + a_2(r_C - r_S)^2 + U'(r_S) \cdot (r_C - r_S) + U(r_S) = 0 \qquad (2.22)$$

and

$$3a_3(r_C - r_S)^2 + 2a_2(r_C - r_S) + U'(r_S) = 0 \qquad (2.23)$$

A combined solution of Eqs. (2.22) and (2.23) yields the values of a_2 and a_3:

$$a_2 = -\frac{3U(r_S) + 2(r_C - r_S) \cdot U'(r_S)}{(r_C - r_S)^2}; \; a_3 = \frac{2U(r_S) + (r_C - r_S) \cdot U'(r_S)}{(r_C - r_S)^3}$$

The switching point r_S can be chosen in relation to the point of inflexion, r_I, of the Morse potential function. The point of inflexion r_I is determined as the abscissa value at which the second derivative of the Morse potential function is zero, i.e.

$$U''(r) = 0 \text{ at } r_I = r_e + \ln(2)/\beta$$

After determining the coefficients in Eq. (2.20), the smoothed potential, $U_S(r)$, is then described within the cut-off interval as:

$$U_S(r) = \begin{cases} U(r), & 0 < r < r_S \\ S(r), & r_S \leq r \leq r_C \end{cases} \qquad (2.24)$$

A switching function is obtained for each of the different Morse potentials that have been parametrized, and the coefficients of the smoothing functions are tabulated in Table 2.6. Diagrams of the Morse potential and its derivative are displayed in Figures 2.6 and 2.8, for non-bonding interactions of water and lysozyme interactions, respectively. The corresponding smoothed functions are displayed in Figures 2.7 and 2.9, respectively. The smoothed function for the bonding interaction is displayed in Figure 2.10.
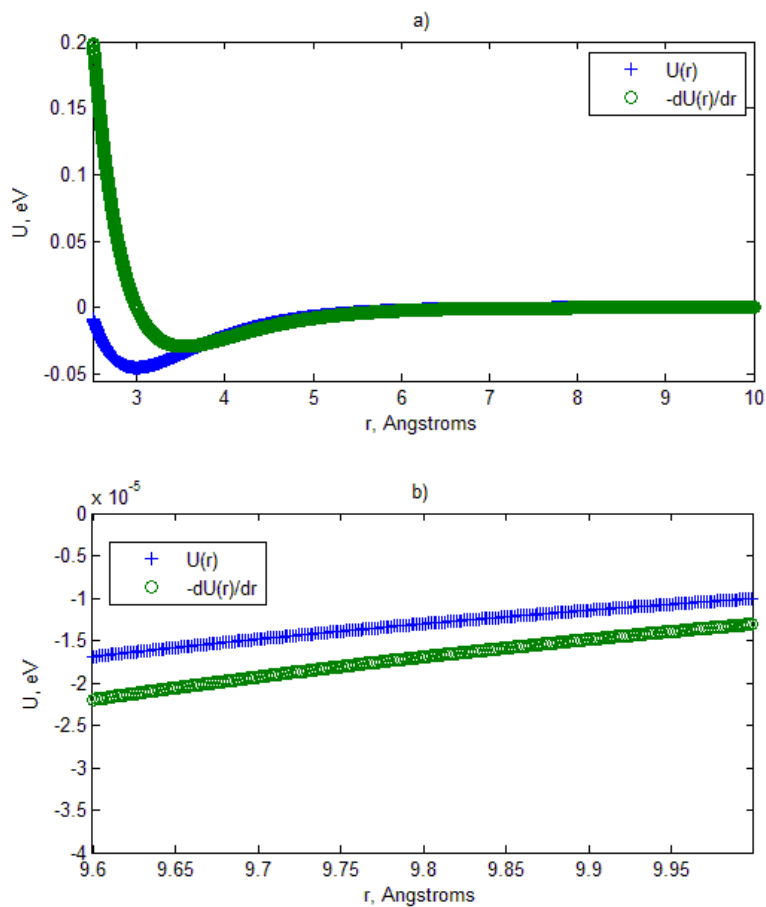
Figure 2.6 – a) Morse potential for water and the negative of its derivative, b) diagram displaying non-zero values of Morse potential and its first derivative at $r_C = 10$ Å.

Table 2.6. Coefficients in smoothing functions employed for different Morse potentials describing the target matrices.

Intermolecular Interaction parameters	$_e$[eV]; β[1/Å]; r_e[Å]	r_C, Å	r_S, Å	a_0; a_1; a_2; a_3
Water	0.045; 1.30; 3.0	10	7.7332	$-1.9121 \cdot 10^{-4}$; $2.483 \cdot 10^{-4}$; $-1.0744 \cdot 10^{-4}$; $1.5492 \cdot 10^{-5}$

Bonding lysozyme	3.5; 2.37; 1.54	6.5	5.3325	$-8.7405 \cdot 10^{-4};\ 2.1 \cdot 10^{-3};$ $-1.6 \cdot 10^{-3};\ 4.2116 \cdot 10^{-4}$
Non-bonding lysozyme	0.15; 0.9; 2.8	10	6.7702	$-8.3 \cdot 10^{-3};\ 7.4 \cdot 10^{-3};$ $-2.20 \cdot 10^{-3};\ 2.1326 \cdot 10^{-4}$

a)
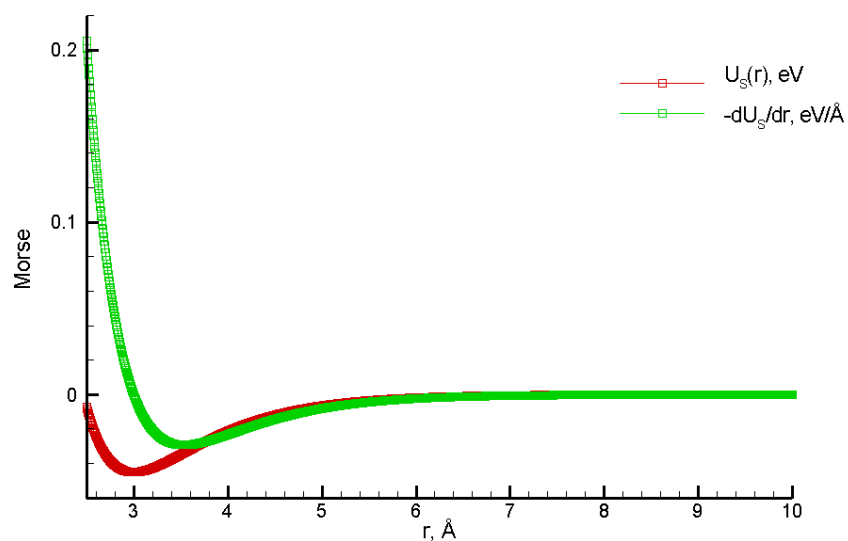
b)
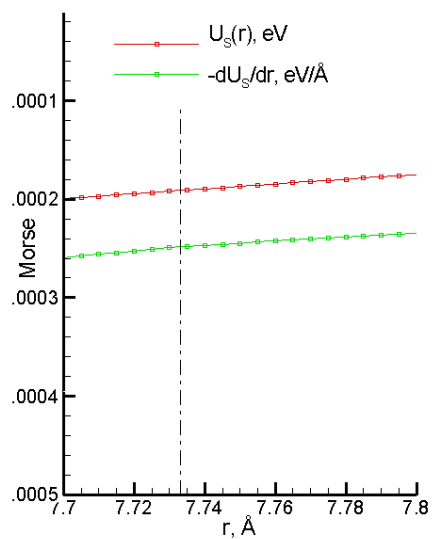
c)
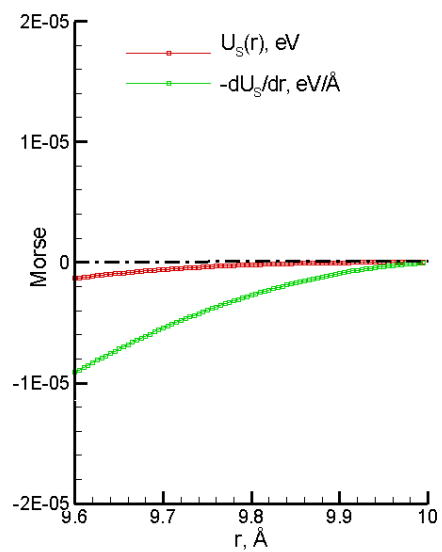
Figure 2.7   a) Smoothed potential for water-water and the negative of its derivative, b)

continuity of potential and its first derivative at $r = r_S$ (vertical dashed line), c) zero values of

potential and first derivative of potential at $r_C = 10$ Å.
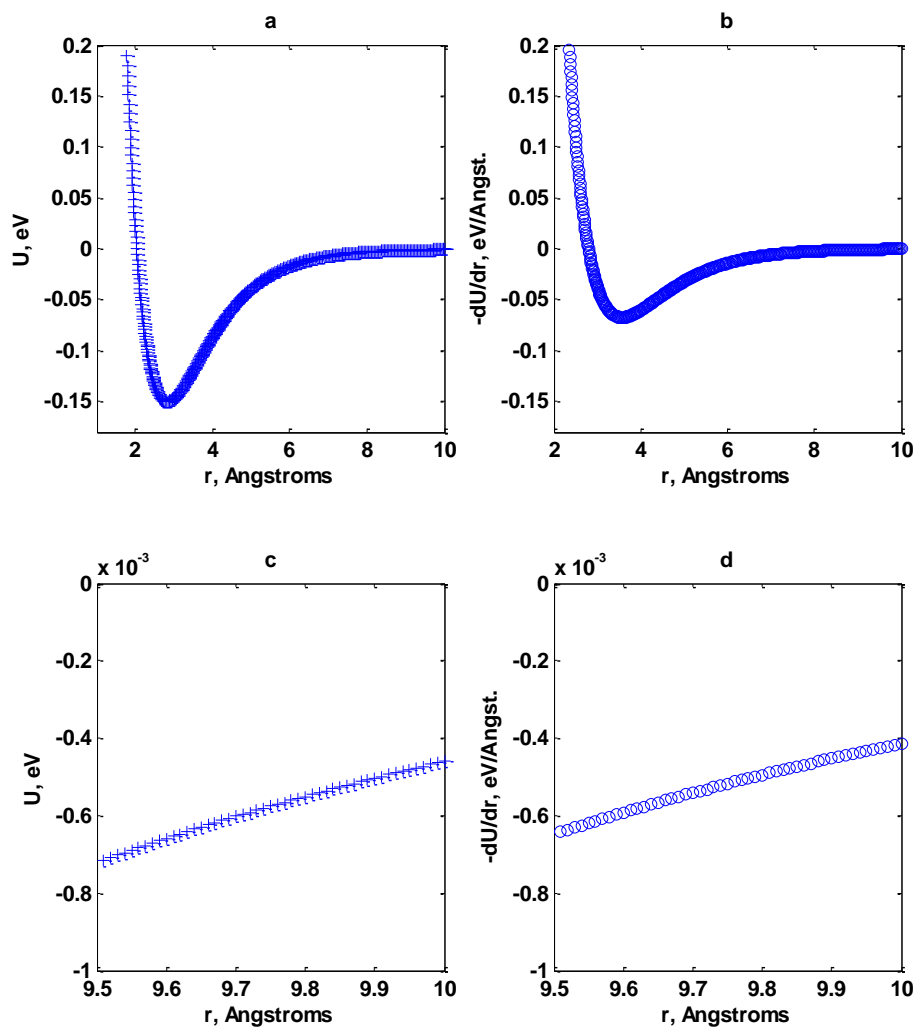
Figure 2.8   a) Morse potential for non-bonding interactions between BS lysozyme molecules,

b) the negative of its derivative, c) display of non-zero value of Morse potential at $r_C = 10$ Å, d)

display of non-zero value of derivative of Morse potential at $r_C = 10$ Å.
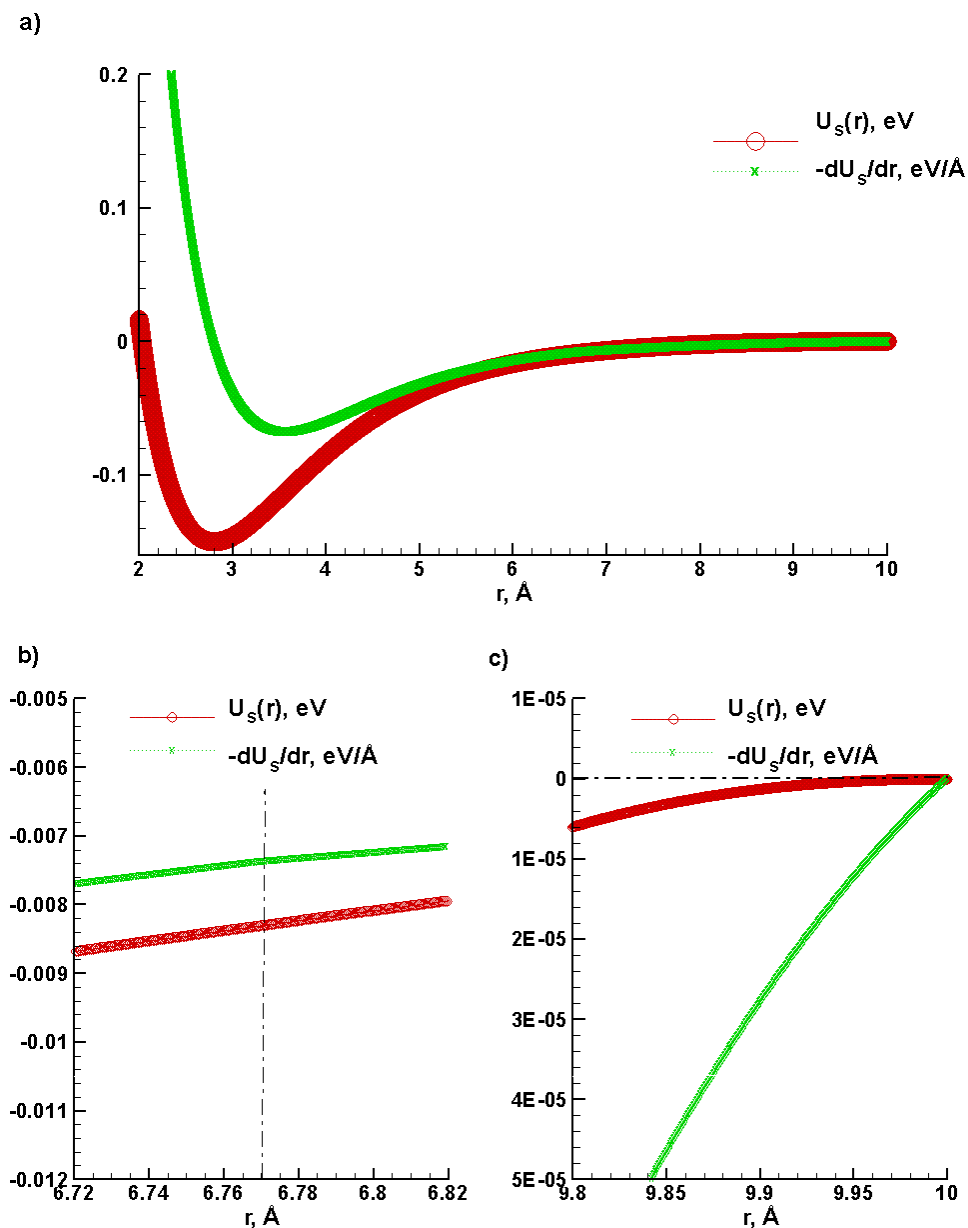
Figure 2.9   a) Smoothed potential for non-bonding interaction in lysozyme and the negative

of its derivative, b) continuity of potential and first derivative of potential at $r = r_S$ (vertical

dashed line), c) zero values of potential and first derivative of potential at $r_C = 10$ Å.
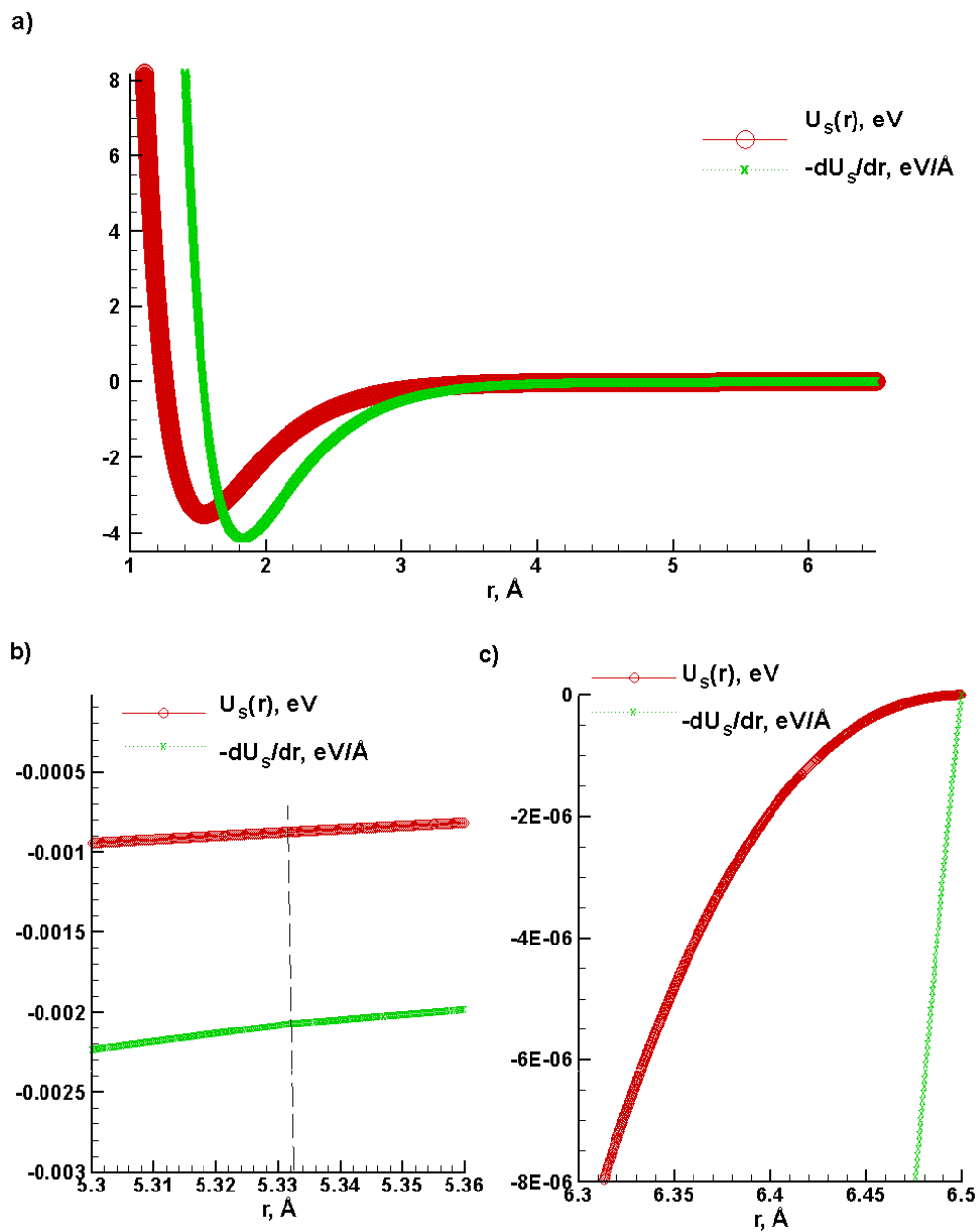
Figure 2.10 a) Smoothed potential for bonding interaction in lysozyme and the negative of its derivative, b) continuity of potential and first derivative of potential at $r = r_S$ (vertical dashed line), c) zero values of potential and first derivative of potential at $r_C = 6.5$ Å.

2.2.1.2   Determination of internal 'breathing' potential

The parameters of the internal breathing motion potential are determined so as to attain a desired energy transfer rate between breathing and translational motions. The coupling of internal and translational modes is generally observed through energy relaxation of excited vibrational modes.

Vibrational relaxation dynamics in water is fast. The lifetimes of O-H stretching and bending modes have been determined by infrared spectroscopy to be about 0.5-1 ps [89, 90]. Hydrogen bonding plays an important role in vibrational population relaxation, as lifetimes get longer (tens of ps) when water molecules are more sparsely distributed in an inert solvent matrix [90]. A coarse-grained BS molecule represents a cluster of H_2O molecules for which vibrational relaxation times of excited O-H modes at the cluster surface are expected to be longer than those in experimental water, due to the lower density of hydrogen bonding sites. We therefore aim here at closely reproducing the relaxation dynamics of liquid molecules that are bigger than H_2O and interact through hydrogen bonding. The relaxation dynamics for such molecules are slower than in experimental water: IR pump-probe signals of phenol-benzonitrile complex in carbon tetrachloride (CCl_4), obtained by exciting the O-H stretching mode with a pump pulse of peak frequency around 3470 cm^{-1}, show relaxation times of ~ 15-20 ps [91]; vibrational lifetimes of the O-H bond of alcohols in liquid CCl_4 have been determined by picosecond infrared pump-probe experiments to be in the range ~ 10-30 ps at 298 K [92]. Parameters of the internal potential for the BS model are chosen to have a coupling time of up to 30 ps (at room temperature) between breathing and translational modes in water, which is adequate for energy transfer within a computational pulse duration of a few hundred ps.

Vibrational energy relaxation has been studied in proteins under the effect of light: classical MD simulations in cytochrome have shown cooling times of up to 20-40 ps [93, 94]; vibrational relaxation times in bacteriorhodopsin have been determined to be 10 ps by femtosecond time-resolved optical pump-infrared probe spectroscopy [95]. A coupling time of up to about 40 ps (at room temperature) between breathing and translational modes is allowed for the choice of internal potential parameters for BS lysozyme; this should be adequate for energy transfer within a computational pulse duration of a few hundred ps.

The set of parameters are fitted in relation to those previously obtained for organic solids [55]: $k_1' = 60$ eV/Å^2, $k_2' = -120$ eV/Å^2, $k_3' = 120$ eV/Å^2, and $M_I' = 1600$ a.m.u – the mass of inertia of breathing motion. The mass of BS molecule for the organic solids is $M' = 100$ a.m.u. The potential is varied by applying a multiplicative factor, S_k, to the parameters k_1', k_2', k_3'; and M_I is varied by changing a scaling factor, S_M, which is the ratio of M_I to the BS mass, M. Otherwise stating, $S_k = k_1/k_1' = k_2/k_2' = k_3/k_3'$, where k_1, k_2, k_3 are parameters to be determined; and $S_M = M_I/M$.

The rate of intermode energy transfer is predicted by the frequency mismatch between vibrational modes of the breathing motion and translational motion. Vibrational spectra are obtained by Fourier transformation of velocity autocorrelation functions (VAFs) [55]. The velocity autocorrelation function (VAF), $Z(t)$, for a system of molecules (or atoms) can be written as

$$Z(t) = \frac{\langle \boldsymbol{v}(0) \cdot \boldsymbol{v}(t) \rangle}{\langle \boldsymbol{v}(0) \cdot \boldsymbol{v}(0) \rangle} = \frac{C_v(t)}{C_v(0)} \tag{2.25}$$

For a system of N molecules, $C_v(\Delta t) = \frac{1}{N}\sum_{i=1}^{N} \boldsymbol{v}_i(t_o) \cdot \boldsymbol{v}_i(t_o + \Delta t)$. Generally, the VAF is calculated as an average over a number of time intervals, say K, during the course of simulation, so that a numerical description of $C_v(\Delta t)$ becomes

$$C_v(\Delta t_j) = \frac{1}{K}\sum_{k=1}^{K}\frac{1}{N}\sum_{i=1}^{N}\boldsymbol{v}_i(t_k) \cdot \boldsymbol{v}_i(t_k + \Delta t_j) \tag{2.26}$$

where $\Delta t_j = (j-1) \cdot dt$ is the length of the time interval, with dt as timestep. The vibrational spectrum is the Fourier transform of the VAF,

$$F(\omega) = \frac{1}{\sqrt{2\pi}}\int_{-\infty}^{\infty} dt\, e^{i\omega t} Z(t) \tag{2.27}$$

and the vibrational density of states (VDOS) is then $\Phi(\omega) = |F(\omega)|^2$. See appendix B3 for numerical implementation of the calculation of the VAF and the VDOS.

The VAFs and the corresponding vibrational spectra, for the choice set of parameters of S_M and S_k, are plotted for both breathing and translational motion in Figure 2.11 for water and lysozyme. Breathing motion is seen to be represented by one vibrational mode. The vibrational spectrum due translational motion is much broader with regions of maximum intensity: water shows one maximum region, representative of a single intermolecular interaction; lysozyme shows two maxima, one representing non-bonding interaction, and the other, of higher frequency, representing bonding interaction. However, the vibrational mode due breathing motion cannot be made to match both maxima regions in the vibrational spectrum of lysozyme, and is modulated here to match the maximum due to non-bonding interactions.

To see how the frequency mismatch in the vibrational spectra translates to the rate of energy transfer, simulations are run to observe how long it takes for temperatures, $\langle T^{TR} \rangle$ and $\langle T^{BS} \rangle$, due

to translational motion and breathing motion, respectively, to equal each other, from originally different values. A *NPT* ensemble of BS molecules, each with equilibrium radius, in a cubic computational cell is heated to 300K with the breathing mode deactivated, so that the translational temperature, $\langle T^{TR} \rangle$, equals 300 K and the temperature of BS mode, $\langle T^{BS} \rangle$, equals 0 K. The breathing mode of the obtained system is then activated in a *NVE* ensemble to observe how long it takes $\langle T^{TR} \rangle$ and $\langle T^{BS} \rangle$ to become equal in a relaxation process. For lysozyme, the computational system is 108 lysozyme globules in a cubic computational cell of side length 115.75 Å; and for water, there are 6912 molecules in a cubic computational cell of side length 82.76 Å. Results of the *NVE* equilibration are plotted in Figures 2.12 and 2.13, for lysozyme and water, respectively; and also for a set of parameters that are close to the choice parameters.

For water, due to the close match of vibrational modes, $\langle T^{TR} \rangle$ and $\langle T^{BS} \rangle$ converge to a single value, as seen in Figure 2.12. The most suitable set of control parameters determines the fastest rate of convergence, ~ 10 ps for the parameters $S_M = 32$ and $S_k = 0.5$, in Figure 2.12c. For lysozyme, $\langle T^{TR} \rangle$ and $\langle T^{BS} \rangle$ equilibrate to stationary values but do not converge to one value, see Figure 2.13, owing most likely to the difficulty in simultaneously matching the vibrational mode due breathing motion with the different vibrational modes due translational motion, as described earlier. Nonetheless, parameters that attempt at equaling $\langle T^{TR} \rangle$ and $\langle T^{BS} \rangle$ within the shortest time, among the different trial parameters, are a choice: $S_M = 32$, $S_k = 1$, in Figure 2.13a. The parameters of the internal BS potential chosen for water and lysozyme are tabulated in Table 2.7.

Although the breathing and translational modes have been determined to couple weakly for the chosen internal potential parameters in lysozyme, under pulsed laser irradiation conditions where the rate of molecular collisions is high, all the different energy modes tend to equilibrate within the pulse duration of 400 ps used in our model simulations. Because coupling of the breathing

and translational modes in the case of lysozyme is of scientific interest to us, a more detailed resolve into parameters that will converge $\langle T^{TR} \rangle$ and $\langle T^{BS} \rangle$ to one value in equilibrium conditions, for lysozyme, will be done in the following sub-section, sub-section 2.2.1.3.

Table 2.7 Anharmonic potential parameters for water and lysozyme.

Material	M_I, Da	k_1, eV/Å^2	k_2, eV/Å^3	k_3, eV/Å^4	S_k	S_M
Lysozyme	3552	60	-120	120	1	32
Water	1600	30	-60	60	0.5	32

a)

velocity autocorrelation functions of breathing sphere lysozyme

Vibrational intensity spectra of breathing sphere lysozyme
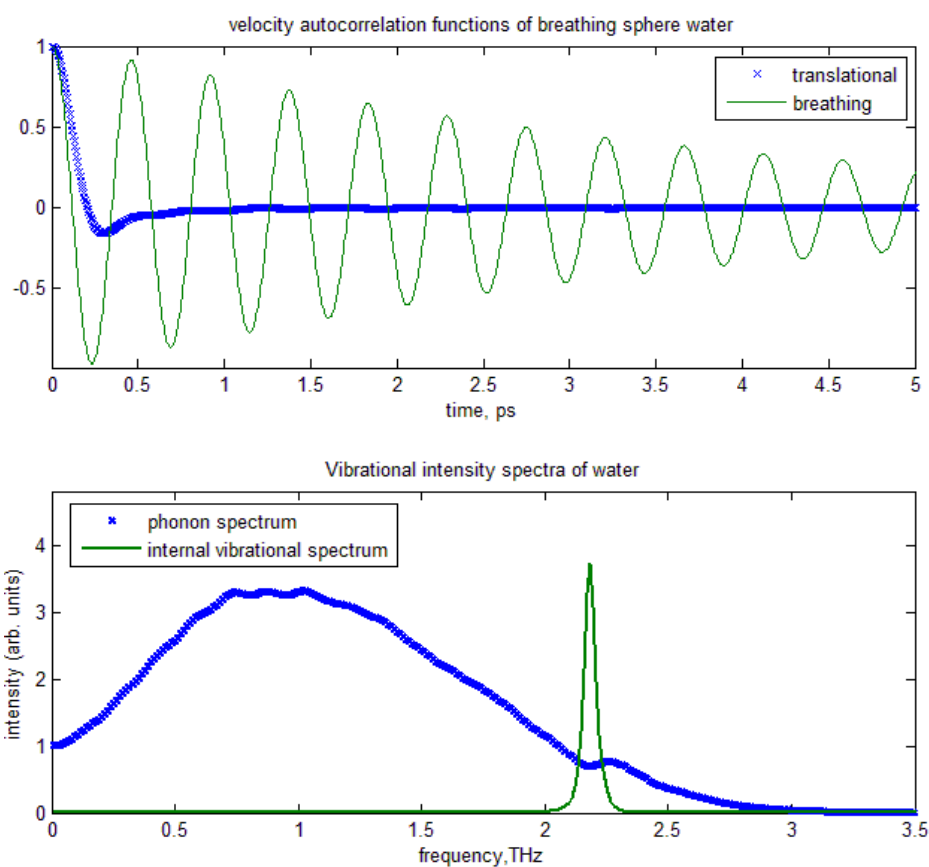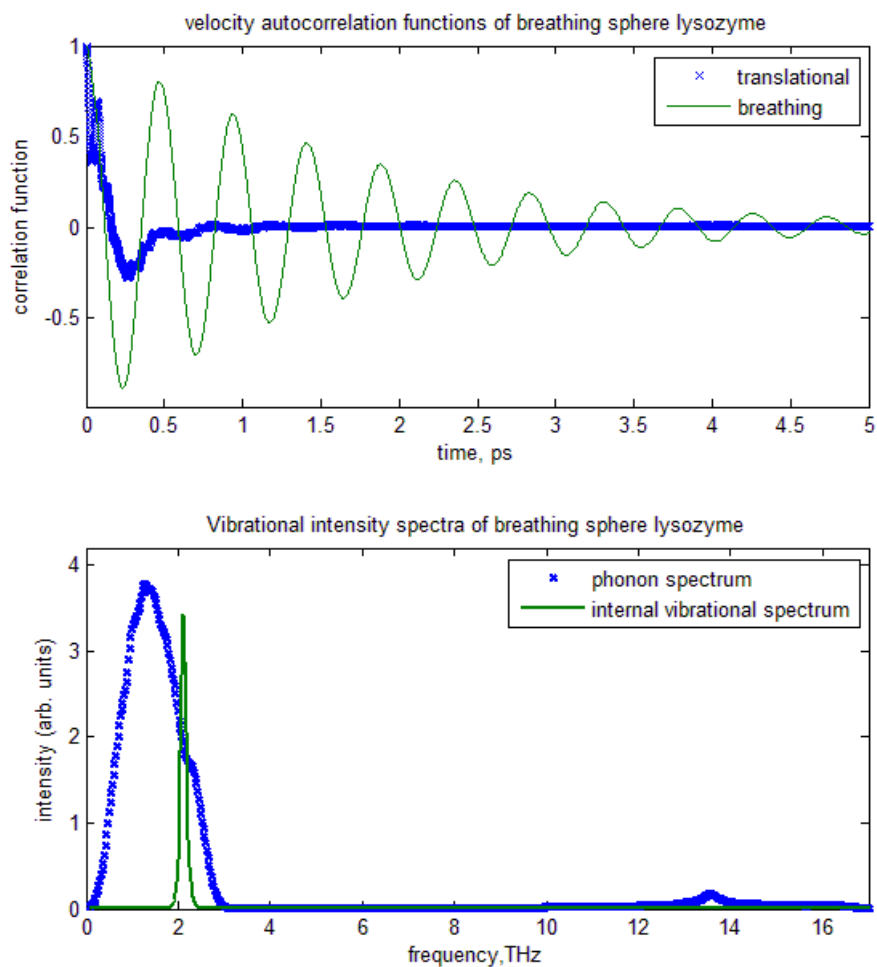
b)

Figure 2.11 Velocity autocorrelation functions (above) and vibrational spectra (below) determined at 300K, with parameters controlling the dynamics of the breathing mode, listed in Table 3.2, for (a) water and (b) lysozyme.
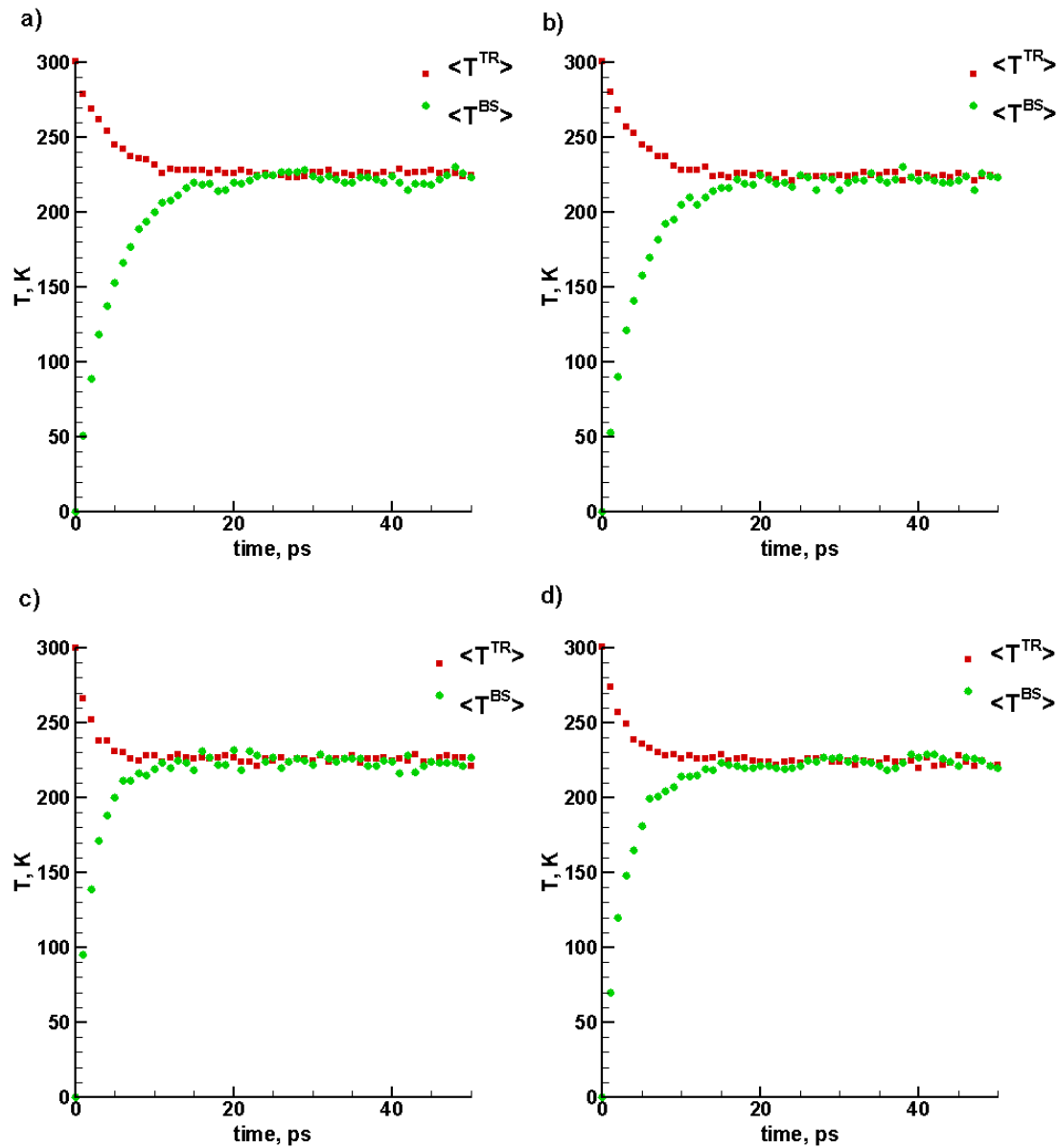
Figure 2.12 Time dependence of breathing and translational temperatures for parameters controlling the dynamics of the breathing mode in BS water: a) $S_M = 32$ and $S_k = 1$, b) $S_M = 64$ and $S_k = 1$, c) $S_M = 32$ and $S_k = 0.5$, d) $S_M = 64$ and $S_k = 0.5$.
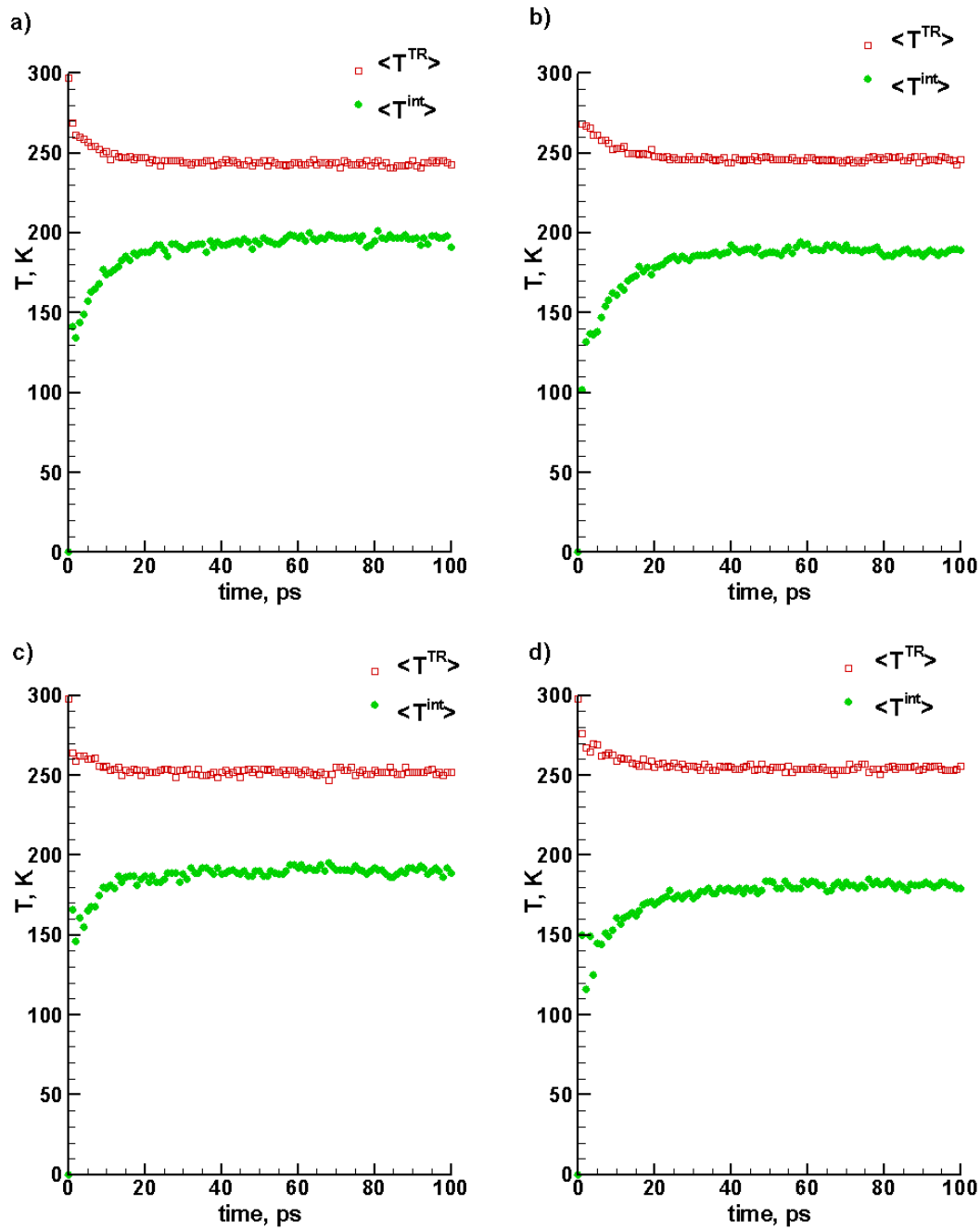
Figure 2.13 Time dependence of breathing and translational temperatures for parameters controlling the dynamics of the breathing mode in BS lysozyme: a) $S_M = 32$ and $S_k = 1$, b) $S_M = 64$ and $S_k = 1$, c) $S_M = 32$ and $S_k = 0.5$, d) $S_M = 64$ and $S_k = 0.5$.

2.2.1.3 *Coupling breathing and translational modes by varying mass of inertia and strength of breathing potential*

In the previous sub-section, breathing and translational modes have been coupled by matching the peak of the vibrational spectrum for breathing motion to the phonon spectrum. For the case of lysozyme, it has been matched close to the phonon spectrum region that relates to weak interactions. It was noticed that at constant energy conditions, the temperatures due translational motion $\langle T^{TR} \rangle$ and breathing motion $\langle T^{BS} \rangle$, did not converge to a single temperature, from initially different values, for the choice parameters of the internal potential, S_M and S_k. We aim at determining an adequate set of parameters that will converge $\langle T^{TR} \rangle$ and $\langle T^{BS} \rangle$, by exploring a broader range of values of S_M and S_k and their effect on the rate of coupling.

We suggest that the parameters of the internal potential S_M and S_k are related to one another, and actually different parameter sets can yield the same vibrational peak position for the breathing mode, although providing significantly different inter-modal (between breathing and translational modes) interactions. This interaction could be determined by quantities such as the amplitude of breathing motion and the velocity of breathing motion.

In order to determine how the parameters of the breathing potential relate to the frequency of breathing mode vibrations, a harmonic approximation can be made to provide a form of the breathing potential that has a force constant, since the force constant in turn relates to the vibrational frequency and the mass of inertia through a simple formula. A harmonic approximation is made to the anharmonic form of the breathing potential in Eq. (2.2). At displacements (expansion or contraction) close to zero, $x = R - R_0$, a second order Taylor expansion of the anharmonic potential yields

$$U(x) \cong k_1 x^2 \tag{2.28}$$

Comparing Eq. (2.28) to the simple harmonic potential form, $U^{harm} = \frac{1}{2}kx^2$, the harmonic

force constant is determined to be $k = 2k_1$. The frequency of breathing mode vibrations in the

harmonic approximation is thus $\nu = (1/2\pi)\sqrt{k/M_I}$, or rather

$$\nu = \left(\frac{1}{2\pi}\right)\sqrt{2\,k_1/M_I} \tag{2.29}$$

It is evident from Eq. (2.29) that the frequency of breathing mode vibrations can be maintained

to be the same by keeping the ratio of the parameter governing the strength of the potential k_1 to

the inertia mass M_I. We will therefore, in many cases, vary the parameters k_1 and M_I, by scaling

the control parameters S_M and S_k, to explore the effect on the inter-modal coupling, for the same

internal vibrational frequency.

   Simulations of the computational cell of lysozyme in the previous sub-section (cubic side

length 115.75 Å), although of NPT ($P = 0$, $T = 300$ K) ensembles this time, are run to determine

how long it takes $\langle T^{TR}\rangle$ and $\langle T^{BS}\rangle$ to converge, for different sets of parameters. Another

difference is that the temperature due translational motion $\langle T^{TR}\rangle$ is initially set to 400 K. The

reason for a constant pressure simulation is to provide more room for interaction, as the

computational cell can contract or expand to equilibrate to zero pressure. Two different groups of

sets of control parameters that yield different internal vibrational peak positions, according to the

harmonic approximation, are explored: the ratio S_M/S_k is kept fixed in each group, but is

different for both groups. For the different sets of control parameters vibrational spectra are

plotted alongside the diagrams displaying the equilibration of temperatures, see Figures 2.14 and

2.16. For differing control parameters within a group, the mean square displacement (MSD) and

the velocity of breathing motion are plotted, see Figures 2.15 and 2.17.
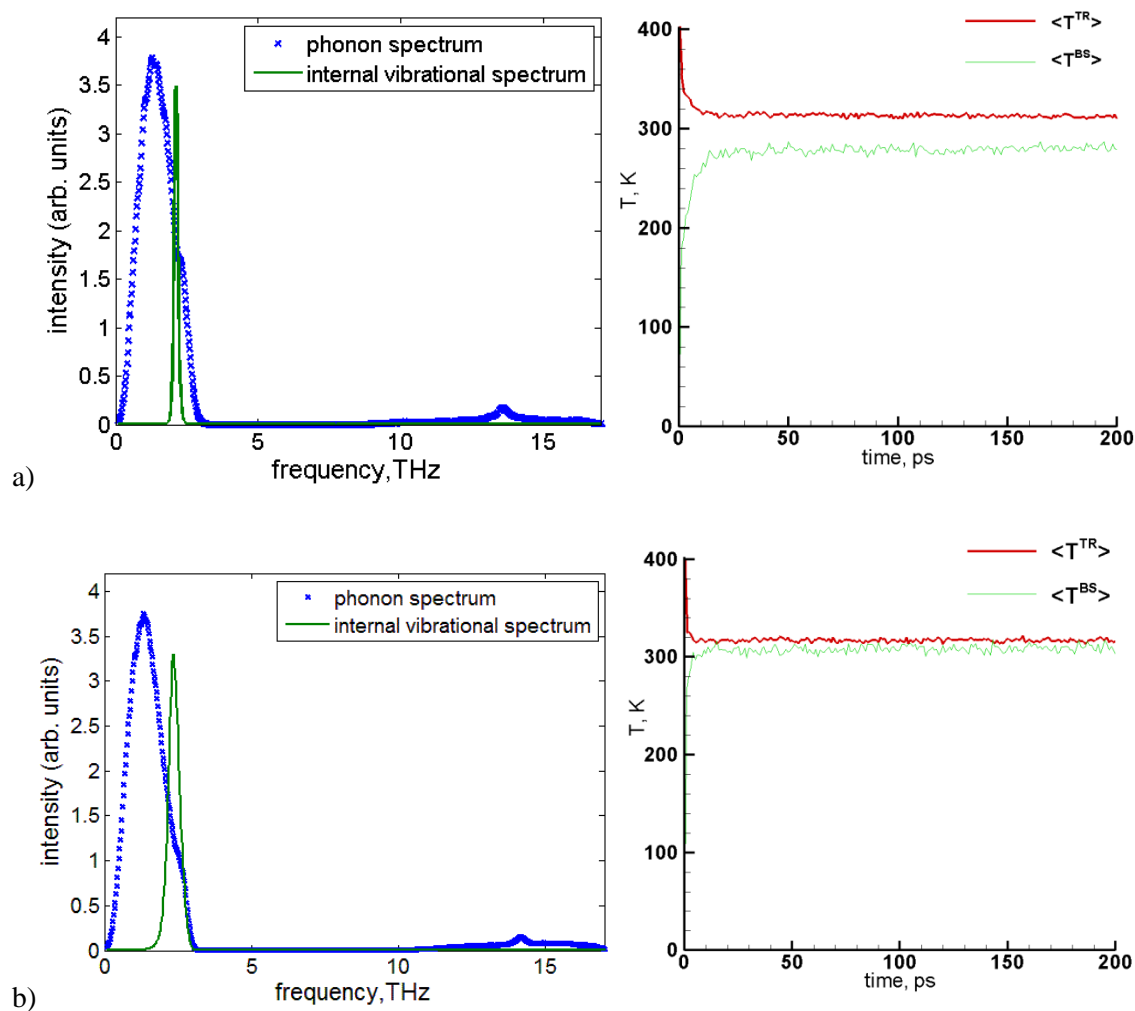
Figure 2.14 Coupling of translational and breathing motions for different parameters controlling the dynamics of the breathing mode in lysozyme – the vibrational spectra are displayed on the left side of the figure, and the time dependences of the breathing mode temperature $\langle T^{BS} \rangle$ and the translational temperature $\langle T^{TR} \rangle$ are displayed on the right side: a) S_M = 32 and S_k = 1; b) S_M = 8 and S_k = 0.25.
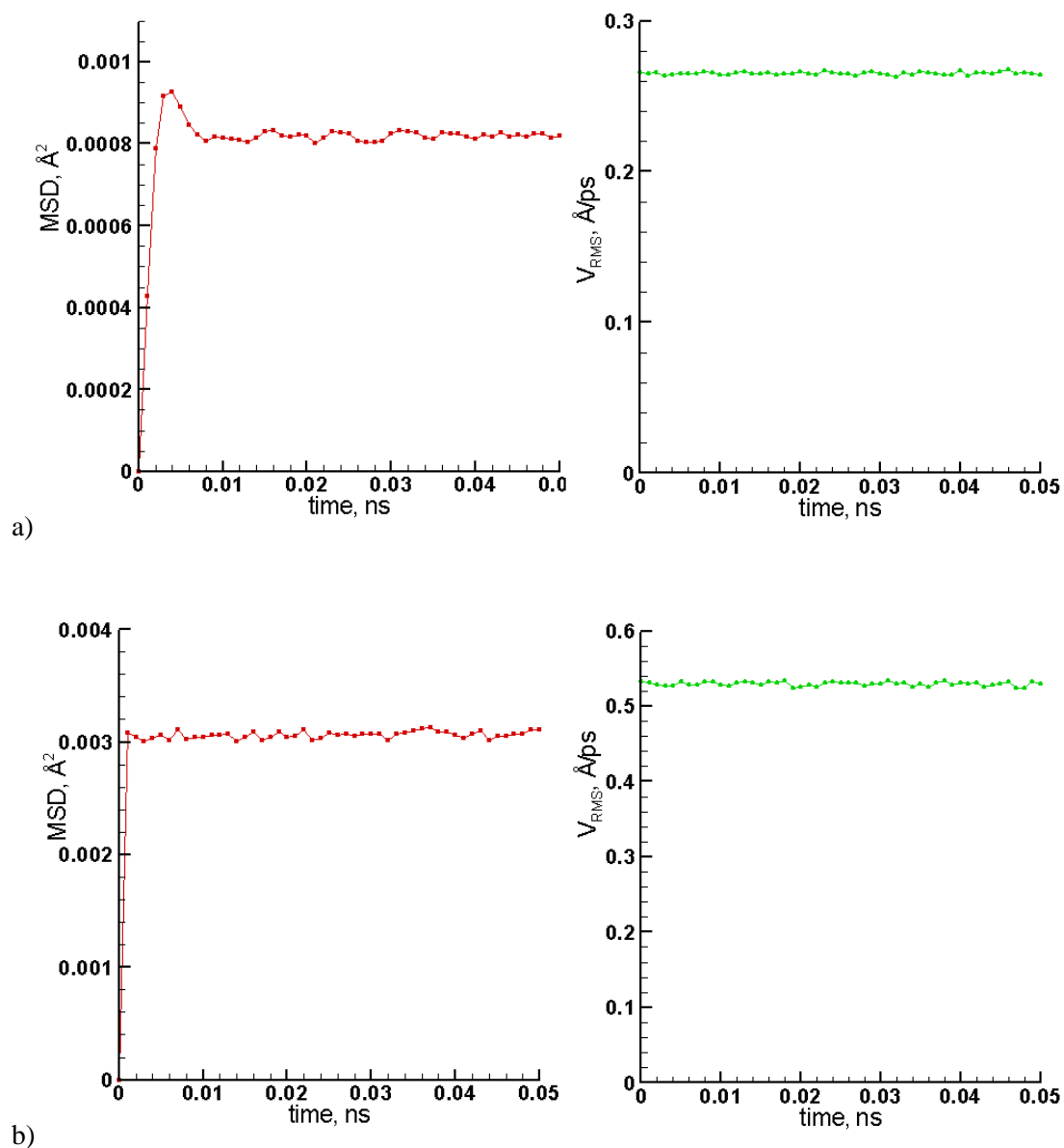
Figure 2.15 Kinetics of breathing sphere motion for different parameters controlling the dynamics of the breathing mode in lysozyme – the time dependence of the mean square displacement displayed on the left side of the figure, and the time dependence of the root mean square velocity is displayed on the right side: a) $S_M = 32$ and $S_k = 1$; b) $S_M = 8$ and $S_k = 0.25$.
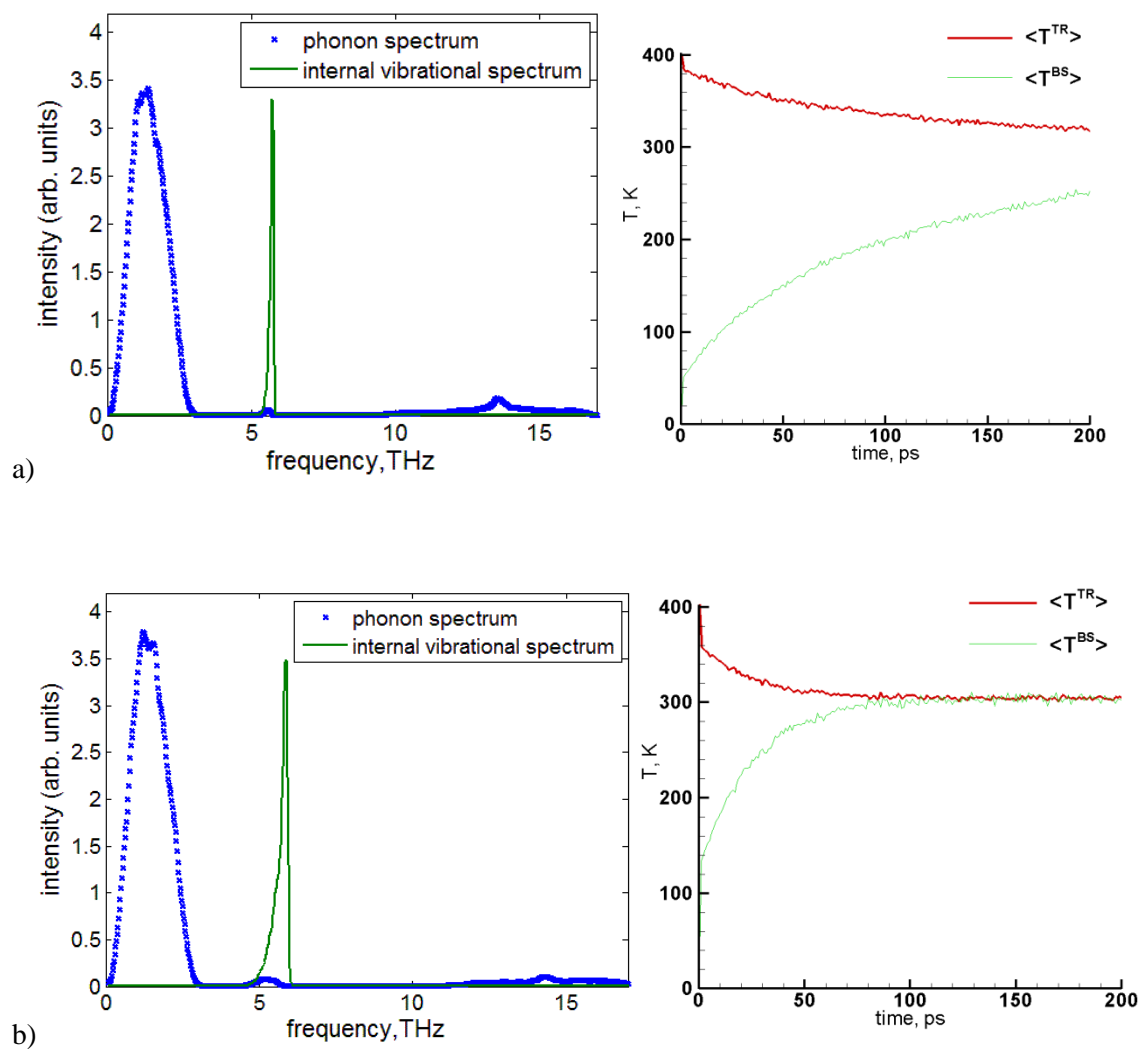
Figure 2.16 Coupling of translational and breathing motions for different parameters controlling the dynamics of the breathing mode in lysozyme – the vibrational spectra are displayed on the left side of the figure, and the time dependences of the breathing mode temperature $\langle T^{BS} \rangle$ and the translational temperature $\langle T^{TR} \rangle$ are displayed on the right side: a) $S_M = 32$ and $S_k = 8$; b) $S_M = 8$ and $S_k = 2$.
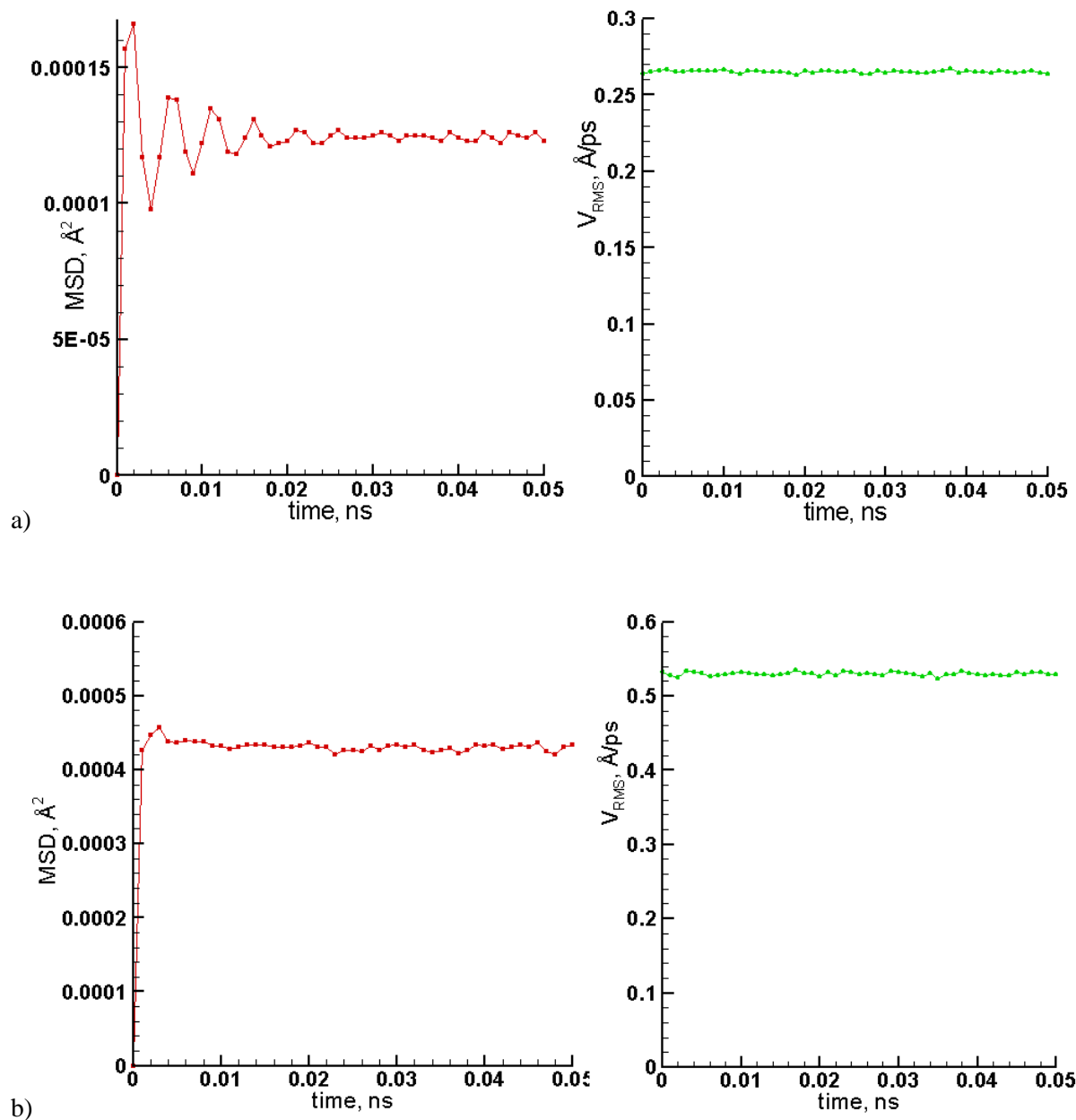
Figure 2.17 Kinetics of breathing sphere motion for different parameters controlling the dynamics of the breathing mode in lysozyme – the time dependence of the mean square displacement displayed on the left side of the figure, and the time dependence of the root mean square velocity is displayed on the right side: a) $S_M = 32$ and $S_k = 8$; b) $S_M = 8$ and $S_k = 2$.

It is possible to draw useful conclusions from the observed dependencies in Figures 2.14-2.17. As predicted by the harmonic approximation, when the mass of inertia of breathing motion and the breathing potential strength (in the force constant) are scaled by the same factor, the peaks of the vibrational spectra are unchanged. It is additionally noticed that reducing the mass of inertia increases the coupling strength between the breathing and translational modes, as can be seen in the faster convergence of temperatures. A lower mass of inertia increases the velocity of breathing motion for a constant energy of the system, and a higher velocity in turn increases the frequency of interaction of a breathing sphere molecule with neighboring molecules. By lowering the scaling factor for the mass of inertia, for the parametrized potential, $S_M = 32$ to $S_M = 8$, with a suitable scaling factor for the strength of the internal potential, $S_k = 2$, coupling the breathing and translational modes in lysozyme has been successfully attained, within $\sim 50 - 100$ ps. It is also noticed that reducing the scaling factor for the strength of the internal potential increases the amplitude of breathing motion, as can be seen that the mean square displacement is higher. It is, however, harder to predict the effect of amplitude on coupling, as lowering S_k for constant $S_M = 8$ in one case results in poorer coupling, and increasing S_k for constant $S_M = 32$ in another case results in better coupling.

2.2.2   Energy Transfer between Heatbath (Implicit) and Dynamic (Explicit) Modes

In this molecular model, as discussed so far, there are three energy modes: the energy of translational motions of the breathing spheres; the energy of the breathing motion of the breathing spheres; and the heat bath representing the energy of the internal degrees of freedom that are active at a given temperature, but are missing in the breathing sphere model. The sum of implicit (unrepresented) internal energy modes of a single molecule will simply be called its heat

bath, and is denoted as E_{int}^i. There is a physical distinction, or significant separation in frequency space, between the internal and dynamic modes, and as a result distinct internal and dynamic temperatures are introduced. The energy distribution due to the internal degrees of freedom of a molecule will be characterized by one temperature, the "heat bath temperature" T_i^{int}. The heat bath energy of different molecules can change in the course of a simulation due to the laser light absorption or energy exchange with translational and breathing modes. Equilibration of all the energy modes is attained in our model by coupling the heat bath with breathing motion, since the breathing motion is already coupled to the translational motions, as described in the above sub-section.

In previous work, energy exchange between the internal and translational degrees of freedom is enabled by modifying the equations of translational motion to include a velocity-dependent force which accounts for the difference between the temperatures due to translational motion and the hat bath temperatures of interacting molecules [96]. The result is particle deceleration if the temperature due to translational motion is higher than the average of internal temperatures of interacting particles, and particle acceleration if the temperature due to translational motion is lower. In this work, thermal equilibration between the internal and dynamic modes is attained by dissipating or accelerating the breathing motion of the breathing spheres, and making corresponding changes in the internal energy to ensure that total energy is conserved. The thermal equilibration between heat bath and dynamic modes can be monitored by observing a temperature evolution of the different modes.

The energy exchange between the heat bath variables and the dynamic degrees of freedom of the coarse-grained molecule is implemented by coupling the heat bath with the breathing motion of the dynamic units of the model. The rate of the equilibration is proportional to the difference

between the local temperature of the breathing motion, T_i^R, and the heat bath temperature T_i^{int} of the dynamic unit. The local temperature of breathing motion at the position of unit i about a molecule T_i^R is defined by the average kinetic energy of breathing motions of units located within the intermolecular potential cut-off distance from the unit i:

$$T_i^R = \sum_{j=1}^{N_i^{loc}} \frac{M_I(v_j^R)^2}{N_i^{loc} k_B} \tag{2.30}$$

where $v_j^R = dR_j/dt$ is the instantaneous velocity of the breathing motion of unit j and N_i^{loc} is the number of molecules within the potential cut-off distance from unit i.

To ensure energy conservation, the energies of the heat bath and the breathing motion are changed at each time-step of the integration of the equations of motion of the dynamic units with rates of the same magnitude but opposite sign:

$$C_i^R \frac{dT_i^R}{dt} = A(T_i^{int} - T_i^R); \ C_i^{int} \frac{dT_i^{int}}{dt} = -A(T_i^{int} - T_i^R) \tag{2.31}$$

where C_i^R is the heat capacity of the molecule due to its breathing motion, C_i^{int} is the heat capacity of the heat bath of a molecule, and A is the proportionality constant that controls the rate of the energy exchange.

Coupling between the heat bath and breathing motion of the dynamic units is realized by scaling the velocities of the radial breathing motion to ensure thermal equilibration between the heat bath and the breathing vibrations. The relation between a gain in kinetic energy of breathing motion of the ith molecule, ΔK_i^R, and the change in the velocity of breathing motion, Δv_i^R is described by the equation:

$$K_i^R + \Delta K_i^R = \frac{1}{2} M_I(v_i^R + \Delta v_i^R)^2 \tag{2.32}$$

The change in heat bath energy of a molecule, E_i^{int}, can be defined in differential form as $dE_i^{int} = C_i^{int} dT_i^{int}$. Energy transferred from the heat bath of a molecule is partitioned to breathing modes of molecules in the neighborhood of the molecule. The rate of change of kinetic energy of breathing motion, due to energy transferred from heat baths of neighborhood molecules j, for BS molecule i is

$$\frac{dK_i^R}{dt} = A \sum_{j=1}^{N_i^{loc}} F_{ij}\left(T_j^{int} - T_j^R\right) \tag{2.33a}$$

where F_{ij} is the distribution gain of molecule i from neighboring molecules j and satisfies the condition

$$\sum_{j=1}^{N_i^{loc}} F_{ij} = 1 \tag{2.33b}$$

In our model, F_{ij} is described by a uniform distribution, as in Eq. 2.33c, in which energy transferred from the internal mode of molecule j is distributed in equal parts to all molecules (including itself) in its neighborhood:

$$F_{ij} = \frac{1}{N_j^{loc}} \tag{2.33c}$$

Eq. (2.33a) is therefore

$$\frac{dK_i^R}{dt} = A_c \sum_{j=1}^{N_i^{loc}} \left(T_j^{int} - T_j^R\right) / N_j^{loc} \tag{2.33d}$$

A relation is determined for the coupling coefficient, A_c. Multiplying the left part of Eq. (2.31) by C_i^{int} and the right part of Eq. (2.31) by C_i^R, and subtracting the resultant equations, the following is obtained:

$$\frac{\partial(T_i^{int} - T_i^R)}{\partial t} = -A_c \frac{C_i^{int} + C_i^R}{C_i^{int} C_i^R} \left(T_i^{int} - T_i^R\right) \tag{2.34}$$

which on integration over time τ, during which $T_i^{int} - T_i^R$ decays by $1/e$, yields

$$A_c = \frac{C_i^{int} C_i^R}{C_i^{int} + C_i^R} \cdot \frac{1}{\tau} \tag{2.35}$$

Equation (2.35) determines the coupling coefficient for a given time τ during which the difference between the heat bath and breathing mode temperatures, decays by $1/e$. This time can be called the decay time constant, as it is fixed during simulations. For large coarse-grained particles with several internal (implicit) degrees of freedom, C_i^{int} is of an order greater than C_i^R, $C_i^{int} \gg C_i^R$, so that the coupling coefficient can be adequately and more simply expressed as $A_c \cong C_i^R/\tau$.

The advantage of the developed method for energy exchange between dynamic modes and heat baths is one of convenience. Given that energy exchange occurs by transferring relevant quantities of energy between dynamic modes and heat baths of molecules, it is more straightforward to monitor the energy distribution over the different modes. This enables easy verification of total energy conservation.

The heat capacity of a heat bath associated with a dynamic unit (the BS molecule) is obtained by subtracting the contributions of the dynamic degrees of freedom from the experimental specific heat capacity of the group of atoms (or molecules) represented by the dynamic unit, C^{exp}, i.e., $C^{int} = C^{exp} - C^{tr} - C^R$, where $C^{tr} = 3k_B$ is the contribution to the heat capacity from the three translational degress of freedom of the dynamic unit, and $C^R = k_B$ is the contribution from the breathing motion of the unit (k_B is the Boltzmann constant). The heat

capacity of water is 4.2 J/(g.K) [82], which translates to $C^{exp} = 2.18\text{x}10^{-3}$ eV/K per BS unit[2] with a mass of 50 Da. The heat capacity of anhydrous lysozyme has been determined at 25 °C to be 0.285 cal/(g.K) [97]; this translates to a heat capacity of $C^{exp} = 1.4\text{x}10^{-3}$ eV/K per polymer unit (also BS molecule or unit) with a mass of 111 Da.

In order to test implementation of the designed energy transfer model to water, the cubic computational system of 6912 breathing sphere molecules at 300 K is assigned a heat bath temperature different from the temperature of dynamic modes (and greater than) 300K, chosen here to be 390K, i.e. at the onset of the simulation the translational and breathing temperatures are the same, $\langle T^{TR} \rangle = \langle T^{BS} \rangle = 300$ K, while the internal temperature $\langle T^{int} \rangle = 390$ K. Equilibration to a single system temperature is observed in a *NVE* ensemble for different values of the decay time constant τ, and hence different values of the coupling coefficient A_c. Demonstrations of the equilibration to single temperature for $\tau = 0.1, 1.0, 5.0$ and 20.0 ps are made in Figure 2.18. A value of τ as small as 0.1 ps renders the energy unstable, as seen in Figure 2.18a; a value of $\tau = 1$ ps equilibrates the system within ~ 10 ps, but mild instabilities can still be observed, see $\langle T^{BS} \rangle$ within first few ps in Figure 2.18b. For a decay constant of $\tau = 5$ ps, equilibration proceeds without any instabilities, and within ~ 60 ps; the equilibration is much slower at a higher value such as $\tau = 20$ ps. The decay constant of $\tau = 5$ ps is deemed suitable for our laser irradiation simulations with pulse durations of ~ 500 ps. It is important to note here that the time it takes for the difference in the temperatures of the dynamic and internal modes to decrease by $1/e$ is determined by the coupling not only between the internal mode and the breathing mode but with the translational mode as well, and is therefore longer than the time constant τ. Since the time constant τ is directly proportional to C_i^R, i.e. $\tau \cong C_i^R/A_c$, it can be

---

[2] The determined value is implemented in error in the simulations as 2.8 x 10^{-3} eV/K.

deduced that the corresponding time decay constant between internal and dynamic modes, τ^{real}, is directly proportional to $C_i^R + C^{tr}$, i.e. $\tau^{real} \cong (C_i^R + C^{tr})/A_c$. The heat capacity due to translational motion is three times the heat capacity due to breathing motion, $C^{tr} = 3C_i^R$, so that $\tau^{real} \cong 4\tau$. It can be witnessed in Figure 2.18c that the time it takes for the difference in temperatures of internal and dynamic modes to reduce to $1/e$ of the initial value is $\tau^{real} \cong 20$ ps, for a time constant of $\tau = 5$ ps. This agrees well with the relation $\tau^{real} \cong 4\tau$.

It was observed earlier in sub-section 2.2.1.2 that the equilibration of breathing and translational temperatures in lysozyme was incomplete, at temperatures close to room temperatures, for the model set of parameters controlling the dynamics of the breathing sphere mode. This, however, led to the suggestion that, with the given set of model parameters, equilibration into a single temperature for the different energy modes will nonetheless be attainable in relatively high energy conditions, as in laser energy deposition. The claim is here verified. For a computational system (11.2×33.6×44.8 nm^3) of 600 lysozyme globules, a internal temperature as high as $\langle T^{int} \rangle = 3000$ K is assigned to the heatbath, while the dynamic modes are assigned temperatures of $\langle T^{TR} \rangle = 300$ K and $\langle T^{BS} \rangle = 300$ K. The system is equilibrated so that a single temperature for all energy modes is attained, for a decay time constant of $\tau = 5$ ps. A diagram of the evolution of temperatures of the different energy modes is displayed in Figure 2.19. It can be seen that although there is initially an order-of-magnitude difference between $\langle T^{TR} \rangle$ or $\langle T^{BS} \rangle$ and $\langle T^{int} \rangle$, the equilibrated temperature difference is less than 5 %. This satisfies our claim that in conditions of laser energy deposition in the polymer (capable of bringing the target to temperatures ~ 1000 K and beyond), a single temperature for all energy modes is attained within satisfactorily low tolerances, $\lesssim$ 5 %, for the model set of parameters controlling the dynamics of the breathing mode in lysozyme.
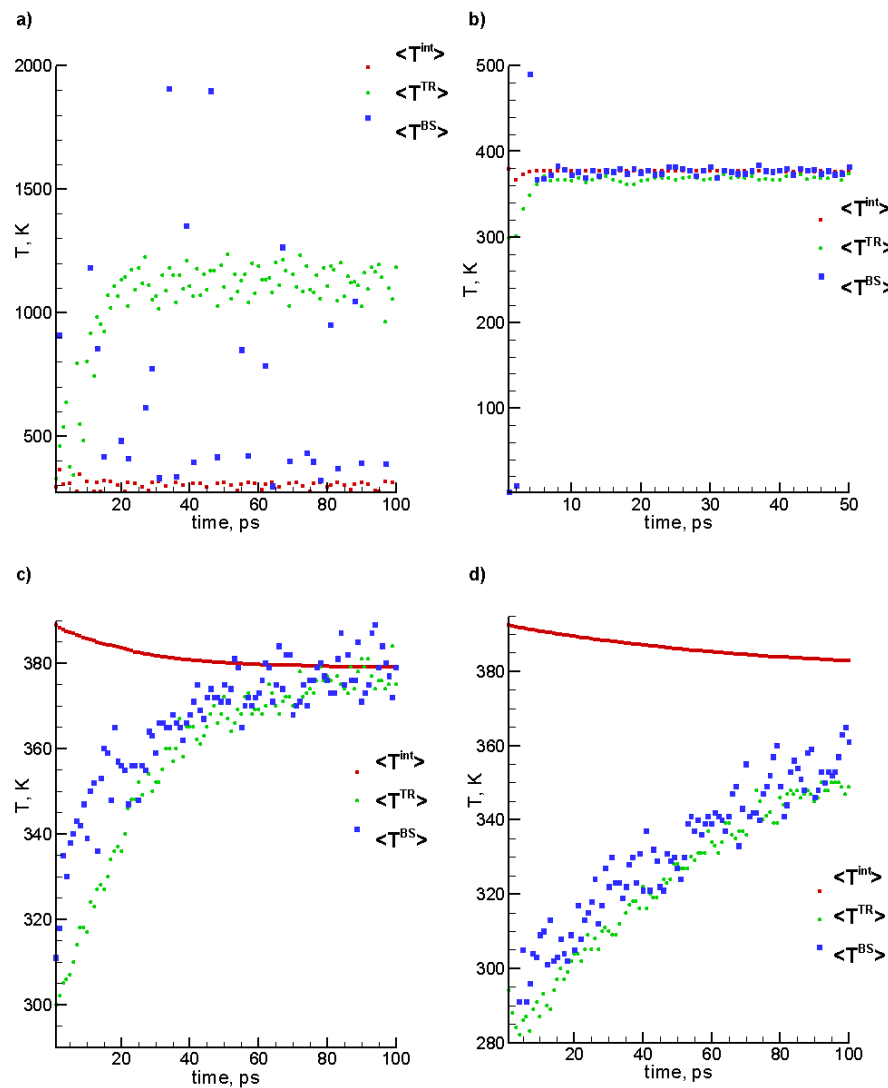
Figure 2.18 Coupling of the different energy modes in water, for different decay time constants – a) $\tau = 0.1$ ps; b) $\tau = 1.0$ ps; c) $\tau = 5.0$ ps; d) $\tau = 20.0$ ps. $<T^{int}>$, $<T^{BS}>$, and $<T^{TR}>$ are temperatures of heat bath, BS and translational modes, respectively.
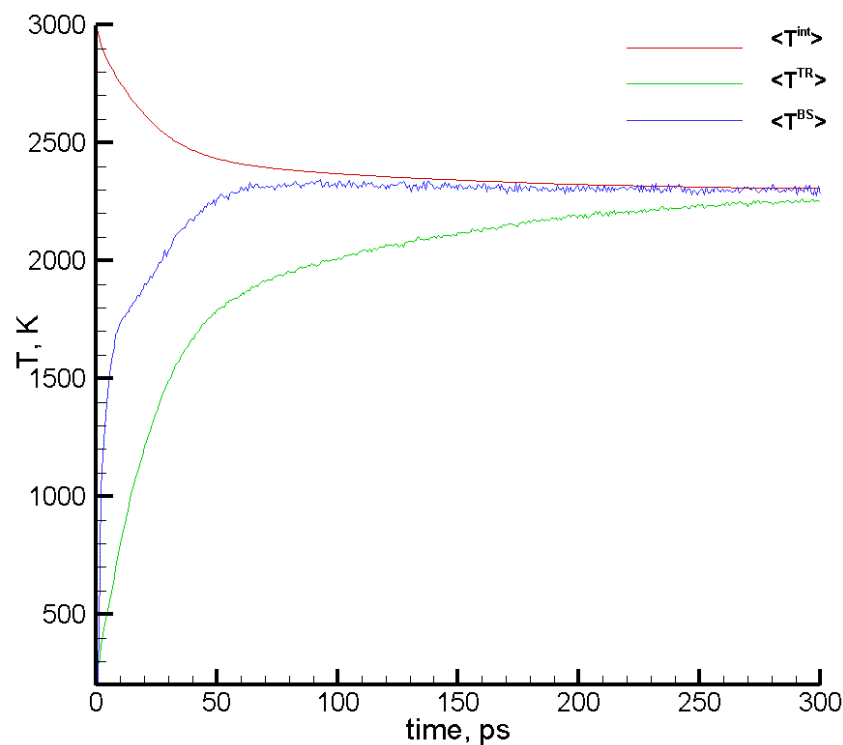
Figure 2.19 Coupling of the different energy modes in lysozyme for $\tau = 5.0$ ps; $\langle T^{int} \rangle$, $\langle T^{TR} \rangle$, and $\langle T^{BS} \rangle$ refer to temperatures of heat bath, translational modes and breathing modes, respectively

2.2.3 Parametrization of the Breathing Sphere Model for the Metalorganic Precursor – Palladium Acetate

Palladium acetate (PdAc, Pd(OAc)$_2$, or Pd(Ac)$_2$) is a metalorganic solid with monoclinic crystal structure, and has a density of 2.19 g/cm^3 [98]. Other material properties of palladium acetate are not well known, but a study has been done on the volatility and lattice energy of palladium chelates [99] – compounds that are both of similar structure and similar properties to palladium acetate. The bulk modulus of PdAc is also unknown, but is assumed to be that for most organic solids.

In Ref. [99], thermal investigations of palladium(II) acetylacetonate (Pd(acac)$_2$) and palladium(II) hexafluoroacetylacetonate (Pd(hfa)$_2$) were done, during which volatilized species of the named complexes were obtained in vacuum. Thermogravimetric (TG) curves − weight loss against temperature curves − of the complexes were determined. The TG curves reveal that complete volatilization of Pd(acac)$_2$ and Pd(hfa)$_2$ samples are observed at ~ 180 ^{o}C and ~ 100 ^{o}C, respectively. Standard values of sublimation energy were experimentally determined to be 121.5 ± 1.4 kJ/mol and 93.5 ± 0.6 kJ/mol for Pd(acac)$_2$ and Pd(hfa)$_2$, respectively. The volatilization temperatures of the investigated compounds are close to temperatures at which complete volatilization of PdAc samples in vacuum is observed: PdAc has completely vaporized after heating to ~ 175°C in vacuum [100]; vaporization of trimeric molecules of PdAc has occurred at 155°C in vacuum [101]. Based on the similarity of volatilization temperatures, assuming that the determined sublimation energies of the investigated Pd compounds are typical to that of PdAc, a sublimation energy value of 100 kJ/mol is assumed for PdAc.

Parameters of the Morse potential between BS molecules of PdAc are analytically fitted to reproduce the density of PdAc (ρ = 2.2 g/cm^3), a typical value of the sublimation energy of solid PdAc (100 kJ/mol), and a typical value of the bulk modulus of a metalorganic solid (5 − 10 GPa) at room temperature. The breathing sphere molecule is adopted to be one PdAc molecule.

The set of Morse potential parameters describing PdAc intermolecular interactions are determined, by adopting a procedure which describes the Morse potential for FCC crystals [102]: the Morse potential parameters β and r_e are analytically related, and the cohesive energy and bulk modulus are calculated for the equilibrium crystal structure. The total cohesive energy here equals the sublimation energy per quantity of substance considered.

A FCC molecular crystal of PdAc is generated with a density of $\rho = 2.19$ g/cm^3. The corresponding lattice parameter of the molecular crystal a is determined through the density, as in Eq. (2.16), to be $a = 8.8$ Å; and this corresponds to an equilibrium distance between PdAc molecules of $a_{eq} = a/\sqrt{2} = 6.22$ Å.

Analytical expressions of the total cohesive energy and the bulk modulus are obtained as a function of the Morse potential parameters $\{D_e, \beta, r_e\}$ for the generated FCC crystal, as in Ref. [102]. The Morse parameters are fitted to the analytical expressions for the known values of cohesive energy and bulk modulus.

For a crystal containing N molecules, with interactions described by the Morse potential, the total energy of the molecular crystal is obtained as:

$$\Phi = \frac{ND_e}{2} \sum_{j=1}^{N-1} \{\exp[-2\beta(r_j - r_e)] - 2\exp[-\beta(r_j - r_e)]\} \tag{2.36}$$

where r_j is the distance of the jth molecule from a molecule situated at the origin and is defined by the position vector

$$\vec{r_j} = m_j\vec{a_1} + n_j\vec{a_2} + l_j\vec{a_3} \tag{2.37}$$

where $m_j, n_j,$ and l_j are integers and $\vec{a_1}, \vec{a_2}$ and $\vec{a_2}$ are primitive basis vectors. For an FCC structure, the primitive basis vectors are defined through the lattice parameter, a by

$$\vec{a_1} = \frac{a}{2}(\vec{e_y} + \vec{e_z}); \quad \vec{a_2} = \frac{a}{2}(\vec{e_x} + \vec{e_z}); \quad \vec{a_3} = \frac{a}{2}(\vec{e_x} + \vec{e_y}) \tag{2.38}$$

so that

$$r_j = \frac{a}{2}[(m_j + n_j)^2 + (n_j + l_j)^2 + (l_j + m_j)^2]^{1/2} = M_j\, a \tag{2.39}$$

For convenience, the following variable is defined:

$$\gamma = \exp(\beta r_e) \tag{2.40}$$

so that Eq. (2.36) is rewritten in the form

$$\Phi(a) = \frac{\gamma N D_e}{2} \sum_{j=1}^{N-1} [\gamma \exp(-2\beta a M_j) - 2\exp(-\beta a M_j)] \tag{2.41}$$

The first two derivatives of Eq. (2.41) are as follows:

$$\frac{d\Phi}{da} = -\gamma \beta N D_e \sum_{j=1}^{N-1} [\gamma M_j \exp(-2\beta a M_j) - M_j \exp(-\beta a M_j)] \tag{2.42}$$

$$\frac{d^2\Phi}{da^2} = \gamma \beta^2 N D_e \sum_{j=1}^{N-1} [2\gamma M_j{}^2 \exp(-2\beta a M_j) - M_j{}^2 \exp(-\beta a M_j)] \tag{2.43}$$

The variable α is evaluated from the equilibrium condition of the crystal:

$$\left(\frac{d\Phi}{da}\right)_{a=a_o} = 0 \tag{2.44}$$

which gives

$$\gamma = \frac{\sum_{j=1}^{N-1} M_j \exp(-\beta a_o M_j)}{\sum_{j=1}^{N-1} M_j \exp(-2\beta a_o M_j)} \tag{2.45}$$

where a_o is the equilibrium value of a. The total cohesive energy U_o is obtained as

$$U_o = -\Phi(a_o) = \frac{\gamma N D_e}{2} \sum_{j=1}^{N-1} [\alpha \exp(-2\beta a_o M_j) - 2\exp(-\beta a_o M_j)] \tag{2.46}$$

The bulk modulus B is written as

$$B = V_o \left(\frac{d^2\Phi}{dV^2}\right)_{a=a_o} \tag{2.47}$$

where V_o is the equilibrium value of the crystal volume V. For an FCC crystal using the relation

$$V = \frac{Na^3}{4} \tag{2.48}$$

Equation (2.47) yields

$$B = \frac{4}{9Na_o}\left(\frac{d^2\Phi}{da^2}\right)_{a=a_o} \tag{2.49}$$

From the above equations, the two parameters $_e$ and β can be adjusted to obtain the cohesive energy (U_0) and the bulk modulus (B) at the equilibrium value a_0. The parameter r_e is readily obtained from Eq. (2.50).

$$r_e = \frac{1}{\beta}\ln\gamma \tag{2.50}$$

The above described analytical fitting is implemented with a cut-off distance of 10 Å – the parameters $D_e = 0.161$ eV and $\beta = 1.0$ Å^{-1} yield a cohesive energy per molecule, ε_{coh}, of 1.04 eV (corresponding to a total cohesive energy of 100 kJ/mol) and a bulk modulus of 8.5 GPa, which is typical of metalorganic solids. The value of r_e from Eq. (2.50) yields $r_e = 6.27$ Å.

MD simulations, of a computational cubic system of 6912 molecules, are run with the analytically determined parameters of the Morse potential, to verify the fitted properties at 300 K. Resultantly, the analytically determined properties are slightly corrected to obtain a density of 2.2 g/cm^3 and a cohesive energy per molecule of $\varepsilon_{coh} = 1.04$ eV, calculated from the total potential energy of -7172 eV. The corrected values are $D_e = 0.160$ eV, $\beta = 1.0$ Å^{-1}, and $r_e = 6.26$ Å. The bulk modulus is then determined, as in 2.2.1.1.1, for simulated *NVE* ensembles, having densities that differ up to within 2.5 % of the equilibrium density, of the parametrized system. The bulk modulus is $B = 7.5$ GPa, within the expected range.

3. COMPUTATIONAL INVESTIGATION OF PULSED LASER ABLATION OF LYSOZYME TARGETS

This section starts with a description on how the model laser target is obtained, sub-section 3.1. It is followed by a description of the laser irradiation and absorption of the target in sub-section 3.2. The results, and the relevant analyses and discussions, of the simulations of the irradiated targets are provided in latter parts of the section.

3.1. Lysozyme Model Target Structure

At room temperatures, lysozyme is mostly grown into tetragonal crystals [103, 104, 105]; other forms can be triclinic, monoclinic or orthorhombic [106, 107]. A conformational view of a unit tetragonal cell [105] reveals a close-packed structure. In our model, due to its close-packed structure crystalline, lysozyme is represented by an FCC crystal, in which the crystal sites are occupied by globules.

A globule of 129 BS monomers (or beads) is obtained by thermal relaxation, in free boundary conditions (FBC), of a randomly generated polymer chain. Snapshots of the initially generated chain and an equilibrated globule are displayed in Figure 3.1. The density of a simulated globule is 1 g/cm^3, calculated within the volume defined by the dimensions of the globule.

a)   b)
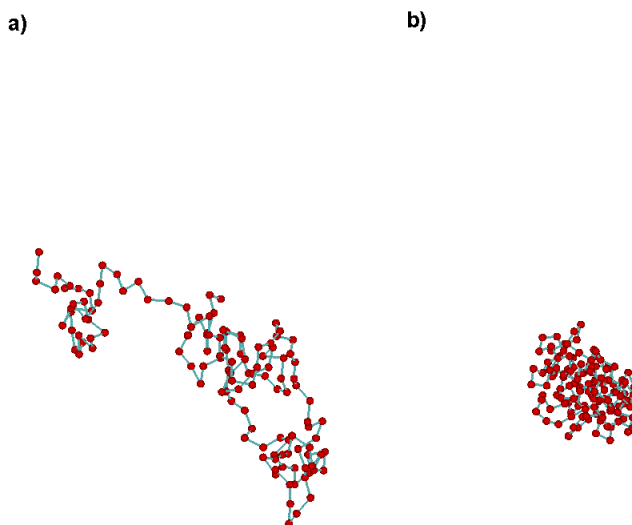
Figure 3.1   a) randomly generated polymer chain; b) globule obtained by thermal relaxation of generated chain. The beads (monomers) are colored red; the green links indicate chemical bonding between beads.

A globule is centered on every FCC crystal site to generate a lysozyme crystal of 1296 globules, which is thermodynamically relaxed at room temperature conditions ($P = 0$, $T = 300$ K), with periodic boundary conditions applied in all three directions, to obtain an equilibrium structure of computational size $11.2 \times 33.6 \times 44.8$ nm^3 and density 1.84 g/cm^3. The equilibrated lysozyme structure is displayed in Figure 3.2a.

Model structures with residual water are produced. Small (~3 nm) water pockets are homogeneously distributed in lysozyme to form structures with water concentrations of 5, 10, 15, and 20 wt.%. The densities of the equilibrated samples are 1.75, 1.68, 1.62, and 1.55 g/cm^3 for 5, 10, 15, and 20 wt.% water, respectively; the structure with 10 wt% water is displayed in Figure 3.2 b.
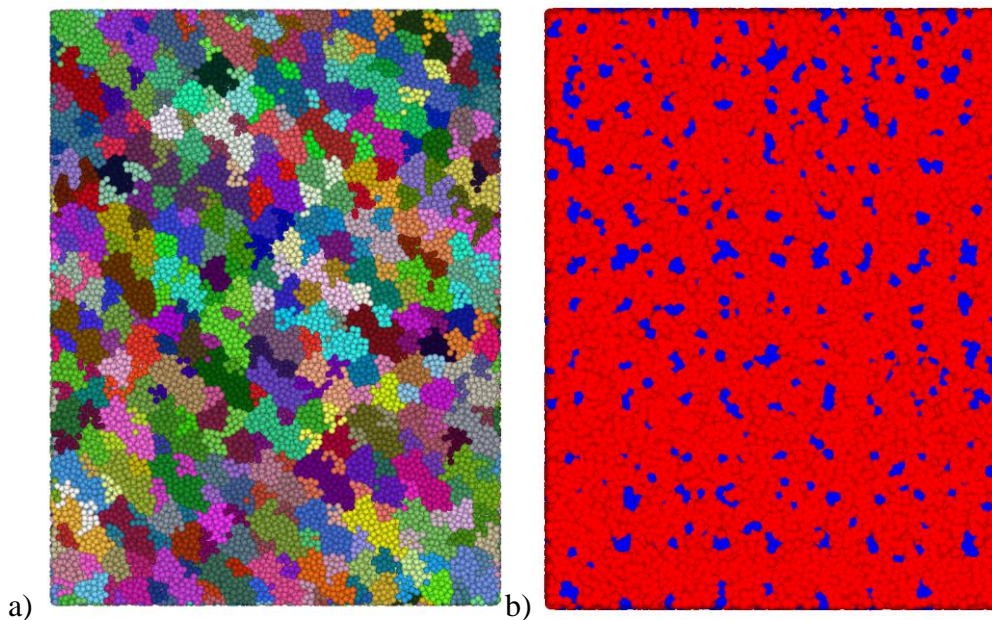
Figure 3.2. a) Model structure of pure lysozyme at 300 K – individual globular molecules are colored by different random colors; b) Lysozyme model structure with 10 wt% water – lysozyme is colored in red, and water is colored in blue.

3.2 Laser Irradiation and Absorption

The laser excitation at a wavelength of 355 nm is simulated by deposition of quanta of energy equal to the photon energy (3.5 eV) into the heatbath energy of polymer units that are randomly chosen during the laser pulse duration. The probability of a molecule to be excited is modulated by Lambert-Beer's law to reproduce the exponential attenuation of the laser light with depth. The laser penetration depth of ~30 μm is used in the simulations. This value is determined in experiments performed for a dry 100 μm thick lysozyme layer confined between two quartz windows and irradiated with a low-energy laser pulse. The depth of a visible "damage" of ~30 μm is used as an estimate of the laser penetration depth for pure lysozyme target in the simulations. The absorption by water is negligible, since its penetration depth is ~ 25 m [108] at

355 nm wavelength. The effective values of the laser penetration depth L_p for samples impregnated with water droplets is dependent on the density of pure lysozyme: L_p is inversely proportional to the density. Although, absorption by bulk water is negligible, in the model samples of lysozyme that have low water concentration, the photon energy is deposited into the heatbath energy of polymer units as well as water units. This is adequate as the photon-deposited energy thermalizes in times lesser than the duration of the laser pulse. The values of L_p for the different lysozyme structures having different densities are summarized in Table 3.1.

Table 3.1. Parameters (density and absorption length) of lysozme target samples used in simulations.

water concentration, wt.%	sample density, g/cm^3	lysozyme density, g/cm^3	L_p, μm
0	1.83	1.83	30
5	1.75	1.663	33.2
10	1.68	1.512	36.5
15	1.62	1.377	40.1
20	1.55	1.24	44.5

A pulse duration of 400 ps, different from the experimental pulse duration of 6 ns, is used in the simulations of the pure and water-impregnated lysozyme material systems. The pulse duration in our model is chosen to replicate the physical regime realized in the experiments. The time of dissipation of laser energy by thermal conduction can be estimated as $\tau_{th} \sim L_p{}^2/D_T$, where T is the thermal diffusivity and L_p is the laser penetration depth. In the laboratory target, $\tau_{th} = 3$ ms for a T value of 3x10^{-3} cm^2/s, calculated from the thermal conductivity of natural proteins,

0.5 W/(mK) [109], assuming a density of 1.3 g/cm^3. Because the pulse duration is shorter than the time required for laser energy to be thermally conducted away, i.e. $\tau_p < \tau_{th}$, the laser deposition regime is one of *thermal confinement*. The relation between the time of the laser energy deposition and the characteristic time of mechanical relaxation (or equilibration) of the absorbing volume, $\tau_s \sim L_p/C_s$, in which C_s is the speed of sound, determines the magnitude of laser-induced stresses and associated photomechanical effects. An estimate of $\tau_s = 13.6$ ns is determined for a value of $C_s = 2.2$ km/s, obtained as an average of velocities along [001] and [110] directions in a tetragonal lysozyme crystal [60]. Because the pulse duration is shorter than, but of the same order of magnitude as, the time for mechanical relaxation, $\tau_p < \tau_s$, the laser irradiation is in a regime of weak *stress confinement*. In the regime of stress confinement, laser heating occurs at nearly constant volume conditions, causing a high thermoelastic pressure buildup. This usually leads to the start of ablation at energy densities lower than those required for explosive vaporization of the material [9].

The thickness of the computational target, L, is only 44.8 nm and, therefore, the simulated target represents the top surface region of the experimental target (the thickness is of order ~ mm), where there is no stress confinement and the laser-induced stresses are low. The computational regime of ablation chosen is one that is within thermal confinement, and away from stress confinement: $\tau_s < \tau_p < \tau_{th}$. Because $L \ll L_p$, the computational ablation regime is defined by the thickness of the target rather than its penetration depth: $\tau_{th} \sim L^2/D_T = 20$ ns; and $\tau_s \sim L/C_s = 20$ ps. The pulse duration chosen for the simulations, $\tau_p = 400$ ps, is within the desired range, 20 ps $< \tau_p < 20$ ns.

For simulations of laser irradiation, the obtained lysozyme structures are placed on a transparent rigid substrate. Periodic boundary conditions are applied in the directions parallel to

the irradiated surface, and the interaction with the substrate at the bottom of the computational cell is assumed to be 3 times stronger than the non-bonded intermolecular interactions. A diagram of the model set-up for laser irradiation is displayed in Figure 3.3.
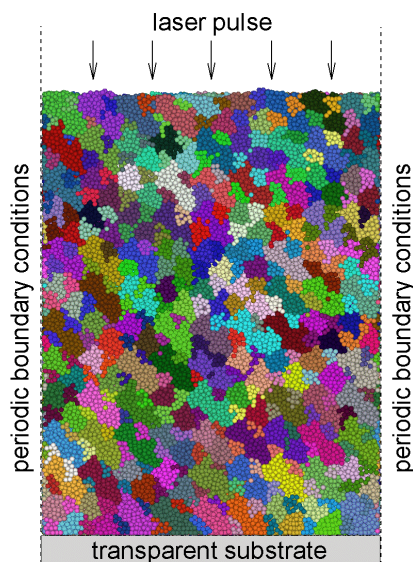
Figure 3.3   Schematic sketch of the simulation setup for modeling of laser ablation of lysozyme films on a transparent substrate.

Simulations of the laser ablation of pure solid lysozyme are performed at fluencies 20 J/cm^2, 25 J/cm^2, and 30 J/cm^2, with the aim of determining whether intact lysozyme molecules can be ejected from the target at any fluence. Simulations of the laser ablation of lysozyme target with water impregnated at concentrations of 5 wt%, 10 wt%, 15 wt%, and 20 wt%, are performed to determine the effect of water on the ejection of lysozyme. The goal of the simulations is to investigate: (i) the effect water has on lowering the threshold fluence to material ejection (or ablation), and (ii) the effect of water on the range of fluencies for which intact molecules of lysozyme can be ejected. For lysozyme systems with the mentioned water concentrations, simulations are run at fluencies as low as 3 J/cm^2 for a system with a water concentration of 20

wt% to determine the ablation threshold, and still at fluencies as high as 30 J/cm^2 to determine the threshold for complete fragmentation of lysozyme molecules.

The timestep of simulation of a system of molecules in molecular dynamics simulations is usually chosen in relation to the highest frequency of oscillations exhibited by the molecules. Because of the presence of a high-frequency component, in bonding interactions between connected beads, in lysozyme, it is deemed important to discuss the choice of the timestep here.

Determination of Timestep in MD simulations

The timestep, δt, here is estimated to be a small fraction, ≲ 0.01, of the smallest characteristic period of oscillations T, i.e. δt ≲ T/100. An attempt is made at a theoretical estimation of the characteristic periods of oscillations, due to motion described by each of the parametrized potentials, in a harmonic approximation; a corresponding MD simulation is run to determine the characteristic period of oscillations due to motion described by the parametrized potential.

At separations close to the equilibrium separation, r_e, a second order Taylor expansion of the Morse potential, Eq. (2.1), $\Phi(r - r_e) \cong U(r)$:

$$\Phi(r - r_e) = -D_e + D_e\beta^2(r - r_e)^2 \qquad (3.1)$$

It can be easily seen in Eq. (3.1) that the Taylor approximation is simple harmonic in displacements from equilibrium, $x = r - r_e$, about the well depth, $-D_e$. Thus, making a comparison to the simple harmonic potential form about the well depth, $U = \frac{1}{2}kx^2$, we obtain the harmonic constant, $k = 2D_e\beta^2$, from which the period is $T = 2\pi\sqrt{\mu/k}$, where μ, the reduced mass equals $M/2$ for interactions between molecules of equal masses. For a BS molecule' mass of 111 Da, the period is

$$T = 2\pi \sqrt{\frac{184,094}{6,4 \cdot (D_e\beta^2)}} \times 10^{-14} \text{ s}$$

for $_e$ in eV, and β in Å^{-1}. Applying the harmonic approximation to the Morse potentials, the periods of oscillations, due to non-bonding interactions and bonding interactions, are determined and tabulated in Table 3.2.

A Taylor approximation of the breathing potential has been done in sub-section 2.2.1.3, see Eq. (2.28). A relation between the harmonic constant in the harmonic potential, k, and that in the Taylor approximation of the breathing potential, k_1, was determined to be $k = 2k_1$, from which the period of the harmonic approximation $T = 2\pi\sqrt{M_I/k}$ becomes $T = (2\pi/\sqrt{2})\sqrt{M_I/k_1}$. From the known parameters of the breathing potential, which are $k_1 = 30\ eV/Å^2$, $M_I = 3552$ Da, the period is determined to be $T = 0.49$ ps in the harmonic approximation of the anharmonic potential.

Plots of the parametrized potentials together with their harmonic approximations are displayed in Figure 3.4a. Although the harmonic approximation can be seen to be a good fit only within ~ 0.1-0.2 Å away from the equilibrium position, comparisons to parametrized potentials will be done for deviations up to within ~ 0.6 Å.

To determine the actual periods of oscillations due to the modes described by the BS intermolecular interaction potentials, MD simulations are run for two BS beads, and the evolution in time of their separation is observed.

The time-dependent separation of the edges of two BS beads, whose interaction is described by the Morse bonding potential is plotted in Figure 3.5a. The period of oscillations can be retrieved from the plot to be ~ 0.09 ps, making it close to the determined period of 0.07 ps (see Table 3.2), obtained in the harmonic approximation of the bonding potential.

The time-dependent separation of the edges of two beads, whose interaction is described by the Morse non-bonding potential is plotted in Figure 3.5b. The period of oscillations can be retrieved

from the plot to be ~ 1.1 ps, also making the predicted period of 1.1 ps, in the harmonic approximation of the non-bonding potential, a reliable estimate.

The actual period of oscillations of breathing motion is determined by observing the change in radius over time for a single BS bead in a MD simulation. The time-dependent radius of a bead in breathing motion is plotted in Figure 3.5c. The period of oscillations for breathing motion described by the anharmonic potential parameters is retrieved to be ~ 0.37 ps. This is roughly comparable to the theoretical estimate of 0.49 ps.

Water Morse potential has a value of D_e close to an order of magnitude smaller than that in the lysozyme bonding interaction, so the period of oscillations is expected to be significantly higher, and its characteristic period of oscillations need not be accounted for in the determination of the timestep.

The smallest characteristic period of oscillations is associated with bonding interactions: it is determined to be T ≅ 0.09 ps in a MD simulation of two BS monomers interacting only through the bonding potential. Taking δt ≲ T /100 leads to the choice of δt = 0.5 fs as a suitable timestep for MD simulations.
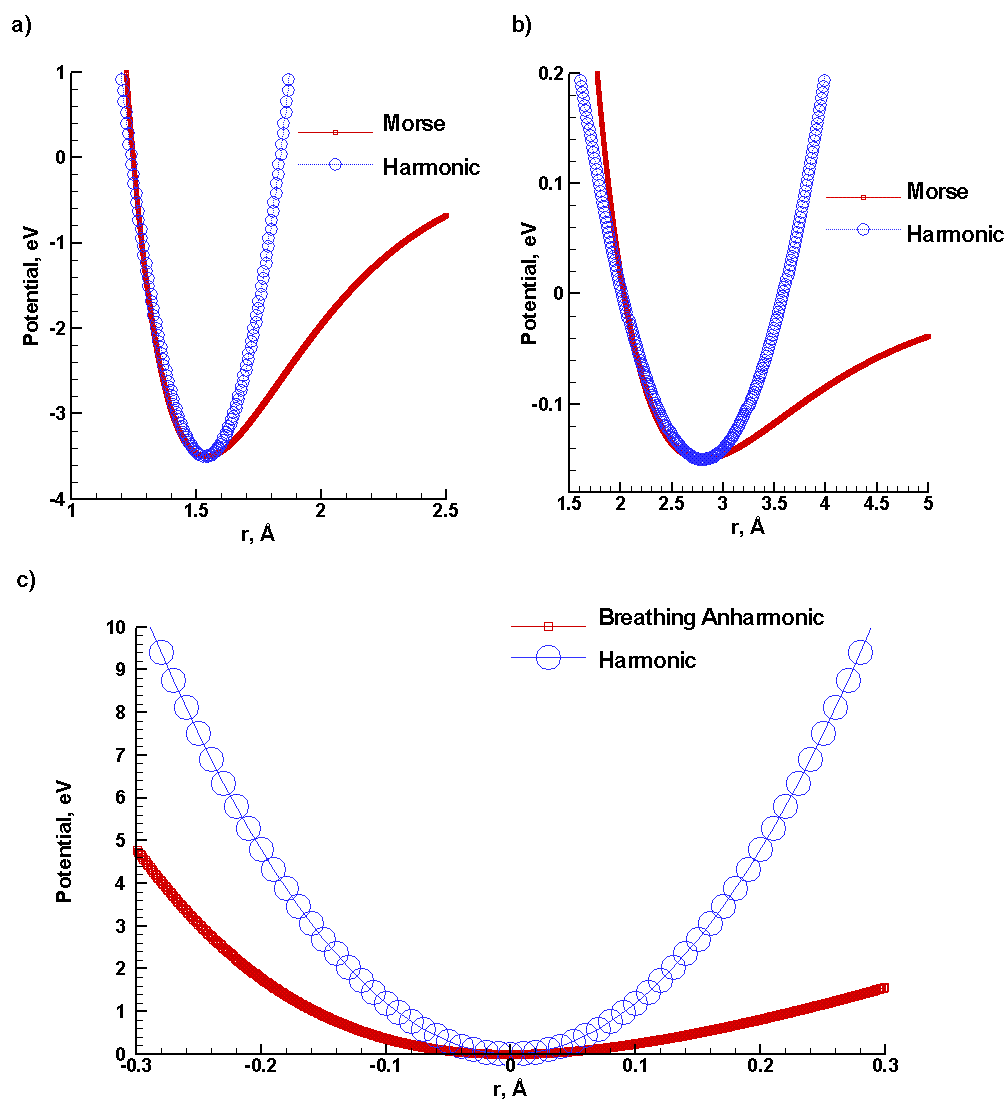
Figure 3.4   Harmonic approximations potential plotted alongside the parametrized potentials for lysozyme – plots for: a) bonding, b) non-bonding, c) Breathing potential – r is separation from equilibrium BS radius.
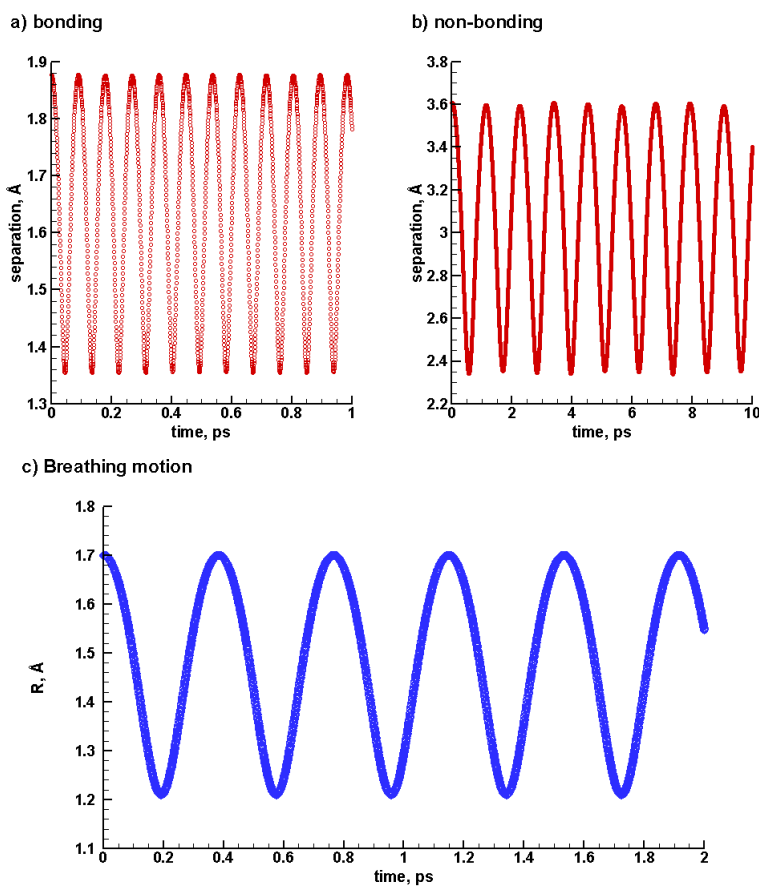
Figure 3.5   Separation between edges of two lysozyme BS beads over time in a) a bonding interaction, b) a non-bonding interaction. c) Time-dependence of the radius of lysozyme breathing sphere.

Table 3.2. Comparison of estimated periods, in the harmonic approximation of interaction potentials, to actual periods obtained in MD simulation, for lysozyme.

Potential type	Bonding	Nonbonding	Breathing motion
Estimated period, ps	0.07	1.1	0.49
MD simulation period, ps	0.09	1.1	0.37

3.3   Laser Irradiation Simulation Results

The simulations of the laser irradiation of pure lysozyme targets and lysozyme targets with various water concentrations are discussed and analyzed. The effect of water concentration on lowering the ejection threshold is also discussed.

3.3.1   Laser Ablation Simulation Results for Pure Lysozyme

Simulations performed at fluencies around the threshold for ablation, 25 J/cm^2 and 30 J/cm^2, show that no globule (macromolecule or biomolecule) in the irradiated target remains intact.

At 25 J/cm^2, the target separates from the substrate after the pulse, but does not ablate in the bulk, as is observed in Figure 3.6. The dependence over time of lysozyme fragmentation, Figure 3.7a, shows that bond breaking starts at ~ 400 ps (end of the pulse), and when the fraction of bonds that are broken attains 5 %, there is no single intact globule. The temperatures of the different energy modes are displayed in Figure 3.7 b: at 400 ps, the onset to bond breaking, the temperature is ~ 3500 K. The temperatures of the translational, breathing, and internal modes, are up to within ~ 5-10 % difference during and after the pulse, as was predicted by the simulation of a fast energy deposition rate in section 2, temperatures of which were displayed in Figure 2.19.

The lift-off of material from the substrate can be explained by the effect of pressure close to the substrate. Energy is deposited evenly in the simulated material target, and so it should expand uniformly. The substrate, however, is non-dynamic and resists expansion of the material in the direction of laser depositon; this results in build-up of pressure close to the substrate. The

discrimination in pressure across the depth of the target can be observed in a contour plot of pressure, Figure 3.8a. The built-up pressure can more actively break bonds or provide an immediate push to the target from the substrate. A higher intensity in bond breaking at the bottom part of the material increases its volatility, easily enabling separation of the target from the substrate. It can be observed in a contour plot of the amount of fragmented material, Figure 3.8b, that: bond breaking starts ~ 300 ps into the pulse in the bottom part of the target, up to ~ 3-5 nm from the substrate; at ~ 700 ps, although the average percentage of fragmented material is ~ 7 %, the percentage of fragmented material in the bottom significantly increases to ~ 20-30 % and grows in thickness into the target in later time. Such a high degree of fragmentation in the bottom material induces volatility, providing a push to the target material from below.
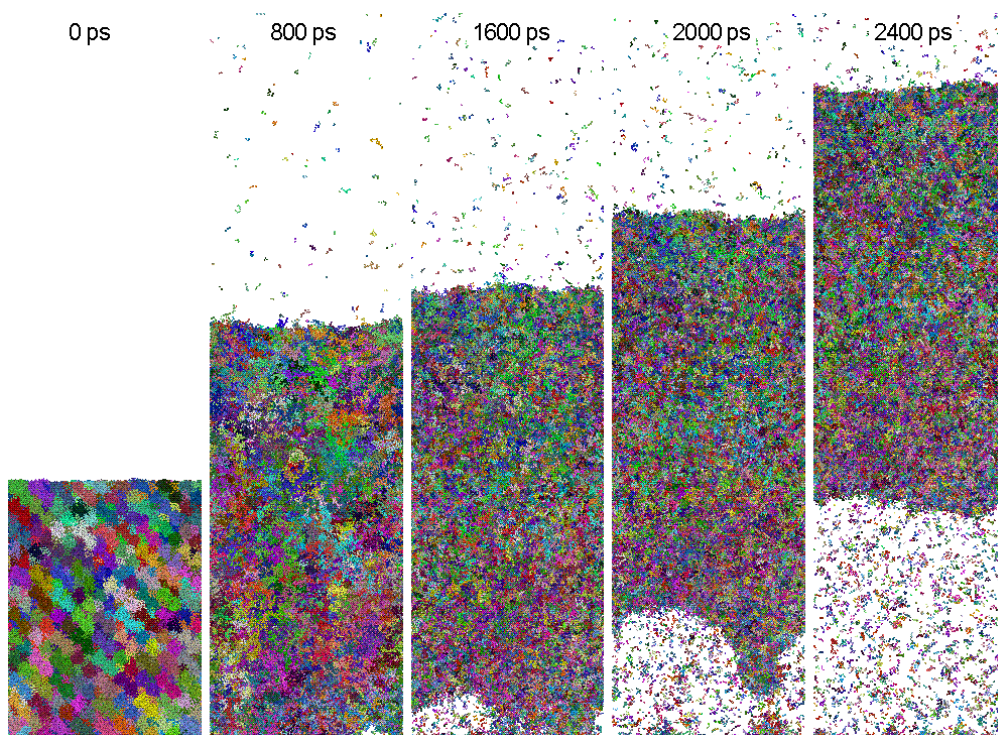
Figure 3.6 Snapshots of molecular configurations of pure lysozyme at 25 J/cm^2: molecular fragments originating from the same molecule are colored by the same random color.
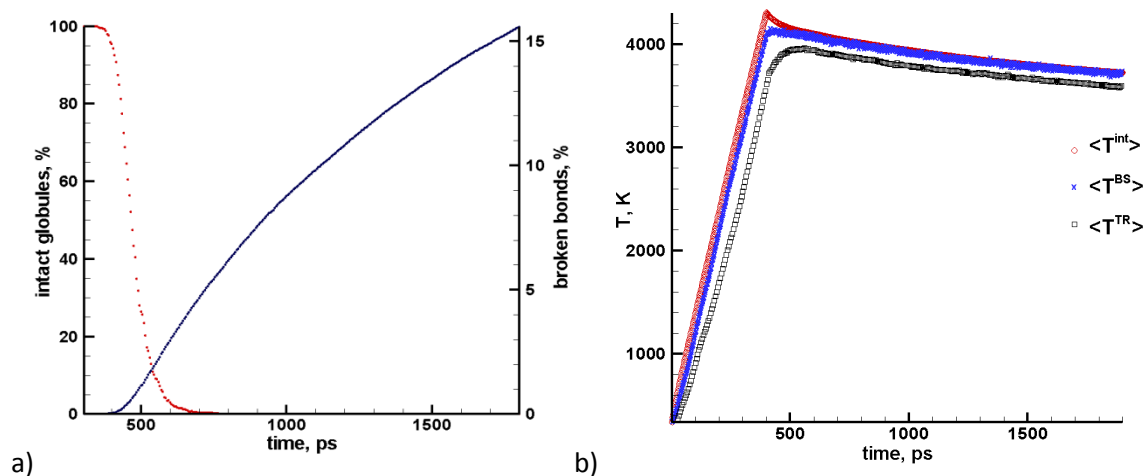
Figure 3.7. A dependence over time, at 25 J/cm^2, of a) lysozyme fragmentation − showing the evolution of the percentage of broken chemical bonds and the number of intact polymer globules, b) the temperatures of translational ($\langle T^{TR} \rangle$), breathing($\langle T^{BS} \rangle$), and internal ($\langle T^{int} \rangle$) modes.
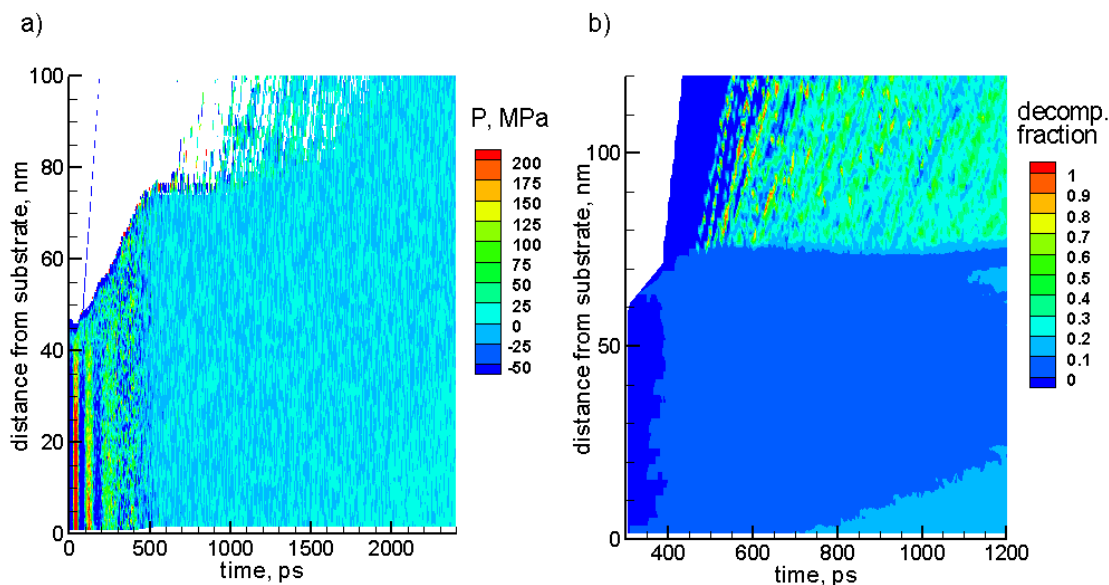
Figure 3.8. Contour plots, for pure lysozyme at 25 J/cm^2, of a) pressure, b) fraction of fragmented material.

At 30 J/cm^2, ablation of the material target into larger molecular droplets can be observed in Figure 3.9a. No globule remains intact shortly after the pulse, as can be seen in Figure 3.9b. The temperature and density profiles, in Figure 3.10, reveal that ablation starts to occur at ~ 3500 K. A high fraction of bond dissociation, up to ~ 15 %, is attained prior to vaporization of the target. A high intensity of volatile fragments due to high bond dissociation rates provides the driving force for the ejection of larger polymer fragments and molecular droplets. The whole material target is no more observed to separate from the substrate as was the case at 25 J/cm^2, since the ablation mechanism is predominant, over pressure build-up effects close to the substrate, to material ejection.

The ablation mechanism described has some similarity to MAPLE, with the volatile products of the thermochemical decomposition serving the role of matrix that drives the ejection process. One important difference, however, is that the thermodynamic parameters of the matrix material, which is actually a solvent, in MAPLE can be chosen so that no thermal decomposition of polymer molecules takes place at the threshold for the explosive boiling of the matrix, whereas in the case of pure polymer target the thermal decomposition is a required step of the ablation process and no ejection of intact polymer molecules can be expected.
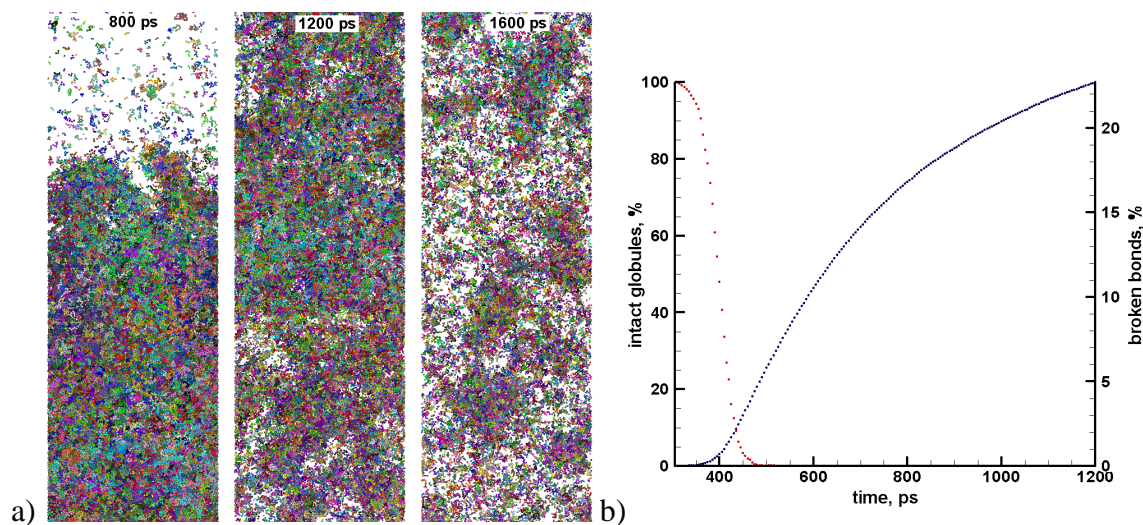
Figure 3.9   The results of a simulation of laser irradiation of a pure lysozyme film performed at an absorbed laser fluence of 30 J/cm^2. Snapshots of molecular configurations are shown in (a), where molecular fragments originating from the same molecule are colored by the same random color. The evolution of the percentage of broken chemical bonds and the number of intact polymer molecules is shown in (b).

a)   b)
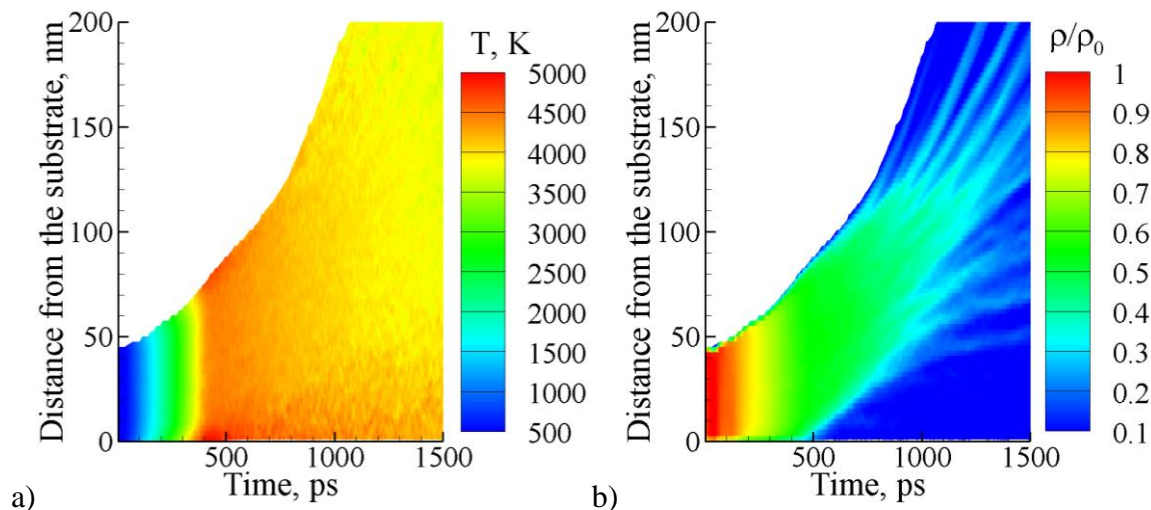
Figure 3.10   The evolution of a) temperature and b) density in simulations of lysozyme films deposited on a transparent substrate and irradiated with a 400 ps laser pulse at absorbed fluences of 30 J/cm^2. The density scale is normalized to the initial density before the irradiation, ρ_0. The areas where the density of the material drops below $0.1\rho_0$ are blanked in the contour plots.

The simulated ablation of lysozyme polymer target leading to the ejection of not a single intact globule clearly does not match experimental observations. Significant yields of intact molecules have been obtained from experimental targets at fluences of ~ 1-4 J/cm^2, that are significantly lower than the simulated ablation fluence. This strongly suggests a different physical picture for the structure of laboratory lysozyme target.

Natural protein crystals retain up to about 50 % water by volume, removal of which may lead to loss of crystallinity [107]. Water in lysozyme crystals forms an integral part of lysozyme protein molecules, or is organized around protein molecules [62, 107]. The solvent content of native crystals is 32.4 % by volume, and is as low as 9.4 % in crystals prepared in relatively dehydrated conditions (relative humidity [R.H.] of 5%) [64]. In addition, a thermogravimetic (TG) analysis of lysozyme – see TG curve in Figure 3.11 – reveals that ~ 8 % of the sample mass is lost at temperatures less than 150 ^{O}C, the loss being attributed to the evaporation of residual water. The made observations on the water content of lysozyme crystals or target material are supportive to investigating the effect of retained water on the ablation process of lysozyme. Results of computational simulations of laser ablation of lysozyme with droplets of water may provide reasonable explanation to the observation of intact molecules in deposited films. In the laboratory target, physisorbed water may partly manifest in the form of water vapor due to processing to obtain pressed lysozyme prior to laser deposition. However, the possible effect of vapor-phase water prior to laser deposition is not included in the model.
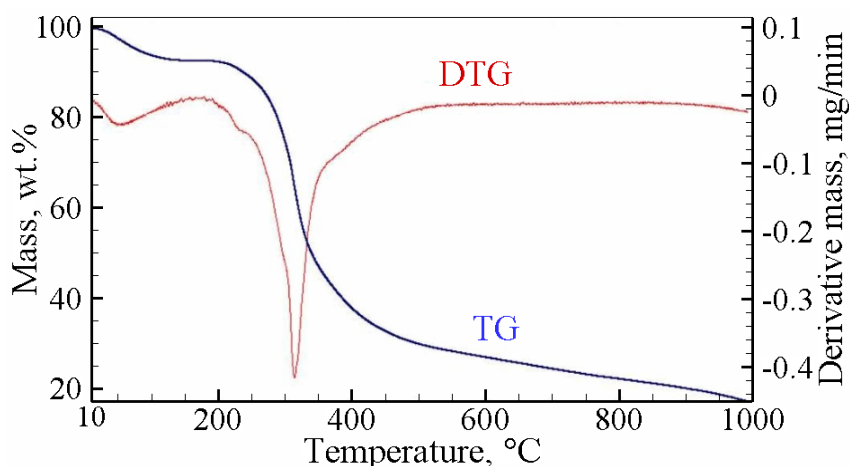
Figure 3.11   The results of thermogravimetric analysis of a lysozyme target used in the laser deposition experiments. The thermogravity (TG) and derivative thermogravity (DTG) curves

show about 8% mass loss at T < 150ºC attributable to the residual water, followed by decomposition of lysozyme at higher temperature. [Courtesy of Jorgen Schou].

3.3.2 Simulation Results for Laser Ablation of Lysozyme Targets with Residual Water

Simulations of lysozyme targets with as little as 5 wt% water are investigated at fluencies 14 J/cm^2, 16 J/cm^2, 18 J/cm^2, 22 J/cm^2, and 25 J/cm^2. In marked contrast with pure lysozyme, ablation already occurs at 18 J/cm^2 and with more than half of the globules intact. Still, though, there is no observed range of fluencies for which there is ablation with all globules intact. As in the case of pure lysozyme, all globules are fragmented at 25 J/cm^2. Snapshots are displayed in Figure 3.12 for some of the simulated fluences, and a diagram of the time evolution of the percentage of broken bonds is illustrated in Figure 3.13. A window of fluences for which some intact molecules are ejected during ablation is approximately determined as 16 J/cm^2 < F < 25 J/cm^2.
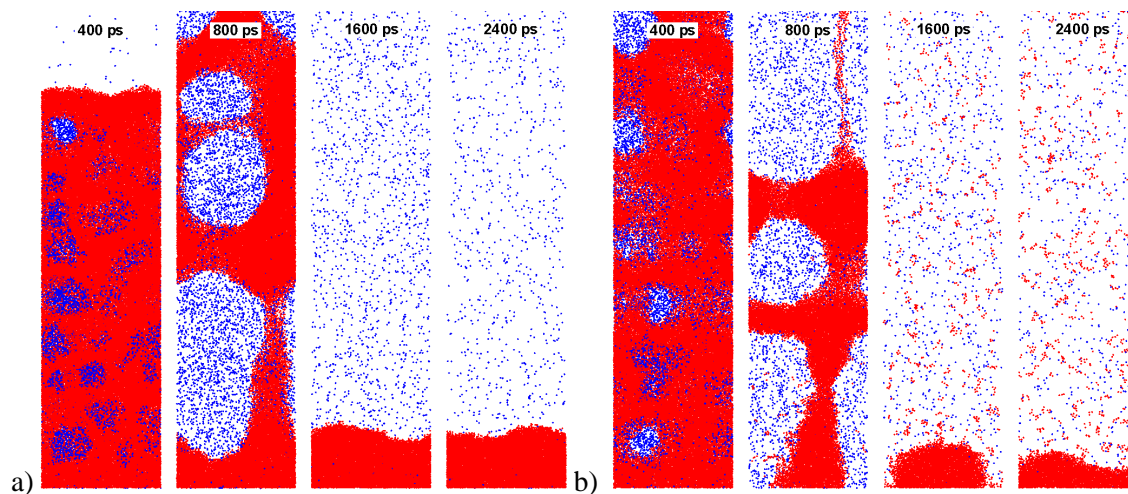
Figure 3.12   Snapshots of molecular configurations obtained in simulations of laser irradiation of a lysozyme film containing 5 wt.% of residual water. The simulations are performed at an absorbed laser fluence of (a) 18 J/cm^2 (ablation regime with partial fragmentation of lysozyme

molecules), and (b) 25 J/cm^2 (complete fragmentation of lysozyme molecules). The units of polymer chains and water molecules are shown as red and blue particles, respectively.
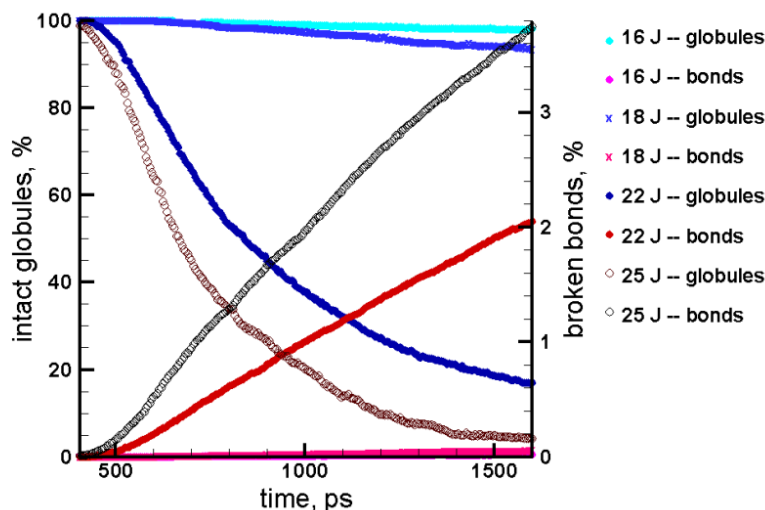
Figure 3.13   The evolution of the fraction of broken chemical bonds and the number of intact lysozyme molecules in simulations of lysozyme film containing 5 wt.% of water. The results are shown for fluencies of 16 J/cm^2, 18J/cm^2, 22 J/cm^2, and 30 J/cm^2.

Simulations of lysozyme targets with 10 wt% water are investigated for fluencies 8 J/cm^2, 13 J/cm^2, 16 J/cm^2, 21 J/cm^2, and 30 J/cm^2. Figure 3.14 displays snapshots of molecular configurations of the simulated targets, and Figure 3.15 displays the fragmentation of lysozyme polymer molecules at fluencies of 21 J/cm^2 and 30 J/cm^2. A greater variation in ablation phenomena is observed compared to simulations of targets with a lower water concentration.

The fluence of 8 J/cm^2 is below the threshold for lysozyme ejection. The explosive boiling of water pockets, which starts when the temperature of the film reaches ~ 500 K, results in the film expansion during the first 2 ns after the laser pulse. The driving force provided by the expanding water vapor, however, is not sufficient for the ejection of entangled lysozyme molecules. At

some later time the large bubble in the surface region bursts, releases the water molecules and gradually deflates. The surface of the target recesses and no lysozyme ejection is observed.

At a fluence of 13 J/cm^2, ablative ejection of lysozyme already occurs. The expanding water vapor entrains the viscous droplets of polymer material and results in the ejection of almost the entire film. Not a single chemical bond is broken in this simulation and all lysozyme molecules are ejected intact.

At a fluence of 16 J/cm^2, only 0.2 % of molecules are fragmented (snapshots are similar to those for 13 J/cm^2 and are not shown).

At a fluence of 21 J/cm^2, slow fragmentation is observed, with the number of fragmented lysozyme molecules reaching 20% by the time of 3 ns. One can expect that more than 50% of lysozyme molecules will survive the ejection process.

At a fluence of 30 J/cm^2 (about 3 times the ablation threshold) fragmentation is extensive, and all lysozyme molecules are fragmented by the time of ~ 1.5 ns when the percentage of broken bonds is ~ 6 %, see Figure 3.15. The ejection of the large polymer fragments is driven by the expansion of a mixture of water vapor and small volatile products of polymer thermal decomposition.

The evolution of temperature and density in simulations of the target irradiated at the different fluences is summarized in Figure 3.16.

The window of fluencies leading to the ejection of intact molecules in simulations of lysozyme targets with 10 wt% water is in the region 8 J/cm^2 < F < 30 J/cm^2, significantly larger compared to that for 5 wt% water, 16 J/cm^2 < F < 25 J/cm^2. The ejection of intact molecules occurs up to ~ 3 times the ejection threshold, and although the magnitude of fluencies is higher (explanations to the difference in magnitudes will be provided in a proceeding sub-section), the simulations are

replicative of experimental behavior, where deposition of intact molecules starts at 1 J/cm^2, and attains its maximum at 3 J/cm^2. The experimental dependence of total yield of intact molecules on fluence is shown in Figure 3.17. Based on the results of simulations discussed above, 10 wt% appears a reasonable minimal water concentration for relating to experimental observations, and demands closer analysis of laser ablation results. For this water concentration the dependence of the yield of intact molecules on fluence is determined, in the next sub-section, and compared to the experimental dependence.
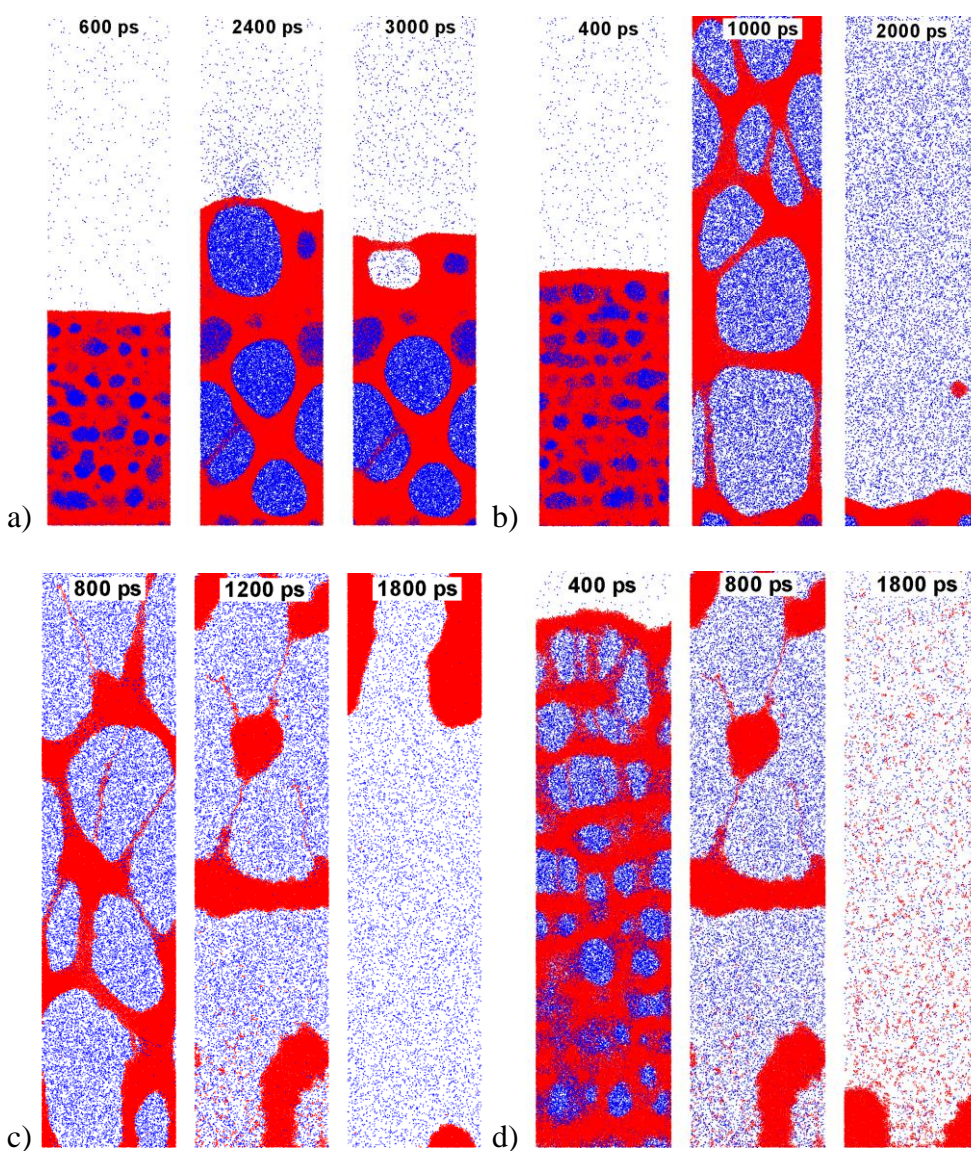
Figure 3.14 Snapshots of molecular configurations obtained in simulations of laser irradiation of a lysozyme film containing 10 wt.% of residual water. The simulations are performed at an absorbed laser fluence of (a) 8 J/cm^2 (below the ablation threshold), (b) 13 J/cm^2 (just above the ablation threshold), (c) 21 J/cm^2 (about twice the ablation threshold), and (d) 30 J/cm^2. The units of polymer chains and water molecules are shown as red and blue particles, respectively.
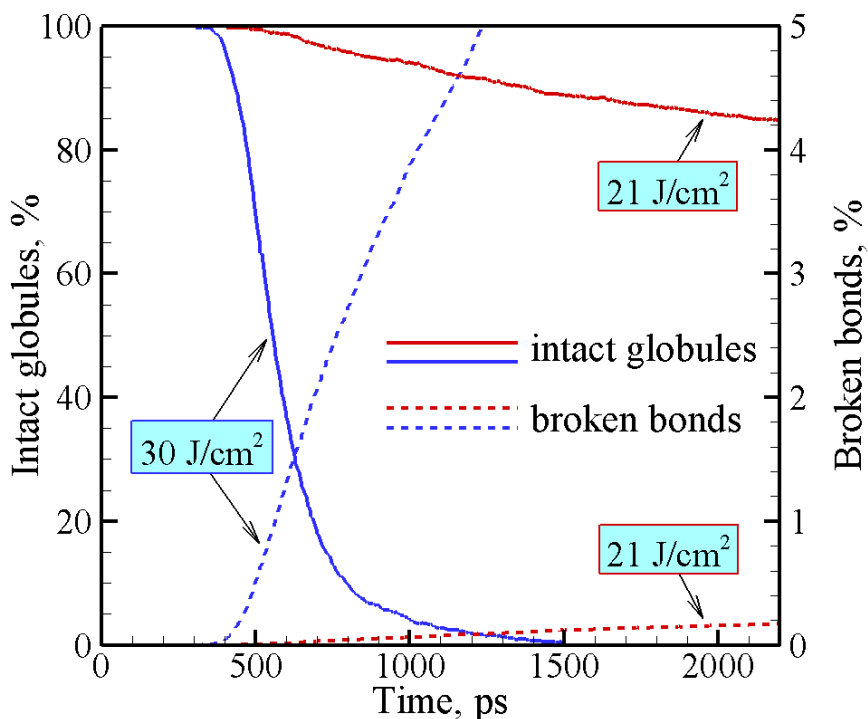
Figure 3.15 The evolution of the fraction of broken chemical bonds and the number of intact lysozyme molecules in simulations of laser ablation of lysozyme film containing 10 wt.% of residual water, with results shown for fluencies of 21 and 30 J/cm^2.

a)

b)

c)

d)

e)

f)

g)

h)
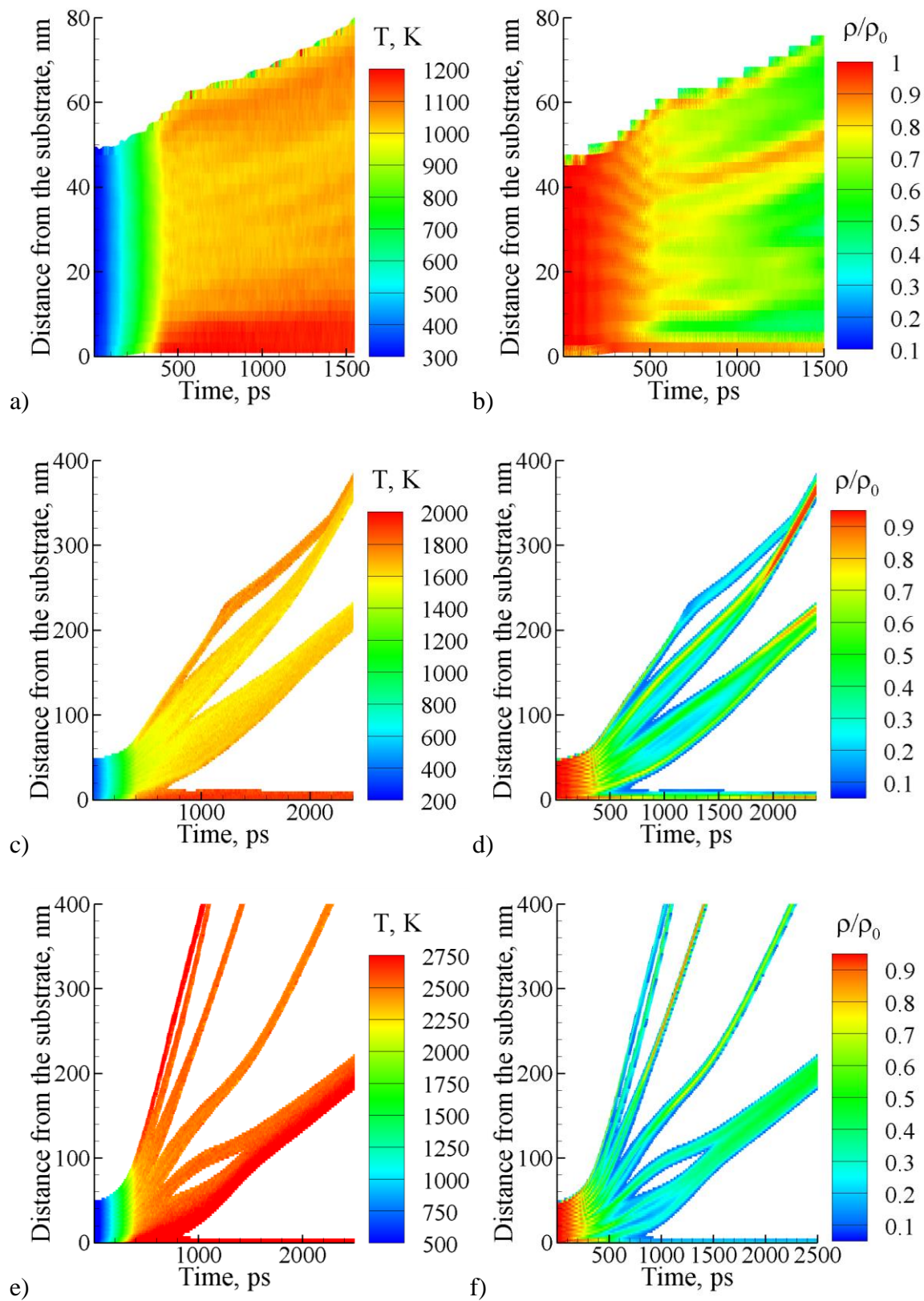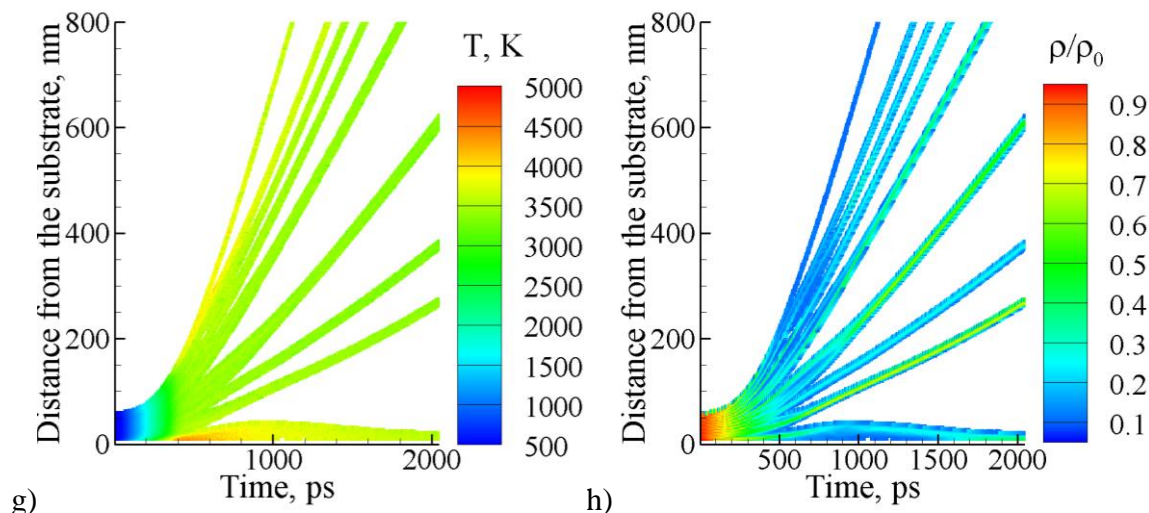
Figure 3.16 The evolution of temperature and density in simulations of lysozyme films containing 10 wt.% of residual water. The films are irradiated with a 400 ps laser pulse at absorbed fluences of 8 J/cm^2 (a,b), 13 J/cm^2 (c,d), 21 J/cm^2 (e,f), and 30 J/cm^2 (g,h). The density scale is normalized to the initial density before the irradiation, ρ_0. The areas where the density of the material drops below 0.1ρ_0 are blanked in the contour plots.

a)

b)
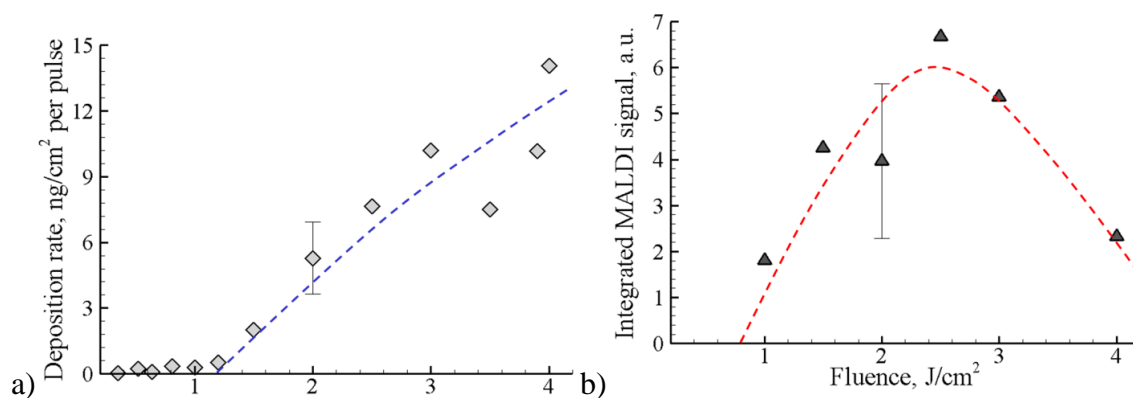
Figure 3.17 a) The deposition rate per pulse as a function of laser fluence in experiments performed for a lysozyme target irradiated in vacuum with 6 ns pulses at 355 nm; b) the integrated MALDI signal for mass 14307 Da obtained for the deposited films with the same thickness of ~140 nm or 17.2×10^3 ng/cm^2.

Yield of intact molecules of lysozyme with 10 wt% water

With an exponential decay of laser intensity given by Beer's law, the energy density deposited in a bulk target by the laser pulse with absorbed fluence F at a depth of z is

$$\epsilon(z) = \frac{F}{L_p} \exp\left(-\frac{z}{L_p}\right) \tag{3.2}$$

where L_p is the laser penetration depth. Eq. (5.1) can be rewritten in terms of the dependence of z on ϵ:

$$z = L_p \ln\left(\frac{F}{L_p \epsilon(z)}\right) \tag{3.3}$$

Using a simple model in which the ablation depth is defined by a critical energy density deposited by the laser pulse, ϵ^*, the ablation depth is

$$z^* = L_p \ln\left(\frac{F}{L_p \epsilon^*}\right) \tag{3.4}$$

and the corresponding ablation yield expressed in terms of the number of molecules ejected from a unit surface area of the target is

$$Y^{tot} = n_m L_p \ln\left(\frac{F}{L_p \epsilon^*}\right) \tag{3.5}$$

where n_m is the molecular number density.

Since the thickness of the films used in the simulations is almost 3 orders of magnitude smaller than L_p, the energy density ϵ^F deposited by the laser pulse with fluence F can be well approximated as the energy density deposited in the surface region of the target, *i.e.*, $z = 0$ in Eq. (3.2) or $\epsilon^F = F/L_p$. The results of the simulations provide us with the fraction of the intact molecules that survive at a given energy density deposited by the laser, $f(\epsilon^F)$. Note that the function $f(\epsilon)$ is evaluated for the initial temperature of 300 K used in the simulations and ε is the

energy added by the laser pulse to the thermal energy of the sample. The fractions of intact molecules are tabulated in Table 3.3 for the different fluences.

The data dependence of intact molecules concentration against energy density is fitted to the function, $f(\epsilon^F)$, in the range of energy densities at which material ejection occurs. Ejection of lysozyme begins at 13 J/cm^2 – this is considered the ejection threshold, ϵ^*; fragmentation of lysozyme molecules ($\leq 0.2\%$ fragmentation) begins at 16 J/cm^2 – this is considered the fragmentation threshold, ϵ^f; no molecule survives intact at 30 J/cm^2 –beyond this fluence, ϵ^m, no intact molecule is ejected.

A simple substitution, $x = (\epsilon^F - \epsilon^*)/\epsilon^*$, is made so that $f(x)$ can be defined in the entire range considered as:

$$f(x) = \begin{cases} 1, & x < x_f \\ P(x), & x_f \leq x < x_m \\ 0, & x \geq x_m \end{cases} \tag{3.6}$$

where $x_f = (\epsilon^f - \epsilon^*)/\epsilon^*$; and $x_m = (\epsilon^m - \epsilon^*)/\epsilon^*$. Here, $P(x)$ is described by a quadratic relation:

$$P(x) = 1 - 0.9286(x - x_f) + 0.5365(x - x_f)(x - x_m) \tag{3.7}$$

See Figure 3.18 for a display of the raw data and the fitted dependence of the concentration of intact molecules on energy density.

For the experimental conditions, the number of ejected intact molecules per unit area, Y^{int}, can be obtained through integration of the fraction of intact molecules ejected from different depths under the irradiated surface:

$$Y^{int} = n_m \int_0^{z^*} f[\epsilon(z)]dz \tag{3.8}$$

where the limits of integration are from the surface of the sample, $z = 0$, to the ablation depth z^* given by Eq. (3.4), the energy density distribution $\epsilon(z)$ is given by Eq. (3.2), and the fraction of intact molecules at a given density of deposited energy $f(\epsilon)$ is obtained from MD simulations as described above. The results of the calculations of Y^{tot} and Y^{int} are shown in Figure 3.19.

F, J/cm^2	ϵ^F, J/mm^3	$f(\epsilon^F)$, %
8	2.22	100
13	3.61	100
16	4.44	99.8
21	5.83	50
30	8.33	0
40	11.11	0

Table 3.3. Absorbed fluence F, energy density deposited at the surface $\epsilon^F = \epsilon(z = 0)$, and fraction of the intact molecules $f(\epsilon^F)$ predicted in MD simulations.
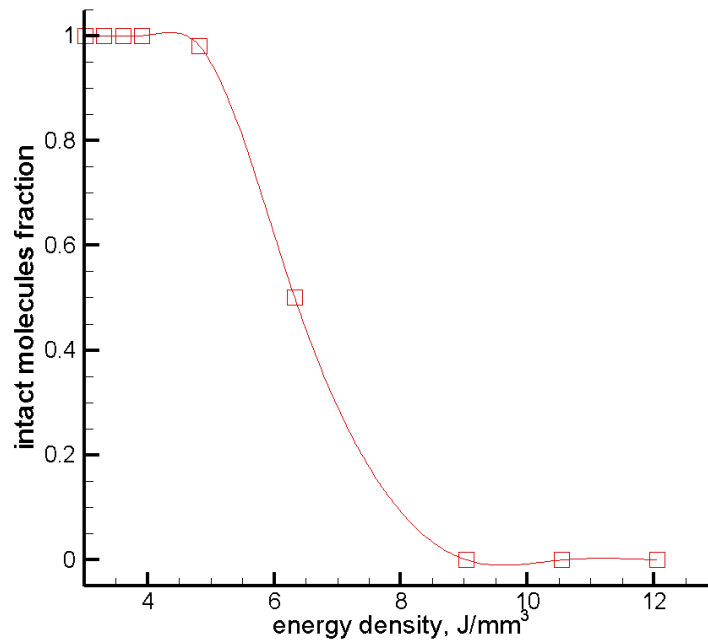
Figure 3.18   Dependence of concentration of intact molecules against irradiated fluence: both the raw data (open squares) and fitted dependence, $f(\epsilon)$, (solid line) are shown.
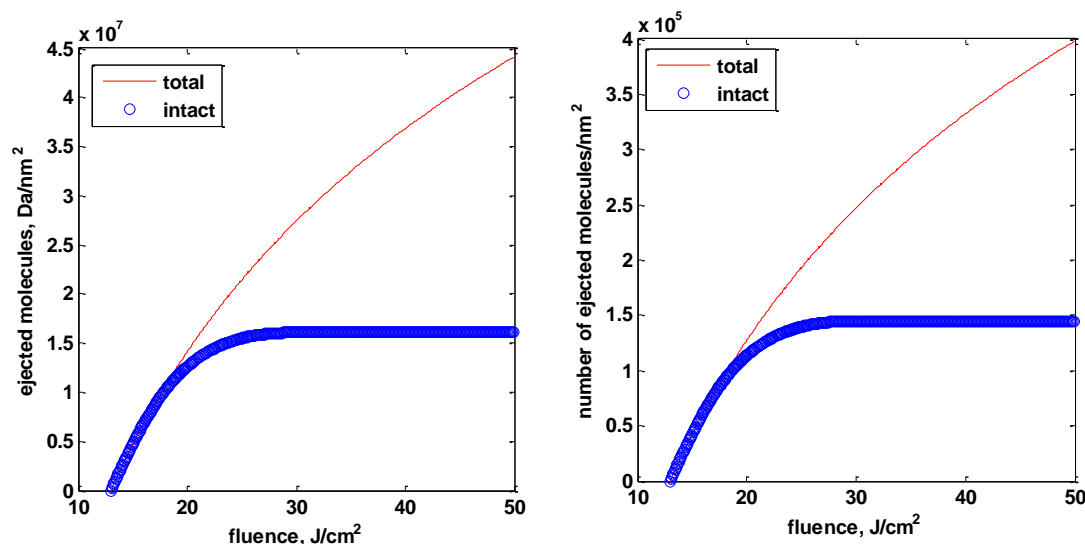
Figure 3.19 The dependences of the total yield of lysozyme molecules and the yield of *intact* molecules on laser fluence predicted based on the results of MD simulations for a lysozyme target containing 10 wt.% of residual water. [two versions of the figure are shown – the yield is shown in the number of lysozyme molecules per nm^2 and in the mass of lysozyme molecules, Da/nm^2]

An important distinction from experiment is that we are only simulating a thin (48 nm) film of lysozyme molecules deposited on a transparent substrate. The conditions created in the film can be related to a layer in the thicker experimental target where the same energy density is deposited by the laser pulse. Assuming that the total yield increases as $Y \sim \ln(F/F^*)$ for a bulk target and using the simulation data on the dependence of the fraction of intact molecules on the energy density deposited by the laser pulse, we can predict the fluence dependence of the yield of intact molecules in Fig. 3.17.

While the total yield increases logarithmically, the yield of intact molecules saturates to a constant value above ~30 J/cm^2, about three times the ablation threshold. It is important to note that all of the intact molecules are coming from the lower part of the ejected plume, have slower

ejection velocities, experience slower cooling, and can be pushed back by the more energetic upper part of the plume and redeposited to the target. With this understanding, the picture suggested by the simulations qualitatively agrees with the experimental observation of the decrease of the yield of intact molecules at higher fluences.

3.3.3   Dependence of Ablation Threshold on Water Concentration

While simulations of the ablation of lysozyme with 10 wt% water (as a minimal concentration) have shown significant yields of intact molecules within a broad range of fluences, and adequately predict experimental behavior, it is of additional interest to determine how the ablation threshold would further decrease with increasing water concentration.

Further simulations are carried out for 15 wt. % and 20 wt. % water in lysozyme, at fluences in the range 3-10 J/cm^2. For simulations with fluences around the ablation threshold (two fluences: closest fluence below threshold and closest fluence above threshold), snapshots are displayed in Figures 3.20 and 3.21, for 15 wt.% and 20 wt.%, respectively.

The threshold fluence is determined as the average of the closest fluence below threshold and the closest fluence above threshold: as an example, the ablation threshold for lysozyme with 15 wt.% is determined to be 6 J/cm^2, the average of 5 J/cm^2 and 7 J/cm^2. The dependence of threshold fluence on water concentration is tabulated in Table 3.4, and plotted in Figure 3.23a.

Temperature contour plots, see Figure 3.22, for the simulations just above the ablation threshold, are displayed, and are used to determine the temperature to the onset of ablation. Ablation in lysozyme with 15 wt% water is seen, see contour plot in Figure 3.22a, to occur at ~ 2500 ps at a temperature of ~ 1000 K. Ablation in lysozyme with 20 wt% water is seen, Figure 3.21b, to occur at ~ 1400 ps at a temperature of ~ 700 K. These temperature threshold values

together with those priorly determined for lower water concentrations are tabulated in Table 3.4, and a dependence on water concentration is plotted in Figure 3.23b.

A diagram that shows how the range of fluencies allowing for ejection of intact molecules changes with water concentration in the lysozyme target is displayed in Figure 3.24. This diagram provides a clear picture of how varying the low solvent content influences ablation behavior. With increasing water concentration, one can see that an increased range of fluencies allows for the ejection of more intact molecules.

Table 3.4.   Ablation threshold fluences at different water concentrations in lysozyme.

Water concentration in lysozyme, wt.%	Ablation threshold fluence, J/cm^2	Temperature at onset of ablation, K
0	28 ± 2	3500 ± 500
5	16 ± 2	2500 ± 250
10	11 ± 2	1750 ± 250
15	6 ± 1	1000 ± 125
20	4 ± 1	750 ± 125
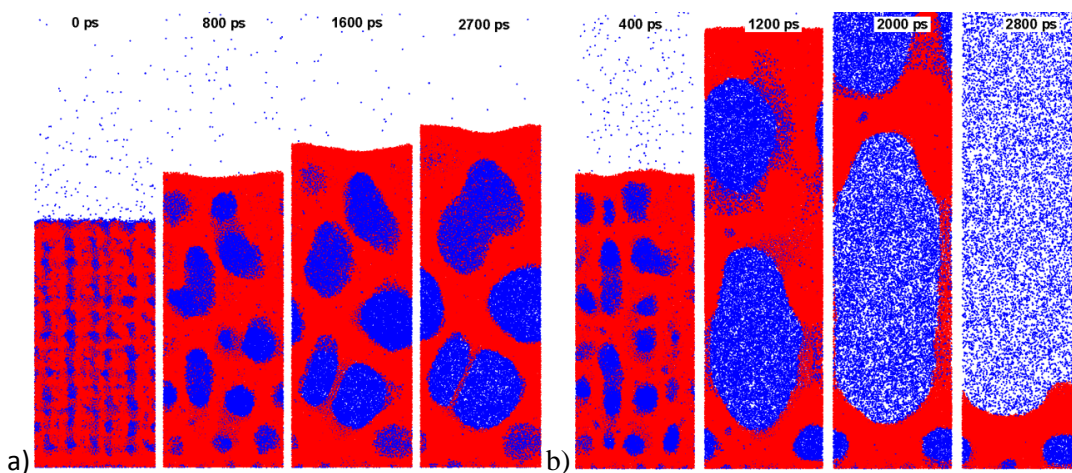
Figure 3.20   Snapshots of molecular configurations obtained in simulations of laser irradiation, at fluences around the ablation threshold, of a lysozyme film containing 15 wt.% of water. Simulations are performed at a) 5 J/cm^2 – below ablation threshold, b) 7 J/cm^2 – above ablation threshold.
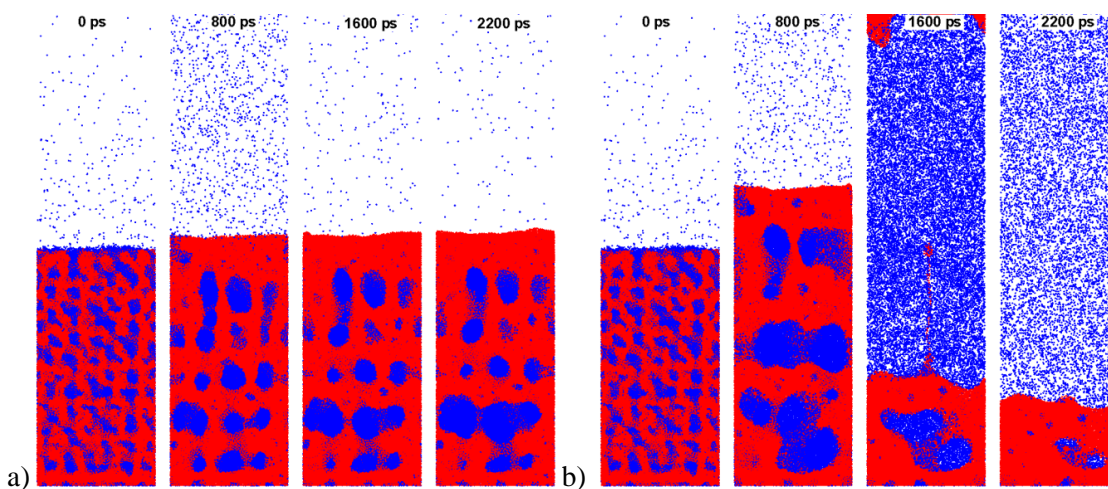
Figure 3.21   Snapshots of molecular configurations obtained in simulations of laser irradiation, at fluences around the ablation threshold, of a lysozyme film containing 20 wt.% of water. Simulations are performed at a) 3 J/cm^2 – below ablation threshold, b) 5 J/cm^2 – above ablation threshold.
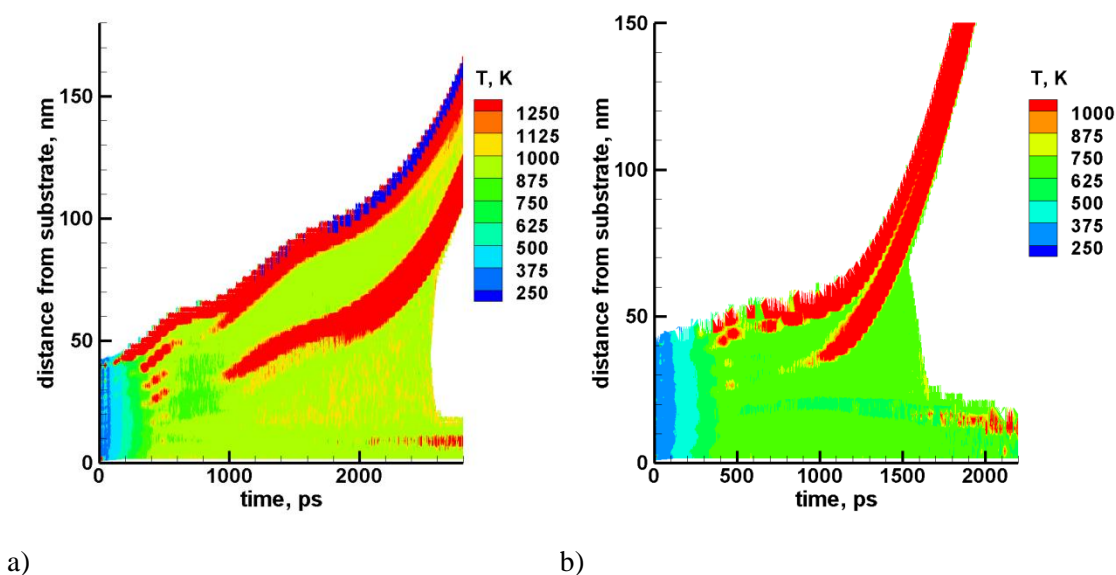
Figure 3.22   Contour plots of lysozyme temperature at closest fluence above ablation threshold for: a) lysozyme with 15 wt% water, irradiated at 7 J/cm^2; and b) lysozyme with 20 wt% water, irradiated at 5 J/cm^2.
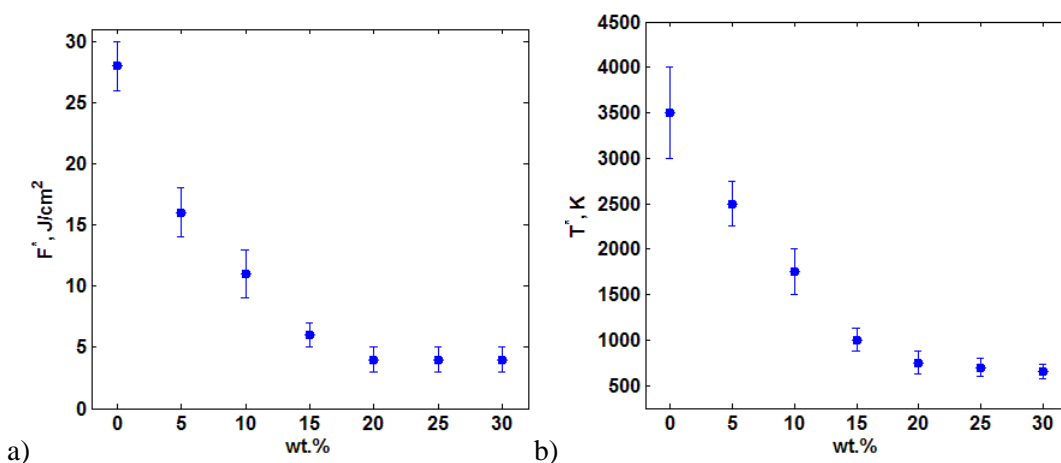
Figure 3.23   Dependence on water concentration in lysozyme, of a) ablation threshold fluence, b) ablation threshold temperature.
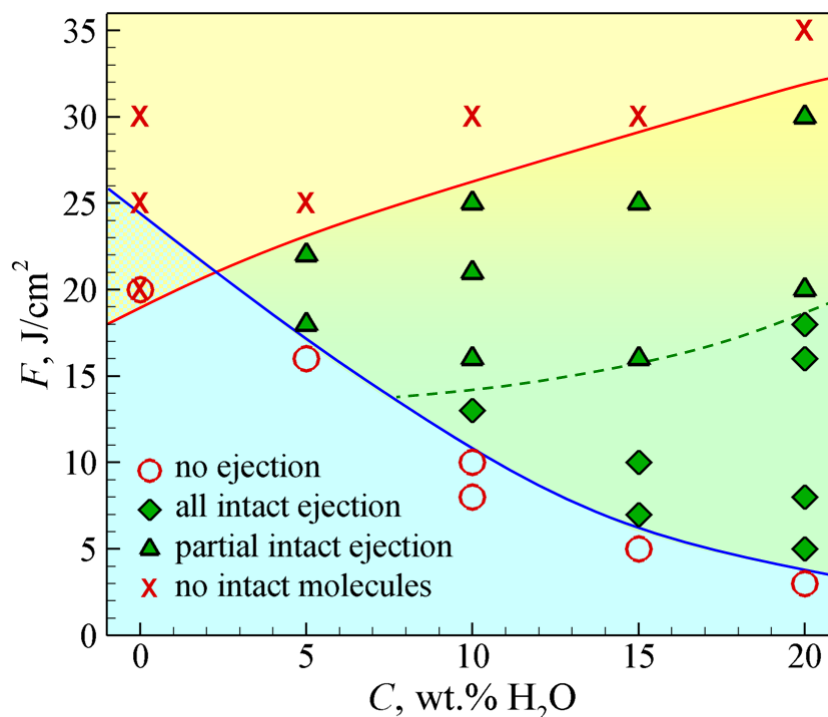
Figure 3.24 The laser fluence – water concentration map of distinct regimes of molecular ejection observed in simulations of 400 ps laser pulse irradiation of lysozyme films containing different amounts of residual water. The blue line shows the ablation threshold; the data points below this line are for simulations where molecular ejection is limited to desorption of water molecules and/or small volatile molecular fragments. The red line shows the threshold for complete decomposition of the lysozyme molecules; no intact molecules survive the laser irradiation in simulations that correspond to the data points above this line. The green rhombs and triangles are for simulations where ejection of intact lysozyme molecules is observed.

3.4   Conclusion on Computational Investigation of the Laser Ablation of Lysozyme Targets

Although simulations of lysozyme with 10 wt% water have demonstrated experimental behavior (the ejection of intact lysozyme molecules in the range of fluences from the ablation

threshold up to 3 times the threshold), the value of the ablation threshold, $\lesssim$ 13 J/cm^2, is significantly higher than the experimental observed threshold, 1 J/cm^2. Explanations related to the nature of the experimental target are provided below to explain this large difference.

The density of the laser irradiation target, a pressed pellet, in the lab is ~ 0.76 g/cm^3, although the densities of most lysozyme crystals are ~ 1.2-1.4 g/cm^3. This difference suggests that the experimental target is significantly more volatile to laser irradiation than native (or lab grown) crystals, which are still of lower density than our modeled target having 10 wt% water and 1.75 g/cm^3 density. A significantly more volatile target is expected to significantly lower the ablation threshold fluence. Taking into account that lysozyme crystals may contain more than 10 wt% water, up to ~ 30 wt% [65], this projects to lower ablation fluences. An ablation threshold of $\lesssim$ 5 J/cm^2 for modeled lysozyme with 20 wt% water is already much closer to the experimental values. Add to this a more volatile nature for the target, and the observed experimental ablation fluences are explainable.

In MAPLE, ablation leading to material ejection occurs at energy densities that are sufficiently low to avoid the destruction of polymer or biological molecules, owing to the high solvent content of the target. We have demonstrated in this work that lowering the solvent matrix content to minor quantities can still lead to the ejection of intact molecules, and we have determined the minimum amount of matrix needed for this to happen for a particular molecular target system.

4. COMPUTATIONAL INVESTIGATION OF NANOPARTICLE FORMATION AND EJECTION FROM AQUEOUS SOLUTIONS OF METALORGANIC PRECURSORS

Metallic nanoparticles, in the laser-irradiated material system, are formed from single atoms released from the effect of laser irradiation on MOP molecules. As discussed already, the metalorganic precursor investigated in this work is palladium acetate (PdAc or $Pd(OAc)_2$), a precursor to palladium (Pd) atom as a result of photochemical decomposition. In water, PdAc is insoluble [110] and, therefore, is found in the form of solid particulates. Since a significant amount of research work has been done on laser interactions with pure solid PdAc systems, literature data on this will provide a starting point for understanding and describing the thermodynamics of the processes resulting from irradiation, although the nature of the laser target is different. The synthesis of Pd metal films from solid acetate-based materials is reviewed.

4.1 Synthesis of Palladium Films and Nanostructures from Acetate-based Materials

Acetate-based materials make up a large library of metalorganic salts that can be readily dissolved in conventional solvents, such as chloroform, acetone, or water. With bond energies on the order of 2 to 3 eV, bond breakage is well within the levels of photon energies in conventional ultraviolet (UV) laser processing.

Experimental research by several groups has been carried out on the decomposition of solid palladium acetate (PdAc or $Pd(OAc)_2$) films in relevance to seeding of Pd layers for subsequent electroless plating of metals, for example Cu, Ni, Au [111,112,113,114,115]. Results of these

experiments have revealed several photochemical reaction pathways leading to the release of Pd atoms. In addition, the equilibration of energy deposited by the radiation source can result in increase of temperature above the PdAc decomposition temperature, $T_d \approx$ 473K–508K [113,116,117,118,119] – mostly determined by thermogravimetry (TG) and differential thermal analysis (DTA), causing thermal decomposition reactions. Experimental characterization techniques have been used for the identification of volatile species (mass spectrometry in vacuum [112,113]) and the detection of formed metal layers (X-ray diffraction [116,120]), following the decomposition of PdAc by different radiation and thermal sources. A number of distinct decomposition pathways leading to the dissociation of the acetate ligand (Ac) [CH_3COO or $(OAc)_2$] have been discussed in literature: (1) isothermal decomposition of unirradiated and pre-γ-irradiated PdAc yielding CH_3^+, CO_2, CH_3CO^- and CO as dissociation products of the acetate ligand [116]; (2) thermal decomposition of PdAc into Pd, CH_3COO^+, CH_3CO^+ and CO_2, with CH_3COO^+ and CO_2 as the major dissociation products of the acetate ligand [117]; and (3) UV photodecomposition of PdAc [113] to release i) CO_2^+, CH_3CO^+, CH_3C^+, H_2O^+, CH_3^+ – with Pd, H_2O and CO_2 as main decomposition products – in the case of excimer lamp irradiation, and ii) Pd, CH_3COO^+, CO_2^+, CH_3CO^+, CH_3C^+, H_2O^+, CH_3^+ – with Pd, CO_2 and CH_3COO^+ as the main decomposition products – in the case of excimer laser irradiation.

4.2 Survey of Computational Model of the Irradiated Aqueous Solution of Palladium Acetate

The computational investigation of the processes responsible for the nucleation, growth, and transport of nanoparticles in matrix-assisted laser ablation synthesis is performed with the

coarse-grained molecular dynamics (CGMD) model including a description of photolytic and thermally-activated reactions. An atomistic model for atomic-level simulations of metal atom diffusion in water is designed for parametrization of the CGMD model. A continuum-level model is designed for an establishment of the laser irradiation regimes. Although with a continuum model one cannot observe the growth of metal clusters, continuum-level simulations run thousands of times faster than molecular-level simulations, and so readily provide estimates of the parameters of laser ablation, as the thermodynamic, kinetic, and absorption parameters of laser material interactions are variables during irradiation. Continuum-level simulations serve to guide molecular modeling by predicting the range of simulating fluences, and highlighting which processes are far more significant than others. A chart is presented in Figure 4.1 to display the connections between the different types of model simulations to be run in the proposed multi-scale computational study.

The modeling of metal atom interactions using the embedded atom method (EAM) potential has been extensive, in investigations ranging from heterogeneous melting in metals to short pulsed laser melting, see Refs. [121,122,123]. A generalized EAM potential that was developed for the simulation of complex alloys [124] is employed in this work; the parameters of the EAM potential for palladium are retrieved from the cited reference.

The interaction between the metal atoms and breathing spheres representing the aqueous solution will be described by a pair potential with parameters chosen based on the results of a set of atomic-level simulations of individual metal atoms in water, performed under different temperature conditions ranging from room temperature up to temperatures approaching the temperature of phase explosion or explosive boiling. The atomistic simulations will be performed with the simple-point-charge (SPC) water model [125] that has been shown to well

reproduce structural and thermodynamic properties of water in solid, liquid and vapor states, e.g. Refs. [126,127,128,129,130]. The metal-H_2O interaction in the atomistic simulations will be described with a modified Spohr's potential suggested in Refs. [57, 131, 132]. The goal of the atomistic simulations will be to determine the mobility of metal atoms under different temperature conditions. The values of the effective diffusion coefficient, D, will be calculated from the time dependences of the mean square displacement (MSD), using the Einstein relation, $MSD = 6Dt$.

In summary, the description of the computational model that has been developed for the investigation of the formation of nanoparticles is inclusive of the following: the determination of quantities from laser irradiation of PdAc film that are useful to this model; continuum-level simulations establishing the irradiation regimes; parametrization of the interaction potential between Pd and water in both atomistic and coarse-grained breathing sphere representations; a description of the absorption model including a definition of Beer's law for a multicomponent system and a description of the absorption of Pd clusters in a solution using Mie's theory; and a description of the computational system, including the laser irradiation and absorption model, for simulations of pulsed laser irradiation of the target.
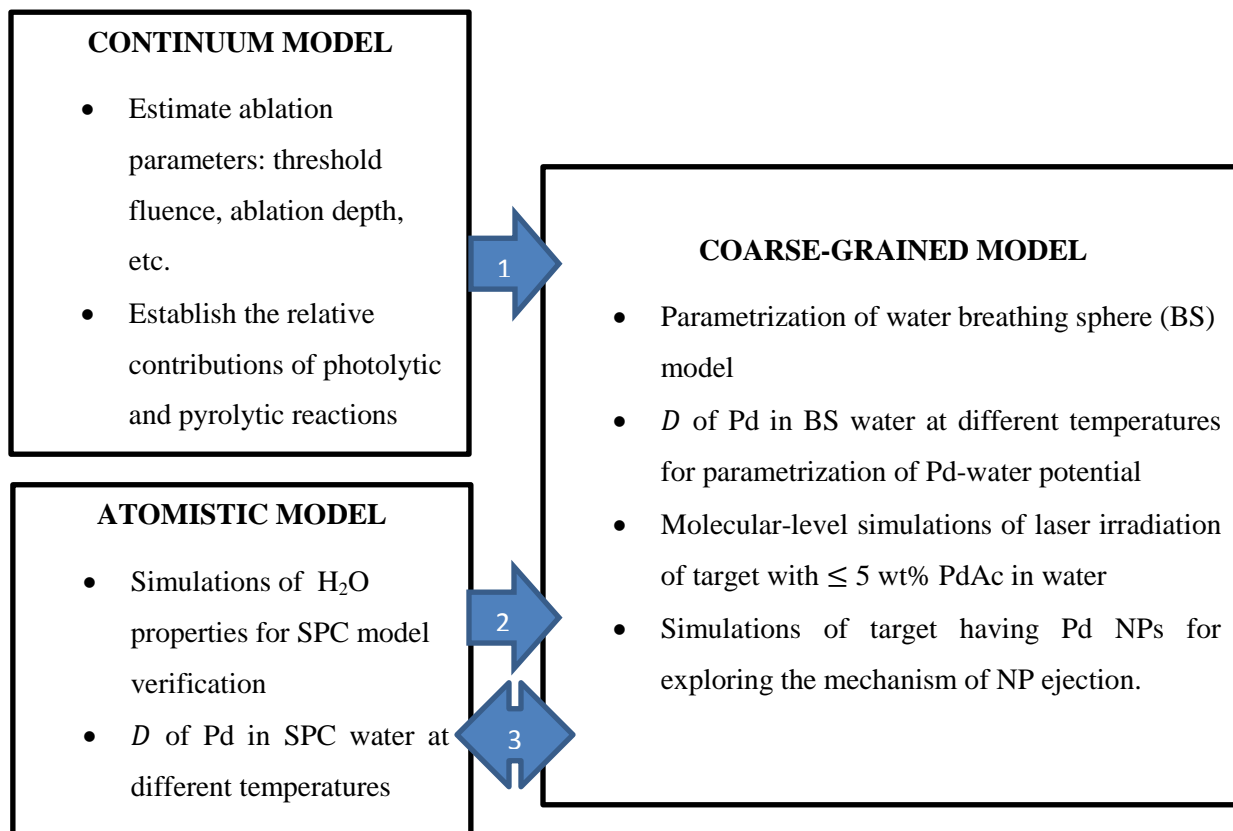
1 – Quick determination of ablation parameters in continuum model provides guidance to molecular modeling.

2 – The Pd-water potential in coarse-grained model is parametrized by matching the diffusion coefficient (*D*) of Pd atom in breathing sphere water to the value of *D* of Pd in atomistic (SPC) water, at room temperature.

3 – To assess the validity of the parameterization of the Pd-water interaction potential in the CGMD model, *D* of Pd in water is determined at different temperatures in both the SPC and BS models, and a comparison of the obtained values is made.

Figure 4.1 Schematic flow of the multi-scale computational model for simulation of laser interactions with MOP aqueous solution

4.3 Determination of Thermodynamic, Kinetic, and Absorption Parameters in the UV Irradiation of Thin Palladium Acetate Film

We summarize the decomposition of PdAc, described in sub-section 4.1, into a chemical equation:

$$Pd(CH_3COO)_2 \rightarrow Pd + H_2O + CO_2 + CH_3COO^+ + CH_3CO^- + CH_3^+ + \cdots$$
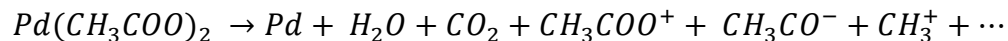
including the most probable products encountered in the experimental investigations listed in section 4.1. It should be noted that this equation is non-stoichiometric with respect to the product molecules and radicals, given that their composition is debatable, in relation to the source and the method of decomposition. Besides, none of the cited experimental investigations provides a stoichiometric equation of the decomposition reaction for similar reasons.

Experimental measurements of the transmission of irradiated PdAc film are used to determine the molar absorption coefficient of solid PdAc, and the thermodynamic and kinetic parameters of the decomposition of PdAc. The absorption cross-section of PdAc molecule is derived from the absorption coefficient of solid PdAc material. The absorption cross-sections of the molecules and atoms in a target of PdAc in aqueous solution are determined. These parameters and values are obtained for $\lambda = 248$ nm, the wavelength of laser irradiation of the aqueous solution of PdAc target.

4.3.1. Photochemical Decomposition of Palladium Acetate

The photolytic process after absorption of laser energy by a reactant can be represented as:

$$A \rightarrow \sum_j g_j B_j$$
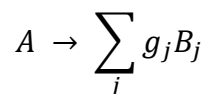
where g_j is the stoichiometric coefficient of the jth product. The rate of the photolytic process for

a given quantum yield (ϕ), is

$$\frac{\partial C}{\partial t}\Big|_{ph} = -a_{mol}\phi I^s C \tag{4.1}$$

where a_{mol} is the molar absorption coefficient of PdAc in m^2/mole, $I^s = I/E_p$ with E_p being the

energy of an einstein (a mole of photons), so that I^s is in einstein/m^{2}s, and C is the molar

concentration of reacting PdAc [133].

The absorption coefficient (α) of the system of reactant and products is then

$$\alpha = a_{mol}C + \sum_j a_j C_j \tag{4.2}$$

where C_j is the molar concentration of the jth product having molar absorption coefficient a_j. For

a given initial molar concentration of the reactant (C_o), C_j can be described by the relation:

$$C_j = (C_o - C)g_j \tag{4.3}$$

Substituting Eq. (4.3) into Eq. (4.2), and expressing the molar absorption coefficient of products

b as

$$b = \sum_j g_j a_j \tag{4.4}$$

Eq. (4.2) can be rewritten as:

$$\alpha = a_{mol}C + b(C_o - C) \tag{4.5}$$

For a sample of absorption coefficient, α, Beer's law relates the intensity of radiation at depth, z,

of the sample, $I(z)$, to the intensity at the surface, I_0: originally described in Eq. (1.6) for the

intensity of light at depth z as $I(z) = (1 - R)I_0 \exp(-\alpha z)$. The scattering coefficient of water is

determined from Ref. [108] to be 0.1 m^{-1}, and so the amount of light scattered off can be

considered negligible to the amounts absorbed in the target. The reflection coefficient R is thus neglected, and Eq. (1.6) for the target system can be described by the equation:

$$I(z) = I_0 \exp(-\alpha z) = I(0) \exp(-\alpha z) \tag{4.6}$$

Taking the natural logarithm on both sides of Eq. (4.6) and making the equality $Tr = I/I_0$, $I_0 \equiv I(0)$, where Tr is the transmittance of the sample of thickness, h, yields an equation relating the transmittance to the thickness of the sample:

$$\ln Tr = -\alpha h \tag{4.7}$$

This equation would be further referred to as the 'transmittance equation'.

Data of transmittance spectra of photodecomposing PdAc thin film to form Pd thin film in Refs. [113, 114] can be used to determine absorption cross-sections of solid PdAc molecule and metal Pd atom. This is done by determining the transmittance for a film of known thickness, and then using the transmittance equation to determine the absorption coefficient, from which the absorption cross-section can be directly related, for a known density of the film, ρ. The absorption cross-section, σ, is related to the absorption coefficient through density ρ, molar mass, A_m, and Avogadro number, N_A:

$$\sigma = \frac{\alpha A_m}{\rho N_A} \tag{4.8}$$

Uncertainties in the obtained absorption cross-sections are also determined. Since they are directly proportional, the relative uncertainties in absorption coefficient and absorption cross-section are equal.

The laser irradiation of thin film solid PdAc in vacuum releases Pd atoms and other absorbing species – the Pd atoms most likely clustering in a nucleation process to form Pd thin film. The kinetics of diffusion of the product species here is expected to be different from that in a water

medium, but given that the same types of absorbing species are involved, the change over time of the transmission of the irradiated film system is useful to understanding cluster absorption.

For a PdAc film irradiated with UV light of a given intensity, the transmittance of the film over time, Tr, is described by the expression given in Refs. [114, 133]:

$$\ln\left[\frac{1-Tr}{Tr}\right] = const - \phi(a_{mol} - b)I_0^S t \qquad (4.9)$$

where a and b are the molar absorption coefficients, in m^2/mol, of PdAc and the products of decomposition respectively, $I_0^S = I_0/E_p$, with E_p being the energy of an Einstein (a mole of photons), ϕ is the quantum yield in Einstein/mole, and t is the exposure time.

The dependence in Eq. (4.9) is linear in time; a slope of the dependence is proportional to $a_{mol} - b$, and the value of the linear relation at $t = 0$ determines the transmittance of solid PdAc, from which a can be determined. In addition, for a film of thickness, h, the absorption coefficient, α, can be determined from its transmittance Tr as: $\alpha = -(\ln Tr)/h$.

In Ref. [114] a plot of the relation described by Eq. (4.9) is provided for a film of thickness $h' = 45$ nm irradiated at a wavelength of 172 nm, see left panel of inserted Figure 4.2. In the same Ref. is a plot of the dependence of the transmittance over the wavelengths 150nm-400nm before and after 360 s of UV (172 nm) exposure for a film of unknown thickness h, see right panel of Figure 4.2.

From the dependence on transmission, a relation between the transmittances at $\lambda_1 = 172$ nm, $Tr(\lambda_1)$, and at $\lambda_2 = 248$ nm, $Tr(\lambda_2)$, can be determined by making use of the transmittance equation:

$$\alpha(\lambda_2) = \alpha(\lambda_1)\frac{\ln Tr(\lambda_2)}{\ln Tr(\lambda_1)} \qquad (4.10)$$

Inserting $\alpha(\lambda_2)$, from Eq. (4.10), into the transmittance equation in λ_2 for the film of thickness $h' = 45$ nm, and applying the transmittance equation in λ_1 to substitute $\alpha(\lambda_1)$, whilst observing the invariance of $\alpha(\lambda)$ for a given wavelength, one obtains

$$\ln Tr'(\lambda_2) \;=\; \ln Tr'(\lambda_1)\frac{\ln Tr(\lambda_2)}{\ln Tr(\lambda_1)} \tag{4.11}$$

relating the value of transmission at 248 nm for the film of thickness 45 nm, $Tr'(\lambda_2)$, to values of transmission of the film of unknown thickness at wavelengths 172 nm and 248 nm, $Tr(\lambda_1)$ and $Tr(\lambda_2)$, respectively. The values of transmission for the film of unknown thickness are read from the transmittance spectrum at time t = 0 s in the diagram in the right panel of Figure 4.2, and their values are $Tr(\lambda_1) = 4 \pm 1$ %; $Tr(\lambda_2) = 42 \pm 2$ %. The value of $Tr'(\lambda_1)$, determined from the linear dependence in the diagram in the left panel of Figure 4.2 and described by Eq. 4.9, is $Tr'(\lambda_1) = 6.3$ % $\pm$ 0.2 %. The determined value of the transmission at 248 nm for the film of thickness 45 nm is thus $Tr'(\lambda_2) = 47.5 \pm 8.2$ %, with a relative uncertainty of 17.2 % in the value of $\ln Tr'(\lambda_2)$. [See appendix C1 for determination of uncertainty in $Tr'(\lambda_2)$]. The absorption coefficient of PdAc film at 248 nm is thus determined to be $\alpha_{PdAc} = (0.017\pm0.003)$/nm, inserting the value of $Tr'(\lambda_2)$ in Eq. (4.7) given that $h' = 45$ nm.

The absorption cross-section of PdAc molecule in solid PdAc, using molar mass A_m of 224.5 g [119] and density ρ of 2.19 g/cm^3 [98] for solid PdAc in Eq. (4.8), is derived as $\sigma_{PdAc} = 0.29 \pm 0.05$ Å^2. The molar absorption coefficient is determined from the absorption coefficient: $\alpha_{PdAc} = aC_{PdAc}$ where C_{PdAc} is the molar concentration of PdAc, to be $a_{mol} = 1743$ m^2/mol.

A Pd film is formed from the photodecomposition of the PdAc film, and as explained in Ref. [114] the transmittance spectrum in Figure 4.2 [right] is that of the thin Pd film. The thickness of the film is determined during and after exposure to radiation, see inserted Figure 4.3. The

thickness of the Pd film is seen to be unchanged after 180 s and it is $h'' = 5 \pm 1$ nm. Its transmittance is the same as that of original PdAc film at 248 nm, which has been determined already, above, to be $Tr(\lambda_2) = 42 \pm 2$ %. The absorption coefficient of the Pd film, α_{Pd}, is determined from the transmittance equation to be $\alpha_{Pd} = 0.164 \pm 0.034$ nm^{-1}. [See appendix C1 for determination of uncertainty in α_{Pd}]. The absorption cross-section of Pd atom in the Pd metal film, σ_{Pd}, is determined by Eq. (4.8), using the atomic mass of 106.4 g [119] and density of 12.0 g/cm^3 [118] for Pd, to equal 0.24 ± 0.05 Å^2.

From the investigations of the photochemical decomposition of solid PdAc, the difference $a_{mol} - b$ is estimated from the dependence described by Eq. (4.9) for a wavelength of 222 nm [113] to be 5 m^2/mol. It can be seen that $a_{mol} - b \ll a_{mol}$, so that one can approximate $a_{mol} \cong b$, to ~ 0.4 %. It can be noticed that the closeness of the values of a_{mol} and b is due to the closeness of the absorption cross-section of Pd atom (in the formed Pd metal film) and that of precursor PdAc molecule. In a MOP aqueous solution, however, there is no formation of metal film, and so an adequate value for the molar absorption of products of the decomposition of MOP, b^{sol}, is still to be determined. It will be determined later, in the study of the absorption model for the irradiated target [section 4.7], that clusters of metal atoms are the sole absorbers among the products of decomposition, so that the total molar absorption coefficient of products is then determined as

$$b^{sol} = \sigma_{Pd} N_A \tag{4.12}$$

where σ_{Pd} is the absorption cross-section of Pd atom in cluster, and N_A is the Avogadro constant. In the latter study, it will be determined that $\sigma_{Pd} = 0.1$ Å^2, so that $b^{sol} = 602$ m^2/mol.

The parameters a_{mol} and b, which are molar absorptions of reacting PdAc and its decomposing products, respectively, in Eq. (4.5) – the equation that describes the absorption coefficient of

irradiated PdAc of varying concentration, have been determined. Related to the parameter a is the absorption cross-section of PdAc (σ_{PdAc}), which has been determined. It has been noted that the molar absorption of the products in an aqueous medium will differ from that determined in the experimental conditions just described. In this regard, the molar absorption coefficient of the products in an aqueous medium has been denoted as b^{sol}, and its value has been cited here, pending descriptions of the determination of its value in a latter section on the absorption model of the target.
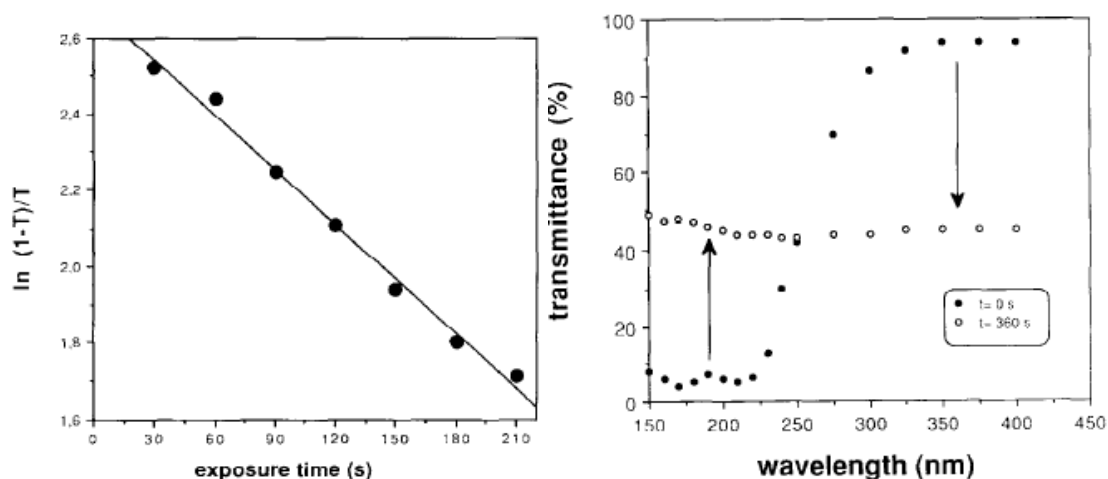
Figure 4.2   Left panel – Dependence of $\ln\left[\frac{1-Tr'}{Tr'}\right]$ versus exposure time t for photoinduced decomposition of a 45 nm thick PdAc film at $\lambda = 172$ nm; right panel – Transmittance of a PdAc film of unknown thickness before and after 360 s of UV (172 nm) exposure. Both displays are copied from Ref. [114].
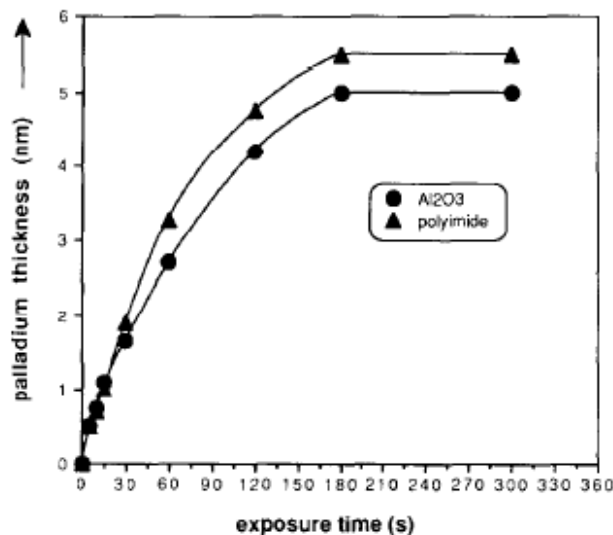
Figure 4.3 Graph showing thickness of palladium film, formed from photodecomposition of palladium acetate film, as a function of UV (172 nm) exposure time; copied from Ref. [114].

4.3.2 Thermal Decomposition of Palladium Acetate

Here, important kinetic quantities of the decomposition reaction of PdAc are determined, or obtained from literature dedicated to the study of the decomposition. The values of activation energy and enthalpy are obtained from literature. A kinetic analysis is done to determine the reaction order of the thermal decomposition, and also the rate constant. The determined quantities, in addition to the activation energy, are relevant to describing the rate of thermal decomposition in our model. The enthalpy determines the heat gain of the system of reactants and products, based on the decomposition of PdAc, be it thermal or photolytic.

The photodecomposition of PdAc in vacuum is endothermic, and the enthalpy of the reaction, ΔH, is equal to 440 kJ/mol [113]. If PdAc is heated up to the decomposition temperature, it thermally decomposes. The rate of change of the fractional residual weight of the reactant, W, can be described by the following equation [134, 135, 136]:

$$\frac{\partial W}{\partial t}\Big|_{th} = -k(T)W^n \tag{4.13}$$

n is the reaction order, and the reaction rate $k(T)$ is defined by the Arrhenius equation,

$$k(T) = k_0 \exp\left(-\frac{E_a}{RT}\right)$$

in which k_0 is the reaction rate constant, E_a is the activation energy (per mole) of the thermal process, and R is the universal gas constant. Data of fractional residual weight of decomposing PdAc as a function of rising temperature, for a given heating rate, $\vartheta = 64$ °C/min, is provided in Table 4.1, derived from Ref. [117].

The unknown parameters (E_a, n, k_0) of the thermal decomposition reaction rate described by Eq. (4.13) are determined by a differential thermal analysis method, Ozawa kinetic analysis (OKA), which is described in Ref. [134]. The reaction order of the decomposition of calcium oxalate, a metalorganic compound, has been determined in the cited reference, and we shall by the same means determine that of palladium acetate here. It has been applied in Ref. [117] to determine E_a for the thermal decomposition of PdAc in N_2, and a value of $E_a = 115$ kJ/mol was found.

Following descriptions of the OKA in Ref. [134], the fractional residual weight of a reacting material for a given heating rate ϑ, for low initial temperatures, can be well described by the following approximation:

$$-\int_1^W \frac{dW}{W^n} \cong \frac{k_0}{\vartheta} \int_0^T \exp\left(-\frac{E_a}{RT}\right) dT \tag{4.14}$$

Equation (4.14) can be obtained after integrating the differential form of Eq. (4.13), $-dW/W^n = k_0 \exp(-E_a/RT)$, and making the substitution $dt = dT/\vartheta$. As obtained in Ref. [134], for $E_a/RT \gg 1$,

$$\int_0^T \exp\left(-\frac{E_a}{RT}\right) dT = \frac{E_a}{R} p\left(\frac{E_a}{RT}\right) \tag{4.15}$$

where

$$\log p\left(\frac{E_a}{RT}\right) \cong -2.315 - 0.4567\,\frac{E_a}{RT} \tag{4.16}$$

For different reaction orders, different dependences of W against $log\frac{k_0 E_a}{\vartheta R} p\left(\frac{E_a}{RT}\right)$ can be obtained

as shown in Fig. 4.4b, which is taken from Ref. [134].

The order of the thermal decomposition reaction is determined by plotting W against

$log\frac{E_a}{\vartheta R} p\left(\frac{E_a}{RT}\right)$ with values obtained from Ref. [117], see Figure 4.4a, and comparing the obtained

curve with the curves in Figure 4.4b. [Note that the abscissa values in our diagram are short of

those in Figure 4.4b by the value $\log k_0$, which is still a constant to be determined here]. A plot

of W against $log\frac{E_a}{R} p\left(\frac{E_a}{RT}\right)$ yields the curve in Fig. 4.4a. Comparing to the curves of Fig. 4.4b, the

thermal decomposition can be approximated to be of order $n = 1$.

Implementing Eqs. (4.15) and (4.16) in the R.H.S of Eq. (4.14), and applying the natural

logarithm on Eq. (4.14) for $n = 1$ after integrating, we obtain Eq. (4.17). [N.B. The natural

logarithm form of Eq. (4.16) has been obtained by multiplying the expression by the natural log

of 10, i.e. if $log(x) = u \Rightarrow x = 10^u$, then $Ln(x) = Ln(10^u) = u \cdot Ln(10)$ or $Ln(x) = Ln(10) \cdot log(x)$.

$$Ln(-Ln(W)) = Ln(k_0) - Ln(\vartheta) + Ln(\frac{E_a}{R}) - 5.33 - 1.0516\,\frac{E_a}{RT} \tag{4.17}$$

Implementing the values $W = 0.8$ and $T = 266.1$ °C = 539.1 K from Table 4.1 in Eq. (4.17), the

value of $Ln(k_0) = 25.45$, so that $k_0 = 1.1 \times 10^{11}$ min^{-1} is obtained. The determined value of

$Ln(k_0)$ is of the same order of magnitude as that for the decomposition of calcium oxalate

($\log k_0 = 28.6$), which is of unity reaction order ($n = 1$), in Ref. [134]. It can also be noticed

that the slope of a linear dependence of $log\vartheta$ against $1/T$, see Eq. (4.17), is directly proportional

to E_a; this is the method of determination of the value of E_a in Ref. [117] for the residual

fractional weights in Table 4.1: for the different W values, the slope is the same for the different linear dependences.

In summary, we have retrieved values of the enthalpy ΔH (440 kJ/mol) and the activation energy E_a (115 kJ/mol) of the decomposition reaction of PdAc from cited references that study the decomposition. We have used data of change in residual weight of PdAc with a rise in temperature to determine the reaction order n to equal unity, and thereafter the thermal reaction constant k_0 to equal 1289 min^{-1}. The parameters in the equations describing the decomposition of PdAc, in addition to physical quantities of PdAc, are summarized in Table 4.2.

Table 4.1. Data of fractional weight of PdAc at 64 ^{O}C/min [117].

W	0.8	0.6	0.4	0.2
T, ^{O}C	266.1	272.8	278.0	282.3

Table 4.2. Parameters in the equations describing the photolytic and thermal decomposition of PdAc.

ρ_{PdAc}, g/cm^3	A_{PdAc}, g	ΔH, kJ/mol	a_{mol}, m^2/mol	b, m^2/mol	b^{sol}, m^2/mol	k_0, min^{-1}	E_a, kJ/mol
2.19 [118]	224.5 [119]	440 [113]	1742.7	1738	602	1229	115
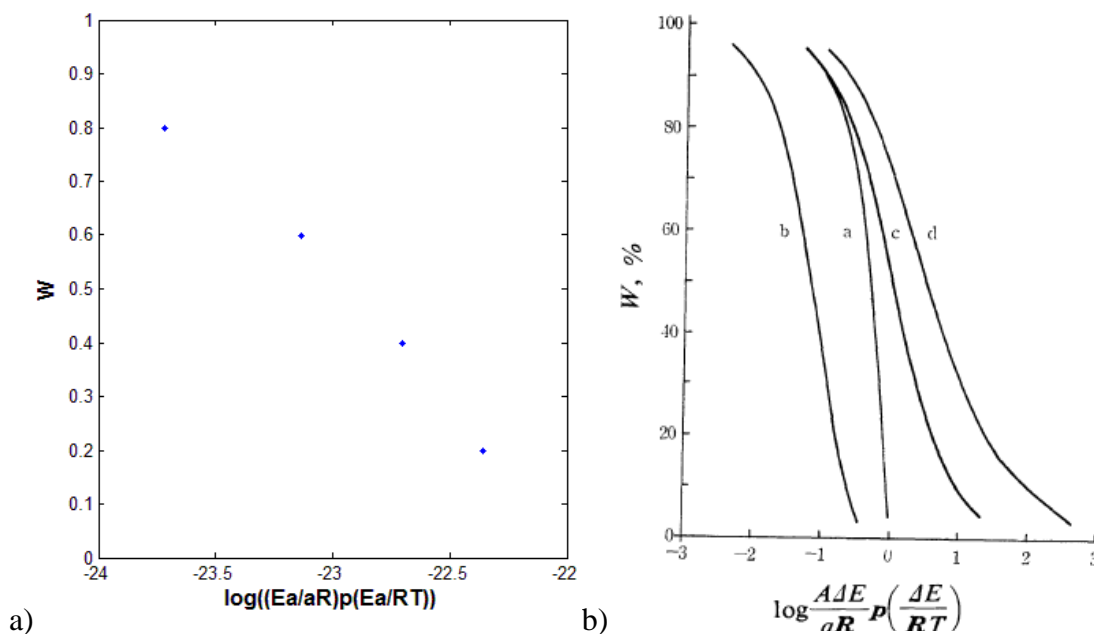
Figure 4.4   a) Thermogravimetric curve for PdAc in N_2 at 64 $^\circ$C/min heating rate. b) Diagram from Ref. [134] displaying theoretical thermogravimetric curves of different orders: a, 0th order; b, 1st order; c, 2nd order; d, 3rd order – N.B. {a, ΔE, A} in the diagrams correspond to {ϑ, Ea, k_0}, respectively.

4.4. Continuum Model

A continuum model of the pulsed laser irradiating system of MOP in aqueous solution is designed for an estimation of the fluences required for ablation, typical ablation depth, concentration profile and temperature profile of the irradiated target over time. The threshold fluence for laser ablation is estimated. Simulations of the continuum model, usefully, show that the rate of thermal decomposition of PdAc is orders of magnitude smaller than the rate of photolytic decomposition, and can thus be neglected.

The continuum-level model describes laser energy deposition in the target material, heat diffusion in the target, and the change in concentration of PdAc. The heat diffusion equation is combined with the equations that describe the rates of photolytic and thermal decomposition of PdAc, for determining the temperature of the irradiated material and the precursor concentration. The enthalpy of the decomposition reaction, as well as the variation of the absorption coefficient due to the changes in the molar concentration of the absorbing material, are accounted for in the model.

4.4.1 Model Description

The model system is made of PdAc at a low percentage weight (wt%) in water, ~1-5 wt%. For a given weight concentration corresponding to a fractional weight f,

$$wt\% = \frac{m_{PdAc}}{m_{PdAc} + m_w} \cdot 100\% \qquad (4.18a)$$

where m_{PdAc} and m_w are masses of PdAc and water, respectively, the mass of one of the medium constituents can be retrieved:

$$m_w = \frac{1-f}{f} m_{PdAc} \qquad (4.18b)$$

The molar concentration of dispersed PdAc in the total volume of system, V_{TOT}, is defined as

$$C_{disp} = \frac{m_{PdAc}}{A_{PdAc} V_{TOT}} \qquad (4.19a)$$

where A_{PdAc} is the atomic mass of PdAc. Expressing V_{TOT} as the sum of constituent volumes, $V_{TOT} = m_w/\rho_w + m_{PdAc}/\rho_{PdAc}$ where ρ_w and ρ_{PdAc} are the densities of pure water and solid PdAc, respectively, Eq. (4.19a) becomes Eq. (4.19b).

$$C_{disp} = \frac{m_{PdAc}}{m_w \rho_{PdAc} + m_{PdAc} \rho_w} \cdot \frac{\rho_w \rho_{PdAc}}{A_{PdAc}} \qquad (4.19b)$$

Substituting the right hand side of Eq. (4.18b) for m_w in Eq. (4.19b), C_{disp} is obtained in terms of wt% and material constants only, in Eq. (4.20):

$$C_{disp} = C_{PdAc} \cdot \frac{\rho_w f}{[\rho_w f + \rho_{PdAc}(1-f)]} \tag{4.20}$$

where $C_{PdAc} = \rho_{PdAc}/A_{PdAc}$ is the molar concentration of solid PdAc. The molar concentration of dispersed PdAc can also be expressed through the density of its dispersed phase, ρ_{disp}: $C_{disp} = \rho_{disp}/A_{PdAc}$; then with the use of Eq. (4.20), the density of the dispersed phase is expressed in Eq. (4.21).

$$\rho_{disp} = \rho_{PdAc} \cdot \frac{\rho_w f}{[\rho_w f + \rho_{PdAc}(1-f)]} \tag{4.21}$$

The area of the irradiated surface is much larger than the depth, that variations in temperature and concentration are going to be only across the depth, allowing the system to be treated as one-dimensional (1D).

The temperature profile of the system at time, t, $T(x,t)$ is determined by the 1D thermal diffusivity equation, Eq. (4.22), with inclusion of a heat source term, $\left.\frac{\partial T}{\partial t}\right|_S$ which is the partial change in temperature due to heat gained (or lost) by the system:

$$\frac{\partial T}{\partial t} = \frac{\partial^2 T}{\partial x^2} + \left.\frac{\partial T}{\partial t}\right|_S \tag{4.22}$$

$_T$ – the thermal diffusivity of water is given by $_T = \frac{K_T}{\rho_w c_P}$, where K_T is the thermal conductivity of water, c_P is heat capacity of water, and ρ_w is the density of water.

The heat source equation defines $\left.\frac{\partial T}{\partial t}\right|_S$ as:

$$\left.\frac{\partial T}{\partial t}\right|_S = -\frac{1}{c_P \rho_w} \times \left[\frac{\partial I}{\partial x} - \Delta H \frac{dC}{dt}\right] \tag{4.23}$$

ΔH is the molar enthalpy of PdAc decomposition, $C = C(x,t)$ is the molar concentration of PdAc, and $I = I(x,t)$ is the intensity of light. The heat source term, as described in Eq. (4.23), is made of the component due to the absorption of laser light, derived from Ref. [137], and the local contribution from the heat released (or gained) in the photochemical decomposition of the precursor following photoabsorption. How the component due to the local heat release is determined is explained in the next paragraph.

The rate of temperature change due to decomposition can be derived as:

$$\frac{dT}{dt} = \frac{1}{mc_P} \frac{dH}{dt} = \frac{1}{mc_P} \left(\frac{\partial H}{\partial m} \right) \frac{dm}{dt} \qquad (4.24a)$$

where m is the mass, and dH is the infinitesimal heat change due to decomposition over time dt. Expressing the mass m in terms of the number of moles (N^m) and the atomic (molar) mass (A_m), $m = N^m A_m$, Eq. (4.24a) becomes Eq. (4.24b). Further expressing N^m as a product of molar concentration and the volume, $N^m = CV$, and substituting $m = \rho V$, Eq. (4.24c) is obtained for a fixed volume.

$$\frac{dT}{dt} = \frac{1}{mc_P} \frac{dH}{dt} = \frac{1}{mc_P} \left(\frac{\partial H}{\partial N^m} \right) \frac{dN^m}{dt} \qquad (4.24b)$$

$$\frac{dT}{dt} = \frac{1}{c_P \rho} \left(\frac{\partial H}{\partial N^m} \right) \frac{dC}{dt} \qquad (4.24c)$$

The quantity $\partial H / \partial N^m$ is the heat change per decomposition of a mole, and is thus the molar enthalpy of decomposition by definition: $\partial H / \partial N^m = \Delta H$. Substituting the obtained equality and applying the subscript to the variables for water in Eq. (4.24c), the component due to local heat release in Eq. (4.23) is obtained.

The rate of change of PdAc molar concentration, dC/dt in Eq. (4.23), is a summed rate due to both photolytic decomposition and thermal decomposition of PdAc:

$$\frac{dC}{dt} = \frac{\partial C}{\partial t}\big|_{ph} + \frac{\partial C}{\partial t}\big|_{th} \qquad (4.25)$$

The rates of the photolytic and thermal processes have been described previously in Eqs. (4.1) and (4.13), respectively, in sub-section 4.3. Additionally, the thermal reaction rate in Eq. (4.13) can be written in terms of concentration for the priorly determined value of the reaction order ($n = 1$):

$$\frac{\partial C}{\partial t}\big|_{th} = -k_0 C \exp\left(-\frac{E_a}{RT}\right) \qquad (4.26)$$

The parameters describing the physical properties of water in the above described equations are listed in Table 4.3

Absorption of water at the irradiation wavelength of 248 nm, 0.6 m^{-1} in Ref. [108], can be neglected in comparison to that of the dispersed PdAc. The absorbing medium is, thus, made of absorbing reactants and products of the already described photodecomposing PdAc film under laser irradiation, with a few modifications: the decomposed products of the organic ligand in PdAc are not expected to be as highly volatile in water as in vacuum; because the precursor concentration is low, released Pd atoms from decomposed PdAc would diffuse to form clusters that are stable over lengthy irradiation times (~ 1s or more). These modifications predict the absorption coefficient in this system to be different from that of decomposing solid PdAc film in vacuum, as metal clusters absorb differently from metal thin films, and ligand products – now present in the irradiated liquid medium as opposed to being volatile in vacuum – may significantly absorb. The absorption of metal clusters and ligand products would be determined in the absorption model for this system in a latter sub-section. The value of the molar absorption coefficient b_{sol} resulting from this determination has been cited in the previous sub-section, and is implemented in the continuum model. In the present continuum model, the absorption

coefficient is, thus, defined as for a solid thin film, with the concentration C being that of a dispersed phase ($C \equiv C_{disp}$) in Eq. (4.5), and the parameter for the molar absorption coefficient of products, b, being substituted for b_{sol}:

$$\alpha = aC_{disp} + b_{sol}(C_o - C_{disp}) \tag{4.27}$$

The model describes the liquid-solid phase transition of water – after attaining the melting point from below, the temperature is allowed to increase beyond it only after gaining energy needed for melting. Likewise after attaining melting point from above, the temperature is allowed to decrease below it only after releasing energy needed for fusion.

Generally, without accounting for phase transformations, after a gain in energy (ΔE), temperature becomes $T = T_{old} + \Delta E/C_p$ with T_{old} being the temperature before the energy gain. However, if the material is undergoing a phase transition – i.e. $0 < x_{mlt} < 1$ with x_{mlt} being the fraction of the material in the molten state, there are modifications to the fraction of molten material and temperature, as described in the different cases below. The corrected temperature becomes T_{new}.

i. $\Delta E < 0$ and $T < T_m$: there are two possible conditions, depending on the magnitude of ΔE, as $0 < x_{mlt} \leq 1$.

   a) $|\Delta E| \leq x_{mlt}H_m + c_P(T_{old} - T_m)$:

   $$\Delta E = \Delta x_{mlt}H_m + c_P(T_m - T_{old})$$

   $$\Rightarrow \Delta x_{mlt} = [\Delta E - c_P(T_m - T_{old})]/H_m$$

   $$x_{mlt} = x_{mlt} + \Delta x_{mlt} \; ; T_{new} = T_m$$

   b) $|\Delta E| > x_{mlt}H_m + c_P(T_{old} - T_m)$:

   $$\Delta E = c_P(T_m - T_{old}) - x_{mlt}H_m + c_P(T_{new} - T_m)$$

   $$T_{new} = T_{old} + (\Delta E + x_{mlt}H_m)/c_P; x_{mlt} = 0$$

ii. $\Delta E > 0$ and $T > T_m$: there are two possible conditions, depending on the magnitude of ΔE, as $0 \leq x_{mlt} < 1$.

    a) $\Delta E \leq (1 - x_{mlt})H_m + c_P(T_m - T_{old})$:

$$\Delta E = \Delta x_{mlt}H_m + c_P(T_m - T_{old})$$

$$\Rightarrow \Delta x_{mlt} = [\Delta E - c_P(T_m - T_{old})]/H_m$$

$$x_{mlt} = x_{mlt} + \Delta x_{mlt}; T_{new} = T_m$$

    b) $\Delta E > (1 - x_{mlt})H_m + c_P(T_m - T_{old})$:

$$\Delta E = c_P(T_m - T_{old}) + (1 - x_{mlt})H_m + c_P(T_{new} - T_m)$$

$$T_{new} = T_{old} + [\Delta E - (1 - x_{mlt})H_m]/c_P; x_{mlt} = 1$$

The intensity of the laser pulse is constant over a pulse width of 25 ns; the wavelength of irradiation is $\lambda = 248$ nm. Fluences are modeled in the ~ 0.1-10 J/cm^2 range.

The lowest possible temperature of the irradiated target is 77 K, the temperature of the liquid nitrogen (LN$_2$) thermostat to which the bottom of the target is connected. Because 77 K is the lowest possible target temperature, investigations for $T = 77$ K are considered.

The modeled thickness of the system is $L = 5$ μm. The initial penetration depth is $L_p = 1/a_{mol}C_{disp}$. For 1 wt% PdAc, as an example, the initial penetration depth is 12.8 μm, and the initial molar concentration is 44.7 mol/m^3. Preliminary simulations are done for this fluence to study the different components of the heat source.

Equation (4.22) is solved numerically by a finite difference method, described by Eq. (4.28).

$$\frac{\Delta T}{\Delta t} = {}_T\frac{T^t_{i+1} - 2T^t_i + T^t_{i-1}}{\Delta x^2} + \frac{\Delta T}{\Delta t}\bigg|_S \tag{4.28}$$

There are 2000 discretization nodes, so that the size of a node is 2.5 nm; the timestep is 8.5 ps.

Table 4.3. Physical properties of water, used in continuum model [82].

c_P, J/kgK	K_T, Wm^{-1}K^{-1}	ρ_w, g/cm^3	H_m, J/g	T_m, K
4.18 x 10^3	0.6	0.997	334	273

It is worth noting the thermodynamic assumptions in this continuum model:

1) The volume of the target is fixed. This means expansion of the heated matrix is not accounted for, and all the laser-deposited energy is related to a temperature increase. This means the temperature increase is overestimated in the model. The density of water changes from 1.0 g/cm^3 at room temperature to about 0.96 g/cm^3 at $T \sim$ 473 K, the boiling point. At temperatures beyond the boiling point, the water matrix is in a superheated metastable state that leads to explosive boiling as it approaches the critical temperature. Explosive boiling or active evaporation is not observed in the model but it is assumed to be so in the target as the surface temperature attains the temperature of explosive boiling.

2) The thermodynamic properties, listed in Table 4.3, are held constant, although they are actual functions of temperature. The actual values of the thermodynamic properties differ mostly within 100 % from the assumed values.

Examining the assumptions, it is easy to tell that the determined quantities as a result of simulation of the model will not drastically differ from actual quantities – they are expected to be closely of the same order of magnitude. The model is expected to reliably describe the variations in temperature and material composition across the depth of the target at a qualitative level.

4.4.2. Continuum-level Simulation Results and Discussions

For a 1 wt% PdAc target at 77 K, simulations are run to determine the threshold fluence F^*. In Figure 4.5 is a diagram of the intensity of light at the surface. The different constituents of the heat source are observed for a discussion of their relative contributions. Again, the different constituents of the heat source are: i) the photothermal source due to the photoabsorption of PdAc and products, ii) the photochemical source due to the photolytic decomposition of PdAc, and iii) the thermal source due to the thermal decomposition of PdAc. In Figure 4.6 is a display of the different heat sources at the threshold fluence, $F^* = 18$ J/cm^2.

Theoretically speaking, the ablation threshold fluence is determined to be that at which the temperature of the surface node attains the temperature of phase explosion of water, $T_b = 550$ K; this relates to a surface region which is about 2-5 nm thick. To be more substantive, however, we expect a surface region of thickness about 100 nm to attain the temperature of phase explosion, prior to considering that the surface has been ablated. The surface temperature for the simulated target at its threshold fluence is displayed in Figure 4.7.

Figure 4.6 shows that the heat source due to the thermal decomposition is several orders of magnitude lower than the other constituents: see in Figure 4.6c that the thermal decomposition source is plotted in units of 10^{-60} J/m^2 while the other sources are represented in J/m^2.

It can also be noticed in Figure 4.6 that it takes less than 1 ns for the photochemical and the thermal decomposition source to become zero. This change is also reflected in the temporal behavior of the photothermal source and the total heat source. We zoom into Figure 4.6 in order to understand the changes taking place within the first (1) ns of the pulse irradiation. The different components of the heat source are plotted for this length of time, see Figure 4.8. The photothermal source is seen to decrease to a constant value, from 4.7 J/m^2 to 1 J/m^2. This means

it decreases ~ 4.7 times within the probed time. Notice that the ratio of the absorption cross-section of PdAc to that of the determined average value of Pd atom in clusters, given in sub-section 4.3.1 and 4.3.2, is $\sigma_{PdAc}/\sigma_{Pd}$= (0.24 $\dot{A}^2$)/(0.5 $\dot{A}^2$) = 4.8. This calculated ratio equals to how much the photothermal source decreases to a constant value, if one were to account for the change in the photothermal source during the first time step. This clearly informs that PdAc in the simulated target has completely decomposed to Pd within the time it takes the photothermal source to decrease to a constant value. When the target is then made only of Pd, the other decomposing products (which are non-absorbing) and water matrix, its absorption coefficient and other material properties are a constant over time, and so the photothermal source which is dependent on the latter assumes a constant value. The time for the complete decomposition of the metalorganic precursor in the simulated target can be seen to be about half a nanosecond. For the same reason, it can be noticed that the photochemical source and the thermal decomposition source become zero at the end of this time, see Figure 4.8b and Figure 4.8c, as the complete absence of PdAc means there are neither photolytic processes nor thermal decomposition processes. Then the heat source assumes a constant value at the end of this time, see Figure 4.8d, which is that of the photothermal source. In Figure 4.9 are contour plots showing the temperature and concentration profile.

Simulations are finally done for a relatively high precursor concentration, 5 wt% PdAc, with an initial target temperature of 77 K. The threshold fluence is determined to be 1.8 J/cm^2 for the target at 77 K initial temperature; see Figures 4.10 for contour plots of temperature and concentration.

The ablation threshold fluences that have been determined for the different initial conditions of temperature and precursor concentration that have been considered are summarized in Table 4.4.

In experiments performed with 1 wt% PdAc in water target irradiated at a fluence of 0.25 J/cm^2, ablation already occurs [47]; the irradiation fluence is an order of magnitude lower than the threshold values determined in our model for 1 wt% PdAc target. It would be relatively easier to make conclusions on the difference in magnitude after studying the ablation process in coarse-grained modeling. Accounting for the different reasons, a better review of the difference in simulated and experimental ablation fluences will then be made. Nonetheless, simulations in the continuum model have revealed useful relations that are worthy of consideration in coarse-grained modeling. It has been established that the yield of thermal decomposition reactions is negligible to the heat source. This component of the heat source need not be included in the coarse-grained model.

It has, usefully, been determined that complete decomposition of PdAc down to a depth of 5 μm in the target occurs during the irradiation of the laser pulse, with the required time for the complete decomposition being longer for higher precursor concentrations. This is an observation that cannot be predicted in the coarse-grained model within our simulation capabilities. We can relate this observation to some experimental observations, based on communications with our experimental collaborators. In experiment, the typical area of the target rastered over is 5 cm^2, while the spot size is typically 1 cm^2. A slow forming dimple about 1 mm deep is observed after irradiation with ~ 5000 – 10000 pulses. For a region of the target having the surface area of the beam spot size, this means about 1 μm of irradiated material is removed per pulse, on average. Although laser energy is deposited in every pulse, material removal only occurs in a later stage of the irradiation. Continuum-level simulations show that a few microns of target material is devoided of PdAc in a single pulse, even if only a few nanometers of the surface attain a state of phase explosion. In a subsequent pulse, the surface which is devoided of precursor molecules

absorbs energy due to its metal cluster content. Its absorption coefficient is lower than its original value, so there is more penetration of light to deeper parts of the target, leading to an increase in the depth of material that is devoided of precursor molecules. The surface material (made of only metal atoms, clusters and other product molecules and radicals) is repeatedly heated during pulse irradiation, in subsequent pulses, enabling the diffusion of metal atoms and clusters, leading to the growth of metal clusters to possibly attain nanoparticle (NP) sizes. In solution, metal clusters grow to a stable NP size – this will be explained in a later sub-section. If material removal occurs only after thousands of pulses that allow for the attainment of NP sizes, an absorption mechanism related to NP size is duly responsible for material removal. At a saturated size, the NPs heat their local matrix environment the most. Local heating to a state of phase explosion may eject the NP and its surrounding material.
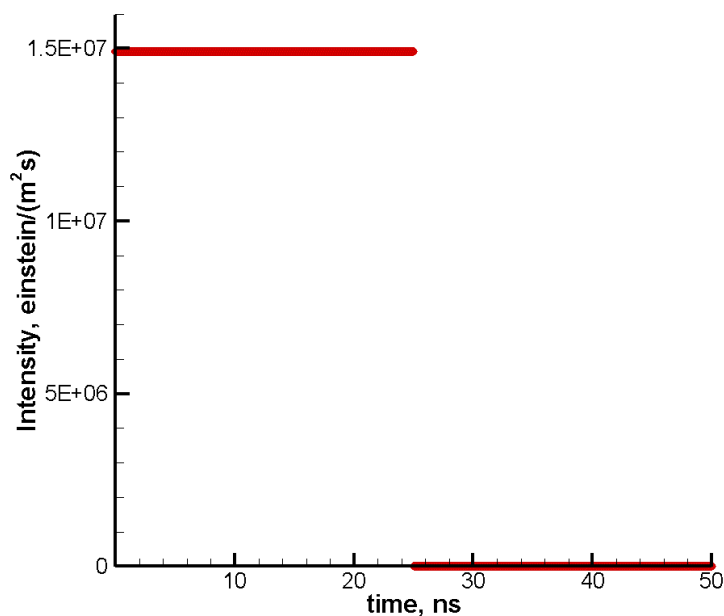
Figure 4.5   Intensity of laser light, at a fluence of 18 J/cm^2, on the surface of 1 wt% PdAc target.
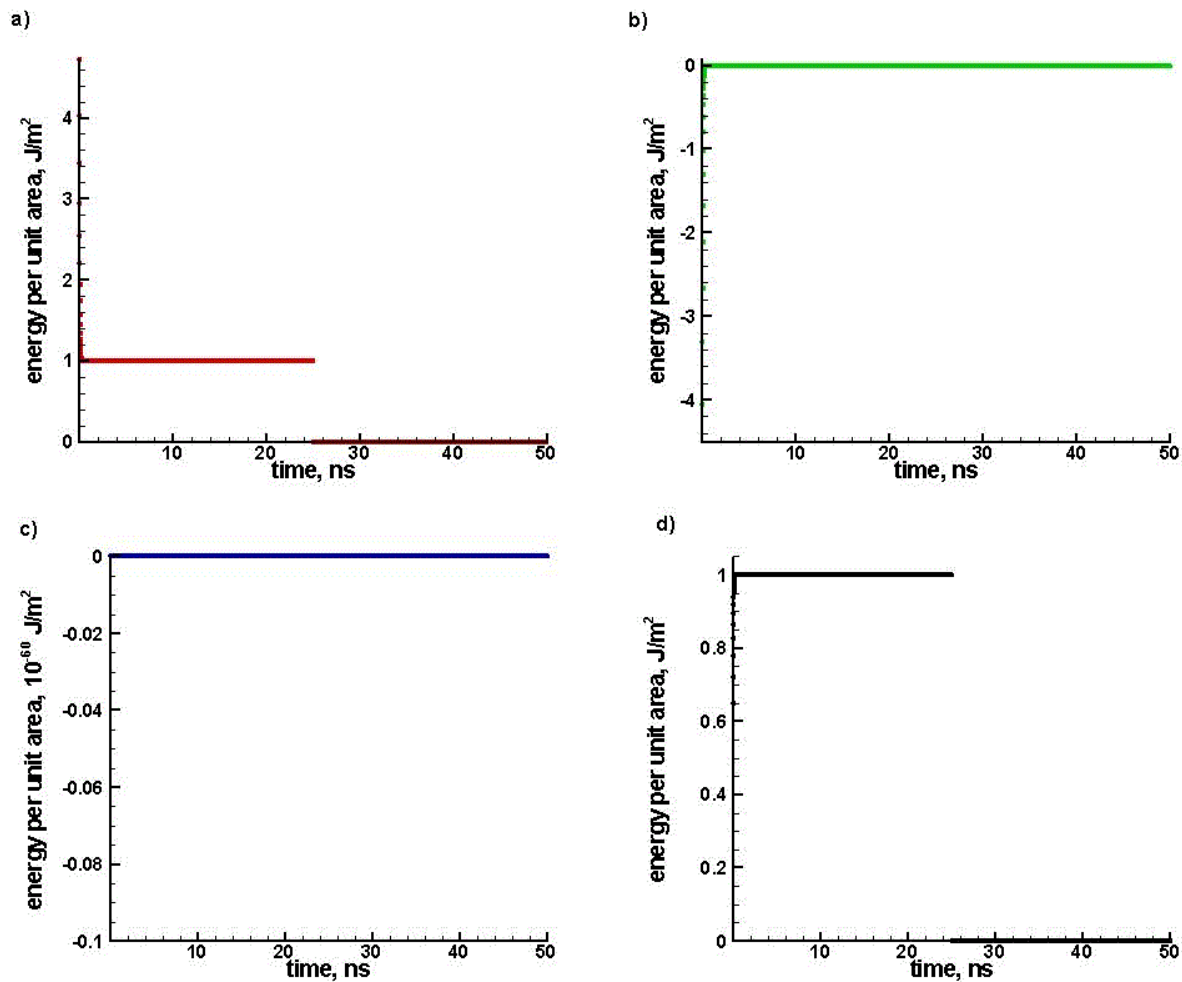
Figure 4.6 Plot of different components of the total heat source per unit area of irradiation at threshold fluence – 18 J/cm^2, for 1 wt% PdAc target, at initial temperature of 77 K – a) photothermal source, b) photochemical source, c) thermal decomposition source, and d) the total heat source.
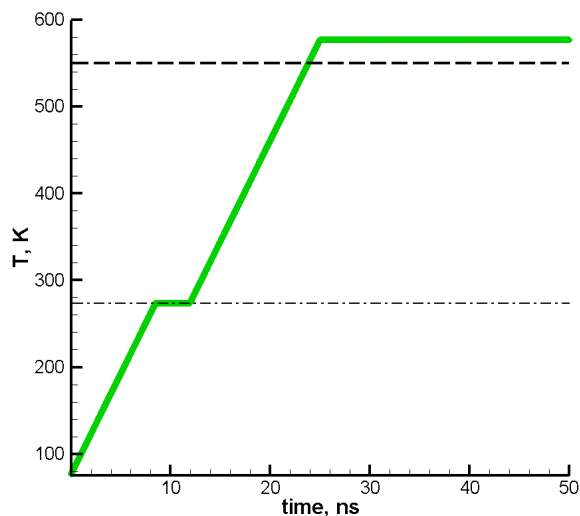
Figure 4.7 Plot of the surface temperature at threshold fluence − 18 J/cm^2, for 1 wt% PdAc target, at initial temperature of 77 K. The thick horizontal dashed-line is the temperature of explosive boiling (T^b), and the thinner horizontal dot-dashed line is the melting temperature (T_m).
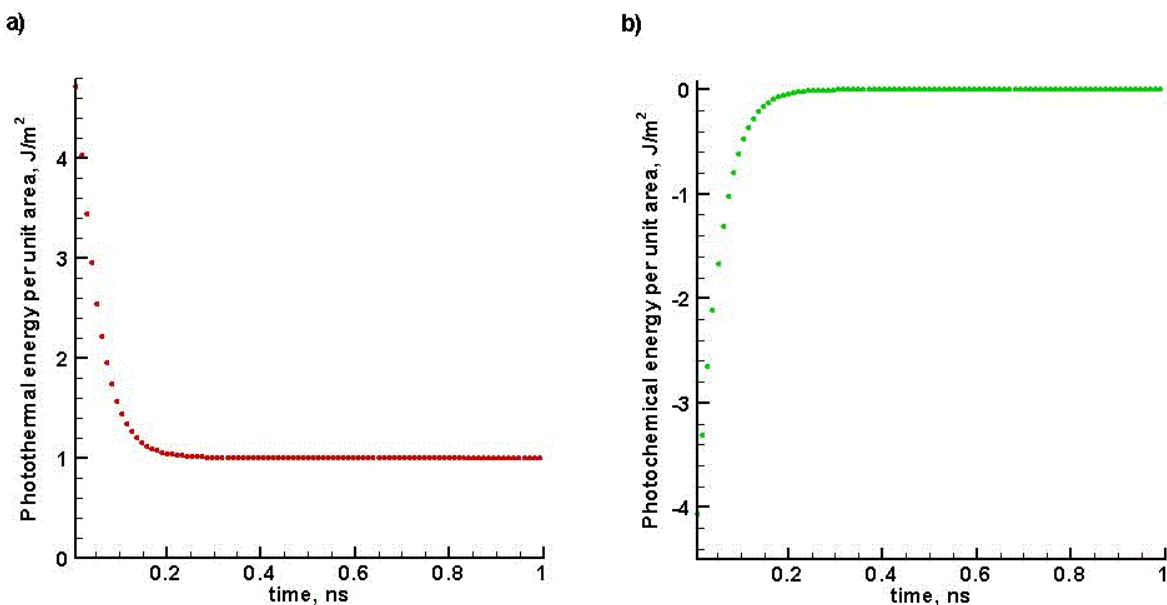
Figure 4.8 Plot of different components of the total heat source per unit area of irradiation at threshold fluence − 18 J/cm^2, fluence for 1 wt% PdAc target having initial temperature 77 K, during decomposition of the precursor– a) photothermal source, b) photochemical source.
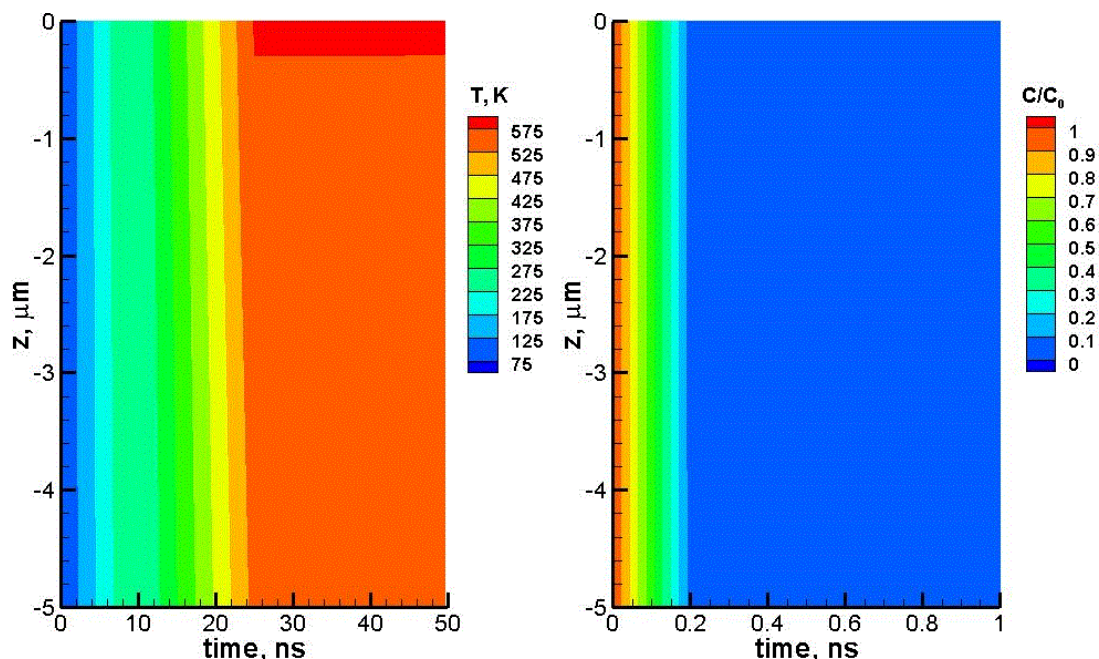
Figure 4.9   Contour plots for target having originally 1 wt% PdAc in water at a temperature of 77 K, at an irradiation fluence of 18 J/cm^2. Left – temperature, right – concentration of PdAc relative to its initial concentration.
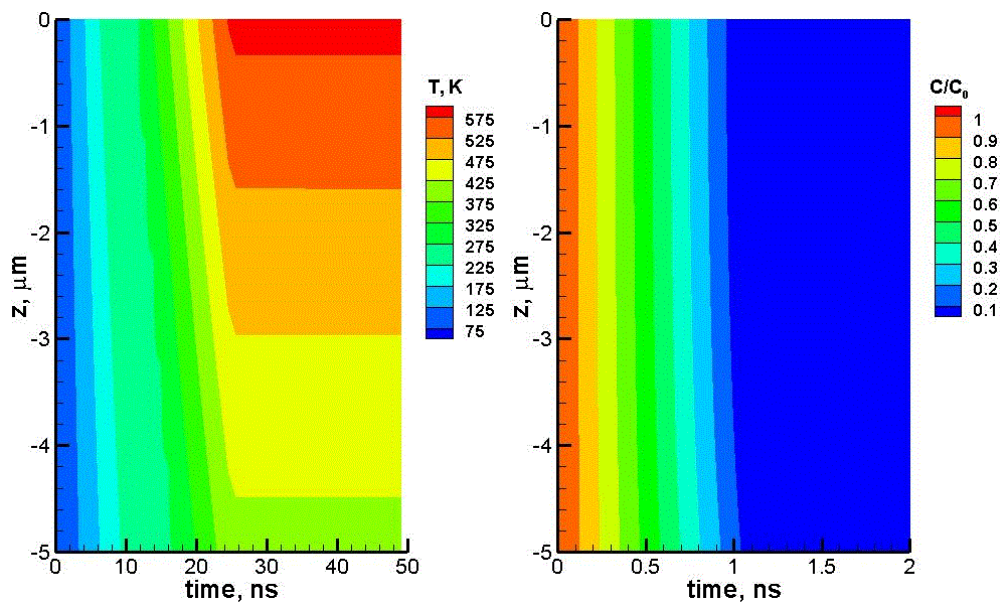
Figure 4.10   Contour plots of a) temperature of target, b) concentration of PdAc relative to its initial concentration, for originally 5 wt% PdAc in water, having initial temperature 77 K, at an

irradiation fluence of 1.4 J/cm^2. Left – temperature, right – concentration of PdAc relative to its original concentration.

Table 4.4. Threshold fluence of ablation in PdAc target having initial temperature of 77 K, determined from continuum model simulations.

T, K	wt.%	F*
77	1	18
77	5	3.6

4.5 Atomistic Model

An atomistic model is used for the determination of the diffusion coefficient of palladium (Pd) atom in water, which is then utilized in the parametrization of the interaction potential between Pd atom and breathing sphere water. To accomplish this, the diffusion coefficient of single Pd atom in atomistic water at room temperature and pressure is determined. The interaction potential between Pd and BS water would be parametrized by determining the diffusion coefficient of single Pd in BS water at room temperature and pressure, and matching it to the value already determined in the atomistic model. To determine how well the parametrized potential predicts the mobility of Pd atom in water at liquid temperatures higher than room temperature, the diffusion coefficients of single Pd in water, both in the atomistic model and the breathing sphere model, are determined at temperatures up to that for explosive boiling, and a comparison of the values obtained in the two models is made. Because the diffusion coefficient of

Pd atom in water would be determined close to the explosive boiling temperature, the explosive boiling temperature of water is also determined in our atomistic model.

4.5.1 Simple-Point-Charge (SPC) Water Model

The atomistic representation of water adopted here is the simple-point-charge (SPC) molecular representation for water. In this representation, the water molecule is rigid, i.e. the bond lengths between atoms of the molecule are fixed, so that the oxygen-hydrogen bond length, $r_{OH} = 1.0$ Å, and the H-O-H bond angle, $\theta_{HOH} = 109.5^{O}$, [57, 138, 139, 140] do not change during the simulations. The charges on oxygen atom and hydrogen atom are respectively, $q_{Ox} = -0.82$ e and $q_H = 0.41$ e [57, 139, 140]. Atoms of the same molecule do not interact in the SPC model. The interactions between atoms of different molecules are described by the Coulomb interaction between all atoms, and the Lennard-Jones (LJ) interaction potential is defined between oxygen atoms only [57, 139, 140]. The potential between two molecules is:

$$V_{ij} = \sum_{l=1}^{3} \sum_{k=1}^{3} \frac{1}{4\pi\epsilon_0} \frac{q_{ik}\, q_{jl}}{r_{kl}} + 4\epsilon_{ij} \left[\left(\frac{\sigma_{ij}}{r_{ij}} \right)^{12} - \left(\frac{\sigma_{ij}}{r_{ij}} \right)^{6} \right] \tag{4.29}$$

where $\epsilon_{ij} = 0.649$ kJ/mol and $\sigma_{ij} = 3.166$ Å [57, 140], and the summation by indices k and l is over the atoms in molecules i and j, respectively.

It is important to note that the assumption that there are point charges is an approximation leading to a slightly misrepresented value for the permanent dipole moment of the water molecule. To correct this, the H-O-H bond angle is changed to 109.5^o from the experimental value of 104.5^{O}.

In this model, a crystal structure of ice water (hexagonal ice Ih) is generated, based on a description of the crystal structure provided in Ref. [141]. Simulations to determine the diffusion coefficient of single Pd atom in SPC water are performed using a package of molecular

simulation routines called 'DL_POLY'. DL_POLY has been used previously to explore the structural and dynamic properties of ice-water interfaces based on a SPC model [142]. In order to test the validity of our atomistic SPC model, some of the physical properties of the simulated water at room temperature and pressure are compared to those of atomistic SPC models, developed by other research groups.

4.5.1.1 Generation of ice crystal

Ice posseses different crystal structures and two amorphous states, but hexagonal ice Ih (also termed ordinary ice), whose crystal symmetry is reflected in the shape of snowflakes, is the common terrestrial form [141]. A description of the crystal structure of ice is obtained from Ref. [141]; a schematic of the crystal structure therein is displayed in Figure 4.11. Each H_2O molecule has four nearest neighbors arranged near the vertices of a regular tetrahedron centered about the molecule of interest. The oxygen atom of each molecule is strongly covalently bonded to two hydrogen atoms, while the molecules are weakly hydrogen bonded to each other. When projected onto the plane perpendicular to the c-axis, the molecular stacking sequence is . . . ABBAABBA . . . . The lattice parameters near the melting point are $a = 0.4523$ nm and $c = 0.7367$ nm. The c/a ratio (1.628) is very close to the ideal ratio (1.633) and is independent of temperature. The ice Ih unit cell is relatively open (packing factor less than 0.34), and this accounts for ordinary ice being less dense than water. The hydrogen atoms are arranged randomly [143] according to the Bernal-Fowler rules [144]: first, two protons must be located near each oxygen; secondly, only one proton must lie on each O-O bond.

The ice crystal described, and illustrated in the schematic of Figure 4.13, is generated, with the O-H bond length set at 1.0 Å and the HOH bond angle at 109.5°. The other pre-defined parameter is: $a = 4.523$Å.

A set of 4 horizontal planes of the …ABBA… stacking sequence, A1B1B2A2, is to be first generated. Two basis atoms at positions, $\boldsymbol{b1}$ and $\boldsymbol{b2}$ are defined, and a vector, $\boldsymbol{rs}$, is defined that repeatedly translates the two basis atoms to generate the periodic structure of plane A1. The remaining planes A2, B1, and B2 are generated by defining a displacement vector, for each of them, that will position the plane in relation to A1. Since, each oxygen atom (O) is linked to four other O atoms, two of the links are randomly chosen to position hydrogen atoms (H) at the distance r_{OH} away from the O atom. The obtained A1B1B2A2 structure with O atoms and H atoms is repeatedly translated in the z-direction by a vector of length c to obtain the entirely generated ice Ih structure.

The positions of basis atoms are: $\boldsymbol{b1} = \vec{0}; \boldsymbol{b2} = (a\sqrt{3}/2, a/2, 0)$. The in-plane translation vector is $\boldsymbol{rs} = (2b2_x, 2b2_y, 0) = (a\sqrt{3}, a, 0)$.

It can be easily seen from the crystal structure schematic (in Figure 4.11) that a is the side-length of the regular tetrahedron, implying that it is related to the O-O distance (d) by the cosine rule thorough angle θ_{HOH} : $a^2 = d^2 + d^2 - 2dd \cos \theta_{HOH}$, so $d = a/\sqrt{2(1 - cos\theta_{HOH})}$.

The displacement vectors of the higher planes in relation to A1 are determined: i) the displacement of B1 in relation to A1 is $\overrightarrow{rA1B1} = (x1, a/2, d \cos(\pi - \theta_{HOH}))$ where $1 = -\sqrt{d^2 - (a/2)^2 - d \cos(\pi - \theta_{HOH})^2}$; ii) the displacement of B2 in relation to A1 is $\overrightarrow{rA1B2} = \overrightarrow{rA1B1} + d\bar{e}_z$ where $\bar{e}_z$ is the unit vector in the z-direction; the displacement of A2 in relation to A1 is $\overrightarrow{rA1A2} = \overrightarrow{rA1B1} + (d + 2d \cos(\pi - \theta_{HOH}))\bar{e}_z$.

Computed values of d and c are: $d = 2.769$ Å, $c = 7.387$ Å; these values are 0.36 % and 0.27 % away from the idealized values in the schematic structure described. The masses of O atom and H atom are 16 Da and 1 Da, respectively. The computed density of the generated crystal structure is 0.93 g/cm^3. A snapshot of the generated crystal structure is displayed in Figure 4.12.
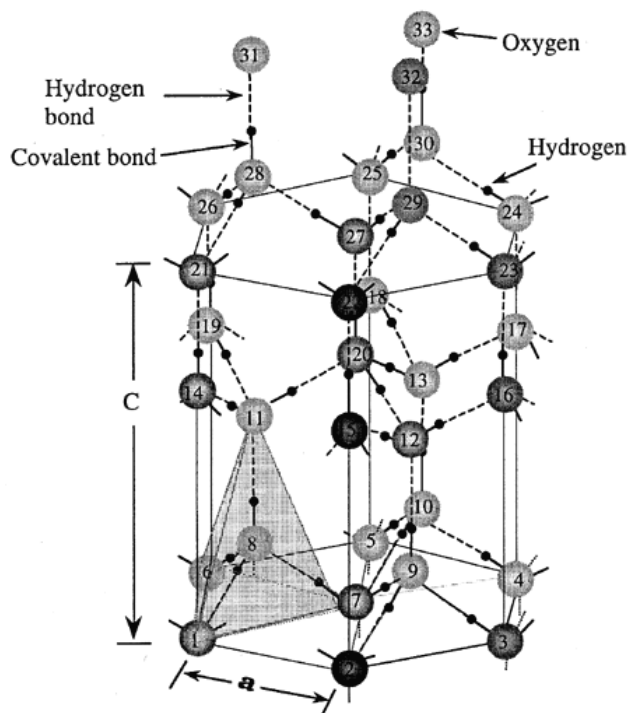
Figure 4.11 A schematic of the crystal structure of hexagonal ice Ih. Each H_2O molecule has its four nearest neighbors arranged near the vertices of a regular tetrahedron (shaded) centered about the molecule of interest. The stacking sequence is . . . ABBAABBA . . . and may be seen from the numbers on the oxygen atoms: numbers 1-7 = A, 8-10 = B, 11-13 = B, 14-20 = A, 21-27 = A, 28-30 = B, 31-33 = B. Near the melting point the O-O distance is 0.276 nm, and the lattice parameters are a = 0.4523 nm and c = 0.7367 nm. [Adopted from Ref. [141]]
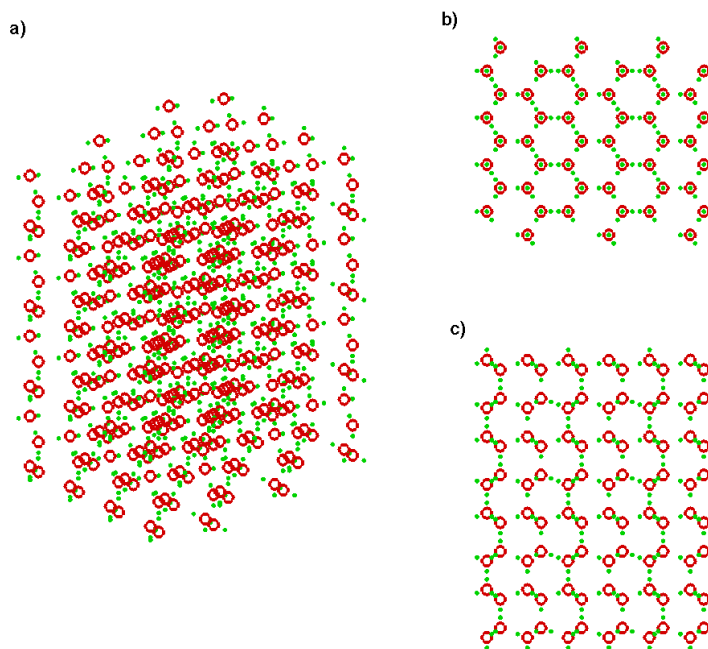
Figure 4.12   Generated Ih H_2O crystal: a) 3D view, b) and c) are side views. O atoms are denoted in red, and H atoms in green.

4.5.1.2. Computation and simulation using DL_POLY software

  To maintain water molecule as a rigid molecule, constraint dynamics are used: in addition to maintaining the O-H bond length at 1.0 Å, the H-O-H bond angle is maintained at 109.5 ^{o}C by constraining the separation between the two H atoms of the H_2O molecule, r_{HH}: $r_{HH} = 2r_{OH}\cos(\theta_{HOH}/2)$, resolving to 1.633 Å. For constraining the bonds and separations, the SHAKE algorithm in the verlet leapfrog integration scheme is employed, with a tolerance of 10^{-5}.

  The Lennard-Jones (LJ) potential is a short-ranged van der Waals potential that falls off very rapidly with distance: at 2.5 σ the LJ potential has just 1 % of its value at σ; it can be computed within a spherical radius (the cut-off radius) of 8 Å in the SPC model.

The Coulomb potential is long-ranged, and direct calculation of it demands consideration of a large number of interactions; a method that still takes into account long-range effects needs to be employed if a van der Waals type cut-off radius is implemented. The 'reaction field' method is employed for computation of the long-range Coulombic interactions. In the reaction field method, any given molecule is surrounded by a spherical cavity of finite radius – which is the cut-off radius – within which electrostatic interactions are calculated explicitly, and outside the cavity the system is treated as a dielectric continuum. The energy of a molecule sums up from that within the cavity plus the interactions beyond the cavity. According to DL_POLY, the model coded into its package is the implementation of Neumann based on charge-charge interactions [145]. The effective pair potential is therefore

$$U(r_{ij}) = \frac{1}{4\pi\epsilon_0} \, q_j q_i \left[\frac{1}{r_{ij}} + \frac{B_o r_{ij}^2}{2R_c^3}\right] \; ; \; B_o = \frac{2(\epsilon_w - 1)}{2\epsilon_w + 1} \tag{4.30}$$

where R_c is the cavity radius (or cut-off distance), and ϵ_w is dielectric constant of the medium. The dielectric constant of water (ϵ_w) is adopted as 78.5 $\pm$0.1 at 298 K, an average of values from a number of differing references [146,147]. There is a step change in the potential energy when a particle leaves or enters the spherical cavity; the net change in energy from particles leaving and entering the cavity is non-zero, and this affects energy conservation. In DL_POLY, this effect is countered by subtracting the value of the potential at the cavity boundary from each pair contribution. The term subtracted is

$$\frac{1}{4\pi\epsilon_0} \, q_j q_n \left[1 + \frac{B_o}{2R_c}\right]$$

An overall cut-off of 8.5 Å is implemented, both for the LJ interactions and Coulombic interactions. Because the use of a cut-off may not dramatically reduce the time taken to compute

the number of non-bonded interactions – given one has to calculate the distance between every pair of atoms before deciding whether it is within cut-off range, and also because an atom's neighbors do not change significantly over 10 or 20 molecular dynamics time steps, it is possible and better to identify each atom's neighbors using a neighbor list. It is important to update the neighbor list at the correct frequency, as a low frequency may calculate energies and forces incorrectly due to atoms moving through the cut-off boundary during the time interval of the update. The update frequency used for these simulations is 10 timesteps for a timestep of 1 fs. DL_POLY uses a 'linked-list' method in which the computational cell is divided into several boxes, the length of each box being equal to the cut-off distance plus a 'skin' thickness. A molecule only has to look for other molecules that are within its cell to determine whether they are within cut-off range for computation. The skin thickness has to be appropriately chosen so that a molecule cannot diffuse across it within the computational time between updates of the neighbor list.

Equilibration periods of at least 10 ps are allotted, after which system properties are evaluated as an average over the remaining simulation time

A Ih ice crystal of 384 molecules with computational side lengths XL = 23.502 Å, YL = 18.092 Å, ZL = 29.549 Å, after being generated is equilibrated at 0 K at constant pressure (P = 1 atm.). A Berendsen algorithm is used to maintain the pressure and temperature; both the thermostat relaxation time and the barostat relaxation time are 5 ps. The equilibrated system is heated to 273 K for 50 ps as an *NPT* ensemble. Further heating of the system as an *NPT* ensemble is continued, with temperature increments of 10 K per 12.5 ps simulation time, up to 383 K.

The thermodynamic properties of SPC water are determined at 298 K and compared to results of other SPC model simulations, in Table 4.5a. Some of the properties − density (through the

computational cell dimensions), self-diffusion coefficient (D) of H_2O, and total potential energy – are directly obtainable from the output of the simulations in DL_POLY_2. The remaining tabulated property, which is the heat capacity, c_P, is calculated from data obtained from the simulation output.

The heat capacity at constant pressure, defined as $c_P = dQ/dT|_P$, is partially calculated using obtained data of potential energy from the simulation ouput. Applying the first law of thermodynamics, $dU = dQ - PdV$, c_P becomes $c_P = dU/dT|_P + P(dV/dT)|_P$, from which the total internal energy, U, can be expressed as a sum of kinetic energy, K_T, and potential energy, P_T: $U = K_T + P_T$. The molar quantity is determined. The second term in c_P is calculated from the volume-temperature dependence about 298 K, from obtained volume data in the simulation output for every temperature about 298 K. The first term in c_P becomes $dU/dT|_P = dK_T/dT|_P + dP_T/dT|_P$, in which $dP_T/dT|_P$ is calculated from the potential energy – temperature dependence about 298 K, obtained directly from the simulation output; and $dK_T/dT|_P$ is determined classically: $dK_T/dT|_P = (N_f/2)R$, where N_f is the number of degrees of freedom of a water molecule, and R is the universal gas constant. Given the imposed intramolecular constraints, the total number of degrees of freedom of a H_2O molecule is made of three (3) translational degrees of freedom plus three (3) rotational degrees of freedom, leading to $N_f = 6$. Two rotational degrees of freedom come from rotation about the axis bisecting the H-O-H plane, summing up from two mutually independent rotations about perpendicular axes; the third rotational degree of freedom comes from rotation about an axis that runs through the O atom and parallelly to the straight line connecting the hydrogen atoms.

Radial distribution functions (r.d.f.), $g(r)$, data at 298 K, obtained from the output of the simulations, for O-O, O-H, and H-H pair separations are plotted in Figure 4.13; the bin width is

0.05 Å. Comparisons are made to other SPC models and experiment in Table 4.5b, by comparing the positions of peak values of the r.d.f.

The equation of state is determined at $P = 0$, within the range of temperatures from room temperature, 298 K, up to temperatures closely beyond the critical temperature of water. The temperature dependence on volume (density) is plotted in Figure 4.14. The slope of the dependence abrubtly increases at $T \sim 550$ K, which serves as an indication of the onset of explosive boiling [148]. The determined value is in the expected range of explosive boiling temperature for water, $T_b^* \sim 0.8T_c - 0.9T_c$ where T_c − which equals 647K [79] − is the supercritical temperature of water.

Table 4.5a. Some thermodynamic properties of SPC water; a comparison is made to other SPC models, and to experimental properties.

property	my SPC	other SPC	Experiment
Density, g/cm^3	0.982	0.971 [149]; 0.98 [150]	0.997 [149]
D, 10^{-9} m^2 s^{-1}	3.4	3.6 [151]	2.4 [151]
Potential Energy, kJ/mol	-41.8	-41.7 [150]; -41.8 [151]	-41.5 [151]
Explosive boiling temperature, T_b^* (K)	~ 550	none	550 [79]

Table 4.5b. Comparison of radial distribution functions in SPC water to other work.

r.d.f. property	my SPC	SPC	Experiment
O-O 1st peak position	2.77	2.8	2.9
O-O 2nd peak position	4.72	4.7	4.7

a) O-O, b) O-H, and c) H-H radial distribution functions at 298K.
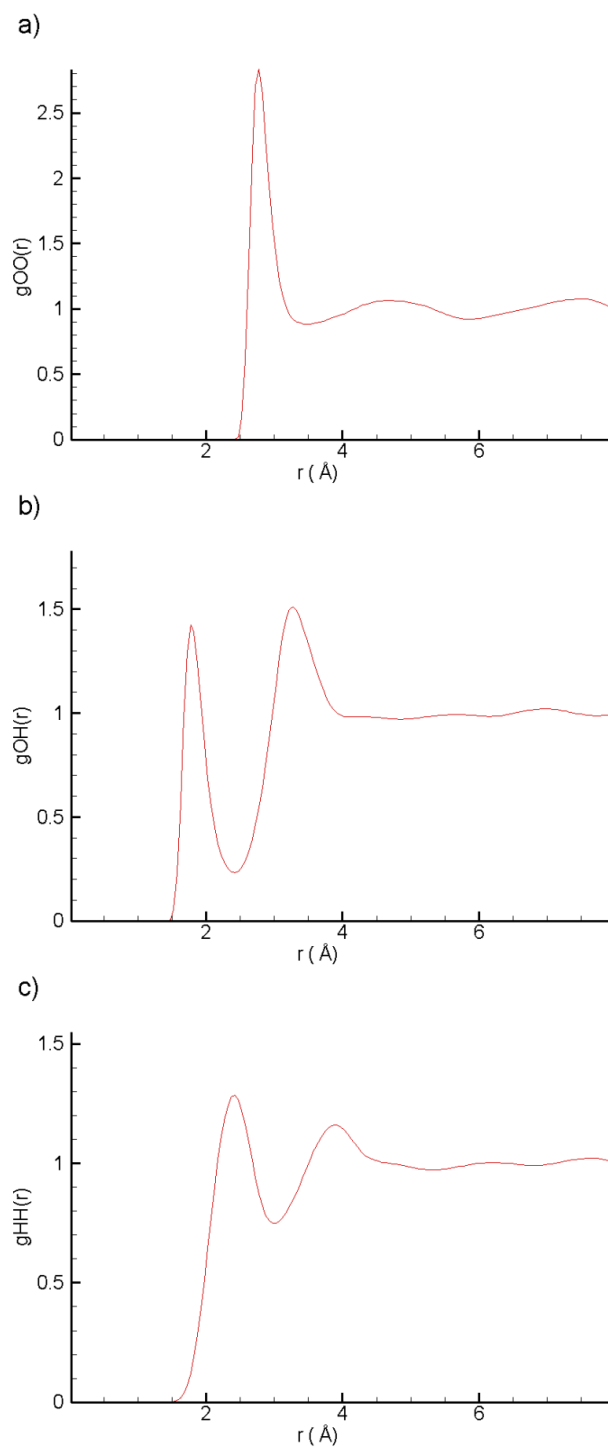
Figure 4.13   a) O-O, b) O-H, and c) H-H radial distribution functions at 298K.
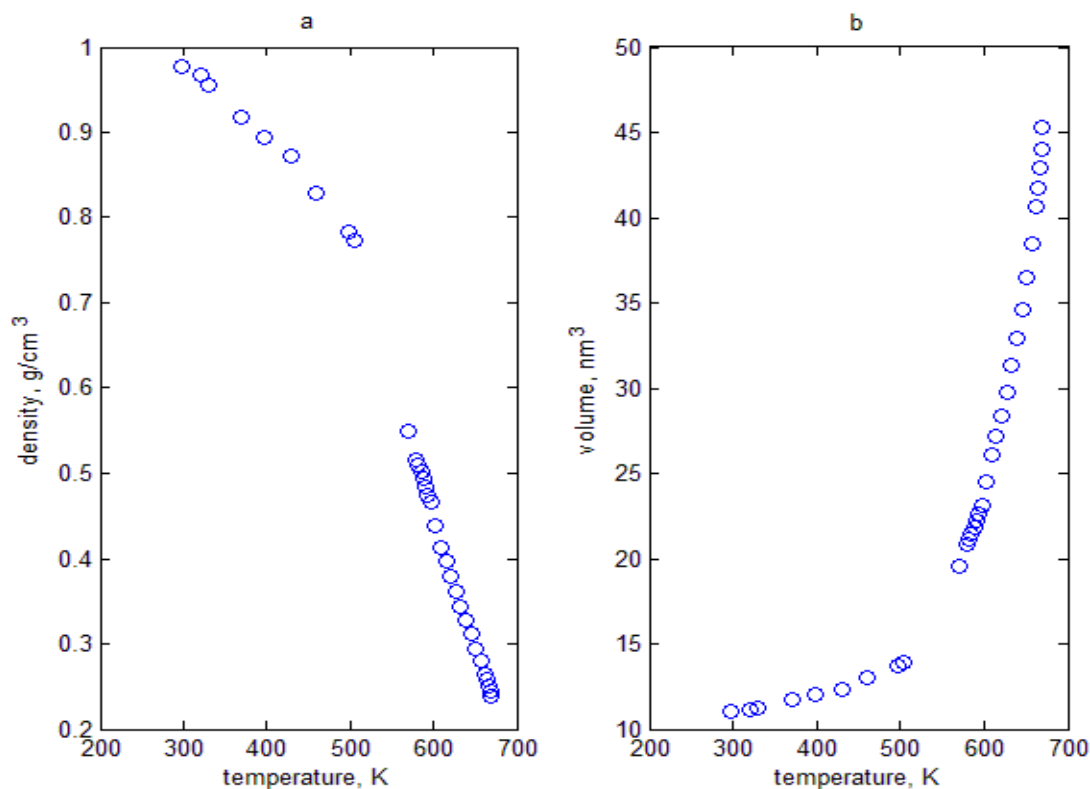
Figure 4.14   Temperature dependence of a) density, b) volume, for SPC water, obtained from data in 'DL_POLY' software.

4.5.2. Metal-Water Atomistic Interactions

The interaction potential between Pd atom and atomistic water, the Spohr potential, is unknown, and, therefore, its parameters have to be determined. There have been experimental [152] and theoretical [153, 154, 155] investigations on the desorption of a water molecule from Pd(111) surface. In these investigations, the adsorption energy of H_2O molecule, E_{ads}, is determined, and the position of O atom, h_{eq}, of the H_2O molecule has been additionally determined in theoretical investigations. We reproduce a model system of H_2O molecule above Pd(111) surface, and the values of E_{ads} and h_{eq} adopted from the cited investigations are aimed at in the parametrization of the Spohr interatomic potential.

In Ref. [152] is a review of experimental reports on thermal desorption spectroscopy (TDS) experiments of water molecules from metal surfaces. According to this review, some measurements may not actually be accounting for water molecule desorbing from the metal surface: water molecules may be binding to other water molecules even at low water coverage (unoccupied metal binding sites). Moreover, water molecules may be recombining from desorbed hydroxyl, oxygen and hydrogen species, which were formed from dissociation of water molecules. Experimental studies provide values of determined adsorption energies of water molecule but do not provide the equilibrium position of the molecule above the metal surface. The reports on theoretical studies are based on density functional theory (DFT) simulations that determine the adsorption energy and the position of water molecule above Pd (111) surface [153-155]. In these studies, the ideal system of a water monomer adsorbed on a metal surface is replicated, and the position of the O atom of H_2O molecule above the surface is determined to be directly above Pd atom.

4.5.2.1. *Literature review of metal-water interactions: the case of palladium*

A literature study is done to determine the adsorption energy of a H_2O molecule and its position above Pd surface. A survey of experimental reports on thermal desorption experiments, adopted from Ref. [152] and theoretical reports based on density functional theory (DFT) simulations is made for understanding the metal-surface interactions and retrieving adequate estimates of the adsorption energy and the position of water molecule above Pd surface.

The ideal system is that of a water monomer above Pd surface. In the lab, this is only closely achievable by having low coverage water (< 0.1 ML) on Pd, and there are still interactions between water molecules. Here, one cannot neglect the hydrogen bonding between water

molecules, ~ 0.2-0.3 eV, about half the predicted values of H_2O-metal adsorption energies, ~ 0.4-0.7 eV. This means a water molecule has a slightly higher preference for a metal site than a water site. There would be a possibility of water molecules binding onto other water molecules at the surface even when there are still unoccupied metal sites; as a result, even at lower coverages there are water molecules on top of first-monolayer water molecules. An adsorbed water molecule can dissociate into hydroxyl and hydrogen species or oxygen and hydrogen species with subsequent adsorption of these species onto the metallic surface. Desorbed hydroxyl and or oxygen species can also possibly recombine to yield water molecules. Since desorption simply involves breaking the water-metal bond, instances of desorption that do not involve this effect, such as those just previously described, would be misleading to the determination of the adsorption energy of water molecule.

  The most widely used experimental method for determining the adsorption energy is thermal desorption spectroscopy (TDS). In such experiments, a surface with an adsorbed specie is heated in vacuum while the concentration of a particular gas-phase species is monitored with a mass spectrometer. As explained earlier, due to multilayer effects or dissociation of water molecule, obtained water molecules in TDS are not necessarily all coming from water that has been desorbed from the metallic surface. Relatively low desorption temperatures in the 110-200 K range are in general a signature of desorption of ice layers or weakly chemisorbed molecular water. At higher temperatures (200-400 K), desorption states are attributed to recombination of hydroxyl radicals (OH) or the recombination of atomic H and O. The temperatures at which different species desorb would have to be considered in order to predict the possibility of desorption of a specie.

There has been work on the determination of water molecule adsorption energy on a Pd single crystal or polycrystalline surface, based on TDS experimental data. Redhead analysis yielded an adsorption energy of 0.45 eV for water molecule on a Pd polycrystalline surface [156]. An experimental determination of the height of adsorbed water molecule is however lacking. Experimental values for different metals may not show consistency: an adsorption energy of water molecule on Au(111) is reported to be 10.5 kcal/mol [57], which converts to 0.45 eV; this is the same value reported for water molecule on Pd(111). These inadequacies lead one to pay attention to theoretically obtained data from computational models that not only replicate the ideal system of a water monomer adsorbed on a metal surface, but also determine the position of the water molecule. Theoretically reported values of adsorption energy (E*ads*) of water molecule on Pd(111) surface are as follows:

i. Based on DFT study, E*ads* at the most favorable site (top site) is 0.22 eV. The distance of O atom from Pd surface is found to be 2.45 Å [156].

ii. DFT model of a monomer on a top site yields E_{ads} = 0.33 eV and 2.28 Å for the height of O atom above Pd(111) [153].

iii. With the DFT slab model, E_{ads} = 0.33 eV has been obtained with O atom at a height of 2.5 Å. In comparison, cluster calculations on 10-15 Pd atoms predict an adsorption energy of 0.29 eV and a separation of O-Pd distance of 2.51 Å [154].

iv. DFT model of a monomer on a top site yields E_{ads}= 0.304 eV and 2.42 Å for the height of O atom above Pd(111) [155].

Given the consistency, from one theoretical report to the other, in predictions of the adsorption energy and the height of water molecule's O atom above Pd(111) surface, the theoretically

described values are relied upon for fitting the Spohr potential that describes Pd-H$_2$O interactions.

<div align="center">

4.5.2.2.   Determination of Pd – SPC water potential

</div>

A system of SPC H$_2$O molecule above a Pd(111) surface is designed. The interaction between SPC H$_2$O molecule and Pd atom is described by a Spohr potential, whose parameters are fitted to obtain the choice values of water molecule adsorption energy (E_{ads}) and the equilibrium height of its O atom, h_{eq}, above the Pd(111) surface. The values of choice are E_{ads}= 0.33 eV and h_{eq}= 2.5 Å, obtained from Ref. [154]. The O atom is placed directly above a Pd atom of the Pd(111) surface, deemed to be a favorable position by most of the DFT analyses described earlier. The Spohr potential describing the interaction between Pd atom and H$_2$O molecule is a modified form that is pairwise additive between the O and H atoms in the H$_2$O molecule, see Ref. [57]:

$$U_{M-H_2O} = U_{M-O}(r_{M-O}) + U_{M-H1}(r_{M-H1}) + U_{M-H2}(r_{M-H2}) \tag{4.31}$$

with

$$U_{M-O}(r) = D_e[\exp(-2\beta_O(r - r_{e1})) - 2\exp(-\beta_O(r - r_{e1})) \tag{4.32}$$

and

$$U_{M-H}(r) = \gamma D_e[\exp(-2\beta_H(r - r_{e2})) \tag{4.33}$$

A Pd(111) crystal is generated. It is then thermodynamically relaxed as a *NVE* ensemble, to obtain a Pd(111) surface, by applying free boundary conditions (FBC) in a direction normal (chosen to be the Z-axis) to its surface while maintaining periodic boundary conditions (PBC) in perpendicular directions.

Palladium crystallizes as a face-centered cubic (FCC) structure in the bulk phase. A three dimensional lattice and a set of basis vectors are employed to generate a FCC crystal in the (111) orientation: lattice + basis = crystal. The lattice is defined by the translational vectors: $\overrightarrow{a1}$ =

$(xshift,\ 0,\ 0)$, $\overrightarrow{a2} = (0, yshift, 0)$, $\overrightarrow{a3} = (0, 0, zshift)$, where $xshift = a\sqrt{3/2}$, $yshift =$

$a\sqrt{\frac{1}{2}}$, $zshift = -3a\sqrt{1/3}$; a is the lattice constant of palladium, and equals 3.89 Å [157,158].

There are three determined basis vectors: $\overrightarrow{b1} = \frac{a}{2\sqrt{2}}(\sqrt{3}\ 1\ 0), \overrightarrow{b2} = a\left(\frac{\sqrt{3/2}}{6}\ \frac{1}{2\sqrt{2}}\ -\right.$

$\left.\sqrt{1/3}\right)$, $\overrightarrow{b3} = a\left(-\frac{\sqrt{3/2}}{6}\ \frac{1}{2\sqrt{2}}\ -2\sqrt{1/3}\right)$. As an example, the position of an atom generated

from the basis vector $\overrightarrow{b1}$ can be determined as: $\overrightarrow{b1}_n = \overrightarrow{b1} + n_x\overrightarrow{a1} + n_y\overrightarrow{a2} + n_z\overrightarrow{a3}$, where

n_x, n_y, and n_z are integers.

A SPC H_2O molecule is placed above Pd(111) surface such that the O atom is directly above a surface Pd atom. The height of the H_2O molecule above the surface is varied, and the total interaction potential between H_2O and the Pd(111) crystal is computed for each height. By adjusting the unknown parameters of the Spohr interaction potential, we make sure to obtain a total interaction potential energy equal to E*ads* at a height equal to h_{eq}. A dependence of interaction energy against height should have a minimum at $(h_{eq}, \text{E}ads)$ for a rightful set of Spohr potential parameters.

The surface of the Pd(111) is on a x-y plane, and the projections of O-H bond lengths along the Cartesian axes are defined as:

$$rOH1_z = rOH2_z = rOH \cdot \sin(\vartheta)\cos(\theta_{HOH}/2)$$

$$rOH1_y = rOH2_y = rOH \cdot \cos(\vartheta)\cos(\theta_{HOH}/2)$$

$$rOH1_x = -rOH2_x = rOH \cdot \sin(\vartheta)\cos(\theta_{HOH}/2)$$

where ϑ is the angle the H_2O plane makes with the surface of Pd(111). A configuration of the system is displayed in Figure 4.15.

The Spohr potentials are modified by cut-off functions, implemented in Ref. [57]. The Pd-H potential is implemented with a cut-off distance, Rh_{off}:

$$U_{M-H}(|RMH|) = \begin{cases} U_{M-H}(r), & r \leq Rh_{off} \\ 0, & r \geq Rh_{off} \end{cases} \quad (4.34)$$

A force-shifting function, $S_1(r)$, is applied to the Pd-O potential: $U_{M-O}(|RMO|) = S_1(r) \times U_{M-O}(r)$.

$$S_1(r) = \begin{cases} 1, & r \leq r_{on} \\ \dfrac{(r_{off}^2 - r^2)^2 (r_{off}^2 + 2r^2 - 3r_{on}^2)}{(r_{off}^2 - r_{on}^2)^3}, & r_{on} < r \leq r_{off} \\ 0, & r > r_{off} \end{cases} \quad (4.35)$$

r_{on} and r_{off} are start and end distances of the force $-$ shifting function, respectively. The cut-off distances are $r_{on} = 7.0$ Å; $r_{off} = 11.0$ Å; $Rh_{off} = 6.0$ Å.

For every adjustment of the Spohr parameters, the interaction energy, E_{M-H_2O}, is calculated at different heights, h. With the set of Spohr parameters: $D_e = 0.104$ eV, $\gamma = 0.2$, $\beta_O = \beta_H = 1.41$ Å^{-1}, $r_{e1} = 3.2$ Å, $r_{e2} = 0.1$ Å, an equilibrium configuration is attained at $E_{M-H_2O} = E$ads and $h = h_{eq}$. A diagram of the dependence of interaction energy on O position, see Figure 4.16, shows a minimum at $(h_{eq}, E$ads$)$.

With the obtained set of Spohr parameters, a molecular dynamics simulation of a SPC H$_2$O molecule above the Pd(111) surface is set up for the determination of the adsorption energy, the height of oxygen atom above metal surface, and the orientation of the H$_2$O molecule. A comparison would be made to the equilibrium configuration, determined in the previously employed method.

In an initial configuration, SPC H_2O molecule is positioned in an arbitrary orientation above the Pd(111) surface. The interaction between Pd atoms is described by an EAM potential, and the interactions between atoms of H_2O molecule and Pd atoms are described by the fitted Spohr potential. A constraint dynamics algorithm, RATTLE [159], is employed to maintain the O-H bond length and the H-H separation to 10^{-5} tolerance. The orientation of the H_2O molecule is determined by the angle between the bisector of the H_2O plane and the normal to the Pd(111) surface.

A constant temperature (T = 0 K) simulation with periodic boundary conditions in directions (X and Y) parallel to the surface and free boundary condition in Z is run. As the system is cooled to 0 K, it does not attain absolute zero as there is some residual kinetic energy in the equilibrated system, seen in the oscillatory nature of the H_2O molecule about the normal to the Pd(111) surface. The system is further cooled: a zero kinetic energy is given to the equilibrated system, which serves as the initial configuration for the next simulation that attempts to cool the system to absolute 0 K. After each cooling procedure, the energetics and dynamics of the system can be analyzed.

Given that to attain absolute zero can be a long computational process, the goal may not necessarily be to attain absolute zero but to observe the tendencies in the behavior of H_2O monomer at different stages of cooling. The H_2O plane tends to be perpendicular to the Pd(111) surface with every cooling process − the angle to the normal, ϑ, decreases from about 8 degrees to 3 degrees, in a number of sequential cooling stages. The energies and orientations are shown in Figure 4.17 for one of the cooling processes. The following observations are true:

i. The potential energy of H_2O is equal to the potential energy of oxygen to 4 significant figures (s.f.), so the potential energy due to hydrogen atoms accounts for less than 10^{-4} of the total H_2O potential energy.

ii. The sum potential energy of hydrogen atoms has peaks and troughs, the troughs corresponding to equal energies of the two hydrogen atoms; see Figure 4.17 c) and d). The angle of the H_2O plane to the Pd surface normal changes in harmony with the energies of hydrogen atoms. The maximum angle subtended to the normal is ~ 2.8 °.

iii. The potential energy of H_2O monomer is -0.33 eV and the height of O atom above Pd surface is 2.5 Å.

Some conclusions can be made from the observed. The Spohr potential has a very low sensitivity to the energy of the hydrogen atoms. The very small maximum angle of H_2O plane to the surface normal can let us conclude that the equilibrium configuration of H_2O monomer in general corresponds to the H_2O plane being perpendicular to the Pd(111) surface. However, the energy of H atom is ~ 10^5 times less than that of the O atom, and so the total energy of SPC H_2O molecule is insignificantly affected by the orientation of the H_2O plane. The adsorption energy of H_2O, E_{ads} from MD simulation is 0.33 eV and the height of O atom above Pd surface h_{eq} is 2.5 Å, matching the expected equilibrium.

The equilibrium configuration of SPC H_2O molecule above Pd(111) in MD simulation is displayed in Figure 4.18a. A variation is made to the height of the SPC HO molecule in the MD equilibrated configuration in order to obtain a dependence of energy on height as has been done previously for a defined configuration. A comparison of the obtained dependence is compared to the height-energy dependence for defined configurations in Figure 4.19. The results of the MD simulations lend robustness to the fitting procedure.
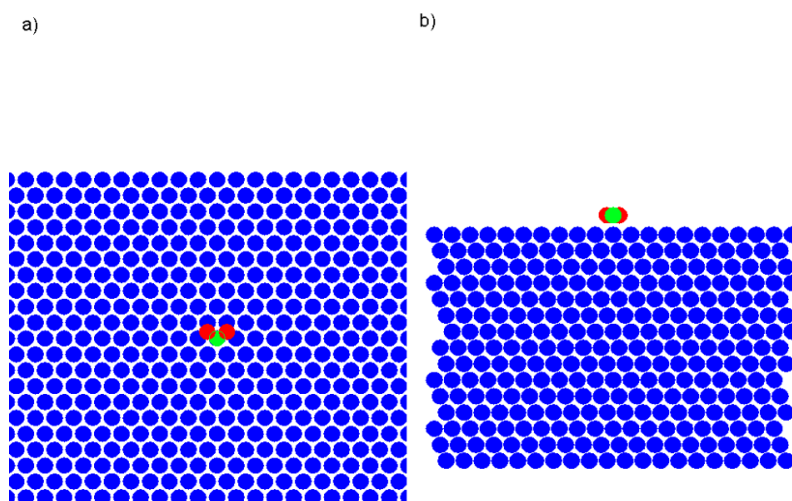
Figure 4.15 A picture of H_2O molecule above Pd(111): a) view from above, b) side view.
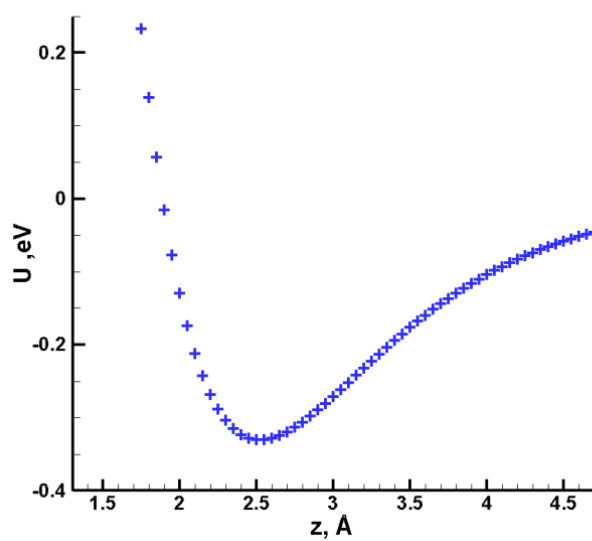
Figure 4.16 A diagram of the dependence of energy of SPC H2O molecule on the height of O

atom above Pd(111).
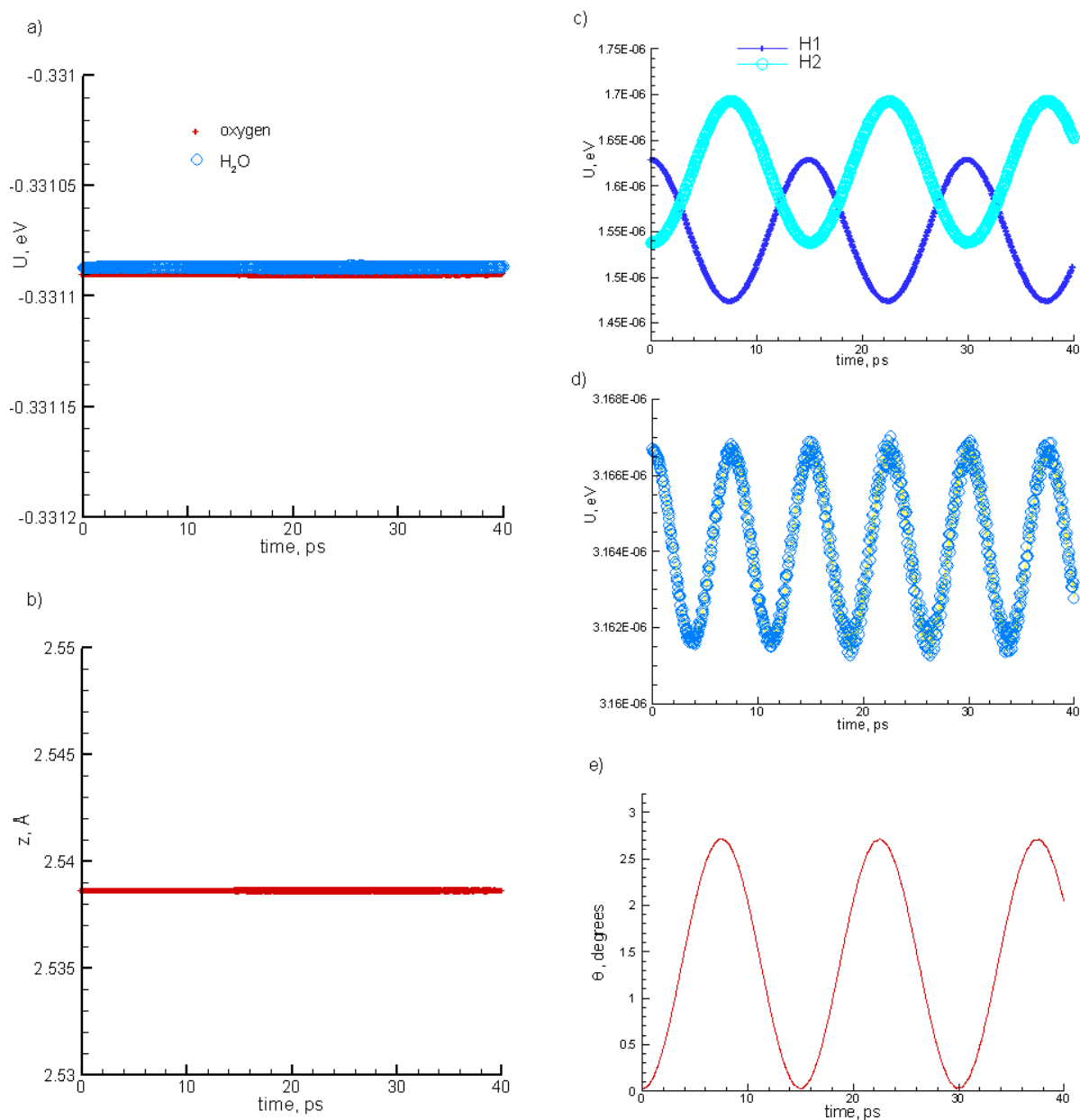
Figure 4.17 For SPC H$_2$O molecule above Pd(111) in MD simulation: a) potential energies of O atom and H$_2$O molecule, b) height of O atom above Pd surface, c) potential energies of hydrogen atoms, d) sum potential of hydrogen atoms, e) angle between H$_2$O monomer plane and normal to Pd(111) surface.
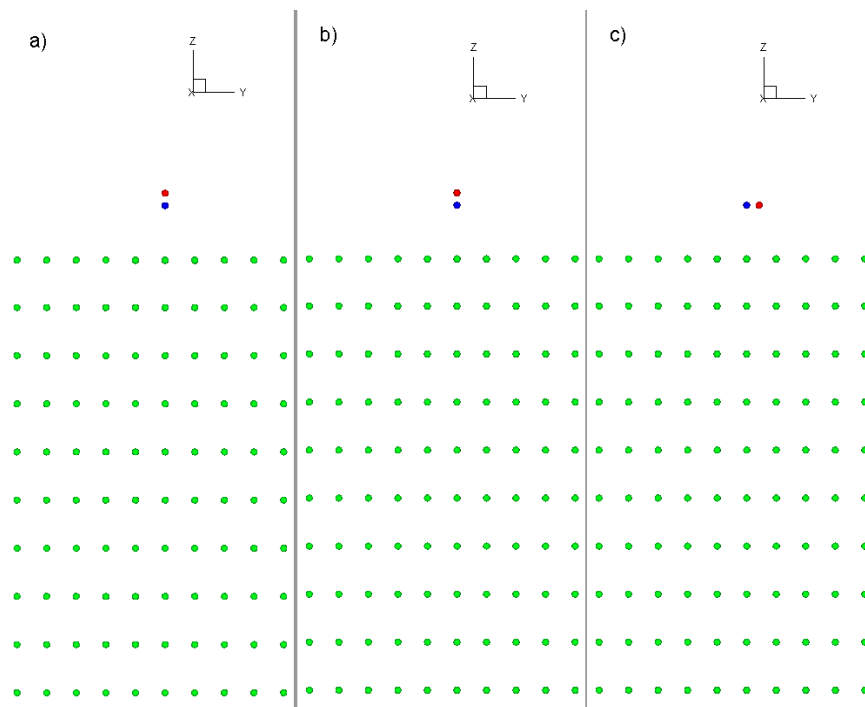
Figure 4.18 Side view of H$_2$O molecule above Pd(111): a) MD simulation configuration b) imposed normal to surface configuration c) imposed flat configuration.
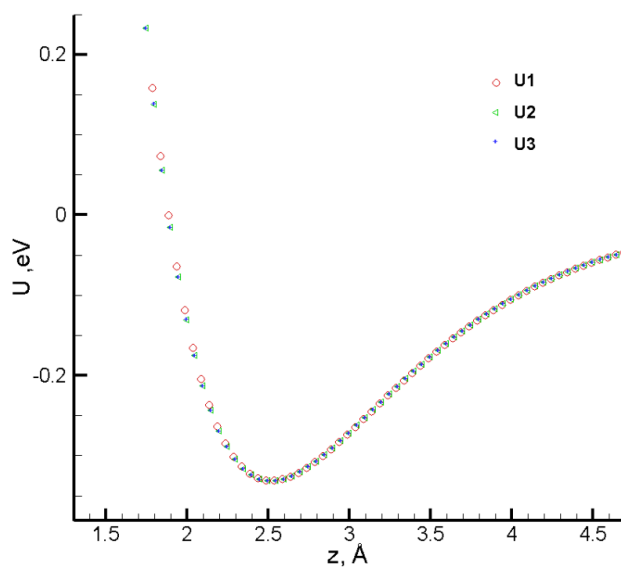
Figure 4.19 Energy of H$_2$O molecule against height of O atom above Pd(111): U1 – MD simulation configuration; U2 – imposed normal to surface configuration; U3 – imposed flat configuration.

4.5.2.3   Determination of diffusion coefficient of single palladium atom in SPC water

The mean square displacement of single Pd atom in water is determined as an average quantity of several mean square displacements of single Pd atom, measured in independent configurations of water. The averaged MSD is thus determined as

$$\overline{MSD(t)} = \frac{1}{N}\sum_{i=1}^{N} MS_{i}(t) \tag{4.36}$$

Twenty (20) different configurations of 360 molecules of SPC water at 300 K are produced by collecting configurations of an equilibrated system at different stages of a MD simulation of a *NPT* ensemble. A Pd atom is inserted into each of the collected configurations, and any offending water molecules to Pd atom are taken off − these are molecules that are positioned from the inserted Pd atom at a distance smaller than a defined separation between Pd and water molecule, ~ half the equilibrium separation. The resulting Pd in water configurations are equilibrated in a *NPT* ensemble to obtain independent equilibrated configurations of single Pd atom in SPC water, in computational cells of size 23.0 Å × 22.1 Å × 21.7 Å, see Figure 4.20 for configuration.   The trajectory of Pd atom in SPC water would be obtained from MD simulation in DL_POLY, with a cut-off of 10 Å implemented to the the Spohr potential; 20 independent trajectories would be obtained.

For a trajectory of time, T, covered by a single atom, the MSD(*t*) is determined as a function of time, *t*. A set of *N* sub-trajectories, each of time length T/2, is retrieved from the main trajectory, so that the time domain of each sub-trajectory is defined: $t_i < t \leq t_i + \text{T}/2$, where $t_i = i\Delta t$ and $\Delta t = \text{T}/2N$; Δt is the time delay between the sub-trajectories. The mean square displacement is then determined, combining the *N* sub-trajectories, as:

$$MSD(t) = \frac{1}{N} \sum_{i=1}^{N} (\boldsymbol{r}(t_i + t) - \boldsymbol{r}(t_i))^2 \tag{4.37}$$

Numerically, for a discrete timestep δt, t is substituted by $t_j = j\delta t : j \in [1, M]$, where M is the number of timesteps in a subtrajectory, so that $\delta t = \mathrm{T}/2M$. The mean square displacement for a given trajectory can thus be numerically written, for an instant of time, as

$$MSD(t_j) = \frac{1}{N} \sum_{i=1}^{N} (\boldsymbol{r}(t_i + j\delta t) - \boldsymbol{r}(t_i))^2 \tag{4.38}$$

A diagram of the trajectory of an equilibrated system of single Pd atom in SPC water is displayed in Figure 4.21a; alongside this is displayed the determined MSD from the trajectory, Figure 4.21b. The timestep of discretization is $\delta t = 1$ ps, so the number of discrete points in a sub-trajectory is $M = 250$.

 MSDs, as a function of simulation time, of single Pd in 300 K SPC water, for the 20 independent configurations, are plotted in one diagram; see Figure 4.22a. The average MSD over the 20 different configurations is plotted over time in Figure 4.23a, and a linear fit is run through it; it can be seen to be close to being linear. The diffusion coefficient determined from the MSD by the Einstein relation is $D = 2.22 \times 10^{-9}$ m^2/s. Although there is no *a priori* determined value of   for Pd in water, for a fair comparison, the determined value of the diffusion coefficient in our model is compared to the values of   for single metal atom in water, determined using molecular dynamics simulations in Ref. [160]. In Ref. [160], diffusion coefficients of a few noncharged metal atoms of differing sizes, ranging from Li, through Na, to Cs, have been determined, from the mean square displacement of the atom, to range from ~ 14×10^{-9} to 2×10^{-9} m^2/s. There is an observed tendency for the diffusion coefficient to become smaller as the size of the metal atom gets bigger; the diffusion coefficients of Rb and Cs

are 2.08×10^{-9} m^2/s and 2.03×10^{-9} m^2/s, respectively. The size of Pd atom (atomic mass 106.4) roughly compares to those of Rb (atomic mass 85.5) and Cs (atomic mass 132.9), and so it is fairly reasonable that Pd atom will have about the same diffusion coefficient, as justified by the value determined in our model – 2.22×10^{-9} m^2/s.
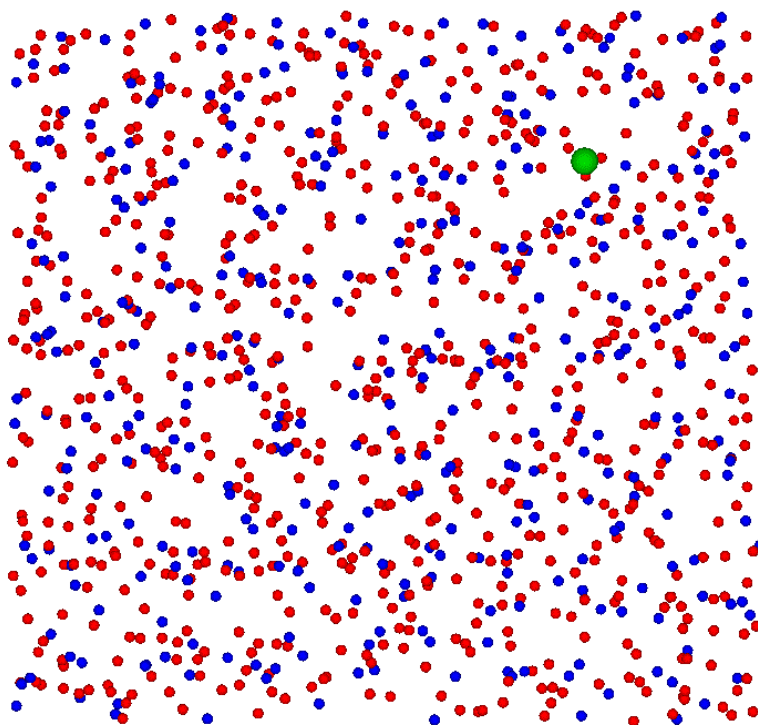
Figure 4.20   Single Pd atom in SPC H$_2$O at 300 K. Pd is green colored, while O and H atoms are blue and red, respectively.
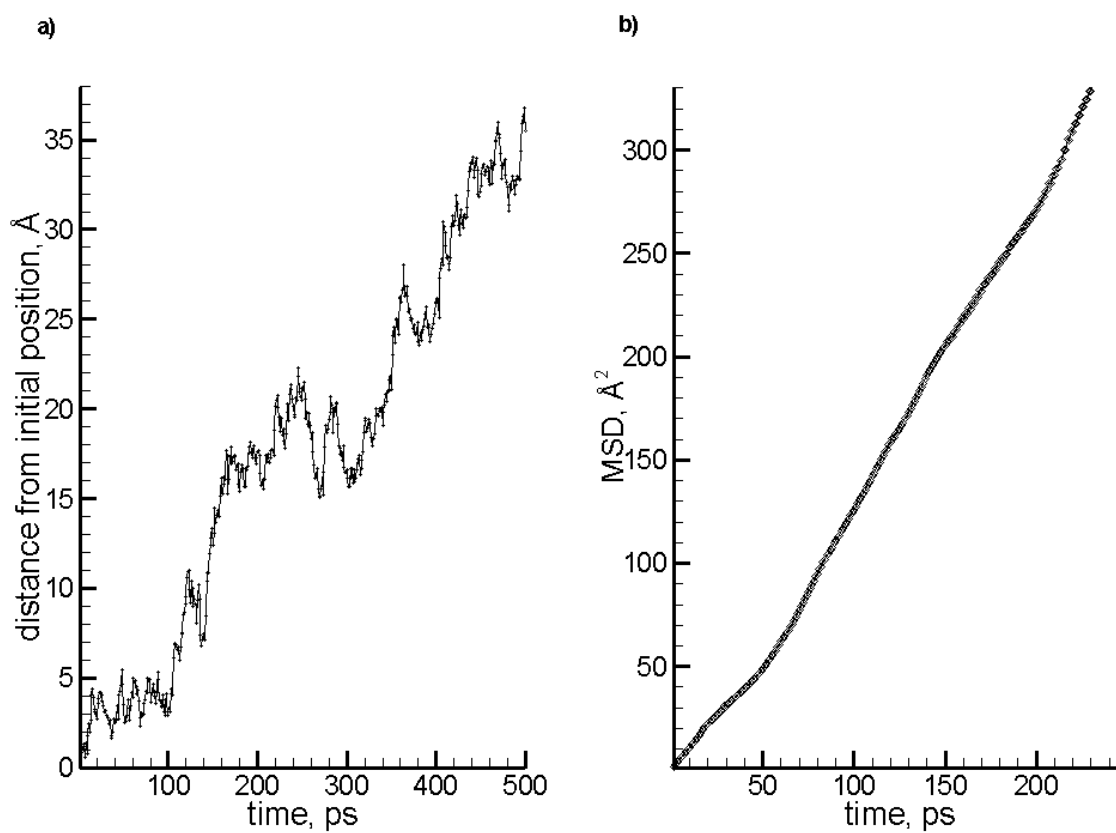
Figure 4.21   a) Distance of single Pd atom from its initial position in SPC water at 300 K; b) mean square displacement of single Pd atom in SPC water at 300 K.
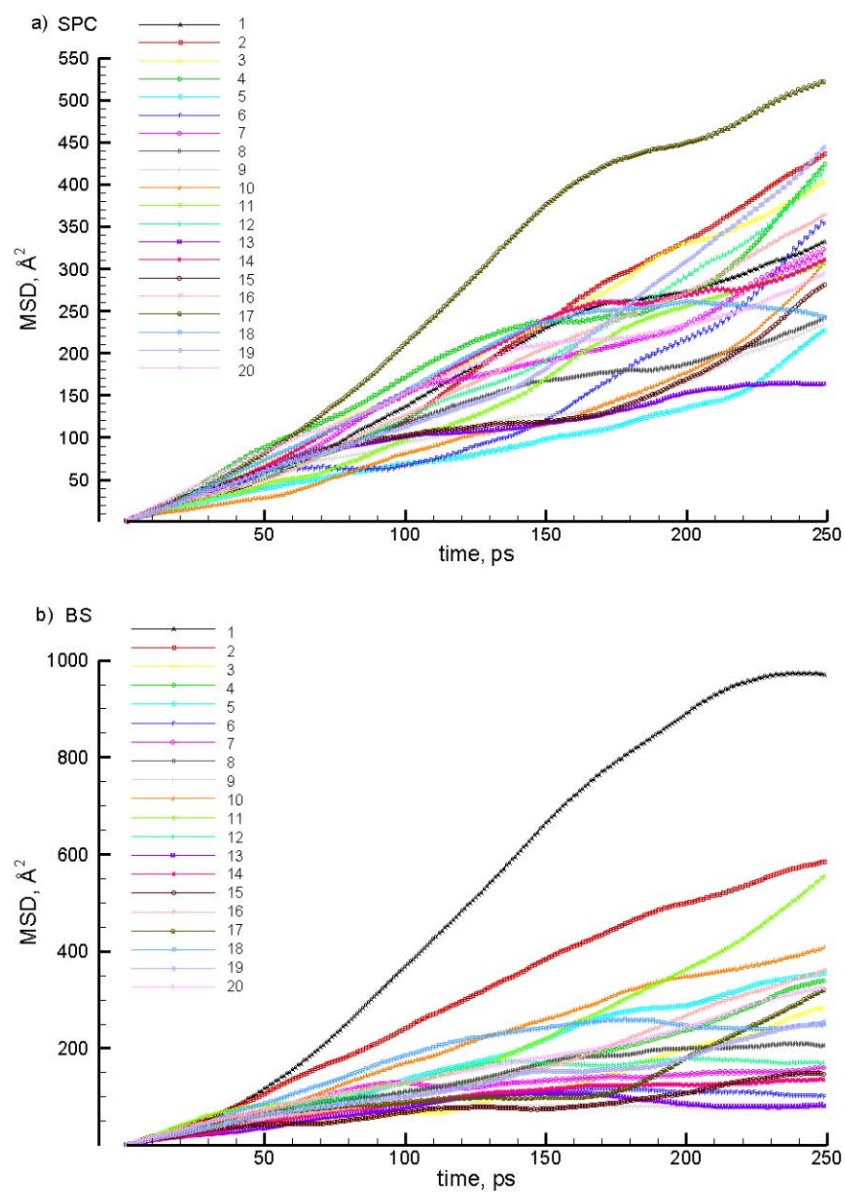
Figure 4.22   MSDs of single Pd atom in a) SPC water, b) BS water, at 300 K.
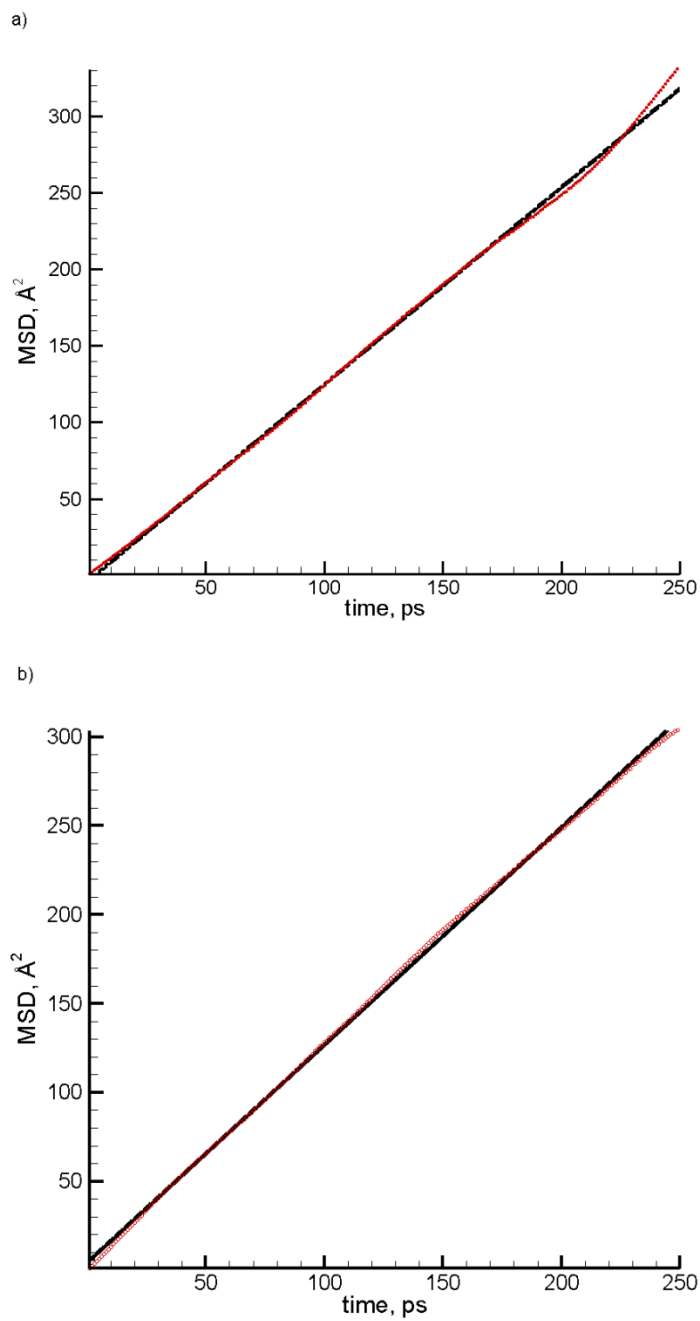
Figure 4.23 Average *MSD* ($\overline{MSD(t)}$) of single Pd atom in a) SPC water b) BS water, at 300 K. The black straight line is the linear fit to $\overline{MSD(t)}$.

4.6 Parametrization of Interaction Potential between Palladium Atom and Breathing Sphere Water

The Pd atom – BS molecule interaction is described by a Morse potential. The parameters of the Morse potential are fitted to obtain the diffusion coefficient of single Pd atom in atomistic SPC water at 300 K. The fitting procedure is partly guided by observing changes in the radial distribution functions of BS water molecules around Pd atom. Furthermore, D of single Pd is determined at higher temperatures – 400K, 500K, 600K – at a fixed volume, for both SPC water and BS water, and comparisons are made, to confirm the adequate reproducibility of atomic diffusion by the BS model. The values of D in both water models are found to be within 11 % of each other for adequate reproducibility of atomic mobility by the BS model.

A NPT ensemble of Pd in a cubic computational cell (82.76Å $\times$ 82.76Å $\times$ 82.76Å) of 6912 BS molecules, at 300 K and $P = 0$, is prepared. The volume of the equilibrated ensemble is fixed and heated, in NVT simulations, to the temperatures at which the diffusion coefficients are to be measured. See Figure 4.24 for configuration.
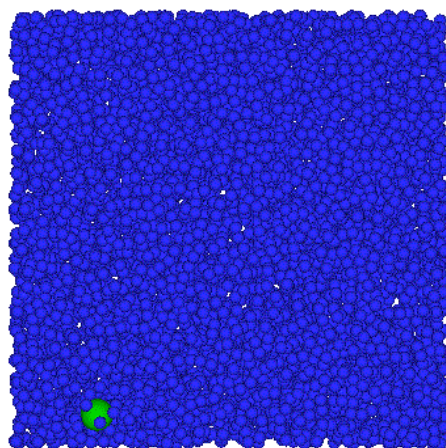
Figure 4.24   Single Pd atom in BS water at 300 K. Pd is green colored, while water molecules are blue colored.

After fitting to a value of   at 300 K, which equals 2.21×10^{-9} m^2/s, a choice set of Morse parameters is arrived at: $D_e = 0.15$ eV; $\beta = 1.0$ Å^{-1}; $r_e = 3.2$ Å. The fitting procedure is described in the next sub-section. The mean square displacements of Pd in BS water with time for the different temperatures are plotted in Figure 4.25. The diffusion coefficients can then be determined from the MSD curves by using Einstein's relation: $MSD(t) = 6Dt + C$. Values of D are determined, and tabulated in Table 4.6, for different temperatures. The temperature dependencies are plotted in Figure 4.26.

We derive an Arrhenius plot of diffusion coefficient D against temperature T. The Arrhenius equation is $= D_o \exp(-\frac{E_a}{kT})$, where $_0$ is a constant, and E_a is the activation barrier. Taking the logarithm of the Arrhenius equation yields

$$\ln D = \ln D_o - E_a \cdot \frac{1}{kT} \tag{4.39}$$

so that the slope of ln   against $1/kT$ yields $-E_a$. The Arrhenius dependence is plotted in Figure 4.27, for both the SPC and BS models. The slope is calculated from linear fits of $\ln D$ in Figure 4.27.

To determine the error in $\ln D$, its differential is first determined:

$$d \ln D = \left(\frac{\partial \ln D}{\partial D} \right) dD = \frac{dD}{D} \tag{4.40}$$

so that the error $\Delta(\ln D) = \Delta D / D$.

Alternative determination: the error in $\ln D$, $\Delta(\ln D)$, caused by the error in D, can be determined as $\frac{1}{2}[\ln(D + \Delta D) - \ln(D - \Delta D)]$, equaling $\Delta D / D$ in a second order Taylor approximation.

Values of ln   and errors in ln   are tabulated in Table 4.6, as well.

From a linear fit to the dependence of $\ln D$ on $1/k_B T$, the value of E_a is determined as 0.076 eV from the slope and the value of $\ln D_o$ is determined from the intercept: E_a= 0.076 eV, and $\ln{}_o$ = -16.95 for the breathing sphere (BS) model; E_a= 0.074 eV, and $\ln D_o$ = -17.04 for the atomistic (SPC) model.

Since the diffusion coefficient D is in units of 10^{-9} m^2/s, $\ln D_o$ can be expressed in the following manner:

$$\ln{}_o = \ln(val) - 9\ln 10$$

yielding $val = 43.51$, so that $D_o = 43.51 \times 10^{-9}$ m^2/s for the BS model; and $val = 35.98$, so that ${}_o = 35.98 \times 10^{-9}$ m^2/s for the SPC model.

Table 4.6. Determined values of the diffusion coefficient of Pd atom in water at different temperatures, in both atomistic and breathing sphere models.

$T = 300$K	Pd in SPC water	Pd in BS water
D, 10^{-9} m^2/s	2.22	2.21
Relative STD	12.228 x 10^{-2}	8.733 x 10^{-2}
STD in D, 10^{-9} m^2/s	0.27	0.19
ln	-19.926	-19.930
Pressure, MPa	0	0

$T = 350$K	Pd in BS water
D, 10^{-9} m^2/s	3.41
Relative STD	4.108 x 10^{-2}
STD in D, 10^{-9} m^2/s	0.14
ln	-19.496

Pressure, MPa	60

$T = 400$K	Pd in SPC water	Pd in BS water
D, 10^{-9} m^2/s	5.19	4.70
Relative STD	6.119×10^{-2}	6.943×10^{-2}
STD in D, 10^{-9} m^2/s	0.32	0.33
ln D	-19.077	-19.176
Pressure, MPa	160	115

$T = 450$K	Pd in BS water
D, 10^{-9} m^2/s	6.01
Relative STD	5.205×10^{-2}
STD in D, 10^{-9} m^2/s	0.31
ln D	-18.930
Pressure, MPa	170

$T = 500$K	Pd in SPC water	Pd in BS water
D, 10^{-9} m^2/s	6.76	6.93
Relative STD	10.770×10^{-2}	7.391×10^{-2}
STD in D, 10^{-9} m^2/s	0.72	0.51
ln D	-18.812	-18.787
Pressure, MPa	350	220

$T = 550K$	Pd in BS water
D, 10^{-9} m^2/s	7.02
Relative STD	5.930 x 10^{-2}
STD in D, 10^{-9} m^2/s	0.42
ln	-18.774
Pressure, MPa	270

$T = 600K$	Pd in SPC water	Pd in BS water
D, 10^{-9} m^2/s	12.34	11.05
Relative STD	7.098 x 10^{-2}	8.154 x 10^{-2}
STD in D, 10^{-9} m^2/s	0.88	0.90
ln	-18.210	-18.321
Pressure, MPa	490	315
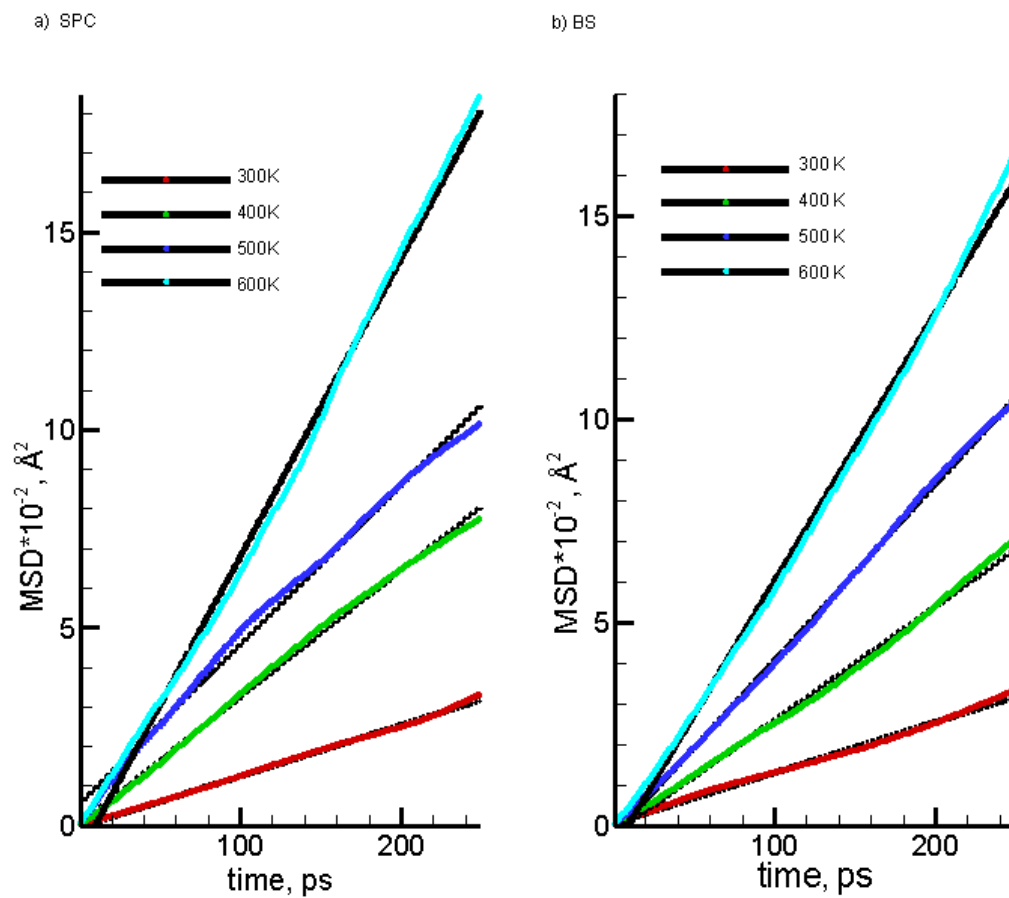
Figure 4.25   Mean square displacement of Pd atom at different temperatures in a) SPC water,

b) BS water. Black straight lines are linear fits.
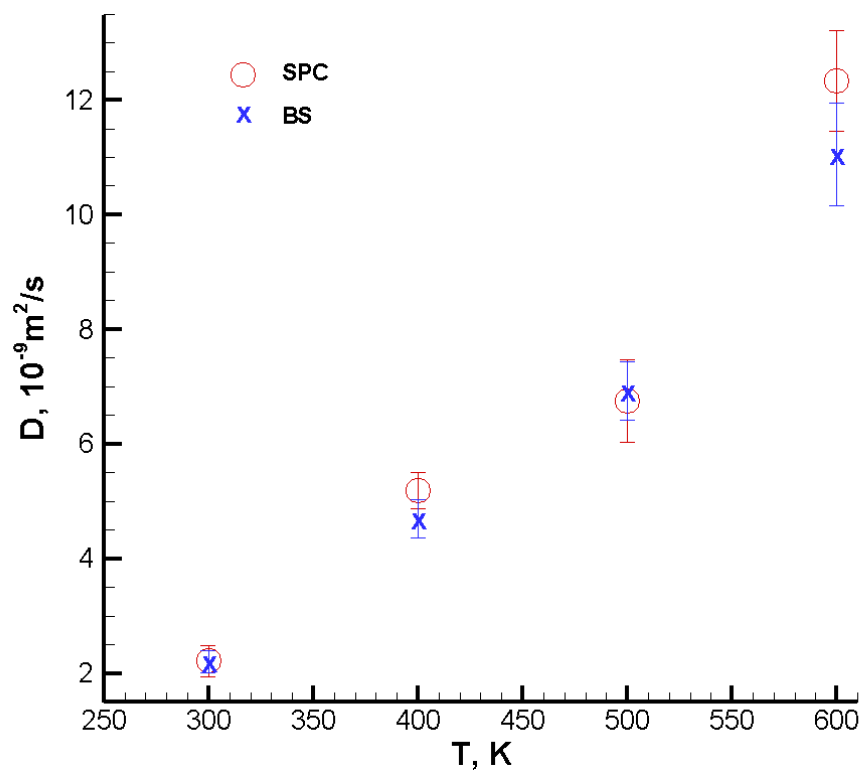
Figure 4.26 Temperature dependences of the diffusion coefficient of single Pd in water at 300

K. Vertical error bars are displayed on the values of the diffusion coefficient.

a)
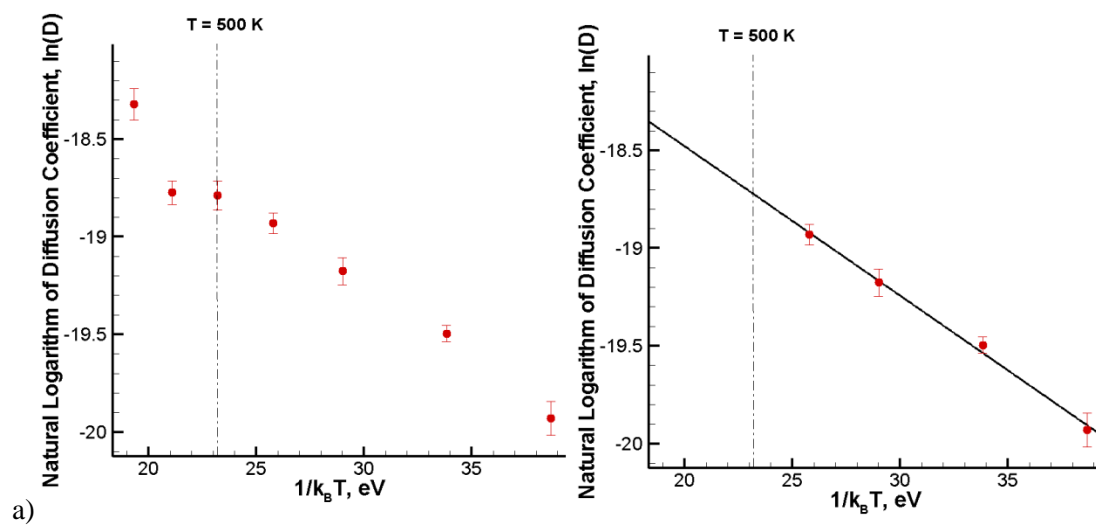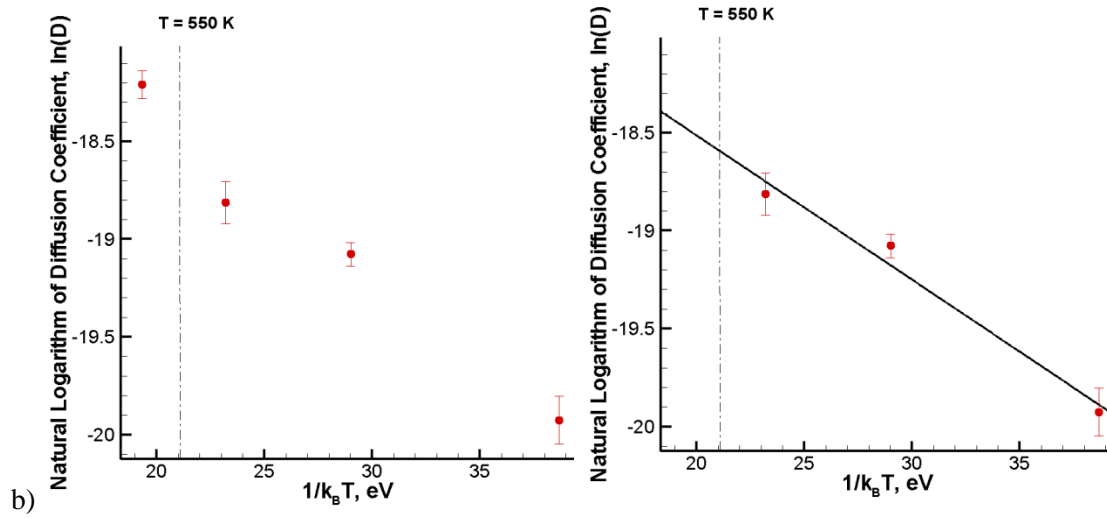
Figure 4.27. The dependence of the logarithm of the diffusion coefficient ($\ln D$) of a *NVT* ensemble of single Pd atom in water on the inverse of temperature, the right side of the figure displays a linear fit of the dependence at temperatures below the temperature for phase explosion: a) BS model, b) SPC model

4.6.1   The Fitting and Adjustment of Morse Potential Parameters

We make use of the assumption that the interface energy of Pd atom and surrounding water molecules should be the same in both atomistic and breathing sphere representations to derive an estimate for the well depth of the Morse potential $_e$. The value of   of single Pd atom is influenced by the radial distribution function of BS water molecules around the atom, $g_{Pd-BS}(r)$, and so $g_{Pd-BS}(r)$ is determined alongside D for varied Morse potential parameters. The resulting dependence between the Morse parameters and   is used to estimate values of β and r_e for a given value of $_e$. A fine adjustment about the estimated Morse potential parameters to determine a value of $D = 2.2\text{x}10^{-9}$ m^2/s results in the values: $_e = 0.15$ eV, $\beta = 1.0$ Å^{-1}, $r_e = 3.2$ Å.

4.6.1.1 Determination of an estimate for the parameter of the Morse potential D_e

For a metal atom surrounded by matrix molecules, we assume the interface energy to be the same for the BS model as it is for the atomistic model. For a dissociation energy of metal-matrix interaction, $_s$, and a number of matrix molecules, N_s, the interface energy can be defined as $E_{interf} = D_s \times N_s$. Maintaining the same interface energy for both models, we describe Eq. (4.41).

$$_s \times N_s = D_s^{BS} \times N_s^{BS} \tag{4.41}$$

For an average molecular separation, a, the number N_s is directly proportional to the square of the ratio of the radius of the interface, R, to the average molecular separation a, i.e.

$$N_s \propto \frac{R^2}{a^2}$$

The density ρ of a matrix of n moles in a given volume V is related to the atomic mass A_m:

$$\rho = \frac{n \times A_m}{V}$$

The volume V is directly proportional to the cube of the average molecular separation a, i.e.

$$V \propto N \times a^3$$

Expressing n in terms of the Avogadro number N_A as $n = N/N_A$, and inserting the above relation of V into the formula for density, ρ, we obtain the proportionality:

$$\rho \propto \frac{A_m}{a^3}$$

For the same densities of BS water and atomistic (SPC) water, which is true in our model, we have the proportionality:

$$a \propto M^{1/3}$$

after substituting $A_m = N_A \times M$, where M is the mass of a molecule.

Finally, making use of the above proportionality relations in Eq. (4.41), we obtain an equation that relates the dissociation energy of Pd – BS interaction to that of Pd – SPC water interaction:

$$D_s^{BS} = D_s \times \frac{a_{BS}^2}{a^2} = D_s \times \frac{M_{BS}^{2/3}}{M^{2/3}} \tag{4.42}$$

The dissociation energy in turn can be characterized by the well depth of the Morse potential – the parameter D_e. The relation is one of direct proportionality, and so substituting D_e for D_s in Eq. (4.42), we have Eq. (4.43), which determines the value of D_e for Pd – BS interaction from a known value of D_e for Pd – SPC water interaction.

$$D_e^{BS} = D_e \times \frac{M_{BS}^{2/3}}{M^{2/3}} \tag{4.43}$$

For known values of the mass of BS water molecule M_{BS}= 50 Da, the mass of SPC water molecule M = 18 Da, and D_e = 0.104 eV for Pd – SPC water interaction, a value of D_e^{BS} = 0.21 eV is obtained in Eq. (4.43).

4.6.1.2. *Radial distribution functions of BS water molecules around Pd atom: the effect on the diffusion coefficient*

Consider a system of two specie types, molecules of which are indexed i and j, respectively. A sketch of the system representation is shown in the left side of Figure 4.30. We wish to find an average density of particles j at a coordinate r relative to a particle i in the system.
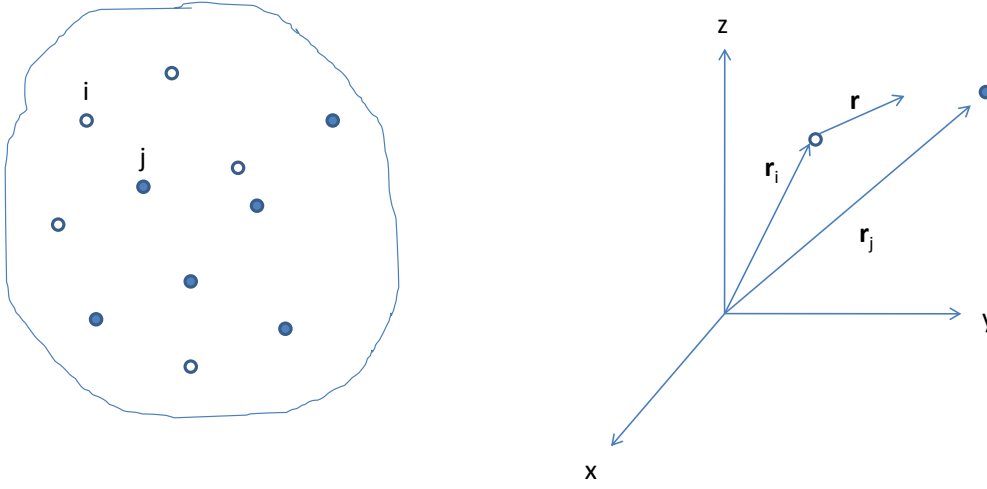
Figure 4.28 Sketch of coordinate representation of particles of two different types.

Let N_i be number of i particles and N_j be number of j particles. The distribution function, $f(\boldsymbol{r}')$, about the total system of particles in an arbitrary position $\boldsymbol{r}'$ can be written as:

$$f(\boldsymbol{r}') = \sum_{i=1}^{N_i} \delta(\boldsymbol{r}' - \boldsymbol{r}_i) + \sum_{j=1}^{N_j} \delta(\boldsymbol{r}' - \boldsymbol{r}_j) \qquad (4.44)$$

The distribution function in relation to particle i follows, for $\boldsymbol{r}' = \boldsymbol{r}_i + \boldsymbol{r}$ in Eq. (4.44):

$$f(\boldsymbol{r}_i + \boldsymbol{r}) = \sum_{i=1}^{N_i} \delta(\boldsymbol{r}) + \sum_{j=1}^{N_j} \delta(\boldsymbol{r}_i + \boldsymbol{r} - \boldsymbol{r}_j) \qquad (4.45)$$

In Eq. (4.45), $\boldsymbol{r} \neq 0$ so that $\delta(\boldsymbol{r}) = 0$, since $\boldsymbol{r}' \neq \boldsymbol{r}_i$. Also, denoting $\boldsymbol{r}_i - \boldsymbol{r}_j = \boldsymbol{r}_{ij}$, the distribution function in relation to particle i becomes:

$$f(\boldsymbol{r}_i + \boldsymbol{r}) = \sum_{j=1}^{N_j} \delta(\boldsymbol{r} - \boldsymbol{r}_{ij}) \qquad (4.46)$$

Averaging $f(\boldsymbol{r}_i + \boldsymbol{r})$ over N_i particles, we get the average distribution function in relation to i:

$$\langle f(\boldsymbol{r_i} + \boldsymbol{r}) \rangle = \frac{1}{N_i} \sum_{i=1}^{N_i} \sum_{j=1}^{N_j} \delta(\boldsymbol{r} - \boldsymbol{r}_{ij}) \tag{4.47}$$

Summing the average distribution function over all angles at $\boldsymbol{r}$, we obtain the function $p(r)$:

$$p(r) = \int r^2 \, d\Omega \, \langle f(\boldsymbol{r_i} + \boldsymbol{r}) \rangle \tag{4.48}$$

Using the relation $\int r^2 \, d\Omega \, \delta(\boldsymbol{r} - \boldsymbol{r}') = \delta(r - r')$, we obtain

$$p(r) = \frac{1}{N_i} \sum_{i=1}^{N_i} \sum_{j=1}^{N_j} \delta(r - r_{ij}) \tag{4.49}$$

Assume for a small enough change in r, Δr, the density of particles is fixed. Then the density

distribution function is related to the function $p(r)$ through Eq. (4.50).

$$\rho(r, \Delta r) = \frac{\int_r^{r+\Delta r} dr \, p(r)}{4\pi r^2 \Delta r} = \frac{\int_r^{r+\Delta r} \frac{1}{N_i} \sum_{i=1}^{N_i} \sum_{j=1}^{N_j} \delta(r - r_{ij})}{4\pi r^2 \Delta r} \tag{4.50}$$

Let ρ_0 be the density of j particles in areas that are far beyond the zone of interaction between i

and j particles. We derive the relative density distribution function, $\tilde{\rho}(r, \Delta r) = \rho(r, \Delta r)/\rho_o$.

The relative density distribution function is called the *radial distribution function (rdf)* in relation

to a particle indexed by i.

$$\tilde{\rho}(r, \Delta r) = \frac{\int_r^{r+\Delta r} \frac{1}{N_i} \sum_{i=1}^{N_i} \sum_{j=1}^{N_j} \delta(r - r_{ij})}{4\pi \rho_o r^2 \Delta r} \tag{4.51}$$

In our case, Pd atom relates to the particle indexed by i, and the BS water molecules relate to the

particles indexed by j.

The diffusion coefficient of single Pd atom in BS water is determined for a set of Morse

parameters altered by one parameter from a given set of parameters: $D_e = 0.15$ eV; $\beta = 1.0$ Å^{-1}; r_e

= 3.2 Å. The altered Morse parameter is indicated in Table 4.7. The radial distribution functions $g_{Pd-BS}(r)$ for the different parameter sets are plotted, see Figure 4.29, and analysed.

Studying the diagrams in Figure 4.29, it can be easily noticed that a higher peak in the radial distribution function reduces the diffusion coefficient of Pd atom, suggesting that a higher density of molecules slows down the diffusing atom.

Increasing the potential depth D_e increases the peak of the radial distribution function, and reduces the diffusion coefficient of Pd atom.

Increasing the equilibrium separation r_e inevitably shifts the peak of the radial distribution function to the right – away from the centre of Pd atom. This has the effect of reducing the diffusion coefficient of Pd atom. This can be explained by a bigger diffusion size of Pd atom as the peak of the radial distribution function shifts to the right.

A longer potential range, meaning a smaller value of β, is seen to reduce the peak of the radial distribution function. This may be due to a more sparse distribution of BS molecules. A lower value of diffusion coefficient is observed with a higher peak of the radial distribution function, as the range of the potential is made shorter.

Table 4.7. Variation in diffusion coefficient of Pd atom in BS water as a function of altering one of the Morse potential parameters.

Morse parameter	$D_e = 0.11$ eV	$D_e = 0.13$ eV	$D_e = 0.17$ eV	$D_e = 0.19$ eV
D, 10^{-9} m^2/s	2.53	2.37	2.02	1.75
Relative STD	5.960 x 10^{-2}	6.039 x 10^{-2}	8.093 x 10^{-2}	4.235 x 10^{-2}
STD in D, 10^{-9} m^2/s	0.15	0.14	0.16	0.07

Morse parameter	$r_e = 2.8$ Å	$r_e = 3.0$ Å	$r_e = 3.4$ Å	$r_e = 3.6$ Å
D, 10^{-9} m^2/s	2.83	2.71	1.74	1.57
Relative STD	6.933 x 10^{-2}	4.165 x 10^{-2}	5.336 x 10^{-2}	7.591 x 10^{-2}
STD in D, 10^{-9} m^2/s	0.20	0.11	0.09	0.12

Morse parameter	$r_e = 2.8$ Å	$r_e = 3.0$ Å	$r_e = 3.4$ Å	$r_e = 3.6$ Å
D, 10^{-9} m^2/s	2.83	2.71	1.74	1.57
Relative STD	6.933 x 10^{-2}	4.165 x 10^{-2}	5.336 x 10^{-2}	7.591 x 10^{-2}
STD in D, 10^{-9} m^2/s	0.20	0.11	0.09	0.12

a)

b)

c)

Figure 4.29 A display of quantities of interaction between Pd and BS water as the parameters of the Morse interaction potential are varied: upper left – Morse potential; upper right – radial distribution function of BS water molecules around Pd atom; lower left – mean square displacement (MSD) of Pd atom in BS water; lower right – diffusion coefficient of Pd atom in BS water. a) The depth of the Morse potential D_e is varied, b) the equilibrium separation r_e is varied, c) the range of the potential is varied by changing β.

4.7   Laser Absorption of Target

In this sub-section we describe the mechanism of photon absorption by the absorbing particles of the medium – the precursor molecules PdAc, and the Pd atoms and clusters. The mechanism of absorption determines the quantity and mode of absorbed energy. The absorption cross-sections of prevailing molecules and particles in the irradiation medium are determined. Beer's law is described for the multicomponent system of precursor molecules and its fragmentation products. A simulation is run specifically to test the absorption model by verifying Beer's law for the system, and the result of the simulation is discussed in appendix C2.

4.7.1   Mechanism of Photon Absorption by Palladium Acetate Molecule

On absorption of a UV photon, the fragmentation of PdAc molecule can be described by a photochemical equation:

$$Pd(Ac)_2 \xrightarrow{h\nu} Pd + 2Ac + \Delta h_{rxn} \tag{4.52}$$
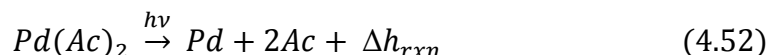
where Δh_{rxn} is the heat of the decomposition reaction of the molecule. In the actual reaction, the acetate ligand decomposes, and among the products are mainly CO_2, H_2O, and radical species (CH_3COO^+, CH_3CO^+, CH_3C^+, CH_3^+). The radical species can be viewed as decomposition fragments of ketones. The latter have absorption cross-sections $\sim 10^{-4}$ $\mathring{A}^2$ [161], which are negligible in comparison to cross-sections of other molecules and atoms considered here. The absorption of other main decomposition products of the acetate ligand, CO_2 [162], and H_2O, is also negligible. So, the total absorption cross-section of the decomposition products of the acetate ligand is set to zero in this model, and all the products are represented by a single BS molecule – the Ac molecule.

In many of the described photochemical reactions, one may possibly project the existence of a Pd^{2+} ion at a preliminary decomposition phase; however, dissociation of the acetate ligand into radicals and molecules is by electron transfer processes, possibly requiring transfer of electrons to reduce Pd^{2+} ion to Pd atom. As an example, it is illustrated in Ref. [116] that the dissociation of CH_3COO^- into CH_3^+ and CO_2 is an oxidative process, requiring the donation of two electrons by the reactants, to form CO_2 from C=O and O^{2-}; release of CO_2 as a major decomposition product provides more support to the reduction hypothesis. Practical observation of the formation of uncharged ultrathin Pd layers in ultra-high vacuum conditions after ejection of volatile species should ascertain that nucleation occurs from a neutral state of Pd atoms. Also, UV excimer laser irradiation of a frozen solution of low %wt. PdAc in weakly absorbing chloroform matrix [46] predicts the release of free $Pd^{(0)}$ metal atoms from precursor decomposition. In a computational model, it would therefore be assumed that Pd atom is neutral.

The change in chemical energy (Δh_{rxn}) is a negative change in mechanical energy, so that the equation of the decomposition reaction in terms of heat flow can be written as:

$$Pd(Ac)_2 \xrightarrow{h\nu} Pd + 2Ac + \Delta q \qquad (4.53)$$
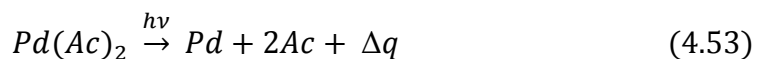
where $\Delta q = -\Delta h_{rxn} + h\nu$ is the heat released by the decomposition reaction, accounting that the absorbed photon energy is thermally relaxed. In experiment, the reaction enthalpy per mole has been measured to be 440 kJ/mol [113], corresponding to $\Delta h = 4.57$ eV – this implies an endothermic reaction. At a wavelength of 248 nm, $h\nu = 5.0$ eV, so that Δq equals 0.43 eV.

The apparition of new fragments changes the local potential energy by some amount, ΔU, so that to conserve mechanical energy, the change in kinetic energy of the products from that of reactants equals $\Delta K = \Delta q - \Delta U$. Momentum conservation is applicable to the motion of the centre of masses of the atoms and molecules in the reaction, implying zero change in the kinetic

energy of the centre of masses. The change in kinetic energy, ΔK, is therefore assigned to kinetic energies of internal modes. As constant heat capacities (temperature-independent) are used in the model, the internal temperatures of the reactant and products at fragmentation are thus defined:

$$T_{Ac}^{int} = \frac{C_{PdAc}^{int} T_{PdAc}^{int} + \Delta q - \Delta U}{2 C_{Ac}^{int}} \tag{4.54}$$

where C_{PdAc}^{int} and C_{Ac}^{int} are the heat capacities of PdAc and Ac respectively; and T_{PdAc}^{int} and T_{Ac}^{int} are the internal temperatures of PdAc and Ac respectively.

The fragments are positioned according to two disintegration rules, derived from Ref. [96].

1. The distance of a fragment away from the parent molecule is inversely proportional to the mass of the fragment.

2. The fragments are separated from each other by the Van der Waals radius of the parent molecule.

Fragmentation of PdAc yields three fragments: Pd atom and two acetate (Ac) breathing sphere molecules. The three fragments should be positioned at the vertices of an equilateral triangle according to the second rule. The length of the equilateral triangle is the Van der Waals radius of PdAc intermolecular interaction. The Van der Waals radius r_o of PdAc intermolecular interaction is half the equilibrium separation, r_{eq} between the centres of PdAc molecules:

$$r_o = \frac{r_{eq}}{2}$$

The positions of the parent molecule and the fragment molecules can be represented in a 3D coordinate axis system (x', y', z') such that all the particles are viewed in the (y', z') plane, see Figure 4.30. The parent molecule is located at the origin of the (x', y', z') coordinate system. This coordinate system orientationally differs from the coordinate axis sytem of the simulation system.

In relation to Figure 4.32, let's define the following variables:

- r_{Pd} is the distance of Pd atom away from PdAc (the origin).

- r_{Ac} is the distance of Ac ligand away from PdAc .

- r_o is the length of side of the equilateral triangle formed by Pd and the two Ac ligands.

- r_{bi} is the distance from Pd atom to the midpoint of line segment connecting two Ac ligands.

- m_{PdAc} , m_{Pd} and m_{Ac} are the masses of PdAc molecule, Pd atom and Ac ligand respectively.

- Additionally define the ratio of m_{Pd} to m_{Ac} as m_{rel} .

- The angles α and β are defined on the figure and a summed angle can be denoted: $\gamma = \alpha + \beta$
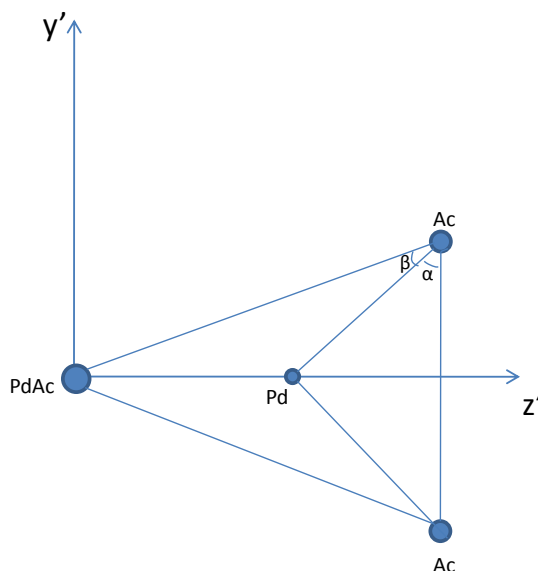
Figure 4.30 Positions of parent precursor molecule and its decomposition fragments. The x′ axis is directed perpendicularly into the paper.

The following geometric relations from Fig. 4.30 can be expressed:

$$r_{bi} = r_o \cos\left(\frac{\alpha}{2}\right); \; \sin(\gamma) = \frac{r_{bi} + r_{Pd}}{r_{Ac}}; \; \cos(\gamma) = \frac{r_o}{2 r_{Ac}} \tag{4.55}$$

Also, the angle $\alpha = \pi/3$ for an equilateral triangle, so that

$$r_{bi} = r_o \sqrt{3}/2 \tag{4.56}$$

From the first disintegration rule, m_{Pd} and m_{Ac} can be related as

$$r_{Ac} = \frac{m_{Pd}r_{Pd}}{m_{Ac}} = m_{rel}r_{Pd} \tag{4.57}$$

Implementing into the trigonometric identity

$$sin^2\gamma + cos^2\gamma = 1$$

substitutions for r_{bi}, as in Eq. (4.56), and r_{Ac}, as in Eq. (4.57), we obtain the following quadratic equation in r_{Pd}:

$$\left(1 - m_{rel}^2\right)r_{Pd}^2 + \sqrt{3}\, r_o r_{Pd} + r_o^2 = 0 \tag{4.58}$$

The solution to Eq. (4.58) is:

$$r_{Pd} = \frac{r_o(-\sqrt{3} \mp \sqrt{4m_{rel}^2 - 1})}{2(1 - m_{rel}^2)} \tag{4.59}$$

But $m_{rel} > 1$ so that for $r_{Pd} > 0$, a true solution pertains only to the minus sign (-) in the numerator of the right hand side of Eq. (4.59).

Implementing the values of m_{Pd}, m_{Ac} and r_o into Eq. (4.59) as: $m_{Pd} = 106.42$ a.m.u; $m_{Ac} = 59.04$ a.m.u and $r_o = 3.13$ Å as half the equilibrium separation of centres of PdAc molecules, we obtain

$$m_{rel} = 1.8025; \; r_{Pd} = 1.155 \times r_o = 3.615 \text{ Å}$$

Implementing the obtained value of r_{Pd} in Eq. (4.57), a value of r_{Ac} is obtained:

$$r_{Ac} = 1.8025 \times r_{Pd} = 2.082 \times r_o = 6.517 \text{ Å}$$

Substitute obtained values of r_{Ac}, r_{Pd} and r_o into Eq. (4.55) to obtain values for $\sin(\gamma)$ and $\cos(\gamma)$: $\sin\gamma = 0.97075$; $\cos\gamma = 0.24017$. The trigonometric identity $sin^2\gamma + cos^2\gamma = 1$ is verified to be correct with the obtained values.

Consider the case in which the fragmentation plane is always perpendicular to the x-axis of the simulation system. The unit vector e_z' is oriented to the unit vector e_z of the simulation system by an angle θ, where $\theta \in [0, \pi]$. The unit vectors in the fragmentation plane can be related to the simulation system unit vectors:

$$\begin{pmatrix} e_x' \\ e_y' \\ e_z' \end{pmatrix} = \begin{pmatrix} 1 & 0 & 0 \\ 0 & \cos\theta & -\sin\theta \\ 0 & \sin\theta & \cos\theta \end{pmatrix} \begin{pmatrix} e_x \\ e_y \\ e_z \end{pmatrix} \tag{4.60}$$

We have determined the amount of heat flow, and in what mode energy is deposited into the system as a result of the photofragmentation of the metalorganic precursor PdAc. The positions of the fragments have been determined in relation to the parent precursor molecule.

4.7.2. Absorption of Palladium Clusters and Atoms

The absorption of Pd atom as a single atom, as well as an atom in a cluster of Pd atoms, at the irradiation wavelength of 248 nm is described here. Because absorption is size-dependent, discussing the size of clusters of Pd that are experimentally observed in solution is deemed relevant. A literature survey has been made on: the nucleation and growth of Pd clusters, and the size distribution of Pd clusters and nanoparticles in solvents. A review is written here on the subject. Conclusions made in the review are that: i) Pd clusters tend to grow in solution to nanoparticles of size mostly about 2 nm; ii) narrow size distributions have been observed in colloidal solutions. There are cases when nanoparticles of size up to ~ 20 nm are observed, but

closer experimental observation (high resolution TEM) has shown that these are actually aggregates of individual clusters of size 2.1 nm.

The absorption of Pd atom in clusters of sizes typically observed in experiment is described, by Mie theory as it is applicable to absorption in the depicted size range. The absorption of single Pd atom is described as well. Because of the relative inaccessibility in determining the absorption of Pd clusters that are smaller than 1 nm in size, as Mie theory is not applicable to the description of their absorption, an approximation, based on the knowledge of single atom absorption and cluster absorption described by Mie theory, is made to determine absorption in the given size range.

4.7.2.1. *Nucleation and growth of metallic clusters: A review, with special attention to Palladium*

Nucleation and growth of clusters is a subject of important study in relation to the formation of metallic clusters of different shapes and, of particular interest to this review, sizes. In this review a survey of popular mechanisms (or theories) that describe the formation or the stability of a nucleus is made. The seeding of nuclei and their subsequent growth, in solution, into nanocrystals of differing shapes is discussed.

The effect of nucleation and growth rates on cluster size distributions is examined. Because most investigations on size distribution have been done for colloidal solutions, the examples drawn are on colloidal preparation experiments. Here, an insight into the roles of the solvent, reducing agents, and stabilizing agents is made.

Techniques that observe size distributions of clusters during their formation, or after their formation are briefly described.

4.7.2.1.1 *Nucleation theories, hypotheses and mechanisms*

The starting point of nucleation and growth studies is classical nucleation theory (CNT). CNT initially pioneered by Volmer and Doring, uses the Gibbs capillary approximation which treats the nucleus as a bulk phase although, rigourously, it is not [163]. According to CNT, the free energy of nucleus formation contains two competing terms: one negative, for the favorable formation of bonds in the nucleus, and one positive, for the unfavorable formation of an interface between the nucleus in its new phase and the matter in its old phase. In terms of cluster radius, the Gibbs free energy is

$$\Delta G = -\frac{4}{3}\pi r^3 |\Delta G_V| + 4\pi r^2 \gamma \tag{4.61}$$

Eq. (4.61) assumes a spherical nucleus, as this shape minimizes the surface area of the nucleus. Here, r is the cluster radius, ΔG_V is the difference in bulk free energy per volume between the old and new phases, and γ is the surface free energy per unit area. In a solution, the cluster free energy can be expressed as a function of the number of atoms in the cluster and the solubility of the cluster specie [164], as in Eq. (4.62):

$$\Delta G = -n k_B T \ln\left(\frac{x}{x^{sat}}\right) + \sigma b n^{\frac{2}{3}} \tag{4.62}$$

where n is the number of atoms in the cluster, k_B is the Boltzmann constant, T is the temperature, σ is the surface tension of the cluster, b is a geometric factor, and the quantity x/x^{sat} is called the supersaturation, in which x is the mole fraction of the species present in solution, and x^{sat} is the mole fraction of the species present in a saturated solution. In Eq. (4.62), the supersaturation can be equivalently expressed in terms of concentration, and becomes C/C_{eq}, where C_{eq} is the solubility (the equilibrium concentration) of the species.

The cluster free energy has a maximum at some size of the nucleus, called the *critical size*. The critical size can be found by differentiating ΔG with respect to the size parameter, r in Eq.

(4.61) or n in Eq. (4.62), and finding the maximum. The dependence of free energy of a cluster as a function of the radius, based on CNT can be found in Ref. [163].

Because CNT treats nuclei as bulk material having macroscopic properties [164], the surface free energy of the cluster is the same as that of an infinite planar surface, leading to limitations in predicting properties of nuclei: failure to account for stress that exists within crystal nuclei arising from the formation of a surface results in poor prediction of the structure of the nuclei; accurate definitions and values of the constant γ are unavailable for small nuclei vs bulk material.

In experiment, the nucleation rate is frequently measured. It can be expressed as

$$I = \Gamma \exp\left[-\frac{16\pi}{3k_B T}\frac{\gamma^3}{(\rho_S|\Delta\mu|)^2}\right] \tag{4.63}$$

where ρ_S is the number density of the solid, γ is the solid-liquid interfacial free energy density, $\Delta\mu$ is the change in chemical potential between the solid and the liquid phases, and $\Gamma = \sum Z \rho_l f_c^+$ [163]. In this last expression, Z is the Zeldovich factor, $\sqrt{|\Delta\mu|/6\pi k_B T n_c}$, where n_c is the number of particles in the critical nucleus and f_c^+ is the attachment rate of particles to the cluster, which is given by $f_c^+ = 24 D_S n_c^{2/3}/\lambda^2$, D_S being a self-diffusion coefficient and λ a diffusion distance. A simpler expression for the nucleation rate is given in Eq. (4.64): B is a collection of terms described above, and ΔG^* is the activation energy for nucleation.

$$J = B\exp\left(-\frac{\Delta G^*}{RT}\right); \quad \Delta G^* = \frac{16\pi r^3 V_m^2}{3|\Delta\mu|^2} \tag{4.64}$$

In addition to predictions on the stability of a cluster beyond a critical size, it is important to take into account the possibility of survival of a metal cluster in dependence of its temperature. The melting point of a solid element in a classical sense is a constant; this is not the case on the nanoscale. For instance, the melting point of gold is 1064 °C; but, gold nanoparticles below ca.

20 nm in diameter begin slowly to melt at lower temperatures. The melting point drastically falls down at a size of 3-4 nm, reaching ca. 500 °C at 1.5 nm [165]. The change in melting temperature is explained by the fact that the percentage of surface atoms becomes larger the smaller the particles become. Assuming a spherical cluster, the fraction of atoms at the surface scales as $N^{-1/3}$ [166]. This scaling law translates to the scaling in cohesive energy, E_{coh}, of the cluster: $E_{coh} \sim N^{-1/3}$, as can be seen for Mg clusters. However, atoms at the surface are of lower cohesive energy than those in the interior as they have a lower coordination number. The melting point of a nanoparticle is related to its radius by the Gibbs-Thomson equation in Eq. (4.65), the relation having been originally described by Thomson in 1871 [167].

$$\frac{T_m - T_m^*}{T_m^*} = -\frac{2V_m(l)\gamma_{sl}}{\Delta H_m r} \tag{4.65}$$

In this equation, T_m is the melting point of the cluster with radius r, T_m^* that of the bulk, $V_m(l)$ the molar volume of the liquid, γ_{sl}, the interfacial tension between the solid and the liquid surface layer, and ΔH_m the bulk latent heat of melting. In terms of free energy, the Gibbs-Thompson relation, formulated in Eq. (4.66), states that the partial molar free energy of a metal atom in a particle of radius R, $\mu(R)$, differs from that in the bulk, $\mu(\infty)$, as a function of the surface free energy of that same metal, γ, and the volume per metal atom of the bulk metal, Ω [163].

$$\mu(R) - \mu(\infty) = \frac{2\gamma\Omega}{R} \tag{4.66}$$

A hypothesis, for transition-metal nanoclusters, has been put forth that the size of the critical nucleus is dependent on the strength of the M-M (metal-metal) bonds. Since a metal's heat of vaporization, ΔH_{vap}, is a measure of the M-M bond strength, a correlation between a metal's ΔH_{vap} and the size of the metal nanocluster is suggested, and investigated in Ref. [163]. It is

expected that a metal with higher M-M bond strength, as reflected by a higher value of ΔH_{vap}, should favor nucleation over growth and result in smaller nanoclusters. Conversely, a metal with lower M-M bond strength and therefore lower ΔH_{vap} should favor growth over nucleation, resulting in larger nanoclusters. This hypothesis has been supported in the rough reproducibility of the expected correlations between ΔH_{vap} and nanocluster size, obtained by: i) analyzing Hirai's transition-metal nanocluster data [168] for six different metals; and ii) analyzing Bonnemann's transition-metal nanocluster data [169] for the preparation of nanoclusters in tetrahydrofuran (THF) and toluene. The analyses have shown that Pd, having a lower ΔH_{vap} than that of Rh, Pt, Ir, Os, and Ru, has larger cluster size than any of the named metals in the same solution and reaction conditions.

The properties of nanocrystals are shape-sensitive, as the shape determines the crystallographic facets exposed on the surface of a nanocrystal and therefore the number of atoms located at the edges or corners [170,171]. As an example, calculations based on the discrete dipole approximation (DDA) method have demonstrated that the resonance peaks of Pd nanostructures can be tuned from the ultraviolet (330 nm) to the visible (530 nm) region simply by tailoring their shape from cubic to icosahedral and then to triangular thin plates [172]. In order to understand why a nanocrystal takes on a given shape, the evolutionary stages – from nucleation to subsequent growth into the nanocrystal – determining the final shape of the nanocrystal have to be scoped. An important phase of this evolution is the formation of a seed. A seed is defined as a nucleus with well-defined crystallinity (having stable crystallographic facets). Possible cluster shapes of a seed are determined by growth rates along [111], [100], and [110] crystallographic directions [170]. The shape of a seed is mostly determined by surface energy minimization. The surface energies of the different crystallographic facets increase in the

order $\gamma_{\{111\}} < \gamma_{\{100\}} < \gamma_{\{110\}}$ [173]; this order can be changed by using impurities or capping agents [170]. The shape and size of Pd nanostructures have been controlled in solution using Na_2PdCl_4 as a precursor to Pd. In a reaction, $[PdCl_4]^{2-}$ ions are reduced to zero-valent Pd atoms, which aggregate to form nuclei (or clusters). As dictated by thermodynamics, the Pd atoms in the vacuum are expected to nucleate and grow into cuboctahedral or quasi-spherical seeds enclosed by a mix of both {111} and {100} facets to minimize the total surface energy [174]. However, in the solution phase, a twin defect—a single atomic layer in the form of a mirror (111) plane— may also be formed in the seed, and the extra strain energy caused by twinning compensated for by maximizing the surface coverage with {111} facets for achieving the lowest surface energy possible [175]. Twinned seeds also have a nearly spherical profile and, consequently, small surface area to maintain a low surface energy. Combined, the seed may take a single-crystal, single-twinned, or multiple-twinned structure. After nucleation, each type of seed can grow into a nanocrystal with several possible shapes: single-crystal seeds evolve into cuboctahedrons, single-twinned seeds assume close to spherical shapes, and multiple-twinned seeds grow into icosahedrons and decahedrons [170]. Simulations have shown that icosahedral, decahedral, and cuboctahedral seeds are favored for Pd at small (with the number of atoms $N<309$), medium ($309<N<561$), and large sizes ($N>561$), respectively [176]. According to theoretical analyses, as multiple twinned seeds grow in size rapidly, the low surface energy of {111} facets can no longer compensate for the excessive strain energy, resulting in their evolution into single-crystal cuboctahedrons [177]. This means, to obtain high yields of multiple-twinned seeds, one has to keep them at small sizes: in particular, the windows of favored sizes for both icosahedral and decahedral Pd are quite narrow, as compared with other metals such as Ag [176]. Theoretical predictions have been in close agreement with experiment: the crystallinity of a seed has mainly

been determined by the reduction rate, which is critical to the size growth of seeds. When the reduction of Pd precursor and the generation of Pd atoms are extremely fast, most seeds become single crystals due to their rapidly increased sizes; as the reduction is substantially slowed down, the multiple-twinned seeds can be kept at small sizes for a long period of time owing to the slow addition of atoms [170]. Multiple-twinned seeds can be formed at high yields in a slow reaction, as has been in the case of using a mild reducing agent such as citric acid or ascorbic acid (rather than ethylene glycol) to promote the formation of twinned seeds [170].

As a result of anisotropic growth, cuboctahedral seeds may evolve into octagonal rods and rectangular bars, respectively [178] When the seeds are multiple twinned, they will evolve into icosahedrons, decahedrons, or five-fold twinned rods, depending on whether or not the side {100} surface can be stabilized [179, 180]. Single twinned seeds can grow into right bipyramids, a structure that consists of two right tetrahedrons symmetrically placed base-to-base, with the {100} surface stabilized [180]. Seeds with stacking faults will evolve into thin plates whose top and bottom faces are {111} facets and side surface is enclosed by a mix of {100} and {111} facets [181].

In relation to experiments carried out for the formation of metallic clusters in solutions, plausible mechanisms that describe the nucleation and growth of metallic clusters from single atoms in solution are of vital interest. LaMer's mechanism, the most famous and widely cited work in application to nucleation theory [182, 183], first used CNT to describe the formation of sulfur sols from the decomposition of sodium thiosulfate in hydrochloric acid in the 1950s. His model describes the concentration of nucleating species (sulfur in this case) versus time: the concentration of elemental sulfur builds up slowly until some critical concentration is reached, or more specifically a critical supersaturation level, C/C_{eq} where C_{eq} is the solubility of sulfur in

the solution [163]. At the supersaturation level, homogeneous nucleation occurs at a rate that is described as "effectively infinite"; this is otherwise described as "burst" nucleation. The burst of nucleation lowers the supersaturation level of monomers in the solution; as a result, nucleation essentially stops at this time. Growth then follows by diffusion of sulfur atoms throughout the solution. While LaMer's mechanism has been suitable to the specific system of *sulfur sol formation*, it is not expected to be the mechanism by which transition-metal nanoclusters nucleate and grow from dilute solutions [163]. It has still nonetheless been applied to transition-metal nanocluster preparations [184], and has been the only available mechanism for almost 50 years as pointed out by Finke and Watzky [185].

4.7.2.1.2   *Growth and size distribution of clusters*

Due to the high sensitivity of optical, electronic, and catalytic properties to size and shape [186] of transition-metal nanoclusters, the ability to prepare nanoclusters with narrow size distributions ("near-monodisperse" nanoclusters of $\leq \pm 15\%$ [187]), to allow for greater uniformity of nanocluster properties, is of emerging importance.

It has been widely accepted in literature that the final size of a cluster is determined by the relative rates of nucleation and growth [188, 189]. The kinetics of particle formation has been followed by UV-vis spectroscopy in several investigations, and a number of analytical measurements have been carried out to determine the size of nanoparticles during growth. In the study [190] of formation of Ag nanoparticles stabilized by hexanethiol, the characteristic absorption peak of silver was first shifted towards lower wavelengths and later, as the reaction progressed, towards higher wavelengths. Since larger particles absorb more at higher wavelengths in the UV-visible region, it was deduced from these observations that in the first part of the reaction large particles were formed, which later fell apart to give rise to smaller ones,

which then later started to grow. The homogeneous nucleation, without stabilizer (without PVP), of palladium particles was studied by observing changes in the spectrum of the system every 1-2 s for 10 minutes [188]. The reduction of palladium chloride is completed instantaneously, as the absorbance spectrum hardly shows any change after 1 s: absorbance at wavelengths above 250 nm is significantly increased, indicating the formation of relatively large palladium particles within this period. Since there is no peak characteristic of palladium nanoparticles, their formation can be monitored by following the increase in absorbance at higher wavelengths: the increase in absorbance indicates an increase in the number and size of the particles formed. The rise in absorbance at 600 nm wavelength is fast within ~ 2 s, after which it slows down and is very gradual after ~ 10 s. Although this dependence does not allow differentiation of nucleation and nucleus growth, the rate of particle formation can be characterized by the slope of the initial rising section of the absorbance *versus* time function, which is termed the apparent kinetic constant (k^*), and is determined therein to be $k^* = 0.098$ s^{-1}. The slope of straight lines obtained by linearization of UV-VIS absorption spectra should decrease with increasing particle size. By employing a fitting procedure used by Furlong et. al [191] for the size determination of colloidal Pt sols, the sizes of particles formed were determined: the size of particles formed in the absence of stabilizer 60 s after reduction is 7.3 nm. TEM images show 6-20 nm aggregates consisting of individual particles with an average diameter of $d_{ave} = 2.1$ nm [188].

In an autocatalytic reaction pathway, growth is by adsorption of metal ions and their subsequent reduction on the surface of the zero-valent metal ions – such growth has been monitored by Heinglein [192], for Ag clusters.

Monodispersity is a consequence of completing the nucleation stage for the clusters before the growth stage begins. Because of the high importance to achieve monodisperse samples, need has

arisen to study the effects of highly influential factors on the nucleation and growth of metal clusters. The factors in concern are: the concentration of the precursor to metal clusters; the strength and concentration of the reducing agent; the temperature of the growth conditions; and the role of a stabilizing agent. It is necessary, and of ongoing importance, to look into the roles of: the solvent, reducing agents, the precursor concentration, and stabilizing agents in the rates of nucleation and growth in determining the dispersities of nanocrystals. It also turns out that nanocrystals of certain nuclearities tend to preferentially stabilize [193], thus playing a siginificant role in size distribution [194, 195]. Such nanocrystals are termed 'magic nuclearity' nanocrystals, and have 'magic numbers' of atoms. The magic numbers correspond to atoms filling up the coordination shells completely around a central atom in a closed packed shell, the nuclearities 13, 55, 309, 561 and 1415, corresponding to closure of one, two, four, five and seven shells, repectively, for the case of Pd [193]. The stability of clusters with a magic number of atoms in relation to clusters with other nuclearities has been revealed by cluster beam studies [196]. Reduction of K_2PdCl_4 by sodium borohydride has yielded Pd nanoclusters of average size 2.58 nm $\pm$ 23% for low concentration and 3.2 nm $\pm$ 14% for high concentration of K_2PdCl_4 [197] The sizes have been assigned to magic nuclearity clusters Pd_{561} and Pd_{1415}, respectively [198]. Polyvinylpyrolidone (PVP) capped Pd_{561} nanoparticles (size of 2.5 nm) have been obtained with a diameter distribution of < 4% [199]. When monodisperse Pd_{561}-PVP nanocrystals were allowed to stand in an aqueous medium, they aggregated into larger-size nanoparticles (giant clusters) of sizes 9.6, 15.6, 21.6, 33.8 nm [200]. The nuclearity of the giant clusters turn out to be magic numbers of nanocrystals: 13, 55, 147 and 561 [193]. Two-dimensional arrays have been obtained from magic nuclearity Pd_{561} and Pd_{1415} capped with alkanethiols (dodecanethiol and octanethiol) [201]. Large polydispersities in size prevents

formation of nanoparticle arrays [202, 203]. The mean size of Pd nanoparticles has increased from below 5 nm to above 5 nm when the concentration of $Pd(OAc)_2$, a precursor to Pd, increased 5 times; here, polyethylene (glycol) was used as a reducing agent and stabilizer [204].

From experimental preparations that have employed sodium borohydride ($NaBH_4$) [205], superhydride (1.0 M solution of lithium triethylborohydride in tetrahydrofuran) [206], lithium aluminum hydride, and lithium borohydride [202] as reducing agents for the reduction of potassium tetrachloropalladate(II) (K_2PdCl_4), it has been observed that stronger reducing agents favor smaller nanocluster formation. In addition, as the reducing agents were changed from $NaBH_4$ and hydrazine(N_2H_4) to sodium hypophosphite (NaH_2PO_2), it was observed that a much narrower size distribution was attained without changing the mean size. This could be explained by NaH_2PO_2 being a weaker reducing agent than sodium borohydride and hydrazine. Stronger reducing agents should favor the formation of smaller nanoclusters as the density of produced nucleation sites is higher [202]. Hoogsteen and Fokkink [207], after the preparation of polymer-stabilized Pd hydrosols using hypophosphorous acid (H_3PO_2) as reducing agent, established that particle size decreases with increasing the concentrations of the stabilizing polymer and the reducing agent. Esumi et al. [208] prepared Pd organosols stabilized by polyvinyl pyrrolidone (PVP) from various precursor molecules by ethanol reduction. Particles generated by reduction of $Pd(OAc)_2$ had a nearly monodisperse distribution (2-4 nm), whereas slow reduction of $Pd(OAc)_2$ resulted in the formation of particles with a relatively wide size distribution. When using PVP as stabilizer to Pd nanoparticles in the previously described investigation in which $PdCl_2$ is reduced, it is clearly observed that the initial rate is much lower than that of reduction without stabilizer; absorbance at 600 nm does not increase after 40 s (A = 0.104) and remains

below the value measured without stabilizer (A = 0.137), meaning that the PVP molecule is capable of binding strongly to the metal surface and significantly slowing down growth [188].

Metal nanoclusters generally have a tendency to lower their surface free energy, making them thermodynamically unstable, to the increment of their size. Stabilizing agents are therefore important to attaining a fixed size. The different modes of stabilization are: electrostatic [209], steric (using polymers) [210], ligand (P, N, S donors) [211], electrosteric [212, 213], and solvent [214, 215].

Electrostatic stabilization results from the electrical double layer formed by the anions and cations interacting with the metallic particle surface. This results in coulombic repulsion between particles. The polarity of the solvent can have an electrostatic effect on nanoparticles, and thus the dispersity. Steric stabilization is brought about by large organic molecules such as PVP that are firmly adsorbed on the surface of the nanoparticle [210, 216]. Polymeric stabilizers establish several weaker bonds, rather than forming fewer strong bonds, with the nanoparticle's surface, making this mode of stabilization versatile. The introduction of "organometallic ligands" as stabilizers by Schmid et al. in 1981 [211] has led to extensive use of P, N, S donor ligands [217] for the obtenance of metallic "full shell clusters," which are well defined in size and shape [218]. Electrosteric (i.e., electrostatic plus steric) stabilization has proven to be a very reliable means of preventing particle agglomeration. Sterically demanding surface-active bulky molecules coordinate strongly to the metal particle's surface and at the same time are very well solvated in the medium. When using tetra(octyl)ammonium halides as protective agents, the halide ions have been shown to bind to the metal surface through the negatively charge chloride while the long alkyl chains shield the metallic core like an umbrella [211, 219]. Solvents such as

tetrahydrofuran (THF) [215] or propylene carbonate [220] can act as colloidal stabilizers for metal nanoparticles.

Increased temperature increases particle size with narrower size distribution [221]. The effects of reaction temperature on the pyrolysis of $[Pd_3(OAc)_6]$ to form thioether-stabilized Pd nanoparticles has been investigated by Obare and coworkers [222]. A 1 h period of pyrolysis of a toluene solution containing a 1:5 ratio of $[Pd_3(OAc)_6]$ to n-dodecyl sulfide was carried out at temperatures of 95, 100, 110, 120, 130 and 140 ^{o}C, and yielded monodisperse Pd nanoparticles with sizes of 1.7±0.2, 2.1±0.2, 2.2±0.2, 2.3±0.1, 2.4±0.1 and 2.5±0.1 nm, respectively. Increasing the reaction temperature was found to result in an increased particle size, accompanied by a narrower size distribution. Prolonged heating led to an increase in size to a mean size of ~ 3.5 nm; this is accounted for by "Ostwald ripening" [223]. Ostwald ripening is the term for growth of larger nuclei at the expense of smaller ones; it is driven by the tendency to lower surface energy [165]. Colloidal Pt sols of size in the range 1.5-4 nm have been prepared at temperatures 90°C-165°C [224, 225]; particle size substantially increases with temperature, with higher monodispersity attained for lower temperatures [191]. Klabunde and coworkers discovered that heating polydisperse gold narrows their size distribution [226, 227, 228, 229]. The explanation provided is that larger particles break down in solution, while at the same time small particles grow until they reach a stable size. This process, coined by Klabunde and coworkers as "digestive ripening", is the exact reverse of Ostwald ripening.

4.7.2.1.3 Methods of observation of cluster size distribution

Mossbauer spectroscopy has been used to obtain valuable information on the interaction between the nucleus of an atom and its surrounding electrons. In the Mossbauer effect, a γ-quantum emitted at the transition of an excited nuclear state (source) into the ground state can be

absorbed by a nucleus in the same ground state under the condition that emission and absorption occur recoilless; an unequal energy difference between the ground and excited states is compensated for by adding Doppler energy to the quantum – this is achieved by moving the source [165]. In Mossbauer spectroscopy, the nuclear resonance in dependence of the speed of the source is measured. There are three different types of interactions between the nucleus and electrons that provide information: the electrical monopole interaction, measured as the isomer shift (IS), gives information on the s-electron density; the electrical quadrupole interaction, measured as quadrupole splitting (QS), informs on symmetry and ligand field splitting; the magnetic dipole interaction provides information on the magnetic state of the system [165]. The chemical environment of metal atoms in nanoclusters has been studied by Mossbauer spectroscopy: i) $Au_{55}(PPh_3)_{12}Cl_6$ has been studied in the temperature range of 30-1.25 K to better understand its geometrical and electronic structure [230]. Au cluster has a single atom in its center with subsequent n^{th} shells, consisting of $10n^2 + 2$ atoms, around the center, resulting in a cuboctahedral geometry for a full-shell cluster. ii) the four-shell $Pt_{309}Phen^*_{36}O_{30\pm10}$ ($phen^*$=4,7-p-$C_6H_4SO_3Na$ substituted 1,10-phenanthroline), with an inner core of 147 atoms, has been investigated [231]. Since platinum is not Mossbauer-active, a fraction of atoms is first transformed from ^{196}Pt to ^{197}Au isotope by irradiation with thermal neutrons, $^{196}Pt + n \rightarrow {}^{197}Pt$, followed by the reaction $^{197}Pt \rightarrow {}^{197}Au + e^- + \nu_e + 0.6$ MeV (ν_e = antineutrino) [232]. From IS and QS observations, the 147 atomic inner core is seen to correspond with that of bulk gold. In contrast to the Au_{13} core in Au_{55}, the "Au_{147}" core of "Pt_{309}" has metallic behavior, at least at the working temperature of 1.8 K.

Tunneling spectroscopy is the most important method to obtain information on inner electronic life and metallic behavior of clusters; it is based on single-electron tunneling (SET), a

quantum mechanical process, through an intermediate island between two metal electrodes [165]. Quantum mechanical tunneling enables electron transport in such devices, and is dependent on the applied potential. Practically, the insulating tunnel barrier consists of the ligand shell that the nanoclusters under investigation in any case have. To observe tunneling of single electrons from one electrode to the counter electrode the nanoparticles, the following condition must be fulfilled: $E_c = e^2/2C \gg k_B T$; E_c is the Coulomb energy which has to be very large compared with the thermal energy $k_B T$, C the total capacitance of the tunnel contact $2\pi\varepsilon_0\varepsilon_r R$ (R, the radius of the particles, ε, the dielectric constant) and k_B, the Boltzmann constant. The chance to observe SET under reasonable temperature conditions increases with decreasing C, i.e. with decreasing size of the particle. Current-voltage measurement of a ligand-protected 15 nm palladium nanoparticle between two platinum electrodes [233] shows a linear behavior between current and voltage at 295 K. This means that the 15 nm Pd particle follows Ohm's law at room temperature and clearly demonstrates bulk behavior. At 4.2 K a Coulomb blockade is observed in the region from ca. -0.1 to 0.1 V as the transfer of electrons is blocked due to the presence of a single electron; at an appropriately higher voltage this electron is transferred to the counter electrode [165]. In other words, the ligand-protected 15 nm Pd particle behaves as a quantum dot at 4.2 K. Similar behavior was observed with the four-shell cluster $Pt_{309}phen^*_{36}O_{20}$, investigated by scanning tunneling spectroscopy (STS) [234, 235], which has a Pt core diameter of 1.8 nm. A Coulomb blockade is observed only at 4.2 K, with the particle showing metallic behavior at room temperature. Since the realization of trapping such a small particle between two tips like in the case of the 15 nm Pd particle is almost impossible, the experimental setup was modified in such a way that nanoclusters were deposited on a gold substrate from very dilute solutions and then an individual particle was contacted by the STS tip [165]. Tunneling measurements [236]

have shown that clusters containing few tenths of atoms with diameters ~ 1 nm^3 are essentially non-metallic at room temperature while clusters with slightly larger diameters are metallic. Pd_{561} nanocrystal with its metal-core diameter of 2.5 nm exists roughly at the metal–non metal boundary; I-V measurement of the PVP-capped Pd_{561} nanocrystal is characteristic of a Coulomb staircase [194].

Dynamic light scattering (DLS) is a non-invasive method used to obtain information about particle sizes in solution, as well as interactions between macromolecules such as proteins, or polymers [237,238]. Particle size from fitting DLS data requires knowledge of the diffusion coefficient of the clusters and viscosity of the solvent [163].

UV-visible spectroscopy, the most popular method for size determination and observation of metal clusters, has been used to study the kinetics of nanocluster formation in solution as well as the sizes of nanoclusters [163, 188, 197]. It requires that the nanoclusters under investigation absorb in the visible region, namely Ag, Au, and Cu, mostly excluding nanoclusters of metals including Co, Ni, Re, Ir, and Pt, that primarily tail off in the UV region [239]. Alternatively, UV-visible spectroscopy has been used to follow the loss of the nanocluster precursor, as in the study of Pt^0_n nanoclusters from the reduction of $[Pt^{II}Cl_4]^{2-}$ by Henglein et al. [240], and in the disappearance of 400 nm absorbance peak due to reduction of Pd(II) in $Pd(OAc)_2$ to Pd clusters [204]. A major problem with UV-vis. spectroscopy is that unless the formation can be studied *in situ*, there is no way to be certain that the observed behavior of the nanoclusters is the same as the actual behavior under the specific reaction conditions. Also, there may be species, other than the nanoclusters, that interfere with the nanocluster spectra: metal ions, solvent, reductant,and added stabilizers [241, 242]. The UV–vis absorption profile in the range of 300 to 800 nm of the palladium solution, obtained by reducing K_2PdCl_4 with sodium hypophosphite, does not show

any well-resolved surface plasmon band [197]; this is consistent with most reports on the solution of thiolated Pd nanoparticles in toluene [243, 244] or in water [245] and with theoretical calculations [239].

The most common ex-situ method in use for observation of size distributions of nanoparticles is *transmission electron microscopy* (TEM). TEM is limited to the characterization of the growth of nanoclusters, as nuclei are typically too small to be seen; in addition, non-high resolution, "routine" TEM is typically being limited to ≥ 1 nm despite stated resolution limits typically of $\pm \geq 0.2$ nm [163]. Because TEM is a solid-state technique, the nanoclusters must be taken out of solution and dried before they can be analyzed, during which further growth and agglomeration of the nanoclusters in the increasingly concentrated solution may take place. Also, some monometallic and other, especially first- or second-row, transition-metal nanocluster precursor complexes yield nanoclusters in the TEM beam [246, 247]. Therefore, TEM may be misleading to the determination of actual sizes of clusters in solution. The TEM beam may also change the nanoparticles under observation, another major disadvantage [248].

Another notable microscopy method for visualizing nanoclusters is *scanning tunneling microscopy* (STM), however, this method requires examination under ultra-high vacuum conditions [249].

Two powerful X-ray spectroscopy methods, X-ray absorption near-edge spectroscopy (XANES) and extended X-ray absorption fine structure spectroscopy (EXAFS) [250], that have been used to obtain information about the identity of atoms in the nanoclusters and the nearest neighbors of the atoms, allowing atomic-level characterization [163]. X-ray spectroscopic techniques have been successful in determining the structure of the nuclei vs the structure of the

final nanocluster, as has been the case in the formation of bimetallic Pt-Ru nanoclusters and carbon-supported Pt nanoclusters [251].

Of the different techniques surveyed, the best characterization techniques are in-situ techniques, because they allow observation of both nucleation and growth processes, and demand less sample manipulation. A major problem with spectroscopy still lies: it measures growth, not nucleation [163].

4.7.2.2   Determination of the absorption of palladium clusters

Metal nanoparticles are depicted to be in the size range of 1-100 nm. The optical properties of a nanoparticle, including the absorption, in this broad range of size can vary dramatically. However, a review of the growth, and observation of sizes thereof, of palladium clusters formed in solution has revealed the range of sizes within which palladium (like other metals) clusters thrive. The absorption cross-sections of clusters in this size range would provide an adequate measure for the estimation of absorption cross-sections of Pd NPs (or clusters) in solution.

Nanocrystals, termed 'magic nuclearity' nanocrystals (or clusters), with magic numbers of atoms tend to preferentially stabilize; the magic numbers correspond to atoms filling up the coordination shells completely around a central atom in a closed packed shell, the nuclearities 13, 55, 309, 561 and 1415, corresponding to closure of one, two, four, five and seven shells, repectively, for the case of Pd [193]. The sizes, assumed for a spherical shape, of full-shell clusters are displayed in Table 4.8 [252]. In Table 4.8, n is the shell number of the cluster, N_s is the number of atoms − equal to $10\,n^2 + 2$ − in the latest shell, N is the number of atoms in the cluster, and d is the size. However, of the magic nanocrystals listed, those routinely observed are Pd_{561} or clusters of slightly higher nuclearity, such as Pd_{1415}. As an example, the reduction of K_2PdCl_4 by sodium borohydride yielded Pd NPs of sizes 2.58 nm ± 23% for low precursor

concentration and 3.2 nm ± 14 % for high precursor concentration, the sizes being assigned to magic nuclearities Pd_{561} and Pd_{1415}, respectively [197]. The stability and long-term survival of clusters beyond ~ 2 nm is here again witnessed.

Pd organosols prepared by ethanol reduction of $Pd(OAc)_2$, and stabilized by the polymer polyvinyl pyrrolidone (PVP), were 2-4 nm in size [208]. Although a stabilizer provides limited growth rate, obtained cluster sizes are still ~ 2 nm and beyond. Other examples demonstrating formation of Pd NPs with mean size ~ 2 nm, using stabilizers in solution are in: the obtenance of PVP-capped Pd_{561} nanoparticles (size of 2.5 nm) with a diameter distribution of < 4% [198, 199]; the obtenance of two-dimensional arrays of nanocrystals, of magic nuclearity Pd_{561} and Pd_{1415}, capped with alkanethiols (dodecanethiol and octanethiol) [202, 203]; and the yield of monodisperse Pd nanoparticles of mean sizes about ~ 2 nm in toluene solution, containing a 1:5 ratio of $[Pd_3(OAc)_6]$ to n-dodecyl sulfide [222].

Optical properties of clusters change with size, in relation to how their size compares with characteristic lengths of the electron mobility. The characteristic lengths of the electron mobility that are responsible for the varied behavior, across the broad range of NP size (~ 1-100 nm), in optical properties are the mean free path of the electron, L_∞, and the Fermi wavelength (or the de Broglie wavelength at the Fermi energy), λ_F, of the electron.

For clusters of sizes below λ_F, $d < \lambda_F$ (d is diameter), the energy states of the electron are discontinuous, i.e. energy spacings, $\Delta > k_B T$, where k_B is the Boltzmann constant and T is temperature [253]. Characteristic Fermi wavelengths are ~ 0.5-1 nm for noble metals [253]. Clusters in this size regime are non-metallic and should be treated quantum mechanically. According to Ref. [236], tunneling measurements have shown that clusters with diameters ~ 1 nm are essentially non-metallic while clusters with slightly larger sizes are metallic in behavior.

The Fermi wavelength is therefore about the same length as the transition size for the onset of metallic behavior.

For cluster sizes bigger than the Fermi wavelength, up to the mean free path of the electron, i.e. $\lambda_F < d < L_\infty$, the UV-vis absorption spectrum is dominated by resonance due to collective motion of electrons, the so-called surface plasmon resonance (SPR). The SPR band of noble metal nanoparticles is adequately interpreted by a classical approach, Mie theory [253, 254]. Clusters of sizes larger than L_∞, i.e. $d > L_\infty$, typically in the region ~ 20-50 nm for noble metals, are not typically met in solution, and a description of their optical behavior here is not relevant.

The absorption cross-section of metal nanoclusters, of radius much smaller than the wavelength ($R \ll \lambda$), in a nonabsorbing host medium of dielectric constant, ε_m, can be simplified in the dipolar approximation to Mie's series [239, 255] :

$$\sigma = 9 \frac{\omega}{c} \varepsilon_m^{3/2} V_o \frac{\varepsilon_2}{(\varepsilon_1 + 2\varepsilon_m)^2 + \varepsilon_2^2} \qquad (4.67)$$

where V_o is the cluster volume (assumed spherical), c is the speed of light in vacuum, $\omega = 2\pi c/\lambda$, and $\varepsilon = \varepsilon(\omega, R) \equiv \varepsilon_1(\omega, R) + i\varepsilon_2(\omega, R)$ is the size-dependent complex dielectric function of the cluster. Expressing V_o in terms of number of atoms, N, of a cluster with density, ρ_{cl},

$$V_o = \frac{A_m}{\rho_{cl} N_A} N$$

where A_m is the molar mass and the Avogadro number, Eq. (4.67) is written for any number of atoms:

$$\sigma = 9 \frac{\omega}{c} \varepsilon_m^{3/2} \frac{A_m}{\rho_{cl} N_A} N \frac{\varepsilon_2}{(\varepsilon_1 + 2\varepsilon_m)^2 + \varepsilon_2^2} \qquad (4.68)$$

The dielectric permittivity, taking into account the free-electron Drude component and the interband susceptibility, $\chi^{ib}(\omega) = \chi_1^{ib}(\omega) + \chi_2^{ib}(\omega)$, is described by Eq. (4.69) [256],

$$\varepsilon(\omega) = 1 - \frac{\omega_p^2}{\omega^2 + i\gamma\omega} + \chi^{ib}(\omega) \tag{4.69}$$

where ω_p is the plasma frequency of conduction electrons and γ is the rate of electron collisions. Eq. (4.69) describes the dielectric permittivity for bulk metals as well [257]. However, the electron collision rate in metallic nanoparticles, γ is dependent on the radius, R of metallic nanoparticle [254] :

$$\gamma(R) = \gamma_0 + A_I \frac{v_F}{R} \tag{4.70}$$

where γ_0 is the bulk collision rate, A_I is a constant of order unity [254, 256, 258], and v_F is the Fermi velocity. The quantity v_F can be calculated as the ratio L_∞/τ, where τ is the electron relaxation time and is equivalent to the inverse of the bulk scattering rate : $\tau = 1/\gamma_0$.

The unknown values of susceptibility can be determined by implementing known parameters, ω_p and γ, in Eq. (4.69) for known values of $\varepsilon_1(\omega)$ and $\varepsilon_2(\omega)$, of bulk material, as is done for silver nanoparticles in Ref. [256] and Ag, Cu, and Au films in Ref. [257]. Expanding $\varepsilon(\omega)$ in Eq. (4.69) into its real and imaginary parts, one obtains

$$\varepsilon(\omega) = 1 - \frac{\omega_p^2}{\omega^2 + \gamma^2} + \chi_1^{ib}(\omega) + i\left[\frac{\omega_p^2\gamma}{(\omega^2 + \gamma^2)\omega} + \chi_2^{ib}(\omega)\right] \tag{4.71a}$$

so that the real and imaginary terms, $\varepsilon_1(\omega)$ and $\varepsilon_2(\omega)$, are written as

$$\varepsilon_1(\omega) = 1 - \frac{\omega_p^2}{\omega^2 + \gamma^2} + \chi_1^{ib}(\omega) \; ; \; \varepsilon_2(\omega) = \frac{\omega_p^2\gamma}{(\omega^2 + \gamma^2)\omega} + \chi_2^{ib}(\omega) \tag{4.71b}$$

Denoting the bulk values of dielectric permittivity, $\varepsilon_1(\omega)$ and $\varepsilon_2(\omega)$, as $\varepsilon_1^\infty(\omega)$ and $\varepsilon_2^\infty(\omega)$ respectively, the real and imaginary parts of interband susceptibility, $\chi^{ib}(\omega) = \chi_1^{ib}(\omega) + i\chi_2^{ib}(\omega)$, can be obtained (the interband susceptibility is not size-dependent) in Eq. (4.72) :

$$\chi_1{}^{ib}(\omega) = \varepsilon_1^\infty(\omega) - \left[1 - \frac{\omega_p^2}{\omega^2 + \gamma_0^2}\right] \; ; \; \chi_2{}^{ib}(\omega) = \varepsilon_2^\infty(\omega) - \left[\frac{\omega_p^2\,\gamma}{\omega(\omega^2 + \gamma_0^2)}\right] \qquad (4.72)$$

Optical constants of palladium films (3000 Å thick), deposited at a rate of 60 Å/s by thermal evaporation of bulk palladium at 10^{-9} Torr, have been determined to be: $n = 1.75$; $k = 2.29$ at 248 nm wavelength [259]; the values of the complex dielectric constant are determined to be $\varepsilon_1^\infty = -2.18$ and $\varepsilon_2^\infty = 8.02$, after making use of the definition of complex refractive index :

$$\tilde{n} = n + ik = (\varepsilon_1 + i\varepsilon_2)^{\frac{1}{2}} \qquad (4.73)$$

which on expansion yields

$$\varepsilon_1 = n^2 - k^2 \; ; \; \varepsilon_2 = 2nk \qquad (4.74)$$

The quantities $\chi_1{}^{ib}$ and $\chi_2{}^{ib}$ at $\lambda = 248$ nm are now obtainable, with the given values of ε_1^∞ and ε_2^∞, in Eq. (4.72) and the absorption cross-section can be described over the range of sizes in Eq. (4.68). A water medium is the choice. Values of relevant constants are tabulated in Table 4.9. The resulting size-dependent absorption cross-section is plotted in Figure 4.31.

It can be seen, from the plot of absorption cross-section per atom in Fig. 4.31d, that absorption cross-section values vary from ~ 0.085-0.095 Å^2 in the radius range ~ 1-10 nm, and thus slowly change in the depicted size range. One can interprete from the observed slow change that the aggregation of clusters, exhibiting SPR behavior, into larger clusters, up to ~ 20 nm in size, little (~ 10 %) changes absorption. This behavior is supported by previously made explanations on experimental investigations, by S. Papp et al., which claimed that formation of large aggregates

(~ 6-20 nm in size) from clusters (~ 2.1 nm in size) resulted in a minor increase (~ 8 %) in absorbance at 600 nm wavelength. In a laser ablation experiment, in which there is material ejection within every second, one would expect that clusters barely have time for aggregation into particles as large as ~ 5 nm and beyond. This likely explains the relatively narrow size distribution (TEM-observed) of Pd nanoparticles formed by matrix-assisted pulsed laser evaporation (MAPLE) of a solution 'target' of $Pd(Oac)_2$ precursor in chloroform [46]: the size distributions are narrow, and NPs exhibit mean diameters ranging from 2.15 nm to 2.62 nm as the laser fluence is varied from 0.25 J/cm^2 to 0.75 J/cm^2.

A survey of experiments ranging from colloidal preparations to laser ablation experiments in solution have shown the formation of Pd cluster mostly of narrow size, ~ 2 nm. Explanations based on the review of nucleation and growth of Pd clusters in solution illustrate key factors that account for a likely encountered size distribution: there is a tendency to grow faster when cluster sizes are small, less than 2nm ; and there is a tendency to stabilize into preferred nanocrystal conformations with magic numbers. A balance of these factors may overall prefer clusters Pd_{309}, $Pd_{561,}$ Pd_{1415}, of sizes 2.0 nm, 2.4 nm, and 3.3 nm respectively.

Finally, in order to make an assessment of the order of magnitude of the determined absorption cross-section of Pd in clusters whose absorption has been described by Mie theory, a table is made which summarizes the determined values of the absorption cross-sections of PdAc molecule and Pd atom thus determined so far. The value of the absorption cross-section of Pd atom in a thin palladium film of thickness 5 nm is closely of the same order of magnitude as the absorption cross-section of Pd atom in a palladium cluster of size 1-10 nm, as one would be expect.

Table 4.8. Relation between number of Pd atoms in full-shell clusters and the cluster size.

N	N	N_s	d [nm]
1	13	12	0.70
2	55	42	1.13
3	147	92	1.56
4	309	162	2.00
5	561	252	2.44
6	923	362	2.88
7	1415	492	3.33
8	2057	812	3.77
9	2869	1002	4.21
10	3871	1212	4.65
11	5083	1442	5.09
12	6525	1692	5.53

Table 4.9. Optical properties of palladium.

Plasmon frequency (ω_p), 1/s	1.04×10^{16} [259]
Bulk scattering rate (γ_0), 1/s	2.4×10^{14} [259]
Mean free path (L_∞), nm	23 [260]
Water dielectric constant, ε_m	1.78 [239]

Table 4.10. Some absorption cross-section values of PdAc and of Pd, determined so far.

Absorption cross-section of PdAc in solid film	0.29 Å^2
Absorption cross-section of Pd atom in ~ palladium film, of thickness ~ 5	0.24 Å^2

nm, formed by decomposed PdAc solid film	
Absorption cross-section of Pd atom in clusters whose absorption is described by Mie theory	0.1 Å^2
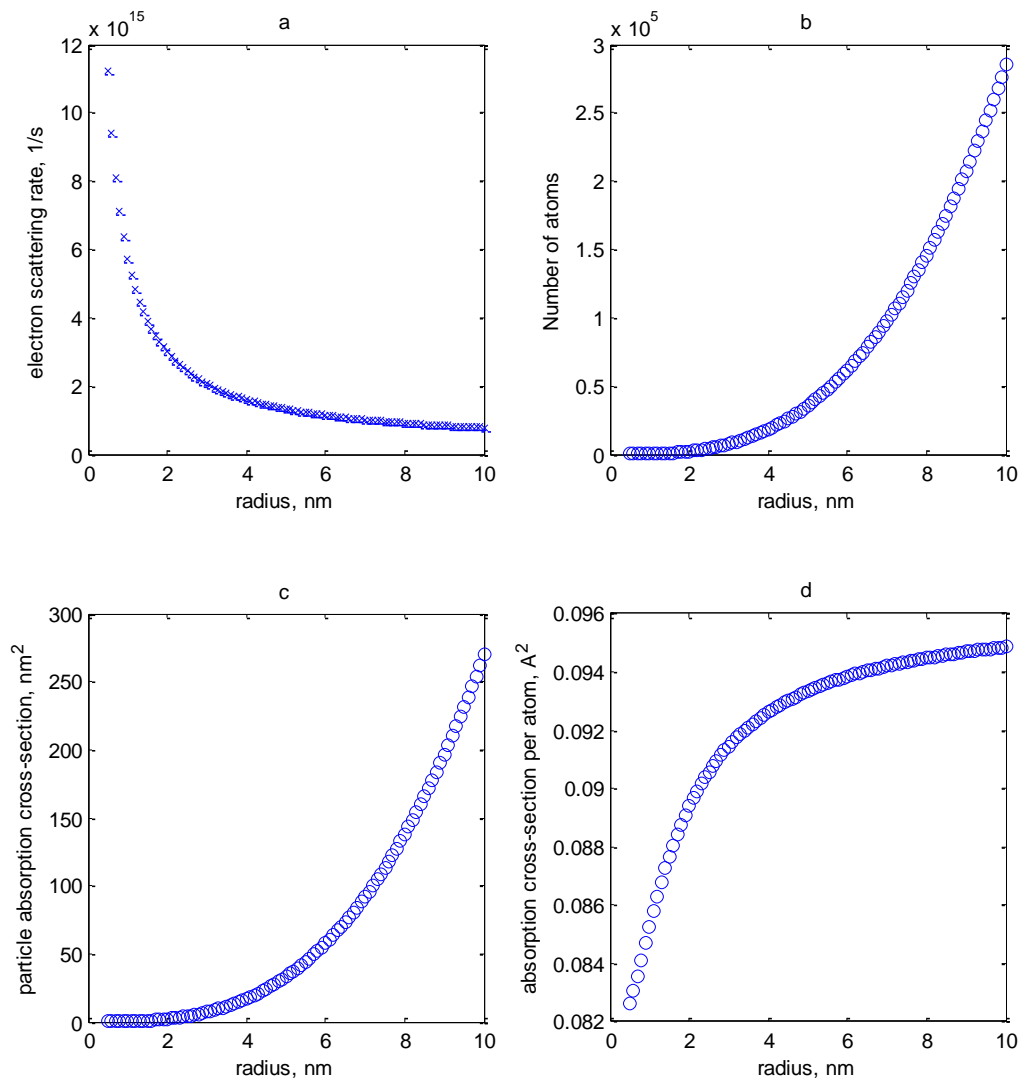
Figure 4.31 Dependencies on nanoparticle radius of a) electron scattering rate, b) number of atoms, c) total particle absorption cross-section, d) absorption cross-section per atom.

4.7.2.3   *Determination of the absorption cross-section of single Pd atom*

The absorption cross-section of single Pd atom at the laser irradiation wavelength of $\lambda = 248$ nm in free space is theoretically determined using available data on the radiative lifetime at $\lambda = 247.64$ nm, which is the closest excitation (or transition) wavelength to the laser irradiation wavelength. An estimate of the absorption cross-section of Pd atom at $\lambda = 248$ nm in water is made after studying the effect of a matrix medium on the absorption spectrum of single Pd atom at the transition wavelength of $\lambda = 247.64$ nm.

Pd(I) has a radiative lifetime of 5.0 ns at the wavelength of 2476.42 Å [261]. The corresponding energy transition to this wavelength is $4d^{10}$ to $4d^9\,5p^1$ [261, 262]. The absorption cross-section of single palladium atom in free space can be determined through Einstein coefficients if the radiative lifetime, τ, is known, as in Ref. [263]. The Einstein coefficient for spontaneous emission, A_{21}, is the reciprocal of the radiative lifetime,

$$A_{21} = 1/\tau \tag{4.75}$$

The Einstein coefficient for induced emission, B_{21}, is related to A_{21} through Eq. (4.76), see Ref. [263].

$$B_{21} = \frac{\pi^2 c^3 A_{21}}{\hbar \omega_{21}^3} \tag{4.76}$$

The Einstein coefficient for induced absorption, B_{12}, is related to B_{21} through statistical weights of the lower and upper transition energy levels, g_1 and g_2 :

$$g_1 B_{12} = g_2 B_{21} \tag{4.77}$$

Finally, the absorption cross-section is related to B_{12} through the relations in Eqs. (4.78-4.79) :

$$\sigma_0 = \frac{\hbar\omega_{12}B_{12}}{c}; \tag{4.78}$$

$$\sigma(\omega) = \frac{\hbar\omega_{12}B_{12}g(\omega)}{c} = \sigma_0 g(\omega) \tag{4.79}$$

The function $g(\omega)$ is a Lorentzian line shape function, described by the dependence in Ref. [264],

$$g(\omega) = \frac{\gamma/2\pi}{(\omega - \omega_{21})^2 + (\gamma/2)^2} \tag{4.80}$$

and is normalised so that

$$\int_{-\infty}^{\infty} d\omega \, g(\omega) = 1 \tag{4.81}$$

In Eq. (4.81), γ is the damping rate of the observed transition; in free space, it is the rate of spontaneous emission, and is equal to A_{21}. The quantity γ is also known as the full frequency width at half maximum (FWHM), $\Delta\omega$, of the transition response, and hence the equivalence $\gamma = \Delta\omega$.

The Eq. (4.78), when resolved in terms of the wavelength λ, becomes

$$\sigma_0 = \frac{1}{4}\left(\frac{g_2}{g_1}\right)\lambda_{12}^2 A_{21}$$

and also the Lorentz function in terms of λ becomes

$$g(\lambda) = \frac{\gamma\lambda^2\lambda_{12}^2}{2\pi[c^2(\lambda_{12} - \lambda)^2 + (\gamma/2)\lambda^2\lambda_{12}^2]}$$

For the $4d^{10} \, ^1S_0 \to 4d^9 \, 5p$ transition, the statistical weights are $g_1 = 1$ and $g_2 = 3$, respectively.

Applying $\tau = 5$ ns in Eq. (4.75) and implementing Eqs. (4.76-4.78) yields the value of σ_0 at ω_{12}:

$\sigma_0 = 9.18 \times 10^{-6} \, m^2/s$

The absorption cross-section is then determined at $\lambda = 248$ nm in Eq. (4.79) to be

$$\sigma(\omega) = 9.46 \times 10^{-3} \, Å^2,$$

after using the substitution

$$\omega - \omega_{12} = c\frac{\lambda_{12} - \lambda}{\lambda_{12}\lambda} \tag{4.82}$$

in $g(\omega)$. Here, $\omega - \omega_{12} = 1.76 \times 10^{12}$ rad/s, making $\omega - \omega_{12} \gg \gamma/2$ in Eq. (4.80).

The dependencies in the Lorentz function and the absorption cross section as a function of wavelength, about the transition wavelength $\lambda = 247.64$ nm, are displayed in Figure 4.32.

The calculated absorption cross-section of Pd atom in free-space at 248 nm wavelength is $9.46 \times 10^{-3} \, Å^2$. Laser absorption of single Pd atom, in our investigation, occurs in a matrix – the water medium. It is relevant to determine the energy spacing of the transition levels in the matrix.

The absorption spectrum of single Pd atom in solidified rare gas matrices (frozen at 4.2 K) at the transition wavelength of 247.64 nm has been studied [265,266]. This study is useful in relating to what the absorption spectrum of Pd atom in a water matrix would be. It has been determined that the energy shift in solid matrices of four noble gases – Ne, Ar, Kr, and Xe – is in the range of $\Delta E = 700 - 1000$ meV [265,266]; this corresponds to a calculated wavelength shift of $\Delta\lambda = 35 - 50$ nm. The large energy shift for Pd atom has been explained both by the smallness of Pd atom and the high spatial extension of the $5p$ orbital. The radius for the maximum charge density of Pd is $r_d = 0.55$ Å, compared to that of Ag which is $r_s = 1.4$ Å [266]. It is suggested in Ref. [266] that the smallness of Pd atom enables it to occupy an interstitial site

in the solid matrix : in an interstitial site, «a tremendously high repulsive interaction is expected for the optically excited atom when an electron is promoted to the very spatially extended $5p$ orbital». In comparison to 850 meV for $4d^9 5p^1$, energy shifts of $4d^9 5s^1$ and $4d^8 5s^2$ transitions are 180 meV and 400 meV respectively for Pd atom in neon (Ne); the smaller energy shift can be accounted for by the localized nature of the latter states. The matrix shift in other transitional metal atoms in the same experiment, such as Ag, Cu, Ni, and Co, are also significantly lower, in the range ~ 100-400 meV, in Refs. [265, 266]. Because of the large size, unlike Pd atom, the atoms occupy a substitutional site and there is weaker interaction with the electron orbitals.

The occupation of interstitial sites by Pd atom in solid rare gases has also accounted for the relatively high thermal mobility of Pd atoms as the matrix is heated slightly above 4.2 K, in Ref. [266]: diffusion via interstitial sites requires less activation than via substitutional sites. The result to diffusion is cluster formation, which led to observation of a decrease in optical transmission through the matrix.

The dimensions of the substitutional and interstitial sites in the solid noble gases are illustrated in Ref. [266], they are: 3.21 Å, 3.83 Å, 4.05 Å, 4.41 Å, for Ne, Ar, Kr, and Xe, respectively, for the substitutional site; and 2.27 Å, 2.71 Å, 2.87 Å, 3.12 Å, for Ne, Ar, Kr, and Xe, respectively, for the interstitial site. Considering ice in which the separation between oxygen (O) atoms is 2.76 Å, a weaker effect on the Pd $4d^9 5p^1$ state is not expected than that exerted in the solid noble gases. There could be additional electrostatic effects – due to the polar nature of the H_2O molecule – that would only increase the linewidth of the $4d^9 5p^1$ state.

In conclusion, the values of energy shift in absorbing Pd atom witnessed in solid noble gases are expected to be about the same or more in a water medium, and so a wavelength shift of $\Delta\lambda = 35 - 50$ nm, or even more, would be typical. Even if the Pd atom may not end up in a H_2O

interstitial site, one would expect an energy shift of at least ~ 100 eV, as a minimum for transition metals in the discussions above, corresponding to a wavelength shift of $\Delta\lambda = 5$ nm. The absorption cross-section at $\lambda = 248$ nm, the absorption wavelength in laser ablation, would be significantly smaller than the calculated value of 9.46×10^{-3} Å^2, taking into account the Lorentz distribution, for an energy transition that is at least $\Delta\lambda = 5$ nm away from $\lambda = 247.64$ nm.
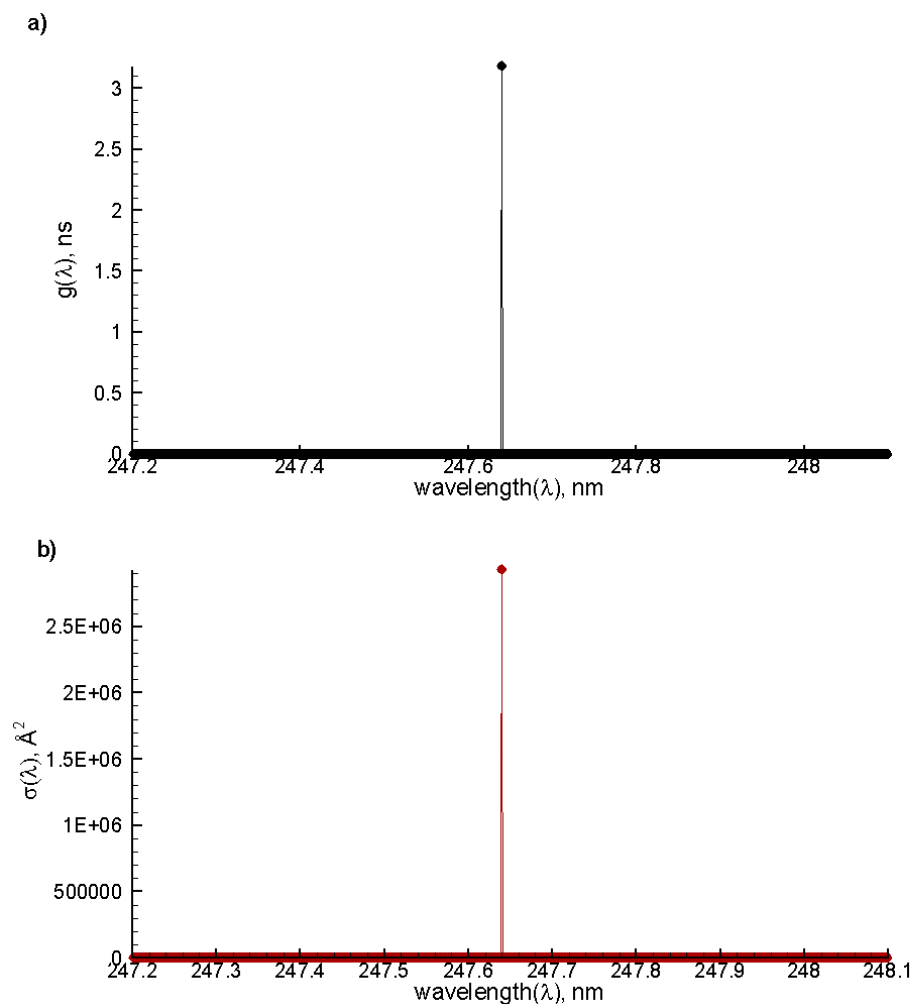
Figure 4.32   The dependence on wavelength of a) Lorentz function, b) absorption cross-section of single Pd atom in free-space.

4.7.2.4   *Summary on the determination of absorption cross-section of Pd atom in*

clusters

So far have been determined the absorption cross-section of single Pd atom and the absorption cross-section of Pd atom in a cluster, which is typically of size bigger than the Fermi wavelength and whose absorption is described by Mie theory. It was discussed that due to the non-metallic behavior of clusters that are of size below the Fermi wavelength, the absorption spectrum can only be described by a quantum mechanical treatment. However, a quantum mechanical descritpion of the electronic structure of Pd clusters for the determination of the absorption spectrum is not considered to be within the scope of this work. We therefore aim at making a reasonable approximation of the absorption cross-section of Pd in clusters within the mentioned size range.

The absorption cross-section of single Pd atom at $\lambda = 248$ nm in a water matrix was determined to be less than the value in free-space, i.e. $\sigma < 9.46 \times 10^{-3}$ Å^2. On the other end the absorption cross-section of Pd atom in Mie theory was determined to slowly increase from 0.085 Å^2 to 0.096 Å^2 in the size range 1-10 nm. The absorption cross-section of single Pd atom is therefore orders of magnitude lower and can be approximated to *zero* in a unified description of the absorption cross-section as a function of size. Due to the decrease in absorption as cluster size decreases in Mie theory, one can project that the absorption of Pd atom in clusters of lower size, i.e. of size lower than the Fermi wavelength, should be lower. Because of the lack of adequate knowledge on the general dependence of absorption of metal atom on size in this regime, a 'simple' linear approximation is adopted. The absorption cross-section of Pd atom in Mie theory slowly changes and within two significant figures can be equalled to $\sigma^{Mie} = 0.1$ Å^2.

The absorption cross-section of Pd atom in a cluster within the size range $0 < d < 1$ nm thus changes linearly from *zero* to σ^{Mie}. The unified dependence of the absorption cross-section of Pd atom is summarized in Figure 4.33.

To relate the size of Pd cluster to the number of atoms in it, the dependence between the nanometric size and the number of atoms is displayed in Figure 4.34. This dependence for a spherical cluster with atomic density assumed to be that of bulk material is given by

$$\frac{4}{3}\pi d^3 = \frac{A_m}{\rho_{cl}N_A}N$$
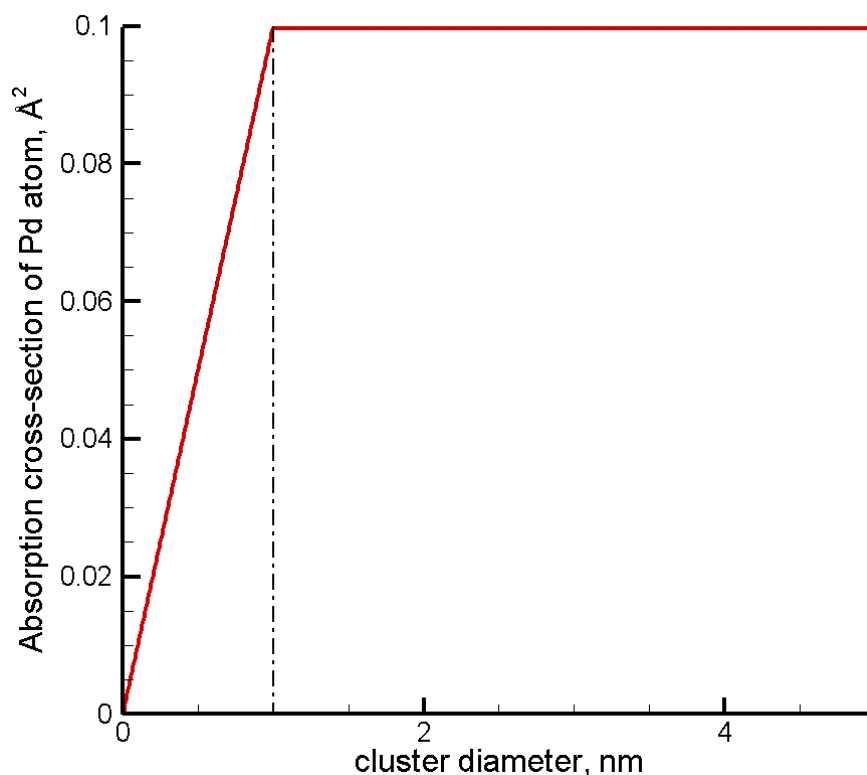
Figure 4.33 The dependence of absorption cross-section of Pd atom as a function of cluster diameter.
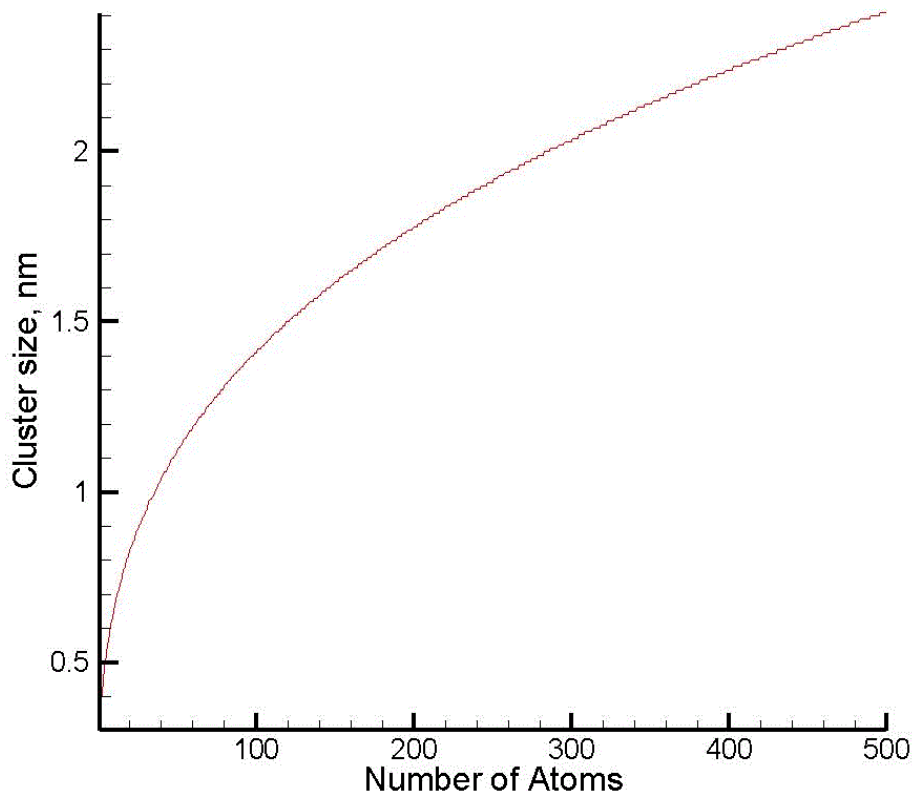
Figure 4.34 A dependence illustrating the relation between the size of Pd cluster and the number of atoms in it.

4.7.3 Beer's Law for Irradiated System of Reactants and Products

An initially prepared target is having a close to homogeneous distribution of absorbing metallorganic molecules. During irradiation, formation of new product species from reactant molecules and the non-uniform expansion of the matrix film in the energy deposition process generate non-uniform concentrations of different absorbing species. This leads to the inevitable treatment of the absorption coefficient of the material system as a space-dependent function over time.

Beer's law for this medium with absorption coefficient dependent on the depth, x ($x > 0, dx > 0$), can be written as:

$$I(x) = I(0) \cdot e^{-\int_0^x \alpha(x')dx'} \tag{4.83}$$

In an ablation experiment, light is irradiated from above the target, so that the intensity of light wanes in the negative z direction, into the depth of the target material. Denoting the target surface as z_s, Beer's law is written for the ablation system after making the substitution, $x = z_s - z$:

$$I(z_s - z) = I(z_s) \cdot e^{\int_{z_s}^{z_s-z} \alpha(z_s-z')dz'} \tag{4.84}$$

where $dz' < 0$.

Applying the logarithm on both sides of the above equation, we obtain:

$$\ln\frac{I(z_s - z)}{I(z_s)} = \int_{z_s}^{z_s-z} \alpha(z_s - z')dz' \tag{4.85}$$

In a discrete approximation, denoting the step size $\delta z = -dz'$ ($\delta z > 0$), and further denoting $z_i = z'$, $z_n = z$:

$$z_i = z_s - i \cdot \delta z; \quad z_n = z_s - n \cdot \delta z \,,$$

a numerical description of Eq.(4.85) is Eq. (4.86):

$$\ln\frac{I(n \cdot \delta z)}{I(z_0)} = -\sum_{i=0}^{n} \alpha(i \cdot \delta z) \cdot \delta z \tag{4.86}$$

in which $z_0 \equiv z_s$, when $i = 0$. The discrete absorption coefficient, $\alpha(i \cdot \delta z)$, is defined as

$$\alpha(i \cdot \delta z) = \sum_{k} \sigma_k n_k^i \tag{4.87}$$

where k runs through all types of absorbing species, and n_k^i is the density of type i specie at z_i .

Computationally, let p denote the ratio $I(n \cdot \delta z)/I(z_0)$: $0 < p \le 1$, then the depth of excitation of an irradiating photon is determined by the relation:

$$\sum_{i=0}^{n-1} \alpha(i \cdot \delta z) < -\frac{\ln p}{\delta z} \leq \sum_{i=0}^{n} \alpha(i \cdot \delta z) \qquad (4.88)$$

for a randomly generated number p in a uniform distribution. In other words, the probability of excitation of target material in the interval $((n-1) \cdot \delta z, \, n \cdot \delta z]$ is described by the above relation. A finite position in the interval $((n-1) \cdot \delta z, \, n \cdot \delta z]$ is then randomly chosen by a uniform distribution.

4.8. Simulation of Laser Irradiation of the Target

The laser ablation system is designed to replicate experimental conditions. The model pulse duration is chosen to reproduce the ablation regime characteristic for experiments.

A target with 5 wt% PdAc, typical concentration of our modeled target, has a penetration depth of L_p = 2.6 µm. The characteristic time of mechanical relaxation in an aqueous medium is $\tau_S \cong L_P/C_s$ = 1.7 ns, and the laboratory pulse duration, 25 ns, is longer: $\tau_p > \tau_s$, implying that laser irradiation conditions are away from the regime of stress confinement. The characteristic time of thermal relaxation is $\tau_{th} \cong L_p^2/D_T$ = 35 µs, implying that $\tau_p < \tau_{th}$. Laser deposition is therefore in the regime of thermal confinement.

Continuum model simulations predict that phase explosion of the homogeneous precursor target, leading to material ejection, can only occur at fluences that are at least an order of magnitude higher than laboratory fluences. This suggests that there are other factors that are accountable for the observed material ejection of NPs. Here, factors that relate to the composition of the precursor target, and to the experimental observations of deposited NPs are considered.

1) The dispersion of the precursor in the target is to be considered: the precursor is only partly soluble in the matrix. The irradiation of precursor particulates in solution may determine both the energy distribution in the irradiated region and the process of formation of clusters of metal atoms.

2) NPs of uniform size distribution that are deposited on the substrate are observed after irradiation of the target with hundreds of pulses. This leads to suggest that ejection of NPs from the target is partly due to laser interaction with nanoparticles in the target after irradiation by several pulses.

The precursor is only partly soluble in the matrix. To study the effect of solubility of the precursor on the formation and ejection of NPs, irradiation targets with the precursor in a monomolecular phase, as well as targets with the precursor in a dispersed phase of nanocrystals are considered in the model. The former is representative of a target with a completely soluble precursor while the latter is representative of a target with a partly soluble precursor.

Model simulations of irradiation of the precursor target by a single pulse will reveal the mechanism of the formation of metal clusters in the preliminary stage of laser irradiation. Irradiation by subsequent pulses will reveal the mechanism of growth of metal clusters in the target at a later stage of laser irradiation.

The precursor target is modelled at an initial temperature of 77 K, which is the boiling point of liquid nitrogen (LN_2). Prior to modeling the irradiation of the target in a later stage of multi-pulse irradiation, it is necessary to determine the temperature of the target before irradiation of the next pulse. For this, the 1D heat diffusion equation is used to determine the temperature profile of the target between irradiation pulses.

In the follow-up to determining the mechanism of NP ejection, we shall make estimate calculations that determine at what fluences ejection of NPs can occur as a function of the distribution of NPs in the target. The size of NPs considered will be ~ 2nm, as this is the average size of deposited NPs in experiment.

4.8.1   Determination of the Target Temperature between Irradiation Pulses

We here determine the temperature to which the irradiated target surface cools from its highest attained value, before irradiation of the next pulse. The time between pulses is 0.2 s for a pulse repetition rate of 5 Hz; the surface temperature will be determined during this time.

In experiment the bottom of the target is in contact with a thermal reservoir of liquid nitrogen (LN_2), which has a boiling point of 77 K. The target – which is at least ~ 1 mm thick – is much thicker than the laser penetration depth, which is only a few μm deep for initial precursor concentrations ≤ 5 wt%, and so laser-deposited energy is not expected to diffuse to the bottom of the target and affect its temperature within pulse duration times of nanoseconds. It can therefore be readily assumed that the bottom of the target is constant at 77 K. Following the same reasoning, it can also be assumed that the lateral sides of the target do not become heated, since the area over which the laser beam is rastered is about 5 cm^2, bigger than the area of the beam size, which is about 1 cm^2.

In a 1D continuum model that closely reproduces experimental conditions, the temperature at the back of a 1 mm thick sample is kept constant at 77 K. Within the pulse duration τ_p laser-deposited energy diffuses across a length scale that equals the diffusion length: $L_D^P = \sqrt{2D_T\tau_p}$, i.e. $L_D^P = 84$ nm for $\tau_p = 25$ ns and $D_T = 1.4$ x10^{-7} m^2/s. For a node thickness dx equal to 1 μm, because $dx \gg L_D^P$ the energy of the node at the end of the pulse can be assumed to be equal to

the amount deposited in the node. Because the energy of a node is not dissipated, the energy density across the target in the direction of irradiation at the end of the pulse $\epsilon(x)$ can be adequately described by the same relation that describes the light intensity (i.e. Beer's law):

$$\epsilon(x) \cong \epsilon(0) \exp\left(-\frac{x}{L_P}\right) \tag{4.89}$$

where x is the depth of the node in relation to the surface. After single pulse irradiation of the precursor target, the absorption coefficient changes significantly only within the light penetration depth (a few microns) which is two orders of magnitude smaller than the model thickness of 1 mm, and so the described relation largely describes the energy profile across the depth of the target.

For a model target having 5 wt% precursor concentration, the penetration depth is 2.6 μm. Assuming the penetration depth is constant during irradiation of a single pulse as discussed already, and the energy density after irradiation is described by Eq. (4.89), the temperature across the target is determined at a time initial to the period, T = 0.2 s, between pulses. The initial temperature profile, assuming a uniform density and a uniform heat capacity, is described by a relation similar to Eq. (4.89),

$$T(x) \cong T(0) \exp\left(-\frac{x}{L_p}\right)$$

in addition to setting the temperature at the back to 77 K.

The temperature profile is determined with the described initial condition as the temperature at the back is maintained at 77 K, for a 10 mm thick target. A surface temperature close to phase explosion, $T(0) \sim 500$ K, is considered.

The target temperature close to the surface immediately after laser irradiation is displayed in Figure 4.35; the temperature is above the reservoir temperature, 77 K, only within ~ 20-30 μm of the surface.

The temperature of the surface during the time period between two irradiation pulses is displayed in Figure 4.36. It can be seen that the surface temperature decays to a temperature only a few Kelvins away from the temperature at the back, as the temperature at the back is maintained at 77 K. This means that making an assumption that the target regains the temperature of the thermal reservoir before irradiation of the following pulse is adequate. Hence, the target temperature will be initialized to the reservoir temperature of 77 K prior to starting subsequent pulsed irradiation.
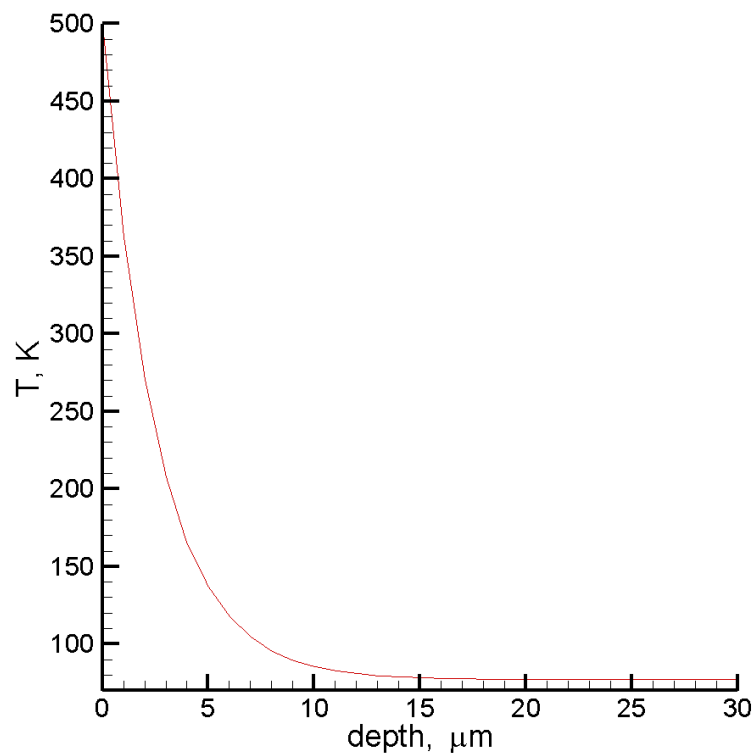
Figure 4.35   Temperature variation close to surface target immediately after pulse-laser deposition. Surface node temperature is 500 K.
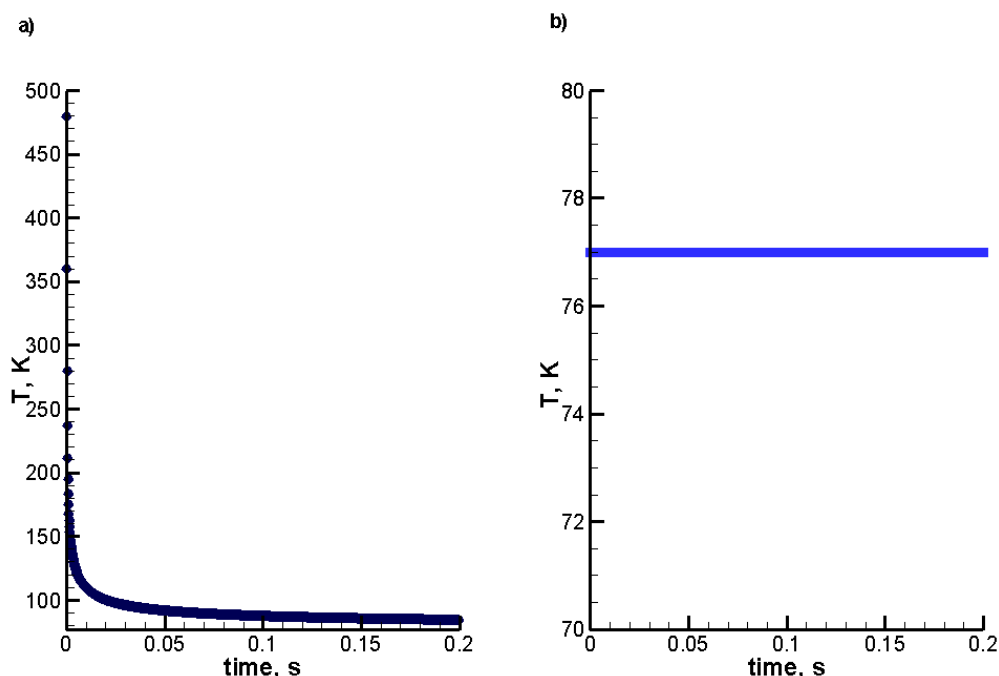
Figure 4.36 Temperature at a) the surface, b) the back, during the time between pulses for model target 10 mm thick with surface temperature 500 K after irradiation.

4.8.2 Calculations for Estimating the Range of Fluences at which NP Ejection Occurs

The ejection of NPs from the target is suggested to be due to their interaction with laser light in the target. According to experimental research work published by Matthew Steiner, William Soffa and James Fitz-Gerald, in Ref. [47], NPs of size ~ 2nm gain energy for ejection from the target due to their photoabsorption. It is unclear in this work, however, how the NPs gain energy for their ejection: does the light energy absorbed by the NPs thermally equilibrate in the aqueous medium, the latter attaining a state of phase explosion for the entrainment of NPs ? Or does the energy absorbed by the NP only heat its local environment beyond phase explosion temperatures, to still provide a push sufficient for the ejection of the NP through overlying frozen or colder material, without any phase explosion of the aqueous medium ?

To assess the possibility of any of the described scenarios of NP ejection, we compare the orders of magnitude of the fluence of ejection in the given scenario to the ablation (or ejection) fluence in experiment. We make calculations to estimate the threshold fluence for the ejection of NPs from the target surface in both scenarios.

It is determined whether the laser energy absorbed by the NPs evenly heats the aqueous medium, and in what conditions would the absorbed energy be partly localized.

A target region with initial precursor $(Pd(OAc)_2)$ concentration of 5 wt% has a corresponding metal (Pd) atom concentration $f^w = 2.4$ wt% after complete precursor decomposition. Assuming the metallic material is in the form of NPs of size 2 nm, the separation between uniformly dispersed NPs, L_{NP}, for low weight concentrations is determined as

$$(L_{NP})^3 \simeq \frac{\rho_m V_m}{\rho_w} \times \frac{1 - f^w}{f^w} \tag{4.90}$$

where ρ_m is the density of pure metal (12.0 g/cm^3 for Palladium), ρ_w is the density of water (1.0 g/cm^3), and $V_m = (4/3)\pi r_m^3$ is the volume of the metal NP. The spacing between NPs that are uniformly dispersed in a water medium calculated from Eq. (4.90) is $L_{NP} \simeq 13$ nm.

To be able to tell whether laser energy absorbed by the NP evenly heats the aqueous medium, half the spacing between NPs is compared to the distance L_D^P over which the laser-deposited energy diffuses during irradiation, i.e. $L_{NP}/2$ is compared to L_D^P in 3D. In 3D the diffusion length is determined as $L_D^P = \sqrt{6 \ _T \tau_p}$, which is $L_D^P = 145$ nm for $\tau_p = 25$ ns.

A much larger distance of diffusion will mean the NP-absorbed energy diffuses well enough for the medium to be evenly heated. This appears to be the case as $L_{NP}/2 \simeq 6.5$ nm is much smaller than $L_D^P = 145$ nm. The fluence at which the medium is heated from the reservoir temperature (77 K) to a state of phase explosion is determined.

4.8.2.1 Theoretical estimation of threshold fluence for ejection of homogeneously dispersed NPs

Here, a theoretical estimate of the threshold fluence for the ejection of NPs from an evenly heated surface region of the target that has attained the temperature of explosive boiling is determined.

The penetration depth of a region with NPs of a given concentration f^w is determined as

$$L_p = \frac{1}{\alpha} = \frac{M}{\rho^m N_A} \cdot \frac{1}{\sigma_{Pd}} \tag{4.91}$$

where σ_{Pd} is the NP atom absorption cross-section, ρ^m is the density of metal NPs in the irradiated region and is determined as

$$\rho^m = \rho_w \cdot \frac{f^w}{1 - f^w}$$

for low weight concentrations in water of density ρ_w. The density of metal NPs is determined to be $\rho^m = 0.024$ g/cm^3 for a 2.4 wt% concentration, and the penetration depth is determined to be $L_p = 7.4$ μm, for the given physical quantities of Pd NP: $M = 106.42$ g/cm^3, $\sigma_{Pd} = 0.1$ Å^2 – the absorption cross-section of a Pd atom in the 2 nm NP. Because the penetration depth L_p is much longer than the thickness of the irradiated region under study – less than a micron in our computational model, the threshold fluence for ejection, F*, can be simply related to the rise in temperature, ΔT, through the density of deposited energy, ϵ:

$$F^* = \epsilon L_p \tag{4.92}$$

where $\epsilon = c_p \rho_w \Delta T$, with c_p the heat capacity, ρ_w the density of the matrix, and ΔT the temperature difference between the the thermal reservoir temperature and phase explosion temperature for water – $\Delta T = 473$ K.

The threshold fluence for the ejection of NPs from an evenly heated surface medium as described in Eq. (4.92), with the above described parameters, is $F^* = 1.5$ J/cm^2.

The estimated threshold fluence for NP ejection is 7-8 times bigger than the reported experimental fluence (0.25 J/cm^2) at which ejection occurs. This indicates that even heating of the matrix (aqueous medium in this case) or complete thermal equilibration of NP-absorbed energy with the matrix to a state of phase explosion for the entrainment of NPs from the target is far from being a likely process leading to the laser ejection and deposition of NPs in experiment. It therefore appears important to explore the alternative scenario of NP absorption leading to localized heating that causes ejection of the NP from the target, without the aqueous medium attaining a state of phase explosion. We had determined that for complete thermal equilibration of NP-absorbed energy with the matrix to occur, the distance over which heat diffuses during irradiation L_D^P should be significantly longer than half the separation between NPs, $L_{NP}/2$. This means that for NP-absorbed energy to be partly (or significantly) localized the NPs should be heterogeneously dispersed in the matrix in such a way that there are sub-regions in which the NP concentration is significantly higher than the NP concentration of the irradiated target region. In this way L_D^P compares to or is smaller than half the average distance between the sub-regions, L_{NP}^{loc}, i.e. $L_D^P \lesssim L_{NP}^{loc}/2$.

4.8.2.2 *Theoretical estimation of the order of magnitude of fluences for the ejection of heterogeneously dispersed NPs*

Here we determine a theoretical estimate for the range of fluences needed for the ejection of NPs from the target surface given that only the region containing the NPs attains a temperature of phase explosion without the remainder of the surface matrix.

Considering close-to spherical sub-regions with an average weight concentration of NPs about the same as that of water, ~ 50 wt%, half the average distance between such sub-regions will be estimated to be comparable to the heat diffusion length L_D^P and will depend on the number of NPs in the sub-region. Similar to the formulation in Eq. (4.90), the average distance between subregions L_{NP}^{loc} is determined by the formula:

$$\left(L_{NP}^{loc}\right)^3 \simeq \frac{\rho_{loc}V_{loc}}{\rho_w} \times \frac{1-f^w}{f^w} \tag{4.93}$$

where ρ_{loc} is the density of the local sub-region, and V_{loc} is the volume of the sub-region and is equivalent to the volume occupied by N^{NP} NPs: $V_{loc} \simeq N^{NP} \cdot (L_{NP})^3$, with L_{NP} here being the spacing between NPs in the sub-region. The density of the sub-region is easily determined, in the approximation that the density of pure metal is an order of magnitude higher than that of water, in Eq. (4.94).

$$\rho_{loc} \simeq \frac{V_m\rho_m + L_{NP}^3\rho_w}{L_{NP}^3} \tag{4.94}$$

The spacing between NPs in the sub-region, L_{NP}, in Eq.(4.94), similar to the relation in Eq.(4.90), is here determined through the weight concentration of NPs in the sub-region, f^{loc}, as

$$(L_{NP})^3 \simeq \frac{\rho_m V_m}{\rho_w} \times \frac{1-f^{loc}}{f^{loc}} \tag{4.95}$$

For a sub-region containing a hundred NPs on average, $N^{NP} = 100$, for example, the distance between sub-regions according to Eq. (4.93) is $L_{NP}^{loc} = 74$ nm. This distance is comparable by order of magnitude to the heat diffusion length, $L_D^P = 145$ nm, and so part of the energy absorbed by NPs in the sub-region will be localized.

If one were to consider that energy absorbed in the sub-region were completely localized in it, the energy density in the sub-region will be determined by Eq. (4.96).

$$\epsilon_{loc} = \frac{F}{L_p} \frac{\left(L_{NP}^{loc}\right)^3}{N^{NP}(L_{NP})^3} \tag{4.96}$$

The fluence needed for the water matrix in the sub-region to be heated from the thermal reservoir temperature (77 K) to the state of phase explosion (T = 550 K) can be estimated in the limit of complete localization, after implementing the relation $\epsilon = c_p \rho_w \Delta T$, and using Eq. (4.96) to be F = 0.02 J/cm^2. [In this limit of complete localization in which the diameter of the described sub-region (100 NPs at local atomic concentration of 50 wt%) is 17 nm, the required pulse duration calculated from the relation $L_D^P = \sqrt{6 D_T \tau_p}$ will be $\tau_p = 0.34$ ns assuming the heat diffusion length L_D^P to be equal to the diameter of the sub-region]. It can be noticed that the calculated fluence is an order of magnitude lower than experimentally reported fluences. In the scenario however that the absorbed energy is only partly localized, as the pulse duration is longer and $L_{NP}^{loc} \sim L_D^P$, the fluence needed for the ejection of NPs from the target will be higher than F = 0.02 J/cm^2, but significantly lower than the fluence needed for homogeneous heating of the matrix medium to a state of phase explosion, i.e. 0.02 J/cm^2 < F < 1.5 J/cm^2.

4.8.2.3 Summary on estimating the range of experimental fluences for the possible ejection of NPs

We aim at running computer simulations that bring the above described scenarios to evidence (or to observation). Replicating the experimental pulse duration of 25 ns in a computational system made of ~ a hundred thousand atoms and molecules may take several weeks to witness the ablation of the target system in simulations. The goal is to run computer simulations with a shorter and more affordable pulse duration while still replicating the irradiation (or ablation) regime, and witnessing the described scenarios leading to ejection of NPs, within a few weeks.

A target with 5 wt% PdAc (the precursor concentration) has a penetration depth of L_p = 2.6 µm. The characteristic time of mechanical relaxation in an aqueous medium is $\tau_S \cong L_P/C_s$ = 1.7 ns, for the speed of sound C_s = 1497 m/s. The laboratory pulse duration, 25 ns, is longer: $\tau_p > \tau_s$, implying that laser irradiation conditions are away from the regime of stress confinement. The characteristic time of thermal relaxation is $\tau_{th} \cong L_p^2/D_T$ = 35 µs, implying that $\tau_p < \tau_{th}$. Laser deposition is also therefore in the regime of thermal confinement.

We are interested in ablation (or ejection of NPs) of the surface region, so we simulate model target samples as thick as 10 nm but less than 100 nm, 10 nm < L < 100 nm. In the case that the target thickness is smaller than the penetration depth, $L < L_p$, the characteristic time of mechanical relaxation is determined as a function of the target thickness:

$$\tau_S \cong L/C_s \qquad (4.97)$$

And the characteristic time of thermal relaxation is determined as:

$$\tau_{th} \cong L^2/D_T \qquad (4.98)$$

The characteristic time of mechanical relaxation for a target thickness of 100 nm is τ_S = 67 ps according to Eq. (4.97); the characteristic time of thermal relaxation according to Eq. (4.98) is τ_{th} = 71 ns. To stay away from the regime of stress confinement, and for thermal energy to be confined within the model target of thickness 10 nm < L < 100 nm, the pulse duration τ_p has to be chosen such that: $\tau_s < \tau_p < \tau_{th}$. A pulse duration of τ_p = 0.5 ns will satisfy this requirement. Practically speaking, even if the regime of thermal confinement, with τ_{th} determined by Eq. (4.98), is not satisfied in the model target, i.e. $\tau_p > \tau_{th}$ instead of $\tau_p < \tau_{th}$, heat cannot dissipate beyond a target of thickness lesser than the penetration depth; and so the condition of thermal confinement in the model target is nonetheless satisfied as in experiment. The condition $\tau_p < \tau_{th}$

truly matters only if the model target is thicker than the laser light penetration depth, preventing the diffusion of deposited energy beyond the penetration depth (or the irradiated region).

Model target samples for laser irradiation within the described conditions (or requirements) are prepared for simulations in which the expected scenarios of NP ejection can be witnessed.

In addition to simulating NP ejection, we consider it important to run computer simulations that demonstrate the nucleation and growth of metal clusters for NP formation as a result of pulsed laser irradiation. This requires having a model target sample made of only precursor molecules. The original precursor concentration in target samples with precursor molecules only is 5 wt%, and so the concentration of NPs in model targets with only NPs in them is 2.4 wt% correspondingly.

4.8.3   Model Targets for NP Formation and Ejection

Descriptions of the preparation of model target samples having both uniform and non-uniform dispersions of NPs in water matrix, and the preparation of a model target sample made up of only precursor molecules, are provided. Model target samples are prepared by thermal equilibration to 77 K of computational systems with periodic boundary conditions applied in all three dimensions of space, after which a substrate is applied underneath the resulting material system for equilibration at 77 K with a free boundary condition in the vertical direction − the direction of laser light propagation − and periodic boundary conditions in the lateral directions. The thermodynamic pressure is maintained at $P = 0$. The interaction with the substrate is assumed to be 3 times stronger than the interactions between molecules. The strength factor (3) is chosen to typically reproduce the average interaction of a molecule positioned in equilibrium above a water matrix, so that the substrate can be closely regarded as a material continuum of the model target.

4.8.3.1 Model laser target of uniform dispersion of Pd NPs

We create a computational system of one (1) Pd NP of size 2 nm in breathing sphere water at 77 K, such that the concentration of NP atomic material is 2.4 wt% in the system. The Pd NP has 292 atoms. [It was estimated that the distance between uniformly dispersed NPs of concentration 2.4 wt% is $L_{NP} \simeq 13$ nm]. The equilibrated on substrate computational material system is of size 122 Å x 122 Å x 116 Å; it is displayed in Figure 4.37. The obtained size of the material system is close to the predicted spacing between NPs uniformly dispersed in a matrix.
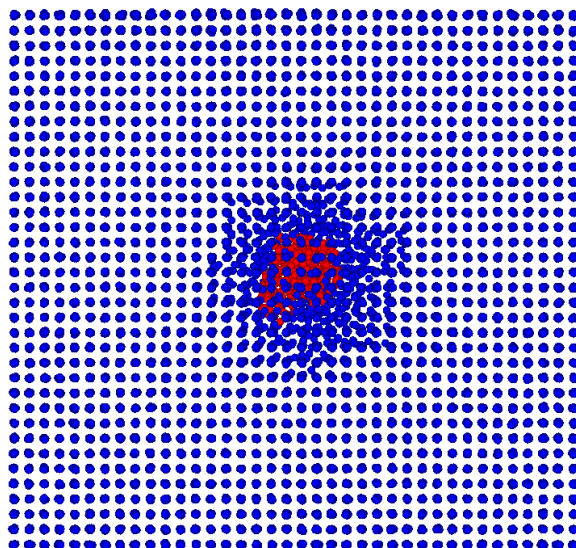
Figure 4.37   Snapshot of a single Palladium NP (of size 2 nm and having 292 atoms) in breathing sphere water at 77 K, thermodynamically equilibrated (P = 0) with a substrate underneath.

Implementing Eqs. (4.97) and (4.98) and using $L = 116$ Å, the values of the characteristic time of mechanical relaxation for this target sample is $\tau_S = 8$ ps, so that the condition $\tau_s < \tau_p$ is satisfied for the model pulse duration of 1 nanosecond, $\tau_p = 1$ ns. During the time of irradiation

the diffusion length is $L_D^P = 29$ nm, and since $L_{NP} < L_D^P$, heating of the target matrix is expected to be mostly uniform.

4.8.3.2 Model laser target of heterogeneous dispersion of Pd NPs

In order to obtain a target sample with a region of NP concentration significantly higher than the average concentration in the sample, a computational cell of randomly dispersed NPs in water matrix with the concentration of NP atoms about the same as that of water is first generated. The generated computational cell is then inserted in a larger computational cell of matrix molecules so that the resulting concentration of NP atoms is the expected average, in this case 2.4 wt%, in the target sample.

A computational cell having 63 wt% Pd NPs in water matrix is generated, and is inserted in a larger computational cell of matrix molecules, so that the resulting NP atomic concentration is 2.4 wt%; the resulting equilibrated on substrate structure at 77 K is of computational size 219 Å x 219 Å x 219 Å. A snapshot of the sample is displayed in Figure 4.38. The size range of the NPs is shown in Figure 6; there are six (6) NPs of sizes ~ 1-3 nm, with the average size being 1.93 nm.

Implementing Eqs. (4.97) and (4.98) and $L = 219$ Å, the values of the characteristic times of relaxation for this target sample are $\tau_S = 15$ ps and $\tau_{th} = 3.3$ ns, so that the condition $\tau_s < \tau_p < \tau_{th}$ is satisfied for the model pulse duration of 0.5 nanoseconds, $\tau_p = 0.5$ ns. And since the diffusion length during irradiation $L_D^P = 21$ nm, is comparable to the size of the computational cell (or the separation between local NP regions) L_{NP}^{loc}, heating of the target matrix is expected to be partly localized.
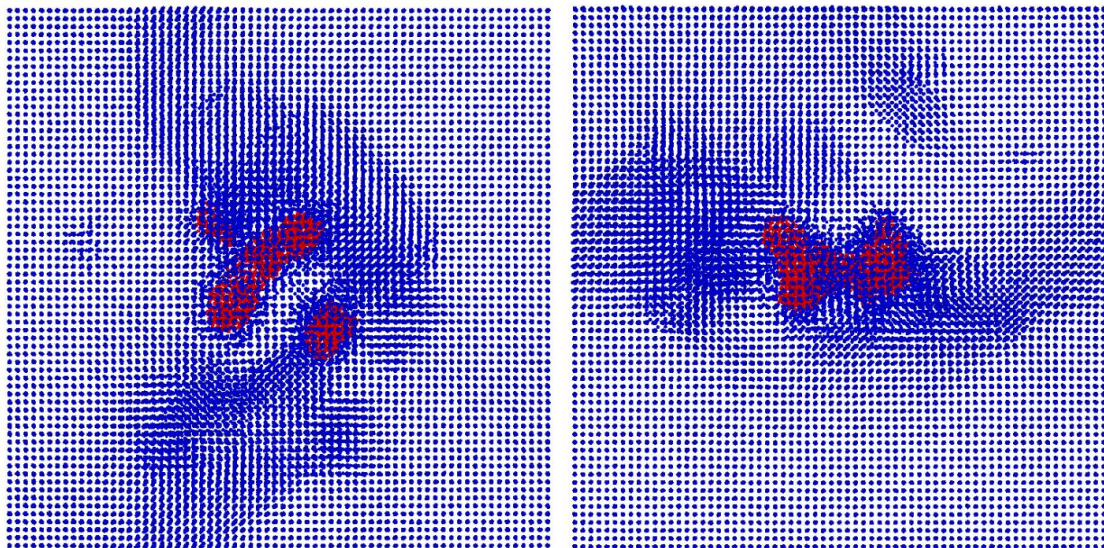
Figure 4.38 Snapshots of computational cell equilibrated on substrate at 77 K and having 2.4 wt% atomic Pd, with an average of 63 wt% atomic Pd in the region containing NPs. Left panel – top view; right panel – side view. NP atoms are colored red.

4.8.3.3 Model laser target of palladium acetate (precursor) molecules

Computational systems of PdAc in water matrix are obtained that are about the size of the computational systems of NPs in the matrix. The lateral sizes are chosen to be 15 nm, while the thickness is made to be slightly longer, 25 nm. As mentioned earlier, we wish here to study the effect of the solubility of the precursor on NP formation. A uniform dispersion (monomolecular phase) of precursor molecules will be representative of a completely soluble target. A clustered phase or nanocrystalline phase of precursor molecules will be representative of a partially soluble target. Snapshots of targets having 5wt% PdAc are displayed in Figure 4.39. The nanocrystals of PdAc are of size ~ 1-3 nm.
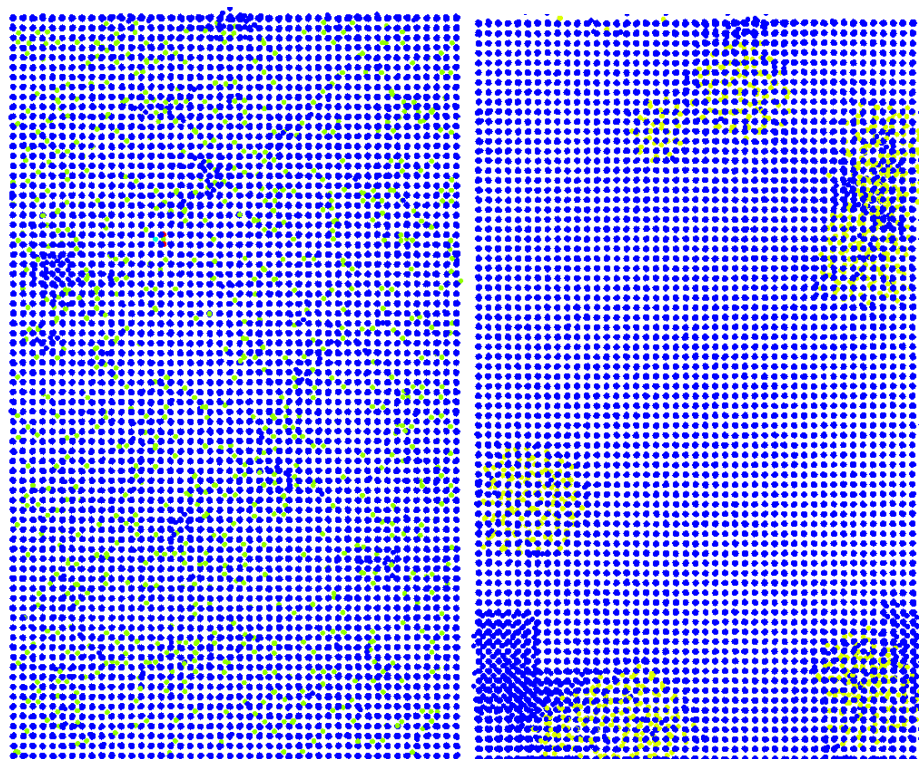
Figure 4.39   Snapshots of computational cell equilibrated on substrate at 77 K and having 5 wt% PdAc. Left panel – uniform dispersion of PdAc moleules; right panel – non-uniform dispersion of PdAc nanocrystals. PdAc molecules are yellowish green.

4.8.4   Results of MD Simulations

We first aim to see the process of growth of metal clusters for NP formation in targets containing precursor molecules, so we start with presenting results of simulations of the precursor targets.

4.8.4.1   Results of simulations of irradiated 5 wt% PdAc targets

Simulation results of the irradiation of completely soluble targets and partially soluble targets are presented. Snapshots during and after irradiation of the pulse are displayed. Cluster growth is illustrated through time dependence of average cluster size and diagrams of size distribution.

In some cases, simulation of the irradiation of the target, after it has been cooled down to 77K, by a subsequent pulse is done. This is in order to study the effect of continued pulsed irradiation and to evidence further cluster growth over a number of pulses.

4.8.4.1.1   Results of simulations of target with uniformly dispersed PdAc

It takes a very high fluence to heat up the precursor target by more than a hundred Kelvin. At a fluence of 16 J/cm^2: the target is completely solid after irradiation; and cluster growth is so slow, only a cluster as large as a tetramer is formed. Simulation of irradiation of the target by a second irradiation pulse shows that the temperature rise is only about ~ 50 K, and cluster growth is so slow that there no evidenced change in the size distribution during and shortly after irradiation. Snapshots of the irradiated target are displayed in Figure 4.40; the temperature contour plots are displayed in Figures 4.42 and 4.44; and diagrams on cluster growth are displayed in Figures 4.41, 4.43 and 4.45.

As a result of the irradiation of a target with uniformly dispersed precursor molecules, the temperatures are low and the matrix remains in a solid state. Cluster formation is mostly limited to single-atom diffusion in a solid state of the matrix. It is extremely difficult for a cluster to diffuse in a solid matrix, so formation is limited to low-number clusters.

Here, the threshold fluence for the ablation of the precursor target in a single pulse is high, $F^* > 16$ J/cm^2. The result is in the same order of magnitude as the threshold fluence determined in the continuum model. The difference, however, can be explained by the over-estimation of the predicted average cluster size during single-pulse irradiation in the continuum model. This means a higher absorption cross-section of Pd atoms and hence a lower threshold for ablation. It has been evidenced that a single tetramer which is only of size 0.5 nm is formed in the irradiated

target. This is in pale comparison to the assumption that each Pd atom on average will be in a cluster of size 0.5 nm in the continuum model.
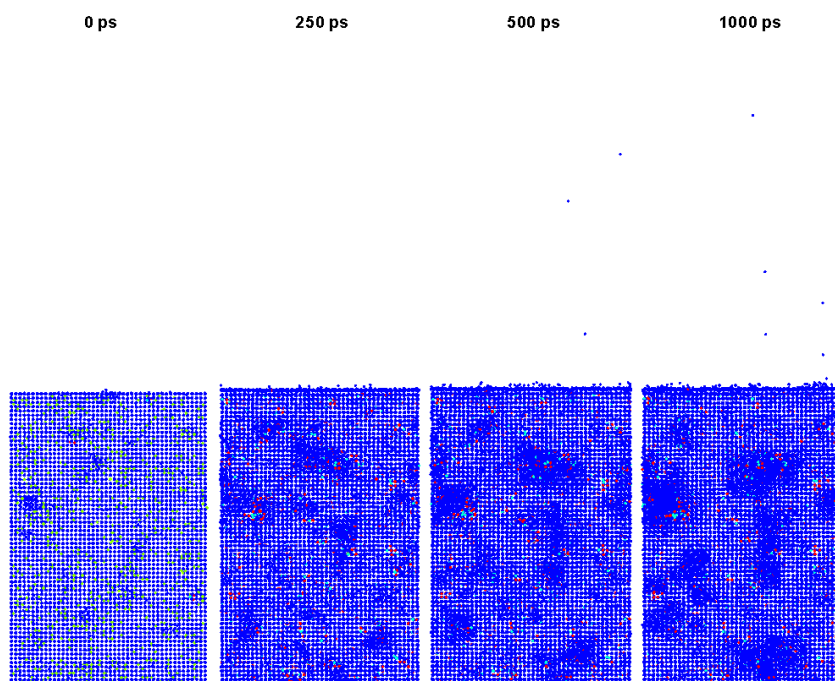
Figure 4.40   Snapshots of target made of 5 wt% uniformly dispersed PdAc irradiated by a fluence of 16 J/cm^2. Water BS molecules are blue-colored, PdAc molecules are yellowish green, Ac ligand molecules are red, and Pd atoms are green.
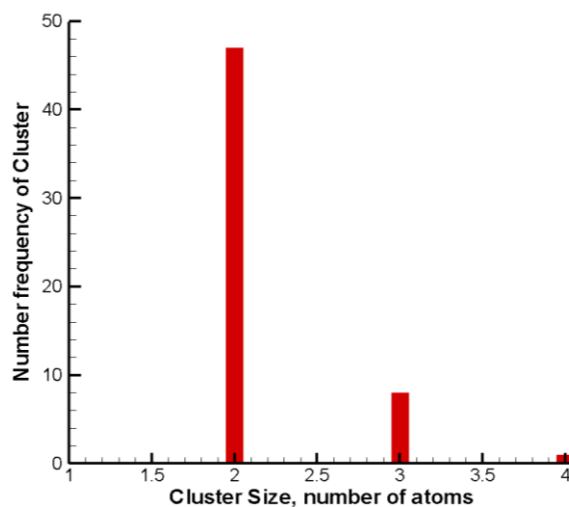
Figure 4.41   Size distribution of Pd clusters in target made of 5 wt% uniformly dispersed PdAc 500 ps after irradiation by a pulse of fluence 16 J/cm^2.
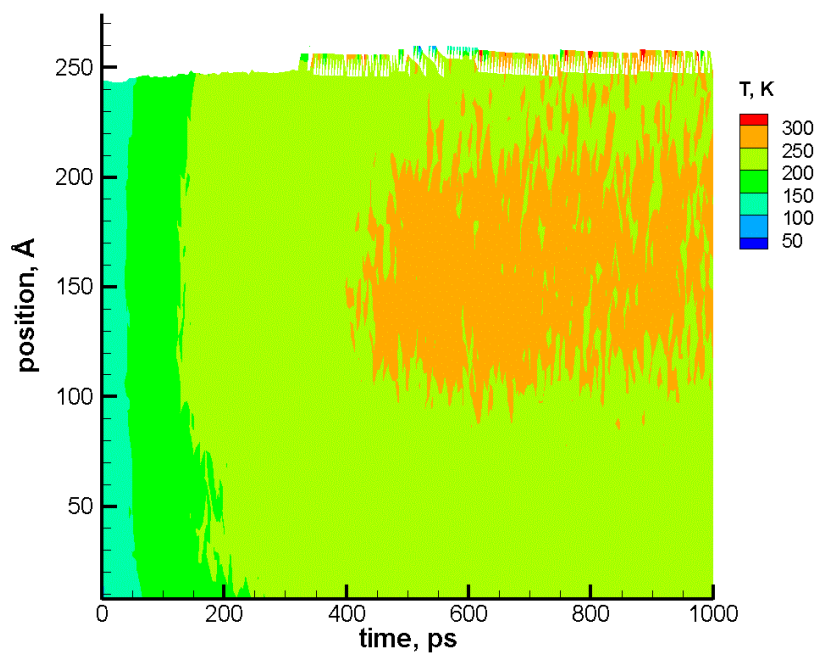
Figure 4.42   Contour plot of the temperature of target made of 5 wt% uniformly dispersed

PdAc irradiated by a laser fluence of 16 J/cm^2.
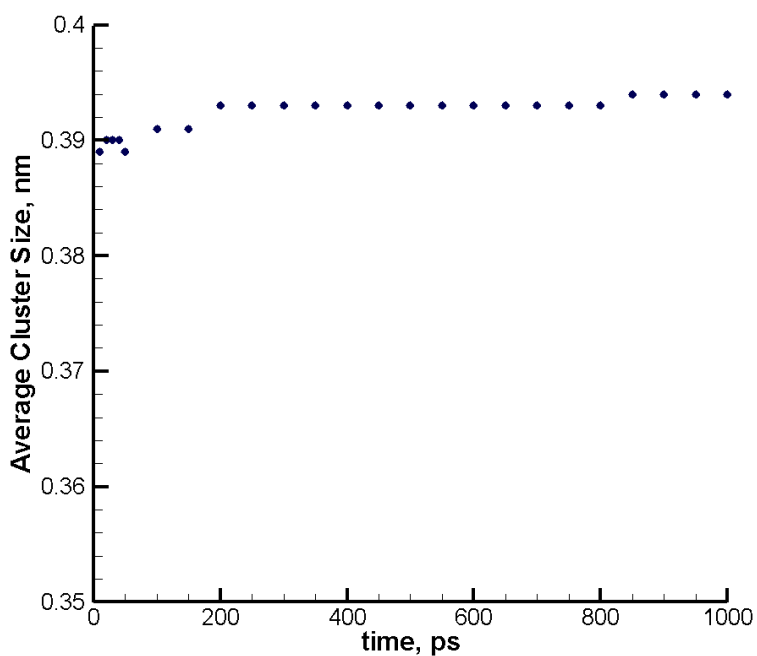
Figure 4.43   Time dependence of average cluster size in irradiated target having 5 wt%

uniformly dispersed PdAc; the fluence is 16 J/cm^2.
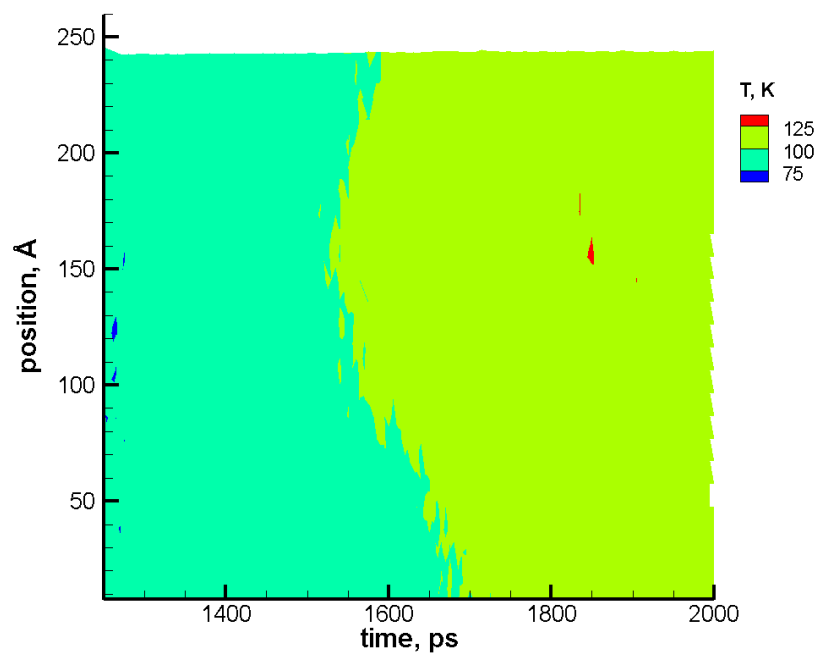
Figure 4.44   Contour plot of the temperature of target having 5 wt% uniformly dispersed

PdAc, during and shortly after irradiation by the second pulse, of fluence 16 J/cm^2.
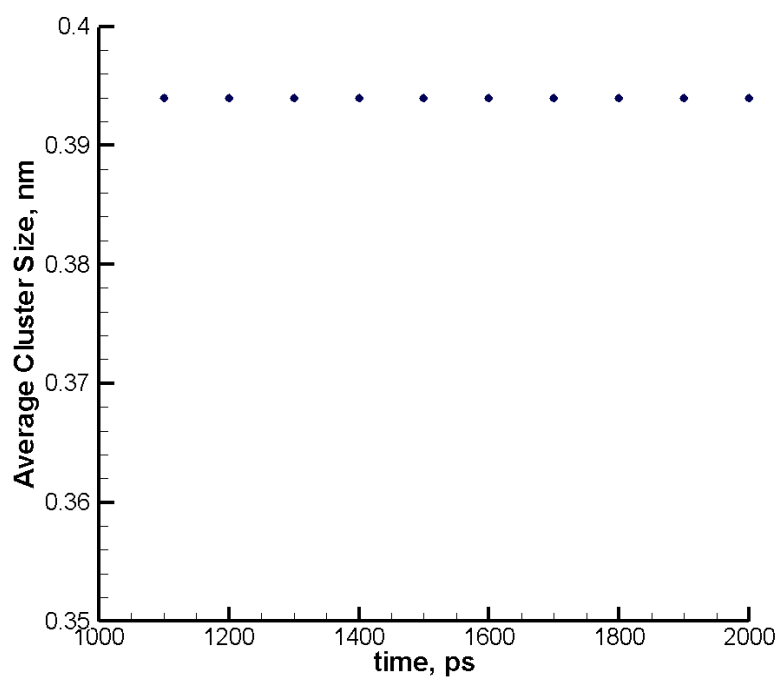
Figure 4.45   Time dependence of average cluster size in target having 5 wt% uniformly

dispersed PdAc, during and shortly after irradiation by the second pulse, of fluence 16 J/cm^2.

4.8.4.1.2   *Results of simulations of target with non-uniformly dispersed PdAc*

While it took a fluence as high as 16 J/cm^2 to raise the temperature of the target with a uniform dispersion of PdAc by a few tens of Kelvins, for a target with non-uniformly dispersed PdAc the temperature rise is significantly higher, and a fluence of only 3 J/cm^2 leads the target to a state of ablation in a single pulse. Snapshots are displayed in Figure 4.47. As seen in the diagram for cluster size distribution in Figure 4.48, NPs of size ~ 1 nm are formed in the target prior to ablation. Ablation is seen to occur not as a result of the whole sample attaining temperatures close to phase explosion, but as a result of local phase explosion of only some regions of the target that provide a push to eject overlying material beyond the target. This local distribution of energy can be evidenced to be due to the local absorption of NPs, for example, at 500 ps – when the target is not yet ablated, the bottom region of the target contains NPs and is at a temperature above 550 K, providing an ejecting push to overlying material; see Figures 4.46 and 4.47. The irradiated area of the computational cell is 15x15 nm^2, much smaller than the area of the irradiated surface in experiment. This means that the push provided by the locally ablated region in this simulation may not be enough for the ejection of overlying material in the actual experimental target. The simulation result however indicates that there is a chance of ejection in the experimental target in similar conditions.

At a lower fluence, 2 J/cm^2, the precursor target does not ablate due to single-pulse irradiation, but irradiation in a multi-pulse regime leads to ablation of the target, in the third pulse, as a number of NPs have been formed in the target; see Figure 4.49 for snapshots. The employed fluence is below the ablation threshold of the precursor target, but leads the target to ablation in a latter stage of the multi-pulse irradiation once there is a sizable number of NPs in it. Cluster formation occurs in the first pulse, growth of the clusters ensues in the second pulse, and in the

third pulse a few NPs are large enough for ablation (or ejection) to occur at a fluence of 2 J/cm^2. As can be seen in the diagram displaying the ratio of the total absorption cross-section of NPs to the total absorption cross-section in the latter stage of irradiation, Figure 4.50 d, absorption by the NPs accounts for almost half of the total absorption. Cluster growth is depicted in Figures 4.50 and 4.52. It can again be seen, in the snapshots of Figure 4.49 and the contour plots of Figure 4.51, that ablation results from a region containing NPs that are of size ~ 1 nm as illustrated in the size distribution in Figure 4.52.
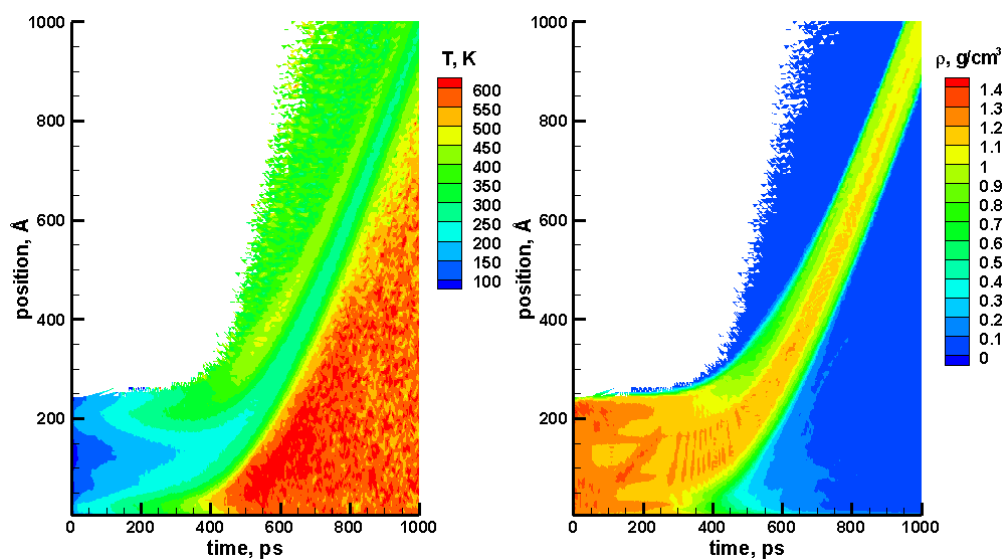
Figure 4.46 Contour plots of target having 5 wt% non-uniformly dispersed PdAc during and shortly after irradiation by a single pulse, of fluence 3 J/cm^2: left – temperature; right – density.
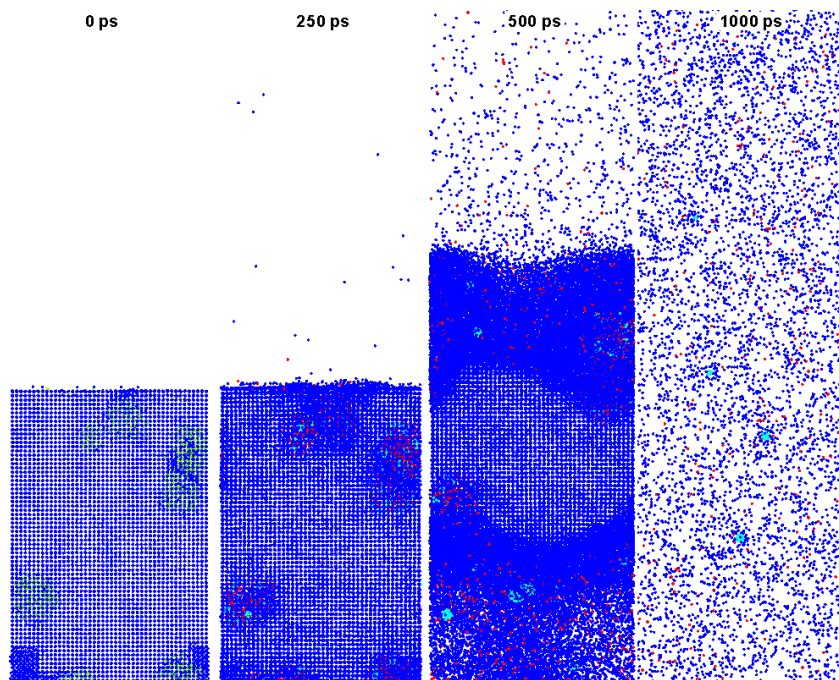
Figure 4.47 Snapshots of target made of 5 wt% non-uniformly dispersed PdAc irradiated by a fluence of 3 J/cm^2. Water BS molecules are blue-colored, PdAc molecules are yellowish green, Ac ligand molecules are red, and Pd atoms are green.
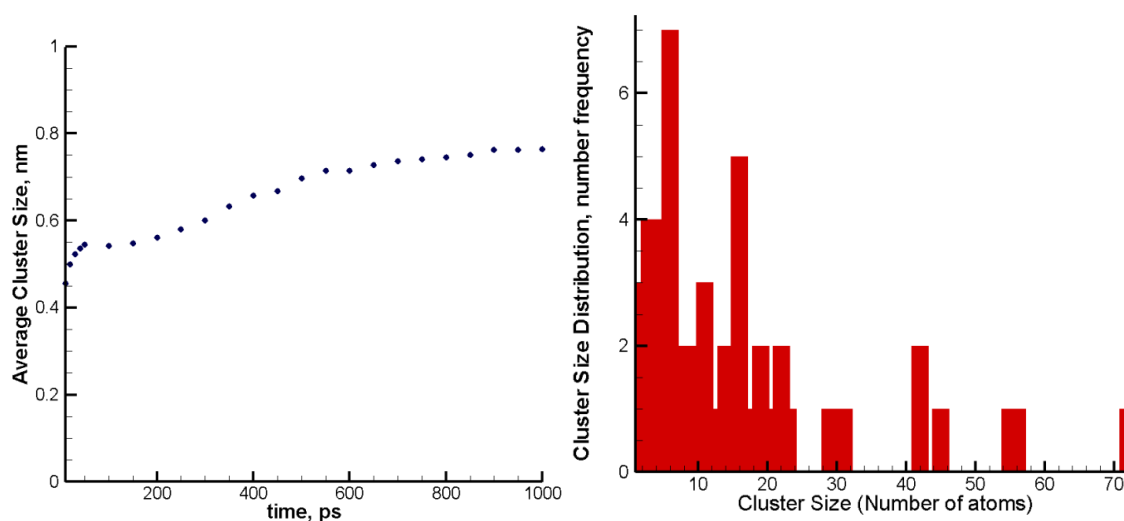
**Figure 4.48** Cluster size growth in target made of 5wt% non-uniformly dispersed PdAc irradiated by a pulse of fluence 3 J/cm^2: left – time dependence of average cluster size, right – size distribution at 1000 ps.
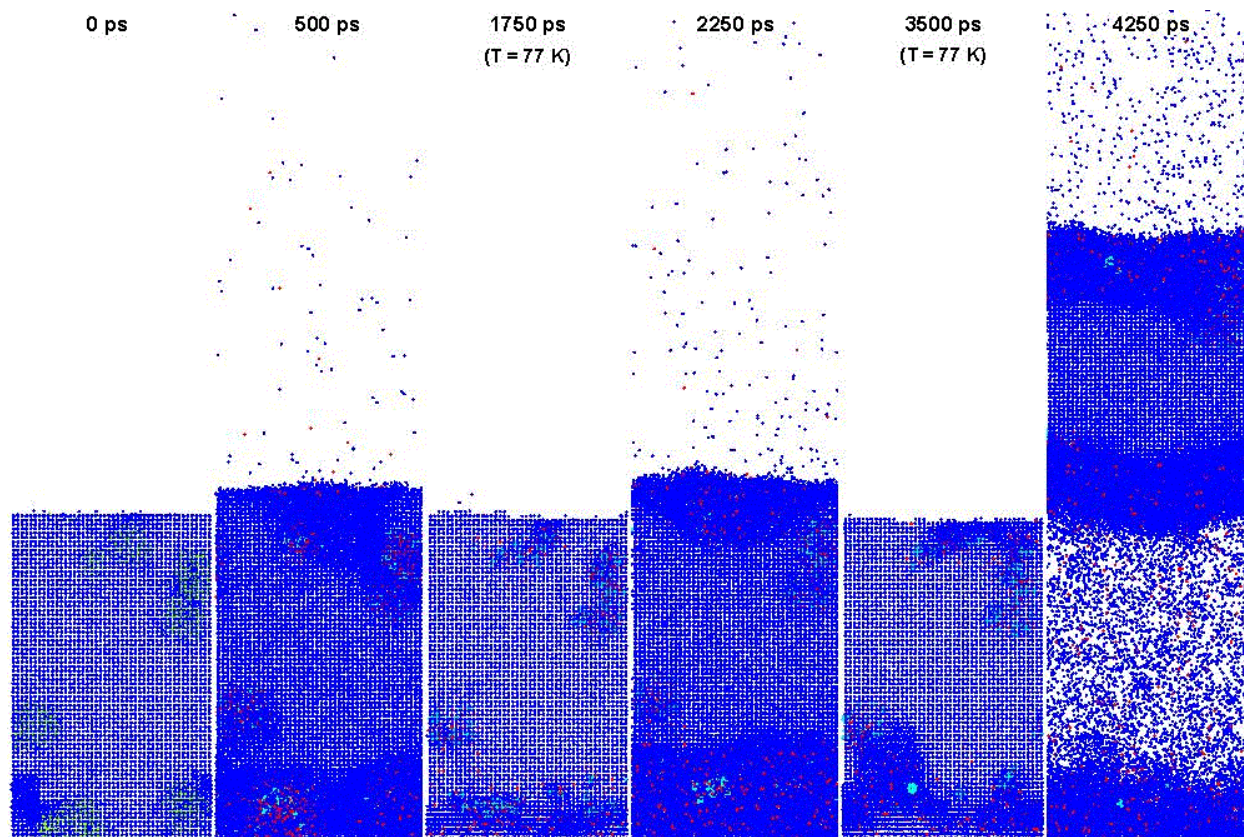
Figure 4.49   Snapshots of target made of 5 wt% non-uniformly dispersed PdAc in a multi-pulse irradiation regime at a fluence of 2 J/cm^2. The second and third pulses start at 1750 ps and 3500 ps, respectively, when the target temperature is 77 K – the temperature of LN$_2$ thermostat applied to bottom of target.

a)
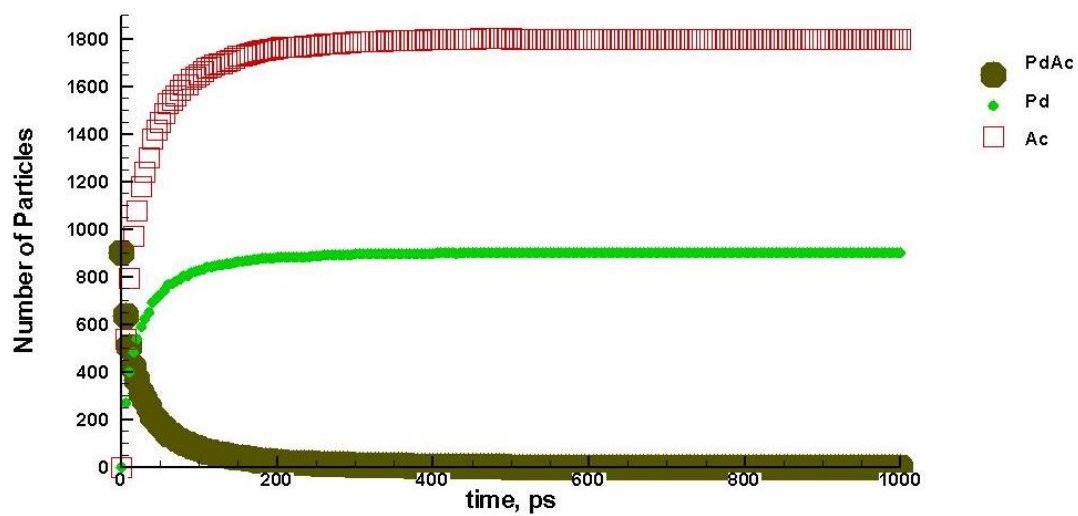
b)
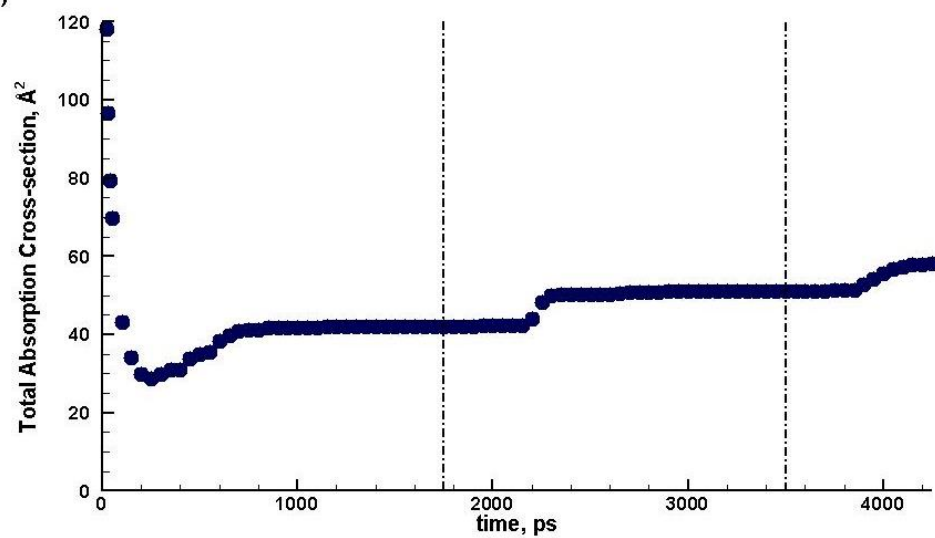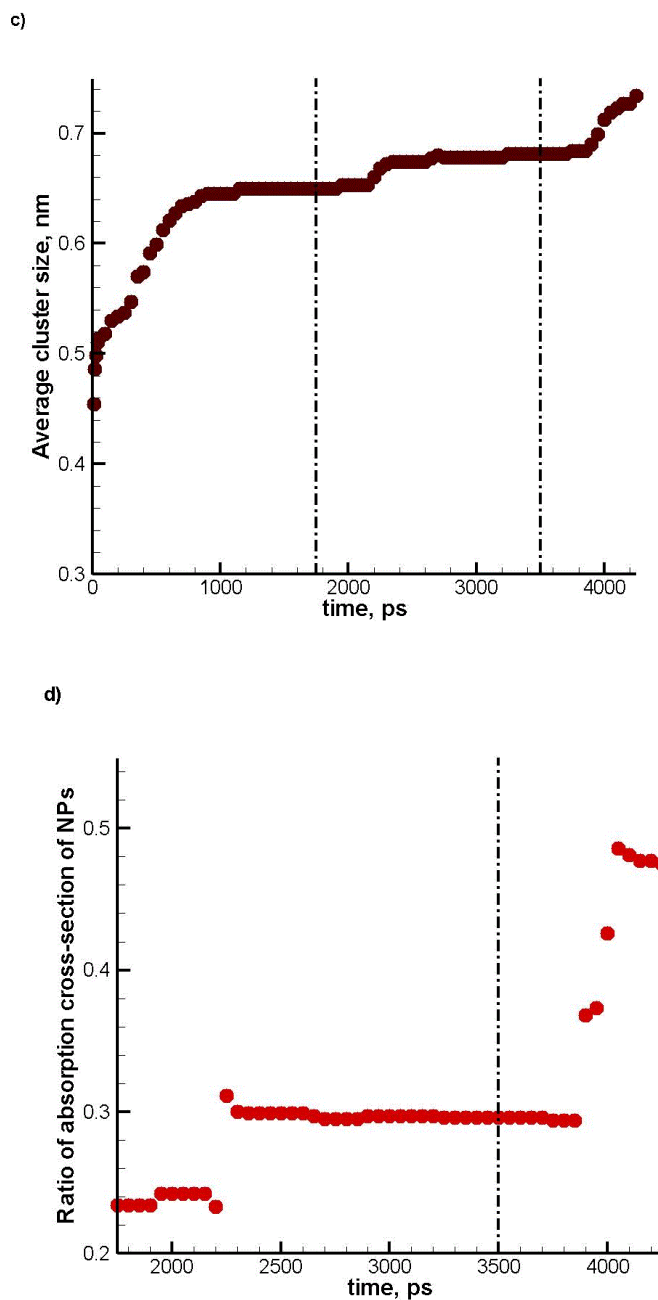
Figure 4.50   Time dependence in the target made of non-uniformly dispersed PdAc irradiated at a fluence of 2 J/cm^2 of a) the number of solute atoms and molecules – PdAc, Pd and Ac, b) the total absorption cross-section of the solute atoms and molecules, c) the average palladium cluster size, d) the ratio of the absorption cross-section of NPs to total absorption cross-section during and shortly after irradiation by 2nd and 3rd pulses. The vertical dashed lines indicate the start of the 2nd and 3rd pulses at 1750 ps and 3500 ps, respectively.
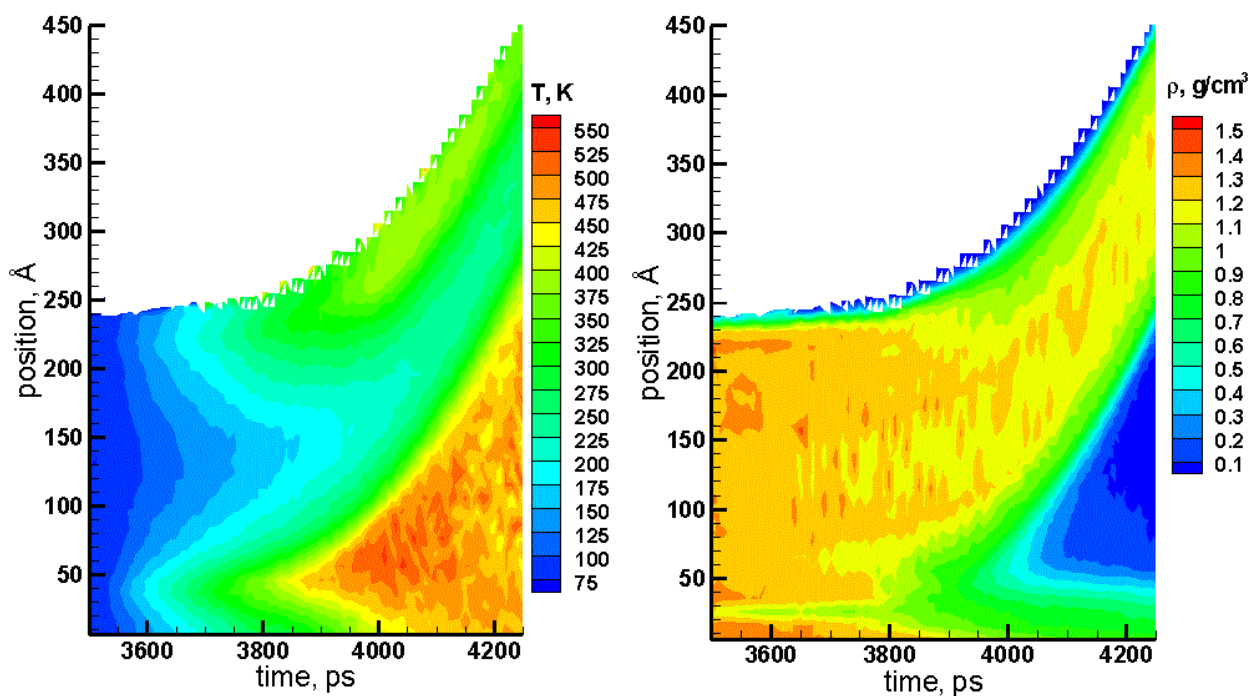
Figure 4.51 Contour plots of target having 5wt% non-uniformly dispersed PdAc in multi-pulse irradiation regime during and shortly after irradiation by the third pulse, of fluence 2 J/cm^2: left – temperature; right – density.
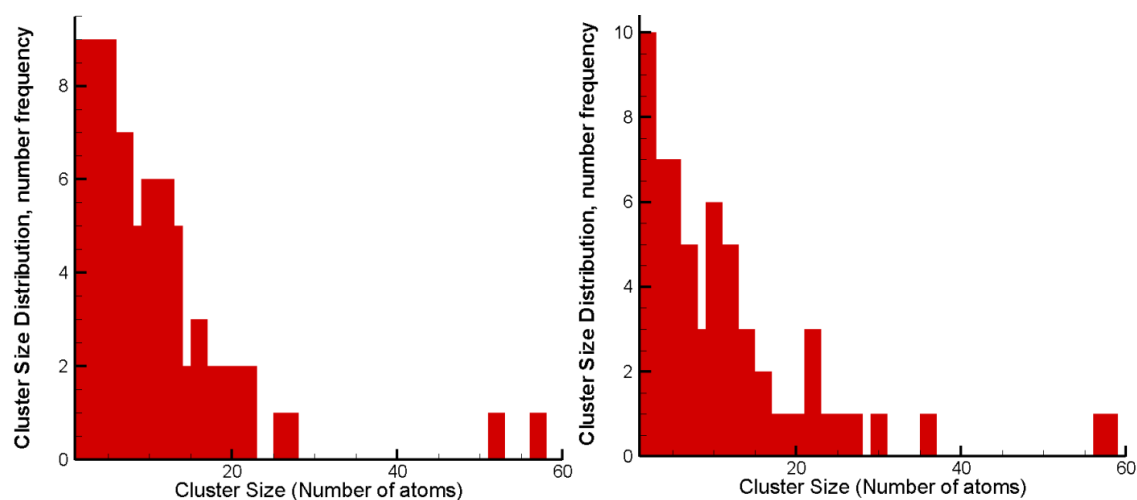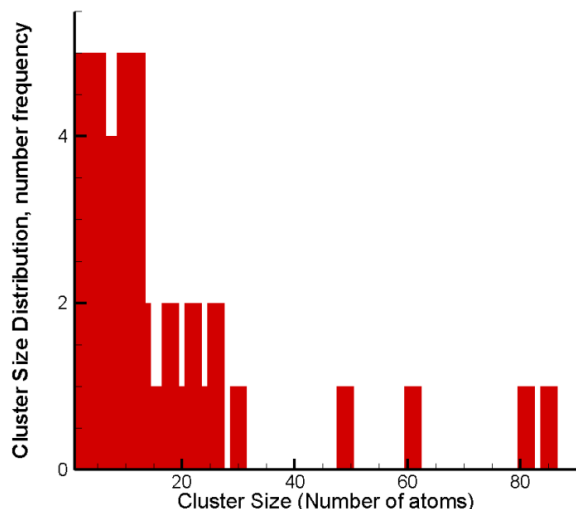
Figure 4.52 Size distribution in multi-pulse irradiation of target having 5wt% non-uniformly dispersed PdAc, irradiated at a fluence of 2 J/cm^2, at different times: top left – at time 1500 ps, between first and second pulse; top right – at 3000 ps, between second and third pulse; at 4250 ps, after third pulse.

4.8.4.1.3   Comparison of the irradiation of targets with uniform and non-uniform dispersion of PdAc at same fluence

It has been witnessed already that the single-pulse ablation threshold fluence is much lower for the target with a non-uniform dispersion of PdAc than the target with a uniform dispersion of PdAc. We present simulations of the irradiation of both targets at the same fluence, 2.5 J/cm^2, in order to make the comparison more evident. The total absorption cross-section is deemed a factor that significantly determines the temperature rise and hence the cluster size growth. See Figures 4.55 and 4.56 for displays of the total absorption cross-section and cluster size growth for the target with uniformly dispersed PdAc and the target with non-uniformly dispersed PdAc, respectively. [The step-decrease in the number of Ac molecules in Fig. 4.56 a) accounts for the evaporated Ac molecules that have moved far above the target and are no longer counted in the

computational cell.] At this fluence the target with non-uniformly dispersed PdAc ablates – see Figures 4.53 and 4.54 for snaphots of the target and contour plots of temperature and density, during and shortly after irradiation, respectively. The target with uniformly dispersed PdAc is not expected to ablate since it does not do so at higher fluences.
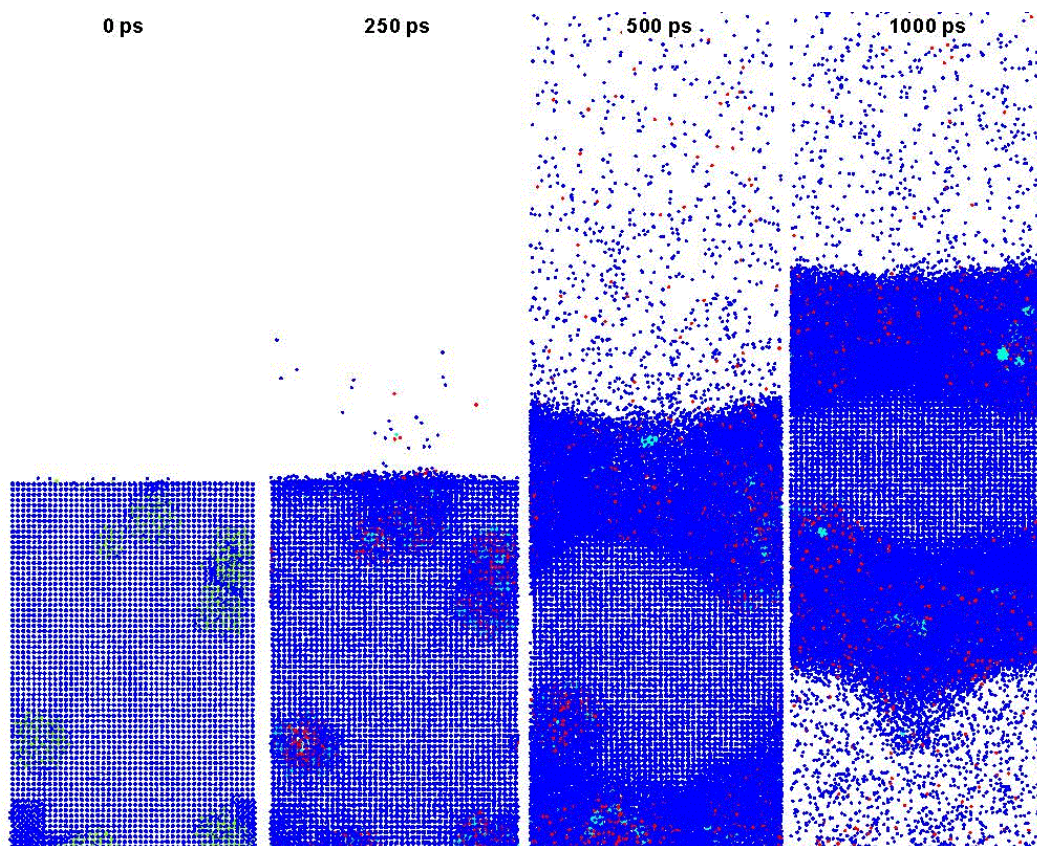
Figure 4.53   Snapshots of target made of 5 wt% non-uniformly dispersed PdAc irradiated by a fluence of 2.5 J/cm^2. Water BS molecules are blue-colored, PdAc molecules are yellowish green, Ac ligand molecules are red, and Pd atoms are green.

The total absorption cross-section in the target with non-uniformly dispersed PdAc decreases as highly absorbing precursor molecules are decomposed, but eventually increases during irradiation as clusters readily form from sites of nanocrystals of the precursor and the absorption cross-section per atom of a cluster increases with cluster growth. The increasing laser-energy

deposition from the time the total absorption cross-section attains a minimum is responsible for increasing the mobility and growth of clusters, leading to the attainment of temperatures in the absorbing regions high enough to cause ablation of the target.
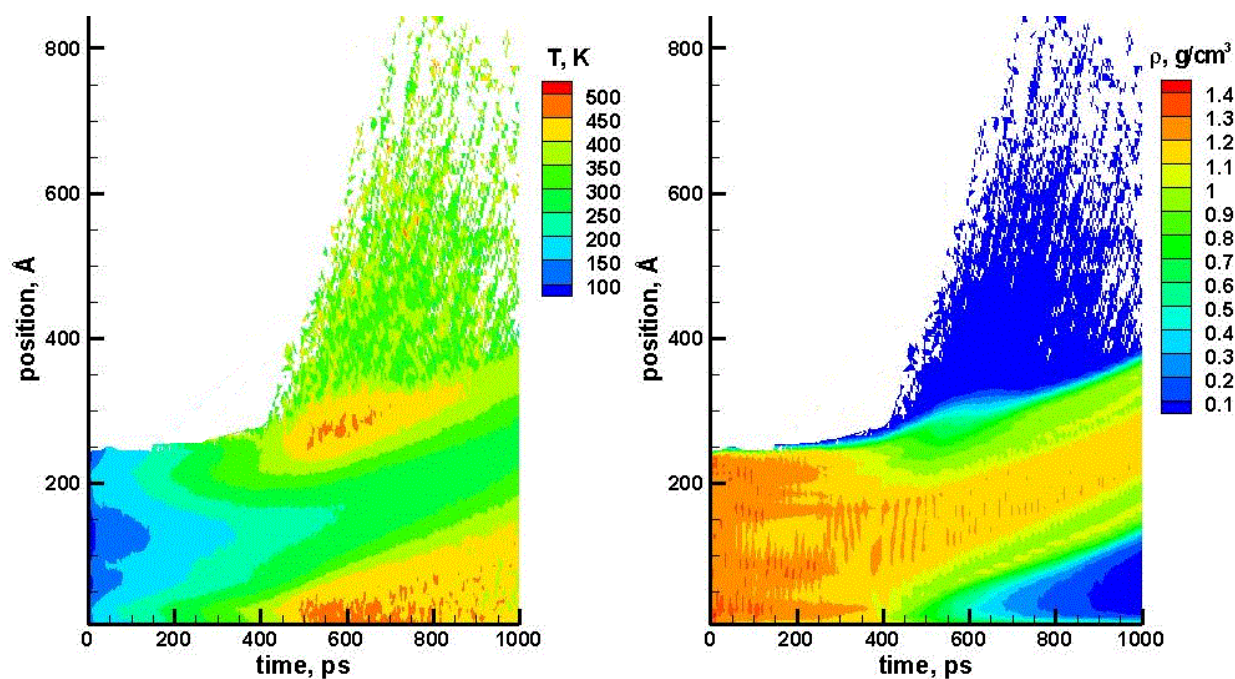
**Figure 4.54**   Contour plots of target having 5 wt% non-uniformly dispersed PdAc during and shortly after irradiation by a single pulse [of fluence 2.5 J/cm^2]: left – temperature; right – density.
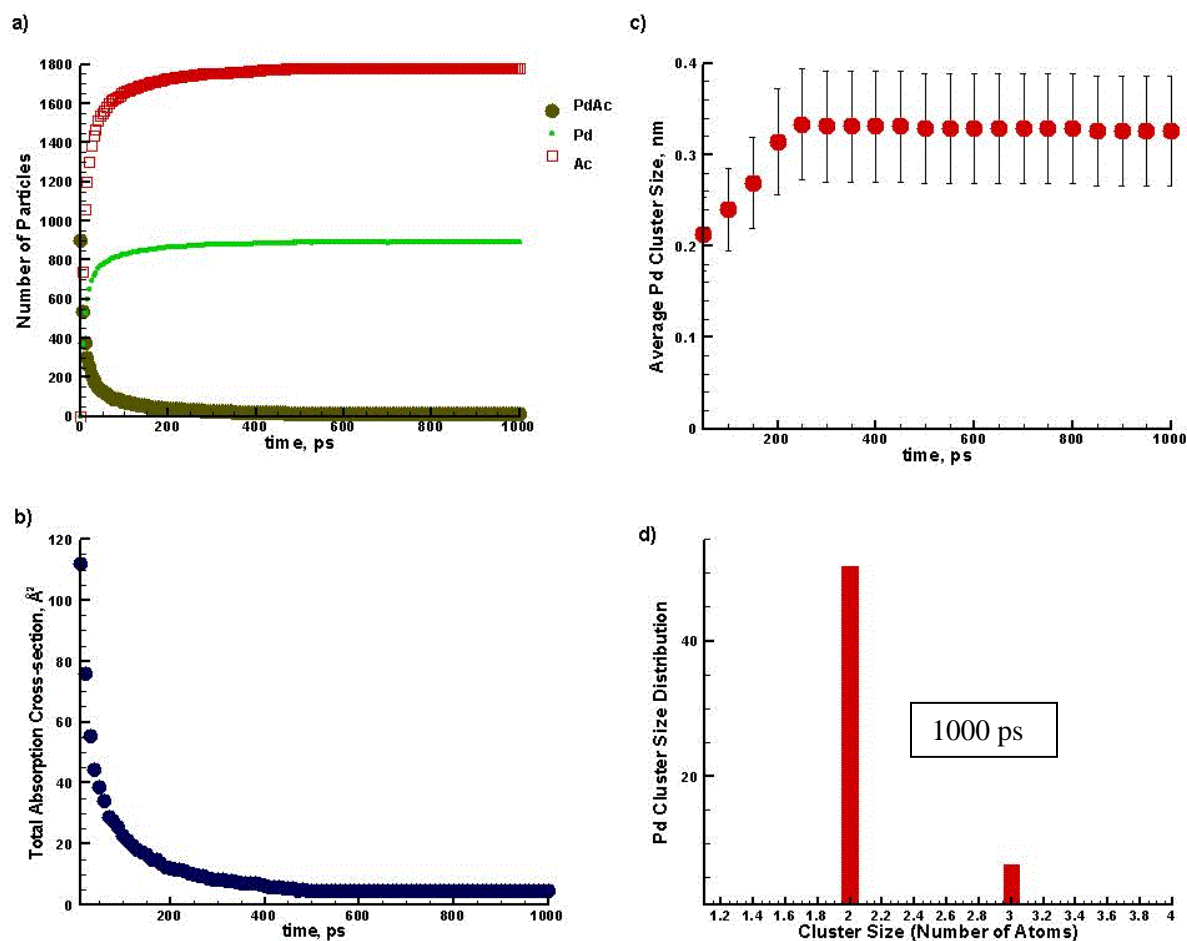
Figure 4.55 Time dependence in the target made of uniformly dispersed PdAc irradiated at a fluence of 2.5 J/cm^2 of a) the number of solute atoms and molecules – PdAc, Pd and Ac, b) the total absorption cross-section of the solute atoms and molecules, c) the average palladium cluster size, d) the Pd cluster size distribution at 1000 ps, i.e. 500 ps after the end of the irradiation pulse.
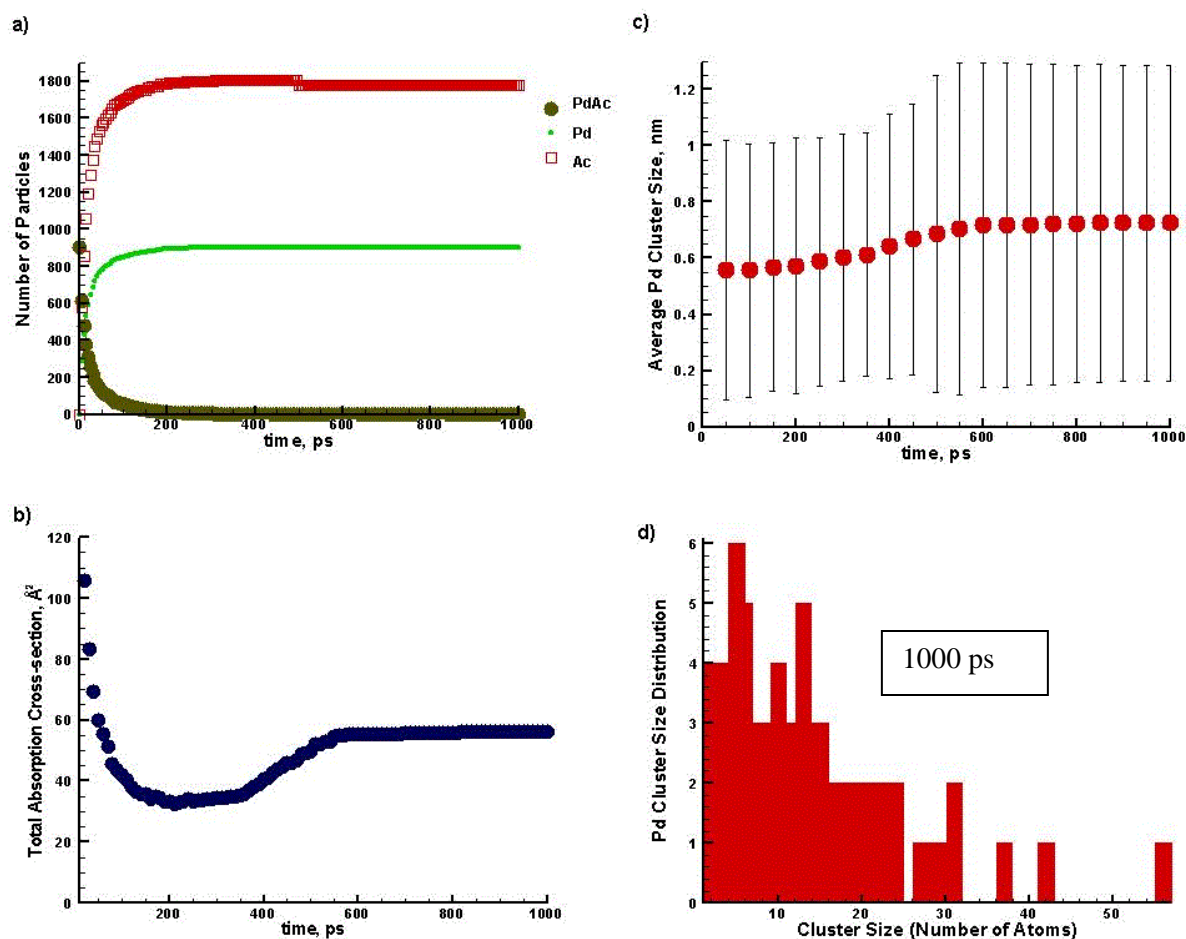
Figure 4.56 Time dependence in the target made of 5 wt% non-uniformly dispersed PdAc irradiated at a fluence of 2.5 J/cm^2 of a) the number of solute atoms and molecules – PdAc, Pd and Ac, b) the total absorption cross-section of the solute atoms and molecules, c) the average palladium cluster size, d) the Pd cluster size distribution at 1000 ps, i.e. 500 ps after the end of the irradiation pulse.

4.8.4.2 Results of simulations of the irradiation of targets containing NPs

Results of simulations of the irradiation of the target with a uniform distribution of NPs and of the target with a region having a high concentration of dispersed NPs are presented.

4.8.4.2.1   Results of simulations of the irradiation of target representative of a uniform dispersion of NPs

The model target having one NP, representative of a uniform dispersion of NPs, is irradiated at fluences that are close to the theoretically estimated value of the threshold fluence for NP ejection in conditions of even heating of the matrix, $F^* = 1.5$ J/cm^2, in determined earlier in this section. A pulse duration of 1000 ps instead of 500 ps here is chosen so as to maximize uniform distribution of laser-absorbed energy through slow heating.

At a fluence of $F = 1.8$ J/cm^2, the surface of the target ablates as the NP is close to being ejected; see snapshots of irradiated target in Figure 4.57. This fluence is characteristic to being the threshold for ejection in the target. It can be seen in the contour plot of temperature, Figure 4.58, that the matrix is close to being uniformly heated.
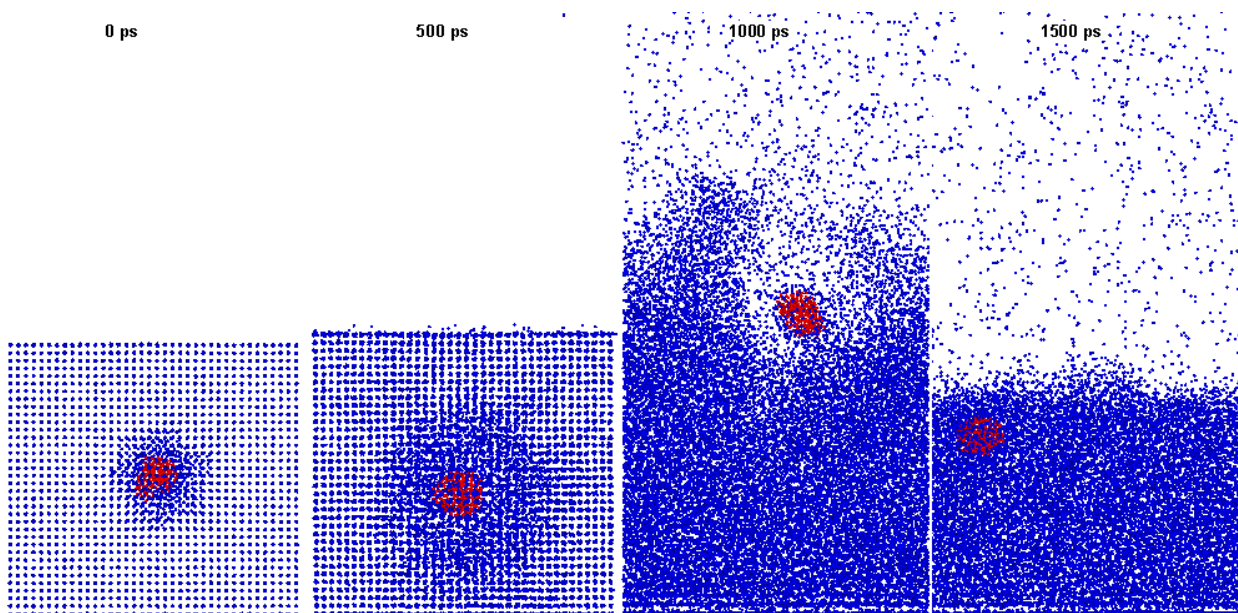
Figure 4.57   Snapshots of target representative of a uniform dispersion of NPs of 2.4 wt% concentration, irradiated by a pulse of 1.8 J/cm^2.

At a fluence of 2.1 J/cm^2, the target ablates providing for ejection of the NP together with the vaporizing matrix; see Figure 4.59. This is the expected mechanism of NP ejection in this target, as was predicted by estimates. At the time of ejection most of the target is at a temperature equal to or above explosive boiling, T ≳ 500 K, see contour plots of temperature and density in Figure 4.60.
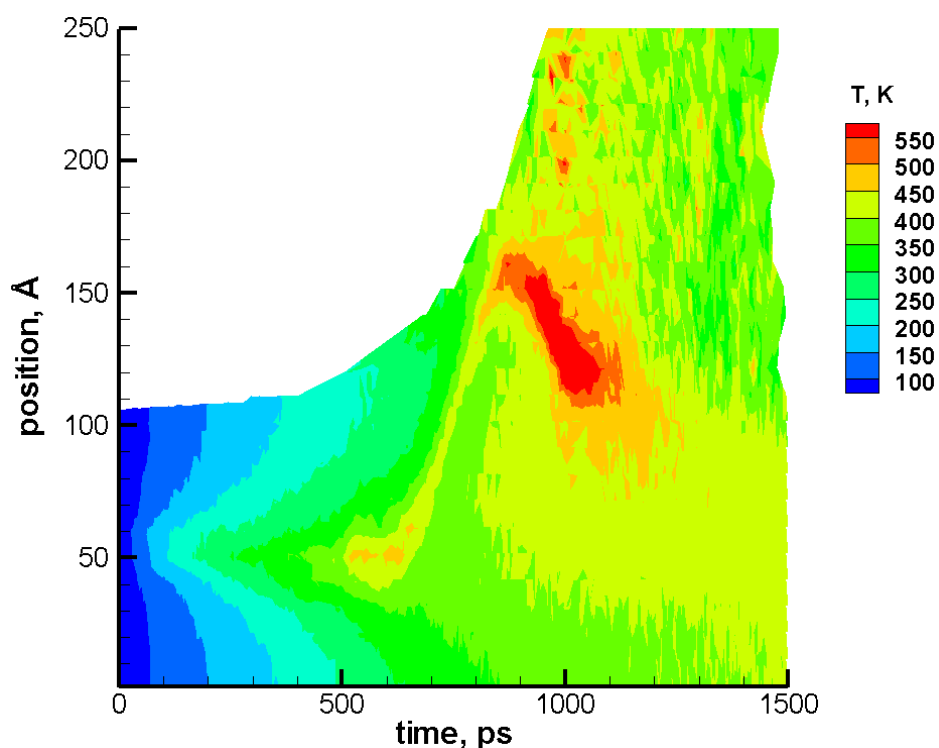
Figure 4.58 Temperature contour plot of target representative of a uniform dispersion of NPs of 2.4 wt% concentration, irradiated by a pulse of 1.8 J/cm^2.
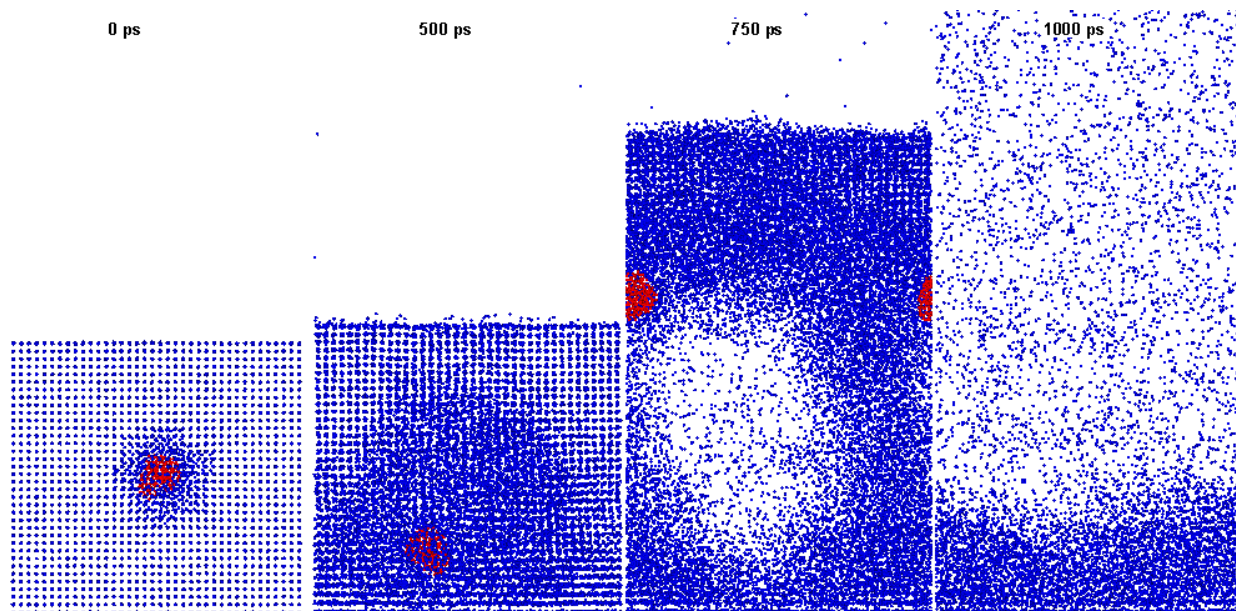
Figure 4.59 Snapshots of target representative of a uniform dispersion of NPs of 2.4 wt% concentration, irradiated by a pulse of 2.1 J/cm^2.

Figure 4.60 Contour plots of target representative of a uniform dispersion of NPs of 2.4 wt% concentration, irradiated by a pulse of 2.1 J/cm^2. Left – temperature; right – density.

4.8.4.2.2   Results of simulations of the irradiation of target representative of a non-uniform

dispersion of NPs

The model target having a region with a local NP concentration of 60 wt% but total NP atomic concentration of 2.4 wt% that is representative of a target with a heterogeneous dispersion of NPs is irradiated at fluences lower than the estimated threshold fluence for NP ejection in conditions of even heating of the matrix, i.e. $F < 1.5$ J/cm^2.

At a fluence of 0.6 J/cm^2, NP ejection is seen to occur without the target ablating; see Figure 4.61. It can be noticed that a significant part of the target remains solid – the bottom part is at a temperature below 200 K, see temperature contour plot in Figure 4.62. In the process of ejection, the NPs stick together; see Figure 4.63 for cluster size distribution. Figure 4.64 displays the z-component of the centre of mass and the velocity of the centre of mass of the NPs. It can be seen that the upward velocity of the NPs starts to increase at ~ 200 ps, until it peaks at ~ 600 ps when the particle is being ejected.

To uncover what gives rise to the increase in upward velocity of the NPs prior to ejection, a contour plot in and around the local region of NPs that reveals the temperature and density is deemed useful, see Figure 4.65. It can be easily noticed that while the temperature of NP material surpasses ~ 1000 K, the matrix up to within ~ 5 nm of the NP local region is at a temperature higher than the phase explosion temperature of water (> 500 K). The described region containing NP material and water matrix at temperatures higher than the temperature of phase explosion can be called a 'bubble'. It can be seen in Figure 4.65 that at 250 ps, at a time when the upward velocity of the NPs starts to increase, the temperature below the NPs is higher than the temperature above the NPs, and at 550 ps, when the upward velocity is dramatically higher, the difference in temperatures is significantly higher. Although the temperature is

symmetric around the centre of mass of the region of NPs when its average upward velocity is steady, material above the region of NPs is exposed to or closer to the surface and has more room for expansion than material below the region. This leads to the material below the NPs region being in a state of higher temperature and pressure. The resulting pressure difference should create a net force upward on the NPs.

To better understand how a net pressure from below the local NP region arises, the simulation of a single NP in a target with similar conditions of local energy deposition is run, and the difference in pressure below and above the NP is determined. The computational system is the same that is used to study the irradiation of a target with a uniform dispersion of NPs. The pulse duration is made to be 200 ps so that energy deposited into the system is partly localized. Snapshots of the irradiated target are displayed in Figure 4.66 a, and the dynamics of the NP prior to ejection are revealed in Figure 4.66 b. It can be seen in Figure 4.66 b that the NP starts to move upward at ~ 40 ps. The thermodynamic conditions that initiate an upward movement of the NP are revealed in Figure 4.66 c-d. The values of pressure below and above the NP, averaged over lateral directions, are determined in the time frame 20-50 ps. The net pressure acting from below the NP and averaged over the 20-50 ps time frame is determined as $P_{net} \cong 350$ MPa -200 MPa = 150 MPa.

At a higher fluence of 1.2 J/cm^2, ejection is more dynamic and the surface is seen to ablate, see Figures 4.67 and 4.68. The temperatures are high and there is mild fragmentation of the NPs, leading to the release of several single atoms; see Figures 4.69 and 4.70 for cluster size distribution.
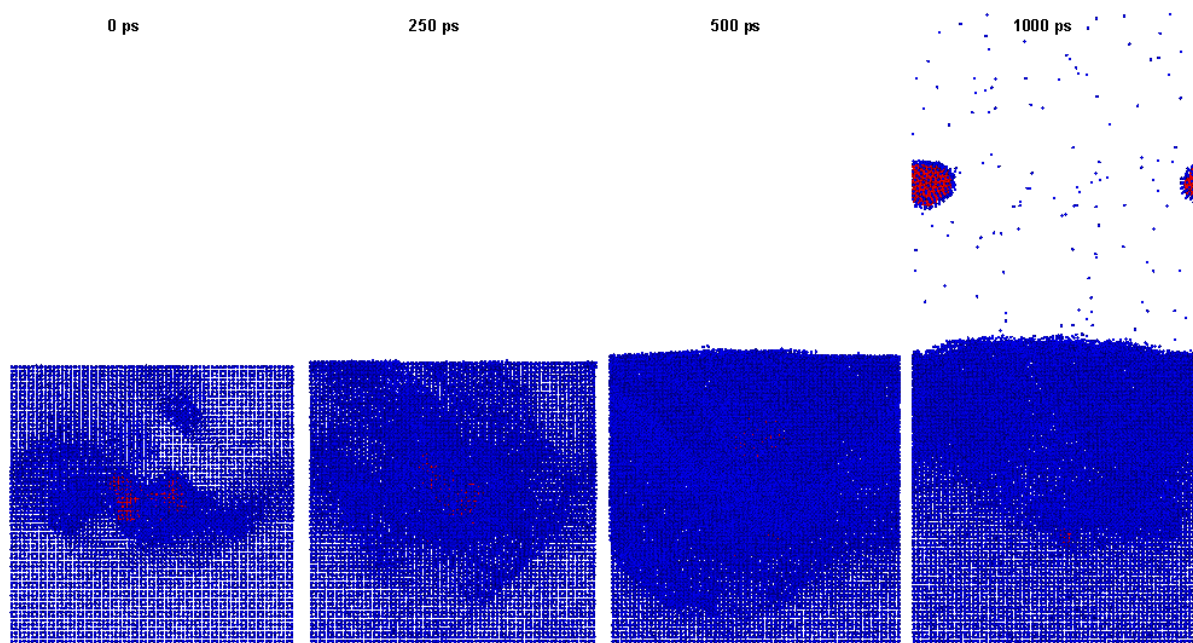
Figure 4.61 Snapshots of target representative of a non-uniform dispersion of NPs of 2.4 wt% concentration, irradiated by a pulse of 0.6 J/cm^2.
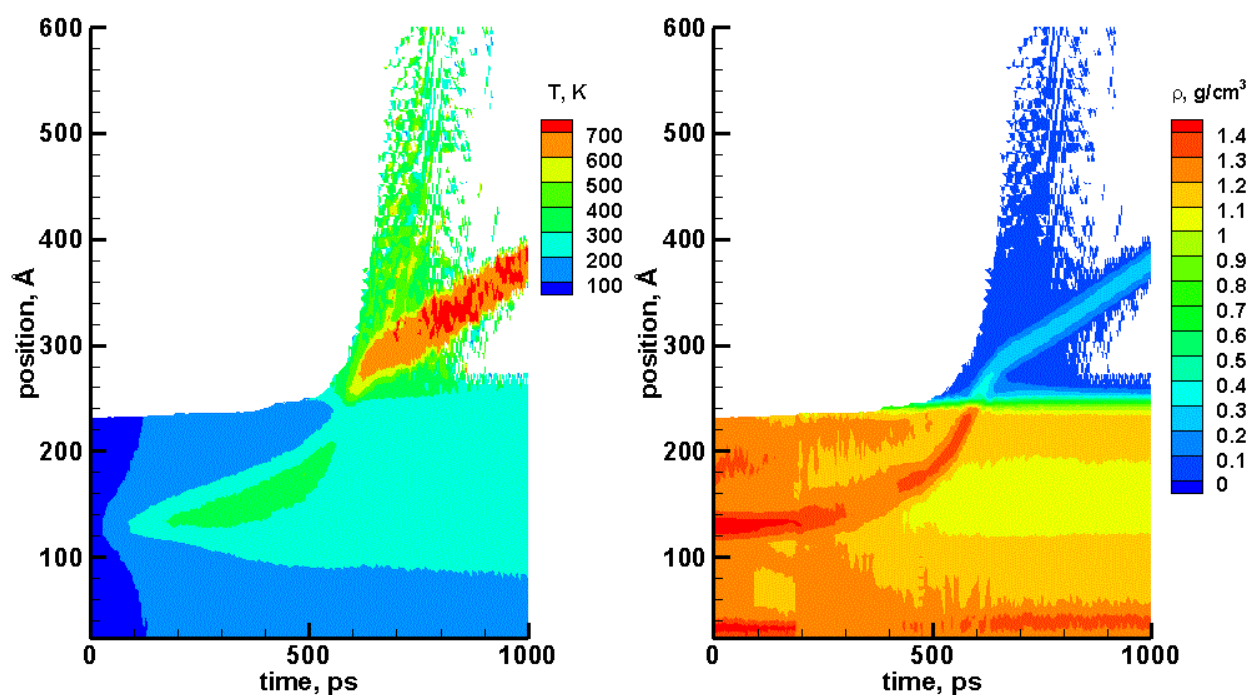
Figure 4.62 Contour plot of target representative of a non-uniform dispersion of NPs of 2.4 wt% concentration, irradiated by a pulse of 0.6 J/cm^2. Left – temperature; right – density.
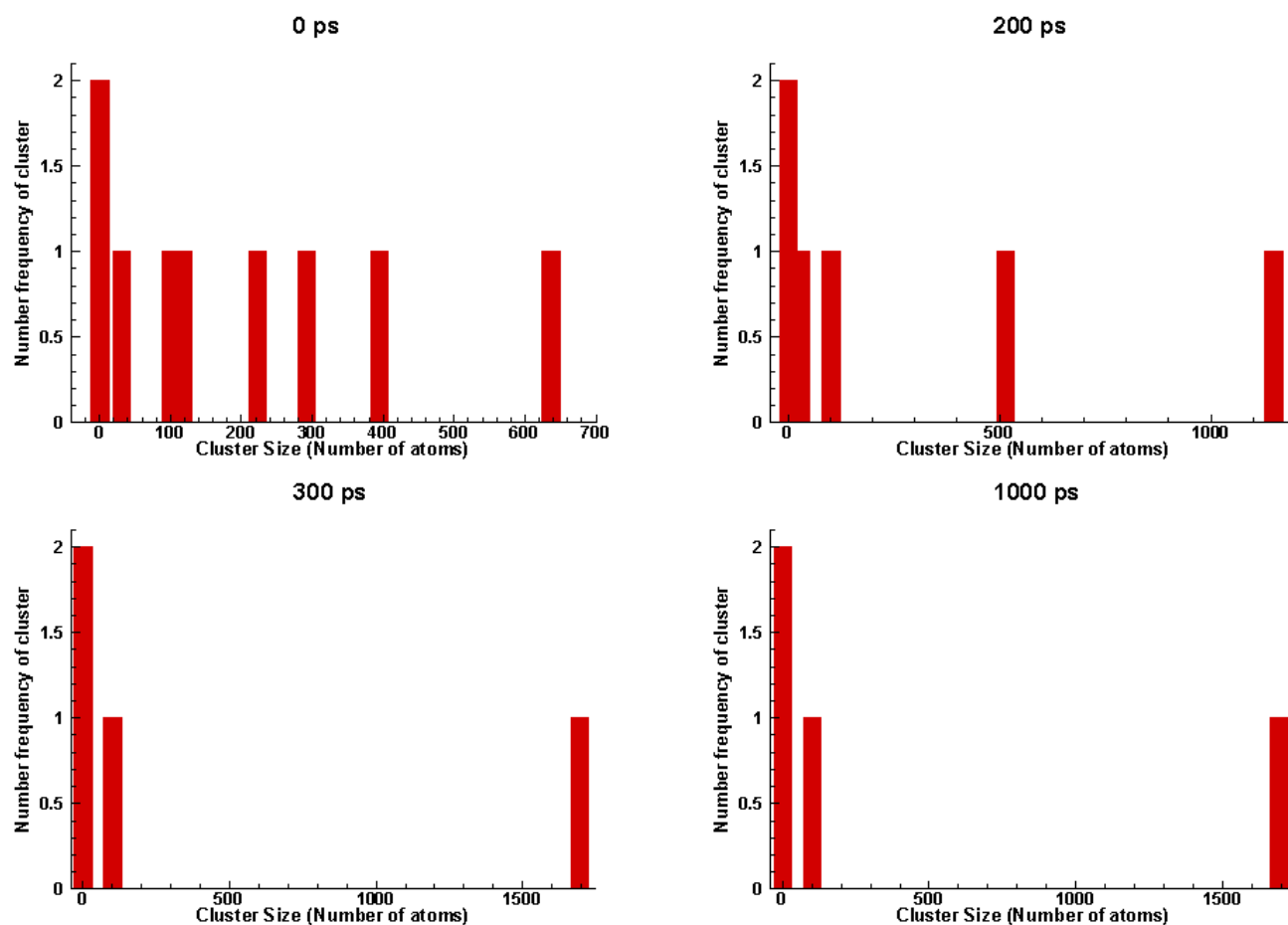
Figure 4.63 Size distribution of clusters in target representative of a non-uniform dispersion of NPs of 2.4 wt% concentration, irradiated by a pulse of 0.6 J/cm^2, at different times during and shortly after irradiation. Top left – 0ps; top right – 200 ps; bottom left – 300 ps; bottom right – 1000 ps.
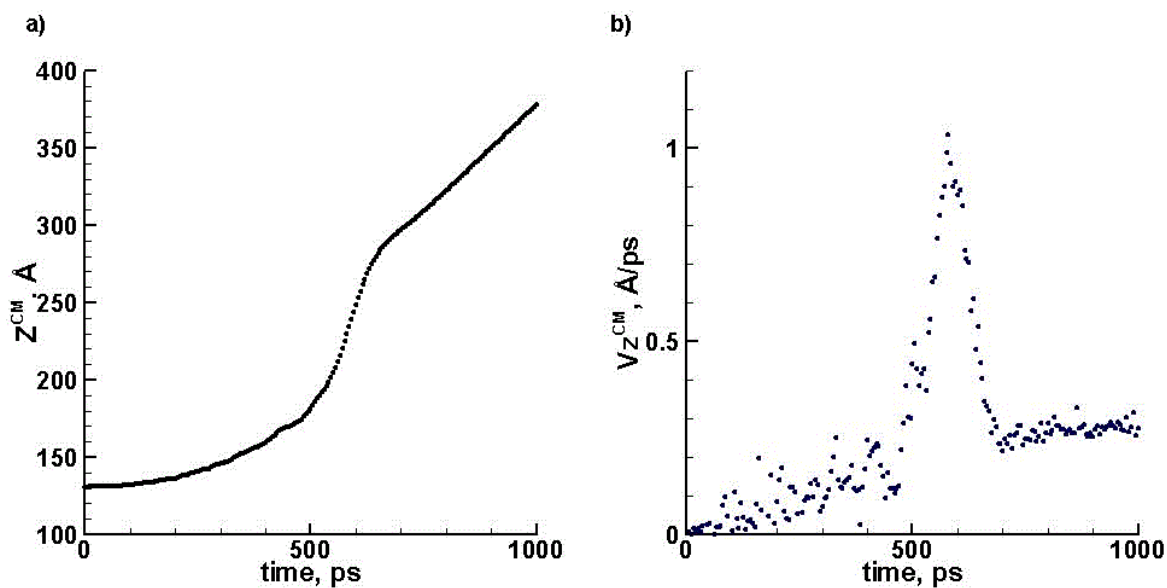
Figure 4.64 Dynamics of region highly concentrated in NP atoms in target representative of a non-uniform dispersion of NPs of 2.4 wt% concentration, irradiated by a pulse of 0.6 J/cm^2: a) z-component of the centre of mass of NP atoms in the region; b) z-component of velocity of the centre of mass of NP atoms in the region.
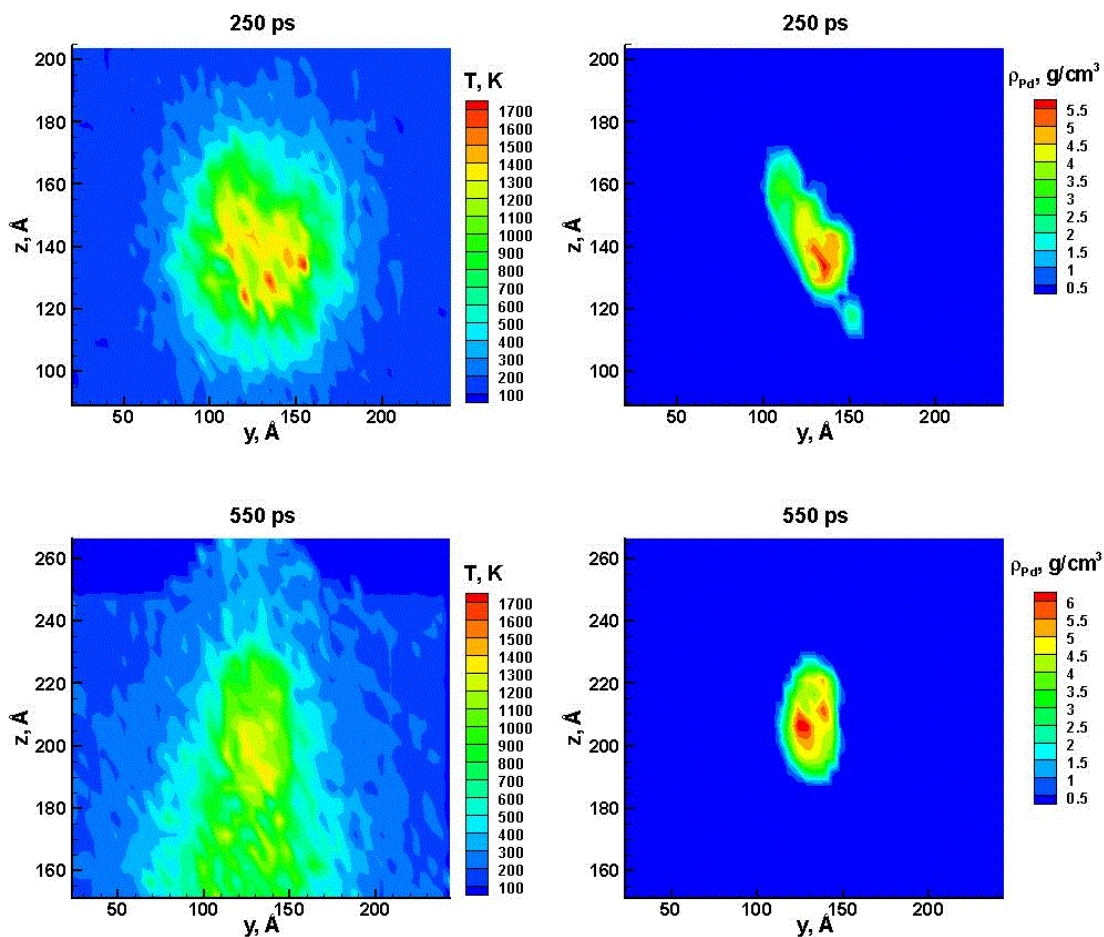
Figure 4.65 Contour plot of temperature in and around the region of NPs in target representative of a non-uniform dispersion of NPs of 2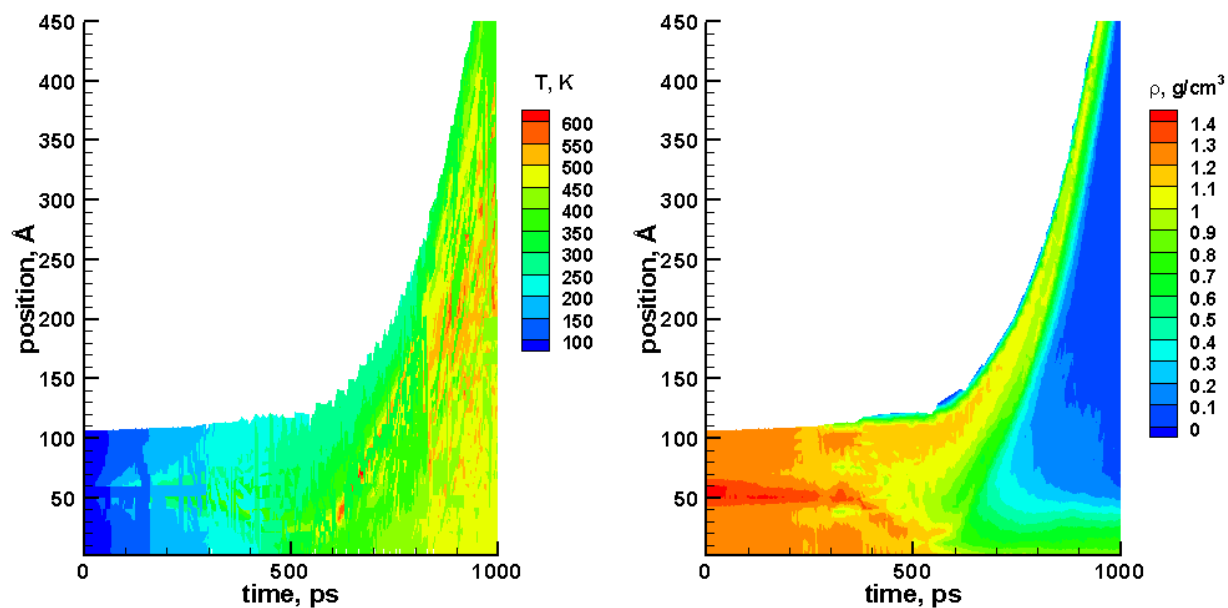.4 wt% concentration, irradiated by a pulse of 0.6 J/cm^2. The geometric centre of displayed area is the centre of mass of the NP atoms in the region. The temperature is averaged over the width of the region of NPs prior to irradiation. Top left – temperature at 250 ps; top right – density at 250 ps; bottom left – temperature at 550 ps; bottom right – density at 550 ps.

a)

b)
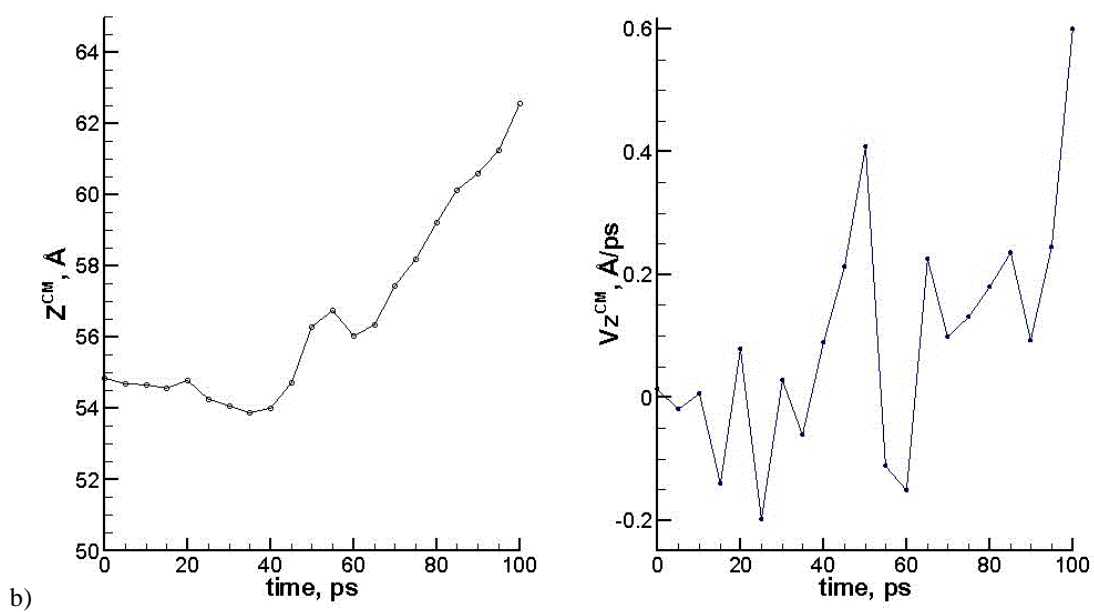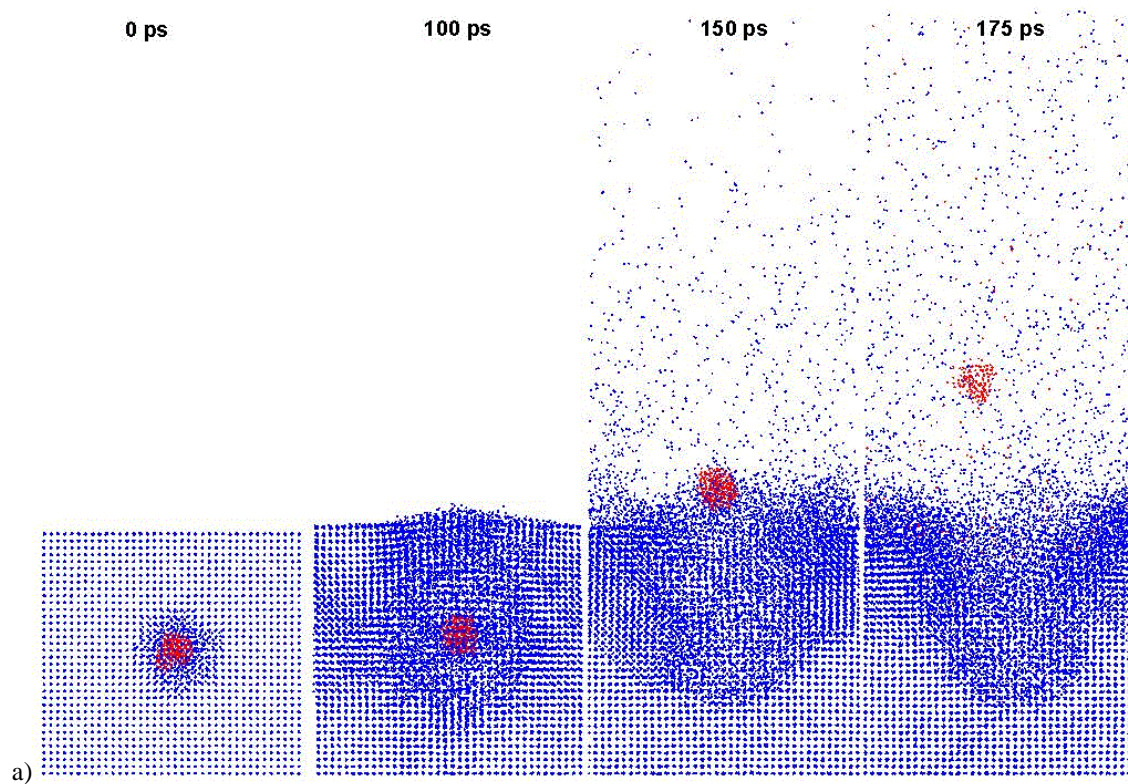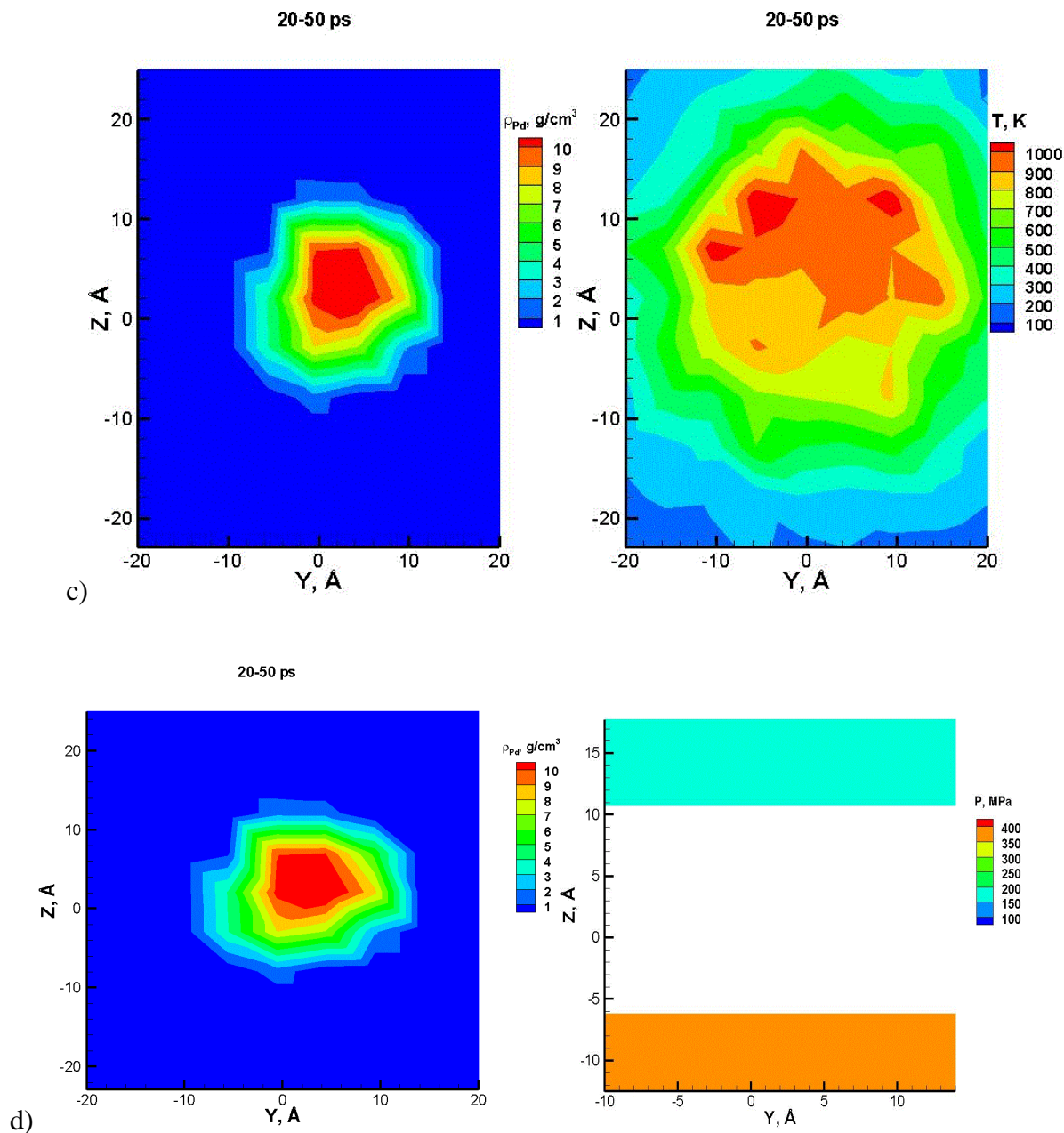
Figure 4.66 Description of target having a single NP irradiated in conditions leading to localized energy deposition. The pulse duration is 200 ps and the irradiation fluence is 1.6 J/cm².

a) Snapshots of irradiated target. b) Dynamics of NP prior to ejection: left – z-component of centre of mass of NP, right – z-component of velocity of centre of mass of NP. c) Contour plot of metal density and target temperature around centre of mass of NP averaged over time 20 to 50 ps

of irradiation: left – metal density, right – temperature. d) Right panel – diagram illustrating the pressure above the NP and the pressure below it, averaged over time 20 to 50 ps. The pressure is averaged over lateral directions and the lateral axis displayed merely indicates the range over which the averaging is done.
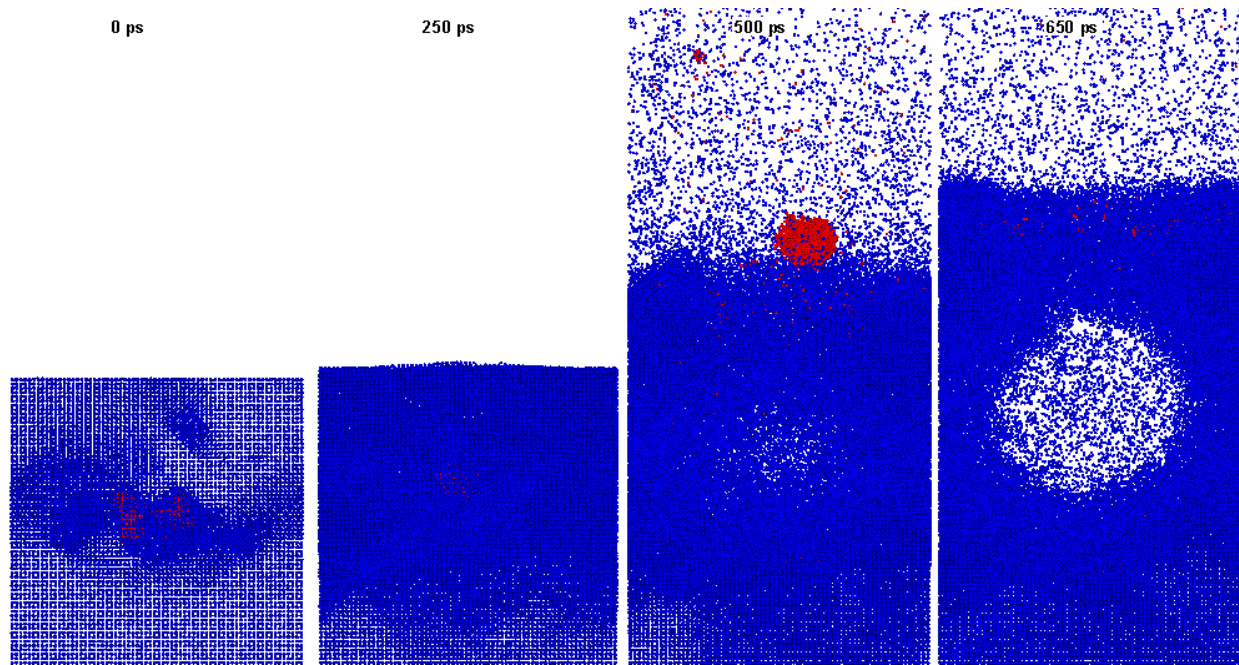
Figure 4.67 Snapshots of target representative of a non-uniform dispersion of NPs of 2.4 wt% concentration, irradiated by a pulse of 1.2 J/cm^2.
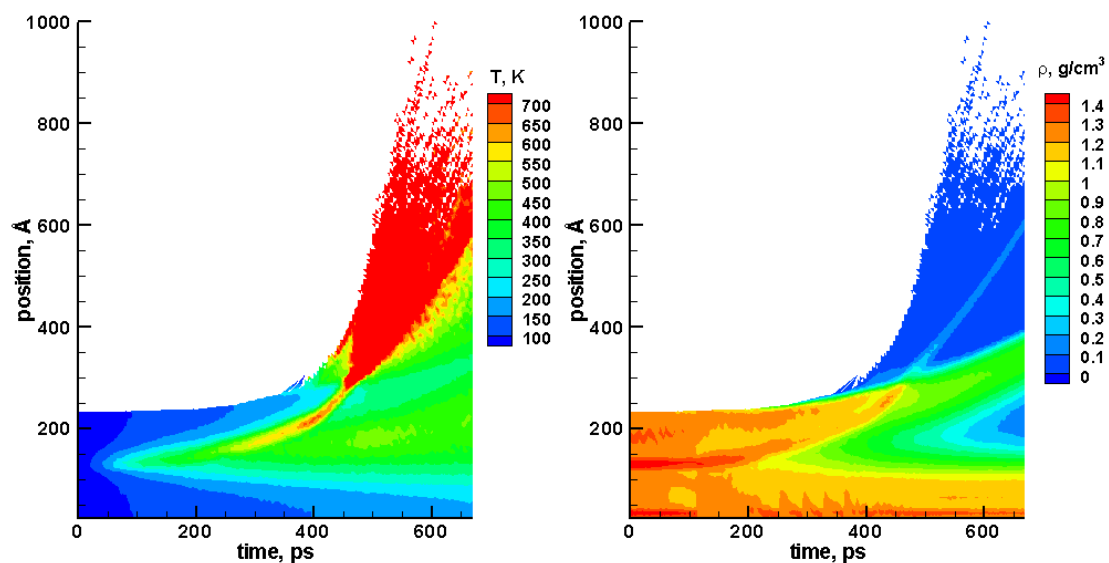
Figure 4.68 Contour plot of target representative of a non-uniform dispersion of NPs of 2.4 wt% concentration , irradiated by a pulse of 1.2 J/cm^2. Left – temperature; right – density.
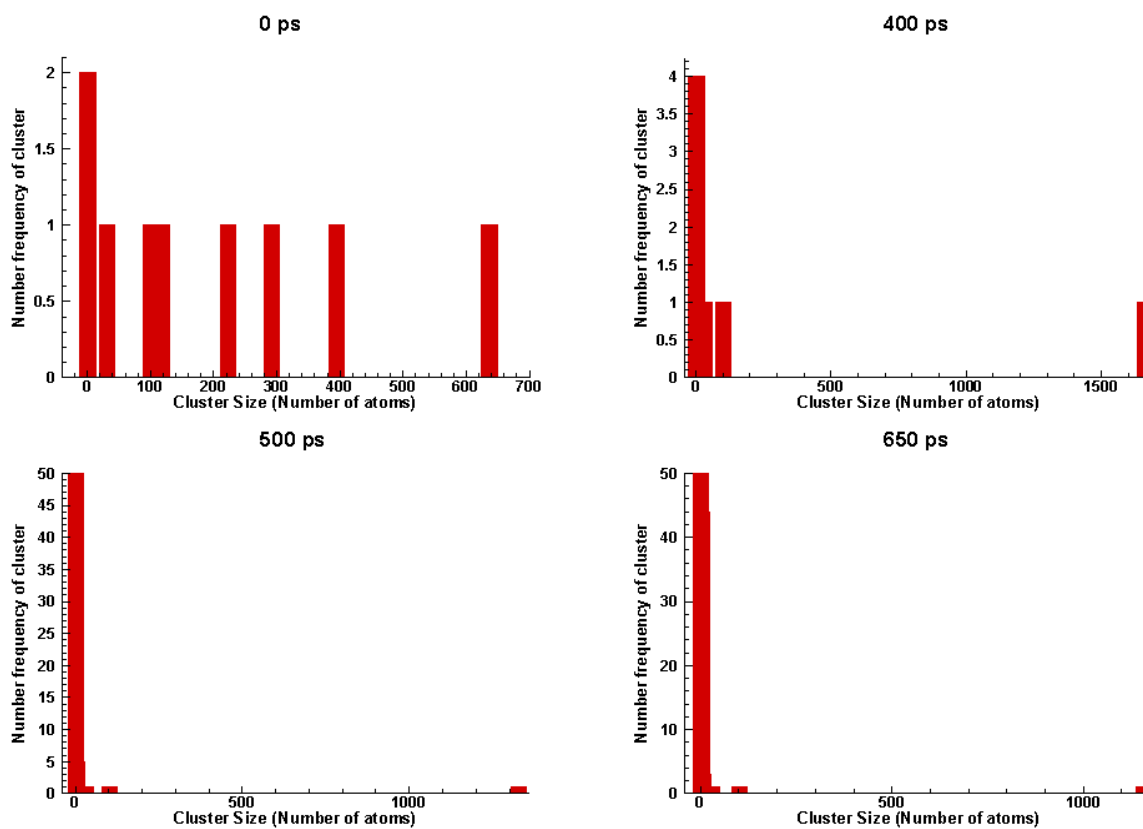
Figure 4.69   Size distribution of clusters in target representative of a non-uniform dispersion of NPs of 2.4 wt% concentration, irradiated by a pulse of 1.2 J/cm^2, at different times during and shortly after irradiation. Top left – 0ps; top right – 200 ps; bottom left – 300 ps; bottom right – 1000 ps.
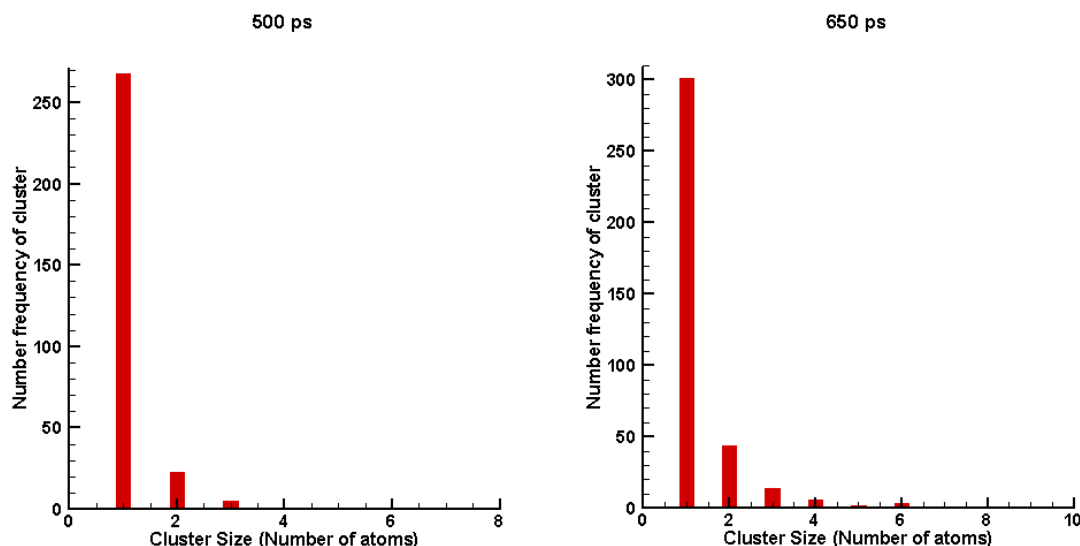
Figure 4.71   Size distribution of clusters in target representative of a non-uniform dispersion of NPs of 2.4 wt% concentration, irradiated by a pulse of 1.2 J/cm^2, at latter times during and shortly after irradiation. Left – 500ps; right – 650 ps.

4.8.5. Conclusions on Simulations of Laser Irradiation of Target

Factors that are suspected to affect the ejection of metal NPs in conditions realized in experiment have been explored.

MD simulations have revealed that metal cluster formation is strongly favored by a clustered (or insoluble) phase of the metalorganic (MOG) precursor in solution. Since absorption of a metal atom linearly increases with the size of its metal cluster, energy deposition is higher in conditions of early cluster formation, enhancing thermal diffusion that leads to growth of the

metal cluster. This observation is concluding to the study of the effect of solubility of the precursor to NP formation in the target. Cluster growth is continued in subsequent irradiation pulses leading to an increase in the number and size of NPs in the irradiated target. The ejection of NPs from the target is more likely to happen from a region in the target having a relatively higher concentration of NPs, as has been revealed by MD simulations of computational systems representative of targets having uniform and non-uniform dispersions of NPs. In the more likely scenario that leads to NP ejection, the energy distribution is partly localized due to a non-uniform dispersion of NPs and the NPs are ejected without active evaporation of the matrix.

The mechanisms of formation and ejection of metal NPs have been explored, and the most likely scenario of NP ejection has been determined.

4.9   Summary and Conclusions on the Computational Investigation of Nanoparticle Formation and Ejection from Aqueous Solution of Metalorganic Precursor Target

A summary of what has been discussed and revealed in the computational investigation of nanoparticle formation and ejection from aqueous solution of metalorganic precursor target is made.

Simulations of the continuum model predicted that single-pulse irradiation of the metalorganic precursor target to the state of phase explosion of the water matrix is unlikely accountable for the formation and ejection of NPs, since the threshold fluence for the surface to attain a temperature of phase explosion, $F^* = 18$ J/cm^2, is orders of magnitude higher than experimental fluences, i.e. $F^* \gg 0.25$ J/cm^2.

In experiment, multi-pulse irradiation of the target results in the deposition of NP films on substrate. It was therefore suggested that laser interaction with clusters of metal atoms, released as a result of the decomposition of the precursor molecules, are an important process leading to NP formation and ejection. Because experimentally observed NPs are mostly of 'mature' or 'ripe' size, it was supposed that the mechanism of ejection is tied to the laser absorption of NPs of the described size. The simulation of the irradiation of a model target having only NPs in it, for witnessing the ejection of the NPs became worth considering. Prior to doing this, an assessment of the possibility of NP ejection in experimental irradiation conditions was made—it showed that NP ejection is probably due to local heating of the NP environment, without explosive boiling of the matrix at the target surface, to temperatures higher than the temperature of phase explosion of the matrix. The described mechanism of ejection only seemed possible, within laser irradiation conditions, with a local concentration of NP atoms that is significantly higher than the average concentration of NP atoms at the irradiated target surface. That is, laser-deposited energy diffuses to evenly heat the matrix in case the NPs are uniformly dispersed; but laser energy deposited in a region having a relatively high concentration of NPs is partly localized.

Calculations were made to estimate the threshold fluence needed for NP ejection from a target with a uniform dispersion of NPs; as well as estimating the range of fluences needed for NP ejection to occur due to local heating of a target region with a relatively high NP concentration. It was determined that the threshold fluence for NP ejection from a target with a uniform dispersion of NPs, $F^* = 1.5$ J/cm^2, is significantly higher than experimental fluences, $F^* > 0.25$ J/cm^2, while the range of fluences needed for NP ejection to occur due to local heating of a target region with a relatively high NP concentration are of the same order of magnitude as

experimental fluences. MD simulations of the irradiation of a target representing a uniform dispersion of NPs, and of a target representing a non-uniform dispersion of NPs were done in the same physical irradiation regime as that in experiment. The fluences at which the ejection of NPs was possible were reasonably comparable to the predicted fluences in the calculations. With a local region of NPs having an atomic concentration about the same as the water matrix, ~ 63 wt%, the threshold fluence for the ejection of the NPs was determined as $F_{loc}^* = 0.6$ J/cm^2. The NPs became ejected from the target surface without active evaporation of the matrix, as was expected, and the mechanism of ejection of the NPs was revealed. Local heating of the NP and its surrounding water molecules to temperatures higher than the phase explosion temperature of water creates a 'bubble' which expands more to the surface, resulting in a net pressure from below the bubble that drives it beyond the target through overlying colder material (liquid and/or solid matrix).

In order to account for the growth of NPs and their dispersion in the target, simulations of the irradiation of the precursor target that reveal the mechanism of formation of NPs were run. Simulations of a target made of soluble (uniformly dispersed) precursor molecules showed little or no prospect of NP formation even at high fluences, as only a Pd cluster as large as a tetramer is formed after irradiation by two pulses. Simulations of a target made of partly soluble (non-uniformly dispersed) precursor molecules showed that NPs are formed in regions of the target that have relatively higher concentrations of the precursor. Metal atoms released as a result of the photodecomposition of the precursor molecules in these regions diffuse within to form clusters which grow in size in a multi-pulse irradiation regime, owing to increased atomic absorption with cluster size that results in increased energy deposition that enhances the thermal diffusion of atoms and clusters, until they become NPs. The number of NPs or their average size may

continue to increase in the target as it continues to be irradiated by multiple pulses, or the NPs may eject from the target if the fluence of the following irradiation pulse is high enough to do so. Not surprisingly, ablation of the target occurred through attainment of temperatures higher than the explosive boiling temperature of the matrix in regions of relatively high NP concentration without the whole target attaining a state of phase explosion of the matrix. The simulations of the precursor target therefore revealed that the dispersion of NPs in the target is predetermined by the solubility and the manner of dispersion of the precursor molecules.

The revealed mechanism of material ejection from the target without active evaporation of the matrix in a MAPLE technique is one that has not been encountered before, and it offers the opportunity to realize a new approach which enables size-selective generation and ejection of clean solvent-free nanoparticles.

5. SUMMARY OF AUTHOR CONTRIBUTIONS AND MAIN FINDINGS REPORTED IN THE DISSERTATION

The author made contributions to the development of the computational models for simulation of laser interactions with molecular systems and used the models for computational investigation of processes responsible for the molecular ejection and nanoparticle formation in laser-driven thin film deposition techniques. The simulations revealed a number of useful relations, mechanisms and phenomena that have direct implications for interpretation of experimental data and advancement of practical applications. The author contributions to the model development as well as the main findings in the simulations are listed below.

5.1   Computational Model Development

The author contributions to the development of the coarse grain molecular model are as follows:

1) The breathing sphere model was for the first time adapted to describe the physical properties of water. Water is a "natural solvent" used in laser deposition and mass spectrometry analysis of biological molecules.

2) Although the strength of coupling between the breathing mode and the translational modes is formally determined by the frequency mismatch between the vibrational spectra of the corresponding modes, it has been determined here that the coupling strength also depends on actual values of the breathing sphere model parameters that describe the breathing motion. The effect of the inertia parameter on the coupling strength has been demonstrated in the breathing sphere model for lysozyme.

3) A significant advancement of the breathing sphere model is the development and implementation of a 'heat bath' approach to couple the missing internal degrees of freedom to the dynamic degrees of freedom of the coarse grained model, so as to reproduce the real material heat capacity in the model.

4) A multi-scale computational model for simulation of the laser interaction with an aqueous solution of the metalorganic precursor molecules is developed. The model includes (A) atomistic simulations of the diffusion of Pd atoms in water and interaction of water molecules with Pd(111) surface, (B) evaluation, based on empirical data and Mie theory, of the absorption cross-sections of PdAc, Pd atoms and Pd clusters at laser irradiation wavelength of 248 nm, (C) continuum-level modeling of heat diffusion and the evolution of the target optical properties due to the photolytic and pyrolytic decomposition of metalorganic molecules, and (D) coarse-grained molecular dynamics modeling of metal nanoparticle formation in laser ablation of an aqueous solution of metalorganic precursors.

5.2   Main Results of the Computational Research

The major findings in the simulations of the laser ablation of lysozyme targets are as follows:

1) A series of coarse-grained molecular dynamics simulations of laser ablation of lysozyme – water system, where the water serves the role of volatile "matrix" that drives the ejection of the polymer molecules, reveal a remarkable ability of small (5-10 wt.%) amount of matrix to cause the ejection of intact bioorganic molecules. This computational prediction suggests a new approach for deposition of thin films of bioorganic molecules with minimum chemical modification of the molecular structure and minimum involvement of solvent into the deposition process.

2) The results obtained for different laser fluences and polymer concentrations are used to establish a "processing map" of the regimes of molecular ejection in matrix-assisted pulsed laser deposition. While this map is produced for a particular system (a thin lysozyme target with residual water), the physical picture emerging from this study can be generalized to other systems where a small amount of volatile solvent can provide the driving force for the ejection of heat-sensitive bioorganic material with minimum chemical modification.

3) The computational predictions are used to explain experimental observation of the ejection of intact lysozyme molecules from pressed lysozyme targets containing small amounts of residual water. The simulations also explain the observation of maximum concentration of intact molecules in films deposited at about three times the ablation threshold.

The main results of multi-scale simulations of nanoparticle generation by laser ablation of aqueous solutions of metalorganic precursors are as follows:

1) A negligible contribution of the thermal decomposition of palladium acetate (i.e., the metalorganic precursor) to the overall heating of the target is established in the continuum-level simulations.

2) It is determined from continuum simulations that complete decomposition of the precursor down to a depth of 5 μm in the target occurs during a single 25 ns laser pulse at a fluence that brings the surface of the target to a temperature of phase explosion. This observation indicates that the formation and ejection of nanoparticles (NPs) in multi-pulse irradiation regime is a result of NP growth from metal atoms released in previous irradiation pulses, as well as the laser energy absorption by the NPs.

3) Relevant to simulations of the metalorganic precursor target in the multi-pulse regime, it is determined that between irradiation pulses the target cools down to the ambient experimental temperature of 77 K.

4) MD simulations of targets containing uniformly dispersed precursor molecules reveal a slow NP formation, as only a Pd cluster as large as a tetramer is formed after irradiation by two pulses. On the contrary, the MD simulations of targets containing non-uniformly dispersed precursor molecules show a rapid formation of NPs in regions of high precursor concentration. Metal atoms released as a result of the photodecomposition of the precursor molecules diffuse within these regions to form clusters which grow in size in a multi-pulse irradiation regime to become NPs, owing to increased absorption with cluster size that results in increased energy deposition and enhanced thermal diffusion of atoms and clusters.

5) Most importantly, MD Simulations of the irradiation of a model target containing metal NPs reveal that the ejection of NPs is the result of local heating in the vicinity of NPs leading to the creation of a 'bubble' which diffuses toward the surface as it seeks to expand and feels more pressure from the bottom. The conditions of local heating are provided by the experimental pulsed irradiation regime.

5.3   Impact on Practical Applications

The major impact of the computational study of laser ablation of lysozyme targets is the conclusion that lowering the matrix content to minor quantities in MAPLE-related targets can still lead to the ejection of intact polymer molecules, thus providing deposition conditions that

can be suitable for nanomedicine, bioelectronics and tissue engineering, where minimization of the interaction of matrix with the deposited films is required.

The major impact of the computational investigation of nanoparticle generation in laser ablation of a solution of metalorganic precursors is in the prediction that the nanoparticles are generated in the irradiated target and play an active role in laser energy absorption and localized heating of the matrix. The mechanistic insights provided by the simulations may inspire the design of new approaches for size-selective generation and ejection of clean solvent-free nanoparticles.

LIST OF PRESENTATIONS AND PUBLICATIONS

LIST OF PRESENTATIONS

1. M. Tabetah and L.V. Zhigilei, "Laser Ablation of Lysozyme: Effect of Trapped Water," *Annual conference of the NSBP and NSHP*, 21-24 September (2011), Austin, TX.

2. M. Tabetah, L.V. Zhigilei, M.A. Steiner, J.M. Fitz-Gerald, and J. Schou, "Computational Investigation of Laser Ablation of Molecular Targets: The Role of Photochemical Reactions and Pyrolysis," *11th International Conference on Laser Ablation,* November 13-19 (2011), Playa del Carmen, Mexico.

3. M. Tabetah and L.V. Zhigilei, "Computational Investigation of the Formation of Metallic Nanoparticles by Laser Ablation of Metalorganic Precursor Solutions," *13th International Symposium on Laser Precision Microfabrication*, June 12-15 (2012), The Catholic University of America, Washington, DC.

4. M. Tabetah and L.V. Zhigilei, "Computational Investigation of the Formation of Metallic Nanoparticles by Laser Ablation of Metalorganic Precursor Solutions," *8th International Conference on Photo-Excited Processes and Applications*, August 12-17 (2012), Rochester, NY.

LIST OF PUBLICATIONS

1. L.V. Zhigilei, A.N. Volkov, E. Leveugle, M. Tabetah, "The effect of the target structure and composition on the ejection and transport of polymer molecules and carbon nanotubes in matrix-assisted pulsed laser evaporation," *Appl Phys A* **105**, 529-546 (2011)

2. M. Tabetah, A. Matei, C. Constantinescu, M. Dinescu, J. Schou, and L.V. Zhigilei "The minimum amount of matrix needed for matrix-assisted pulsed laser deposition of biomolecules," submitted (2014)

Appendix A1: The Gaussian Function

The Gaussian function is defined by the form:

$$g(x) = a \exp\left[-\frac{(x-b)^2}{2c^2}\right]$$

where b is the position of the centre of the peak, and c determines the width. Here, we derive some of the key properties and relations of the Gaussian function.

The points of inflexion of the Gaussian curve can be found by zeroing the second derivative of the Gaussian function:

$$g'(x) = -\frac{(x-b)}{c^2}g(x) \tag{A1}$$

so that

$$g''(x) = -\frac{(x-b)g'(x) + g(x)}{c^2} \tag{A2}$$

Inserting $g'(x)$ from Eq. (A1) into Eq. (A2), and setting $g''(x)$ to zero obtains

$$g(x)[-(x-b)^2 + c^2] = 0 \tag{A3}$$

yielding

$$x = b \pm c$$

as points of inflexion.

Abscissa values at half the maximum (full-width at half maximum)[FWHM] of the Gaussian are obtained from the condition:

$$\frac{a}{2} = a \exp\left[-\frac{(x-b)^2}{2c^2}\right] \tag{A4}$$

yielding

$$x = b \pm c\sqrt{2\ln 2}$$

after applying the natural logarithm on both sides.

A normalized Gaussian function is obtained by setting the total area under the Gaussian curve equal to 1:

$$\int_{-\infty}^{\infty} g(x)dx = \int_{-\infty}^{\infty} dx\, a \exp\left[-\frac{(x-b)^2}{2c^2}\right] = 1 \qquad (A5)$$

Making use of the definite integral,

$$\int_{-\infty}^{\infty} \exp(-su^2)\, du = \sqrt{\pi/s} \qquad (A6)$$

with substitutions: $u = x - b$; and $s = 1/2c^2$, Eq. (A5) resolves to

$$ac\sqrt{2\pi} = 1 \qquad (A7)$$

Applying the relation in Eq. (A7) to the Gaussian function, one obtains

$$g^N(x) = \frac{1}{c\sqrt{2\pi}} \exp\left[-\frac{(x-b)^2}{2c^2}\right] \qquad (A8)$$

which is the normalized Gaussian function. Here, c is referred to as the standard deviation of the distribution described by the function $g_N(x)$.

Appendix B1: Error Propagation Theory

Consider a quantity that is a function of n other measured quantities. The said relation can be described as

$$y = f(x_1, x_2, \dots, x_n) \tag{B1.1}$$

where x_i are the various indirect measurement values of the quantities on which the quantity of interest y depends.

The *error* in y, denoted as Δy, can be determined from known values of errors in the measured quantities, Δx_i, using a Taylor series expansion that is not inclusive of second and higher-order terms [267]:

$$\Delta y = \sum_{i=1}^{n} (\partial y / \partial x_i) \, \Delta x_i \tag{B1.2}$$

To ensure that the error in y is a positive number, the absolute value of the derivatives is assumed in Eq. (B1.2) [268], and the error is thus given by Eq. (B1.3)

$$\Delta y = \sum_{i=1}^{n} |(\partial y / \partial x_i)| \, \Delta x_i \tag{B1.3}$$

The above description is applicable if the measured quantities x_i are not independent of each other. In case they are independent, i.e. their uncertainties are uncorrelated and the variables are independent, the error in y is obtained by applying Pythagoras' theorem and adding the components that are in Eq. (B1.2) in quadrature [263]. For n independent variables, the error in y becomes

$$\Delta y = \left[\sum_{i=1}^{n} \left(\frac{\partial y}{\partial x_i} \Delta x_i \right)^2 \right]^{1/2} \tag{B1.3}$$

Eq. (B1.3) can also be referred to as the *squared error propagation law* [262].

We aim to determine the error in the speed of sound, for known error values in the bulk modulus and in the density, which is determined as a function of the latter quantities through the equation

$$C_s = \sqrt{B/\rho} \qquad (B1.4)$$

The bulk modulus is dependent on density, and so the error in the speed of sound is determined using Eq. (B1.2):

$$\Delta C_s = \frac{\partial C_s}{\partial B} \Delta B + \frac{\partial C_s}{\partial \rho} \Delta \rho \qquad (B1.5)$$

This equation expands to

$$\Delta C_s = \sqrt{\frac{B}{\rho}} \left(\frac{\Delta B}{2B} + \frac{\Delta \rho}{2\rho} \right) \qquad (B1.6)$$

which can be easily converted to a form relating the relative error in the speed of sound to the relative errors in the bulk modulus and in the density:

$$\frac{\Delta C_s}{C_s} = \frac{1}{2} \left(\frac{\Delta B}{B} + \frac{\Delta \rho}{\rho} \right) \qquad (B1.7)$$

Appendix B2: Determination of Uncertainty in Measurement

For a set of data points $\{y(i)\}$ for $i \in [1, N]$, the mean value, $\bar{y}$, is defined as:

$$\bar{y} = \sum_{i=1}^{N} \frac{y_i}{N} \tag{B2.1}$$

The value of the difference between the mean value and every data point is denoted as

$$\Delta y_i = |y_i - \bar{y}| \text{ for } i \in [1, N] \tag{B2.2}$$

A histogram of $nhist$ intervals is created in the range $[Hmin, Hmax]$ where

$Hmin \leq \min\{\Delta y_i\}$, and $Hmax \geq \max\{\Delta y_i\}$.

The histogram interval is defined as:

$$\Delta h = \frac{Hmax - Hmin}{nhist} \tag{B2.3}$$

The histogram midpoint values are:

$$h_j = Hmin + \Delta h \left(j - \frac{1}{2}\right) \text{ for } j \in [1, nhist] \tag{B2.4}$$

Let nf_j denote the number of difference values in the histogram interval about the midpoint value h_j. The said interval is the range $[h_j - \frac{\Delta h}{2}, h_j + \frac{\Delta h}{2})$. The set $\{nf_j\}$ defines the number frequency distribution of absolute error values.

The normalized frequencies, f_j, are determined from the number frequencies:

$$f_j = \frac{nf_j}{N} \tag{B2.5}$$

The normalized frequency f_j is the probability of finding an absolute error in an interval about midpoint value h_j . The following condition must be fulfilled:

$$\sum_{j=1}^{nhist} f_j = 1 \tag{B2.6}$$

Consider a continuous distribution of probability density $p(x)$, the mean value $\bar{x}$ is called the mathematical expectation, $E(x)$, and is defined as

$$\bar{x} = E(x) = \int_{-\infty}^{\infty} xp(x)dx \tag{B2.7}$$

The variance (or dispersion) of the distribution is defined as $\sigma^2 = E((x - \bar{x})^2)$:

$$\sigma^2 = \int_{-\infty}^{\infty} (x - \bar{x})^2 p(x)dx \tag{B2.8}$$

which expands to

$$\sigma^2 = \overline{x^2} - \bar{x}^2 = E(x^2) - [E(x)]^2 \tag{B2.9}$$

For a discrete distribution of points, as in our case, the variance defined in Eq. (B2.9) translates to

$$\sigma^2 = \sum_{j=1}^{nhist} h_j^2 f_j - \left(\sum_{j=1}^{nhist} h_j f_j \right)^2 \tag{B2.10}$$

The standard deviation is the square root of the variance. The standard deviation is standardly accepted as the error bar to the determined average value of the distribution.

Application to the determination of the average temperature of co-existing solid-liquid water during equilibration

The temperature of a co-existing solid-liquid breathing sphere (BS) water structure is seen to change, in Figure B2.1, until it equilibrates to a value which is deemed to be the melting temperature (T_m) of BS water. The data values at equilibrium can be seen to fluctuate, and we wish to determine the melting point as the average value of the data points. A distribution of the differences between the data points and the average value can be obtained; the standard deviation of the distribution is determined as the error bar to the determined average. The obtained distribution is displayed in Figure B2.2. Here, a state of equilibrium is assumed to be attained at 1300 ps; the average value is determined as 329.8 K, and the standard deviation is determined as 1.5 K. Hence, the melting temperature is 329.8 ± 1.5 K.

Appendix B3: **Numerical Implementation of the Calculation of the Velocity Autocorrelation Function (VAF) and the Vibrational Density of States (VDOS)**

Rewriting Eq.(2.25) – the velocity autocorrelation function (VAF) for a system of molecules(or atoms),

$$Z(t) = \frac{\langle \boldsymbol{v}(0) \cdot \boldsymbol{v}(t) \rangle}{\langle \boldsymbol{v}(0) \cdot \boldsymbol{v}(0) \rangle} = \frac{C_v(t)}{C_v(0)} \tag{B3.1}$$

For a system of N molecules, $C_v(\Delta t) = \frac{1}{N} \sum_{i=1}^{N} \boldsymbol{v}_i(0) \cdot \boldsymbol{v}_i(\Delta t)$. As explained in Eq.(2.26), the VAF is calculated as an average over a number of time intervals, say K, during the course of simulation. In a discrete representation the VAF for a given time displacement, $\Delta t_j = j \cdot \delta t$, from some original time (t_k) is therefore written as:

$$Z(k,j) = \frac{\langle \boldsymbol{v}(t_k) \cdot \boldsymbol{v}(t_k + \Delta t_j) \rangle}{\langle \boldsymbol{v}(t_k) \cdot \boldsymbol{v}(t_k) \rangle}, k = 1,2,\dots,K \tag{B3.2}$$

The average VAF over the K time intervals is thus

$$\hat{Z}(j) = \frac{1}{K} \sum_{k=1}^{K} Z(k,j) \tag{B3.3}$$

For a given simulation of N_{sim} timesteps, the time interval over which a VAF is calculated can be chosen to have N_T timesteps, i.e. $j = 1,2,\dots,N_T$. In our implementation, the number of such time intervals is given by $K = (N_{sim} - N_T)/N_{per}$, where N_{per} is the number of timesteps between the intervals, and the intervals overlap as a result.

Exemplary implementation: In a simulation of 6912 molecules of water (82.80 Å $\times$ 82.80 Å $\times$ 82.80 Å), with timestep $\delta t = 0.005$ ps, $N_{sim} = 82000$. A single VAF is calculated over $N_T =$

$N_{sim}/2$, and the number of timesteps between VAFs is $N_{per} = 100$. The average VAF is thus calculated over 41 VAFs.

The vibrational spectrum is the Fourier transform of the VAF,

$$F(v) = \int_{-\infty}^{\infty} dt \, e^{i2\pi vt} Z(t) \qquad (B3.4)$$

and the vibrational density of states (VDOS) is then $\Phi(v) = |F(v)|^2$.

The VDOS is therefore the product of the VAF Fourier Transform and its conjugate:

$$|F(v)|^2 = F(v) \cdot F^*(v) = (\mathrm{Re}[F(v)])^2 + (\mathrm{Im}[F(v)])^2 \qquad (B3.5)$$

so that

$$|F(v)|^2 = \left(\int_{-\infty}^{\infty} dt Z(t)\cos(2\pi vt)\right)^2 + \left(\int_{-\infty}^{\infty} dt Z(t)\sin(2\pi vt)\right)^2 \qquad (B3.6)$$

The real part of the spectrum is more representative of the spectral shape around the peak frequency, while the imaginary part of the spectrum has a broader extent to higher frequencies. In our application, the peak frequencies are of greater interest, so, only the real part of the spectrum is computed.

Let T_0 denote the length of the time domain VAF, which has N_T samples each separated by timestep δt. The sampling frequency is determined as: $F_s = 1/\delta t$. The highest frequency is defined as: $f_{max} \leq F_s/2$. In other words, the highest frequency is lesser than or equal to the Nyqist frequency. The frequency resolution is defined as $\delta f = 1/T_0 = F_s/N_T = 1/(N_T \delta t)$. In practice, the number of frequency samples, $M > N_T$; this usually results from adding zeroes to

the time-domain function after the defined range (zero-padding) to obtain a finer frequency mesh. The frequency resolution, then, is $\delta f = 1/(M\delta t)$.

Because zero-padding introduces a step-like discontinuity in the time-domain function, which transforms to a rippled sinc function in the frequency domain, the discontinuity is avoided by applying a suitable function which smoothes the time-domain function at the discontinuity. A suitable smoothing function is the Gaussian function.

In our application, the time range of the VAF is defined by $N_T = 4100$, δt=0.005 ps, and $T_0 = 20.5$ ps. The average VAF is zero-padded such that the number of samples $M = 2N_T$. The frequency resolution is thus $\delta f = 1/M\delta t = 0.0024$ THz. The sampling frequency is $F_s = 1/\delta t = 200$ THz.

A Gaussian of the form

$$g(t) = a \exp\left[-\frac{(t-b)^2}{2c^2}\right] \qquad (B3.7)$$

is applied to the VAF, with parameters: $a = 1$, b =0, $c = 4.5$ ps.

The VAFs for both translational and breathing motion are displayed in the diagram below; the smoothing-out of the discontinuity due to zero-padding is illustrated.
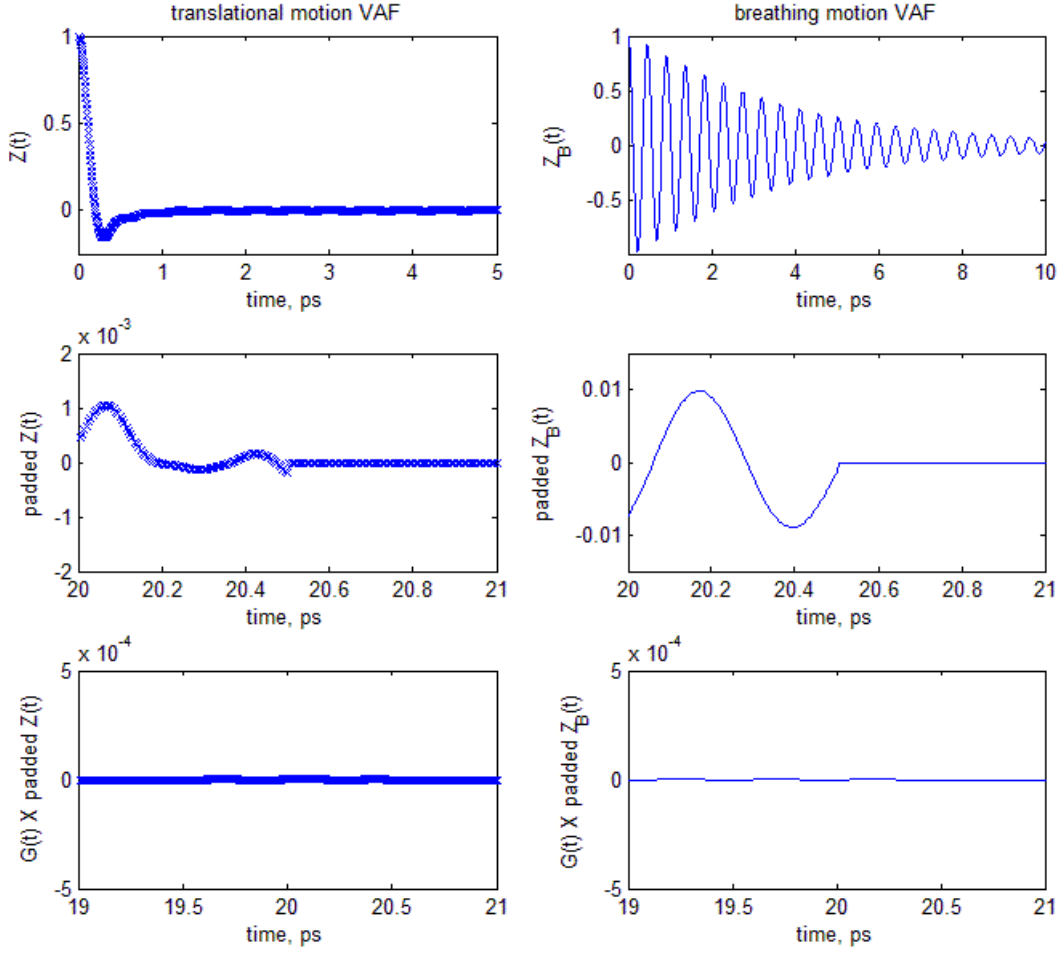
Figure B3.1   Velocity auto-correlation functions (VAFs) of translational motion (left side) and breathing motion (right side). The middle diagrams show the discontinuity in the padded VAF, and the bottom diagrams show that the discontinuity smears out after applying the Gaussian function G(t) to the padded VAF.

The numerical form of the Fourier Transform of the VAF modified by zero-padding and the Gaussian function, $\check{Z}$, is

$$F(v_q) = \sum_{j=1}^{M} \check{Z}(t_j)\cos(2\pi v_q t_j), q = 1,2,\dots,M \qquad (B3.8)$$

The VDOS is obtained as the real part of Eq.(B3.5), implementing the Fourier Transform in Eq.(B3.8). It is displayed in Figure B3.2.
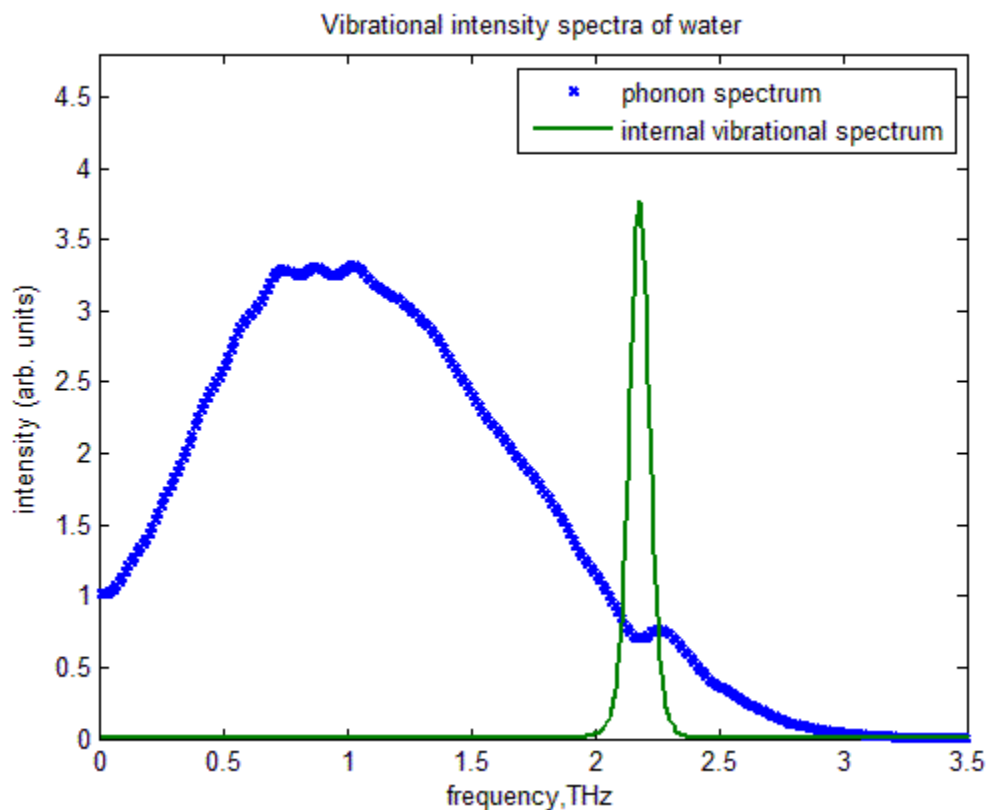
Figure B3.2 Vibrational density of states (VDOS) obtained as the real part of the square of the absolute value of the Fourier Transform of the modified velocity auto-correlation function.

Appendix C1: Determination of Uncertaintities in Determined Values of the Transmittance of PdAc film and Pd film

C1.1   Determination of uncertainty in the determined value of transmission of PdAc film

The uncertainty in $\ln Tr'(\lambda_2)$, $\Delta \ln Tr'(\lambda_2)$, is determined after applying the differential to Eq. (4.11)

$$d \ln Tr'(\lambda_2) = \frac{\ln Tr(\lambda_2)}{\ln Tr(\lambda_1)} \frac{dTr'(\lambda_1)}{Tr'(\lambda_1)} - \frac{\ln Tr(\lambda_2) \ln Tr'(\lambda_1)}{(\ln Tr(\lambda_1))^2} \frac{dTr(\lambda_1)}{Tr(\lambda_1)} + \frac{\ln Tr'(\lambda_1)}{\ln Tr(\lambda_1)} \frac{dTr(\lambda_2)}{Tr(\lambda_2)} \qquad (C1.1)$$

To combine the different obtained uncertainties into obtaining $\Delta \ln Tr'(\lambda_2)$, one needs to take into account the correlation of the uncertainties. The dependencies, in Figure 4.2 [right panel], used to obtain $Tr(\lambda_1)$ and $Tr(\lambda_2)$ are not related, so their uncertainties, $\Delta Tr(\lambda_1)$ and $\Delta Tr(\lambda_2)$ are uncorrelated. $Tr'(\lambda_1)$ is obtained by linear extrapolation of $\ln\left[\frac{1-Tr'}{Tr'}\right]$ in Figure 4.2 [left], a dependence unrelated to any of those used to obtain $Tr(\lambda_1)$ and $Tr(\lambda_2)$. So, $\Delta Tr'(\lambda_1)$ is uncorrelated to either of $\Delta Tr(\lambda_1)$ or $\Delta Tr(\lambda_2)$. The quantity $\Delta \ln Tr'(\lambda_2)$ is a combination of uncorrelated uncertainties. In Eq. (C1.1), denoting

$$\frac{\ln Tr(\lambda_2)}{\ln Tr(\lambda_1)}, \quad \frac{\ln Tr(\lambda_2) \ln Tr'(\lambda_1)}{(\ln Tr(\lambda_1))^2} \quad \text{and} \quad \frac{\ln Tr'(\lambda_1)}{\ln Tr(\lambda_1)}$$

as A, B and C respectively, $\Delta \ln Tr'(\lambda_2)$ is obtained as:

$$(\Delta \ln Tr'(\lambda_2))^2 = \left(A\frac{\Delta Tr'(\lambda_1)}{Tr'(\lambda_1)}\right)^2 + \left(B\frac{\Delta Tr(\lambda_1)}{Tr(\lambda_1)}\right)^2 + \left(C\frac{\Delta Tr(\lambda_2)}{Tr(\lambda_2)}\right)^2 \qquad (C1.2)$$

Applying the differential to $\ln\left[\frac{1-Tr\prime}{Tr\prime}\right]$ obtains

$$d \ln\left[\frac{1-Tr\prime}{Tr\prime}\right] = -2\frac{dTr\prime}{Tr\prime},$$

from which one deduces that $\frac{\Delta Tr'(\lambda_1)}{Tr'(\lambda_1)} = \frac{1}{2}\Delta \ln\left[\frac{1-Tr\prime}{Tr\prime}\right]$, equaling 0.025. The values of the

constants are: $A = 0.2695; C = 0.8589; B = AC = 0.2315.$

The uncertainty $\Delta \ln Tr'(\lambda_2)$ is then obtained from Eq. (C1.2) to be equal to 0.12826, leading to

a relative uncertainty of

$$\frac{\Delta \ln Tr'(\lambda_2)}{\ln Tr'(\lambda_2)} = 17.2 \text{ \%},$$

which is also the relative uncertainty in absorption coefficient of PdAc at 248 nm.

C1.2   Determination of uncertainty in the determined value of transmission of Pd film

As explained in Ref. [114], the transmittance spectrum in Figure 4.2 [right panel] at $t = 360$ s

is that of a thin palladium film. The thickness of such a film is determined from the dependence,

displayed in Figure 4.3, obtained from Ref. [114].

The thickness of Pd film is unchanged after 180 s and is seen to be $h'' = 5 \pm 1$ nm. The

thickness is measured from transmittance using Beer's law. Its transmittance is 42 ± 2 %, as

determined already to be $Tr(\lambda_1)$ in Figure 4.2 [right]. The absorption coefficient of Pd film, α_{Pd},

is determined from the transmittance equation to be $\alpha_{Pd} = 0.164$ nm^{-1}.

The absorption cross-section of Pd atom in Pd metal, σ_{Pd}, is determined by Eq. (4.8), using the material properties for Pd to equal 0.24 Å^2. Its relative uncertainty is that of α_{Pd}, which is obtained after applying the differential on α_{Pd}:

$$d\alpha = -\frac{1}{h''}\frac{dTr}{Tr} - \alpha\frac{dh''}{h''} \qquad (C1.3)$$

yields

$$\frac{d\alpha}{\alpha} = -\frac{1}{\alpha h''}\frac{dTr}{Tr} - \frac{dh''}{h''} \qquad (C1.4)$$

The relative uncertainty in absorption cross-section, $\frac{\Delta\sigma}{\sigma} = \frac{\Delta\alpha}{\alpha} = \delta_{Pd}$, is then

$$\delta_{Pd} = \sqrt{\left(\frac{1}{\alpha h''}\frac{\Delta Tr}{Tr}\right)^2 + \left(\frac{\Delta h''}{h''}\right)^2}$$

equaling 20.7 %. The absorption cross-section of σ_{Pd} is thus

$$\sigma_{Pd} = 0.24 \pm 0.05 \text{ Å}^2.$$

Appendix C2: Test of Absorption Model

A test of the described absorption model is carried out on a model MAPLE target (5 %wt. precursor) system, of thickness $d = 1164.39$ Å, with the number of precursor (PdAc) molecules equaling 2292, and computational side lengths 77.7 Å, 155.5 Å, 1164.4 Å. The model system thickness, and hence the absorption length, is scaled 20 times smaller relative to the real system thickness.

Using an absorption cross-section of 0.6 Å^2 for PdAc molecules, and the multiplicative scale factor (N_{sc}) of 20, while assuming an average number density ($\bar{n}$) for precursor molecules, the absorption coefficient of initial model target is $\alpha = \sigma \cdot \bar{n} \cdot N_{sc}$, equaling 0.002 Å^{-1}. The absorption cross-section of Pd atom here is made equal to that of PdAc, so that the absorption coefficient of the target is constant during irradiation.

A fluence of 2J/cm^2 is irradiated on the target, with allowance of decomposition of precursor molecules, but no motion of atoms and molecules, and the number of absorbed photons as a function of the depth of the film is determined. Out of 150931 photons irradiated, 135725 are absorbed and 15206 are unabsorbed. Beer's law should be adequately described by the equality

$$\ln N(d)/N(0) = -\alpha \cdot d \qquad (C2.1)$$

where $N(0)$ is the number of irradiating photons, and $N(d)$ is the number of unabsorbed photons. Substituting the already known values of the variables into Eq. (C2.1), the left hand side (L.H.S) of the equation yields -2.3 and the right hand side yields -2.3, validating the equality.

Diagrams of the initial distribution of precursor molecules, over 100 layers, and the number of absorbed photons as a function of position are displayed in Fig. C2.1. An exponential fit made to the dependence in Fig. C2.1b yields an absorption coefficient of 0.002 Å^{-1}, coinciding with the pre-calculated value.

The above calculations resulting from the simulation show that the absorption of the multicomponent medium, described by a more complexed form of Beer's law, in section 4.7.3, converges to the simple and conventional description of Beer's law when the absorption coefficient of the absorbing medium is maintained constant.

a)
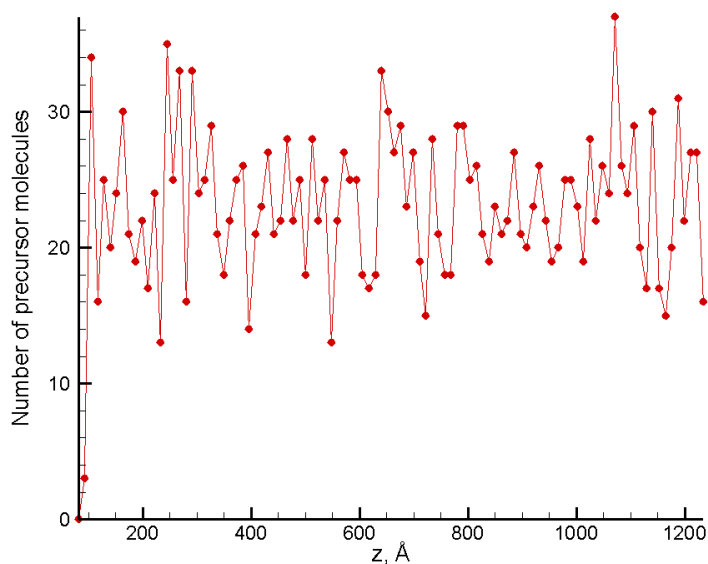
b)
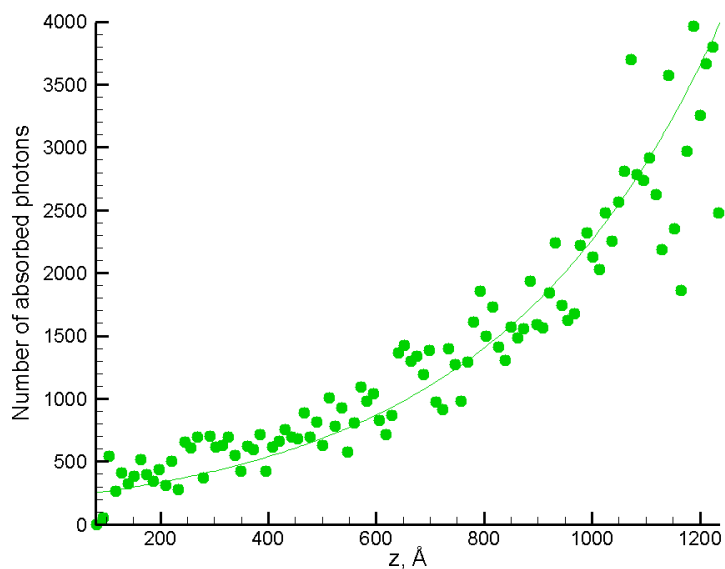
Figure C2.1   Distributions of a) precursor molecules initially, b) number of absorbed photons in model target as a function of position. z =0 corresponds to the bottom (lowest position) of the target.

References

[1] T.H. Maiman, "Stimulated Optical Radiation in Ruby," Nature (London) **187**, 493-494 (1960)

[2] R.S. Quimby, *Photonics and Lasers* (Wiley-Interscience, 2006)

[3] R. Menzel, *Photonics: Linear and Nonlinear Interactions of Laser Light and Matter* (Springer-Verlag Berlin Heidelberg, 2007)

[4] A.L. Schawlow, "Lasers," *Science* **149,** 13 (1965)

[5] F. Brech and L. Cross, "Optical micromission stimulated by a ruby maser," *Appl. Spectrosc.* **16**, 59 (1962)

[6] H.M. Smith and A.F. Turner, "Vacuum Deposited Thin Films Using a Ruby Laser," *Appl. Optics* **4**, 147 (1965)

[7] E. Hecht, *Optics* (Addison Wesley, San Francisco, 2002)

[8] E. Leveugle and L.V. Zhigilei, "Molecular dynamics simulation of the ejection and transport of polymer molecules in matrix-assisted pulsed laser evaporation," *J. Appl. Phys.* **102**, 074914 (2007).

[9] L.V. Zhigilei and B.J. Garrison, "Microscopic mechanisms of laser ablation of organic solids in the thermal and stress confinement irradiation regimes," *J. Appl. Phys.* **88**, 1281-1298 (2000)

[10] L.V. Zhigilei, E. Leveugle, B.J. Garrison, Y.G. Yingling, M.I. Zeifman, "Computer Simulations of Laser Ablation of Molecular Substrates," *Chem. Rev*. **103**, 321-347 (2003)

[11] B. Christensen and M. S. Tillack, "Survey of mechanisms for liquid droplet ejection from surfaces exposed to rapid pulsed heating," preprint UCSD-ENG-100 of the University of California, San Diego (2003)

[12] N.M. Bulgakova, A.V. Bulgakov, "Pulsed laser ablation of solids: transition from normal vaporization to phase explosion," *Appl. Phys. A* **73**, 199–208 (2001)

[13] J.C. Miller, R.C. Haglund, *Laser ablation and desorption: Experimental Methods in the Physical Sciences*, **30** (Academic Press, San Diego, CA 1998)

[14] T.D. Bennett, C.P. Grigoropoulos, and D.J. Krajnovich, "Near-threshold laser sputtering of gold," *J. Appl. Phys.* **77**, 849-864 (1995)

[15] X. Zhang, S.S. Chu, J.R. Ho, and C.P. Grigoropoulos, "Excimer laser ablation of thin gold films on a quartz crystal microbalance at various argon background pressures," *Appl.Phys. A* **64**, 545-552 (1997)

[16] B.N. Kozlov and B.A. Mamyrin, "Mass spectrometric analysis of clusters formed in laser ablation of a sample," *Tech. Phys.* **44**, 1073-1076 (1999)

[17] M. Fiebig, M. Kauf, J. Fair, H. Endert, M. Rahe, D. Basting "New aspects of micromachining and microlithography using 157-nm excimer laser irradiation," *Appl. Phys. A* **69**, S305-S307 (1999)

[18] P. Delaporte, M. Gastaud, W. Marine, M. Sentis, O. Uteza, P. Thouvenot, J.L. Alcaraz, J.M. Le Samedy, D. Blin "Dry excimer laser cleaning applied to nuclear decontamination," *Appl. Surf. Sc.* **208**, 298-305 (2003)

[19] M. Khaleeq-ur-Rahman, K. A. Bhatti, M. S. Rafique, A. Latif, P. Lee, and S. Mahmood, "Laser Irradiation Effects on Gold," Laser Physics **17**, No. 12, 1382–1388 (2007)

[20] S. Amoruso, G. Ausanio, A.C. Barone, R. Bruzzese, L. Gragnaniello, M. Vitiello and X. Wang, "Ultrashort laser ablation of solid matter in vacuum: a comparison between the picosecond and femtosecond regimes," *J. Phys. B: At. Mol. Opt. Phys.* **38**, L329–L338 (2005)

[21] K. Dreisewerd, "The Desorption Process in MALDI," *Chem. Rev.* **103**, 395-426 (2006)

[22] M. Karas and R. Kruger, "Ion Formation in MALDI: The Cluster Ionization Mechanism," *Chem. Rev.* **103**, 427-440 (2003)

[23] R. Knochenmuss and R. Zenobi, "MALDI Ionization: The Role of In-Plume Processes," *Chem. Rev.* **103**, 441-452 (2003)

[24] L.V. Zhigilei, Y.G. Yingling, T.E. Itina, T.A. Schoolcraft, and B.J. Garrison, "Molecular Dynamics Simulations of Matrix Assisted Laser Desorption − Connections to Experiment," *Int. J.Mass Spectrom.* **226**, 85-106 (2003)

[25] F. Hillenkamp, M. Karas, R.C. Beavis, and B.T. Chait, "Matrix-assisted laser desorption/ionization mass spectrometry of biopolymers," *Anal. Chem.* **63**, 1193A-1203A (1991)

[26] B.T. Chait, R. Wang, R.C. Beavis, and S.B.H. Kent, "Protein ladder sequencing," *Science* **262**, 89-92 (1993)

[27] C. Fenselau, "MALDI MS and strategies for protein analysis," *Anal. Chem.* **69**, 661A-665A (1997)

[28] A. Pique, R.A. McGill, D.B. Chrisey, D. Leonhardt, T.E. MsIna, B.J. Spargo, J.H. Callahan, R.W. Vachet, R. Chung, and M.A. Bucaro, "Growth of organic thin films by the matrix assisted pulsed laser evaporation (MAPLE) technique," *Thin Solid Films* **355**, 536-541 (1999)

[29] D.M. Bubb, P.K. Wu, J.S. Horwitz, J.H. Callahan, M. Galicia, A. Vertes, R.A. McGill, E.J. Houser, B.R. Ringesein, and D.B. Chrisey, "The effect of the matrix on film properties in matrix-assisted pulsed laser evaporation," *J. Appl. Phys.* **91**, 2055-2058 (2002)

[30] A.L. Mercado, C.E. Allmond, J. Hoekstra, and J.M. Fitz-Gerald, "Pulsed laser deposition vs. matrix assisted pulsed laserevaporation for growth of biodegradable polymer thin films," *Appl. Phys. A* **81**, 591-599 (2005)

[31] J.M. Fitz-Gerald, G. Jennings, R. Johnson,a nd C.L. Fraser, "Matrix assisted pulsed laser deposition of light emitting polymer thin films," *Appl. Phys. A* **80**, 1109-1113 (2005)

[32] A.T. Sellinger, E.M. Leveugle, K. Gogick, L.V. Zhigilei, and J.M. Fitz-Gerald, "Laser processing of polymer nanocomposite thin films," *JVST A* **24**, 1618-1622 (2006)

[33] P. Ayyub, R. Chandra, P. Taneja, A.K. Sharma, R. Pinto, "Synthesis of nanocrystalline material by sputtering and laser ablation at low temperatures," *Appl. Phys. A* **73**, 67–73 (2001)

[34] A.P. Caricato, M. Epifani, M. Martino, F. Romano, R. Rella, A. Taurino, T. Tunno and D. Valerini, "MAPLE deposition and characterization of SnO2 colloidal nanoparticle thin films," *J. Phys. D*: *Appl. Phys.* **42**, 095105 (2009)

[35] S. Barcikowski, A. Hahn, A.V. Kabashin, B.N. Chichkov, "Properties of nanoparticles generated during femtosecond laser machining in air and water," *Appl. Phys.* **87**, 47–55 (2007)

[36] N. Barsch, J. Jakobi, S. Weiler and S. Barcikowski, "Pure colloidal metal and ceramic nanoparticles from high-power picosecond laser ablation in water and acetone," *Nanotechnology* **20**, 445603 (2009)

[37] D. C. Schinca, L. B. Scaffardi, F. A. Videla, G. A. Torchia, P. Moreno and L. Roso, "Silver-silver oxide core-shell nanoparticles by femtosecond laser ablation: core and shell sizing by extinction spectroscopy," *J. Phys. D*: *Appl. Phys.* **42**, 215102, (2009)

[38] C. Liu, Z. Hu, Y. Che, Y. Chen and X. Pan, "Nanoparticle generation in ultrafast pulsed laser ablation of nickel," *Appl. Phys. Lett.* **90**, 044103 (2007)

[39] S. Eliezer, N. Eliaz, E. Grossman, D. Fisher, I. Gouzman, Z. Henis, S. Pecker, Y. Horovitz, M.Fraenkel, S. Maman, and Y. Lereah, "Synthesis of nanoparticles with femtosecond laser pulses," *Phys. Rev. B* **69**, 144119 (2004)

[40] G. Bajaj, R.K. Soni, "Effect of liquid medium on size and shape of nanoparticles prepared by pulsed laser ablation of tin," *Appl. Phys. A* **97**, 481-487 (2009)

[41] J. Maehara, Y. Yamada, H. Kumagai, K. Midorikawa and T. Yabe, "Comparison of Simulations of and Experiments on Femtosecond Laser Ablation of Nickel in Gaseous and Water Environments," *Jpn. J. Appl. Phys*. **43**, 172-175 (2004)

[42] V. Amendola and M. Meneghetti, "Laser ablation synthesis in solution and size manipulation of noble metal nanoparticles," *Phys. Chem. Chem. Phys*. **11**, 3805-3821 (2009)

[43] T.E. Glover, G.D. Ackerman, R.W. Lee, D.A. Young, "Probing particle synthesis during femtosecond laser ablation: initial phase transition kinetics," *Appl. Phys. B* **78**, 995–1000 (2004)

[44] N. Jegenyes, J. Etchepare, B. Reynier, D. Scuderi, A. Dos-Santos, Z. Toth, "Time-resolved dynamics analysis of nanoparticles applying dual femtosecond laser pulses," *Appl. Phys. A* **91**, 385–392 (2008)

[45] J. Perriere, C. Boulmer-Leborgne, R. Benzerga and S. Tricot, "Nanoparticle formation by femtosecond laser ablation," *J. Phys. D: Appl. Phys*. **40**, 7069–7076 (2007)

[46] C.E. Allmond, A.T. Sellinger, K. Gogick, J.M. Fitz-Gerald, "Photo-chemical synthesis and deposition of noble metal nanoparticles," *Appl. Phys. A* **86**, 477-480 (2007)

[47] M.A. Steiner, W.A. Soffa, J.M. Fitz-Gerald, "Matrix assisted growth of nanoparticles and nanoporous films," *Appl. Phys. A* **105**, 593-603 (2011)

[48] A. Pique, "The Matrix assisted pulsed laser evaporation (MAPLE) process: origins and future directions," *Appl. Phys. A* **105**, 517-528 (2011)

[49] A.P. Caricato, A. Luches, "Applications of the matrix-assisted pulsed laser evaporation method for the deposition of organic, biological and nanoparticle thin films: a review," *Appl. Phys. A* **105**, 565-582 (2011)

[50] A.L. Mercado, C.E.Allmond, J.G. Hoekstra, J.M. Fitz-Gerald, "Pulsed laser deposition vs. matrix assisted pulsed laser evaporation for growth of biodegradable polymer thin films," *Appl. Phys. A* **81**, 591-599 (2005)

[51] I.A. Paun, V. Ion, A. Moldovan, M. Dinescu, "MAPLE deposition of PEG:PLGA thin films," *Appl Phys A* **106**, 197-205 (2012)

[52] F. Bloisi, M. Barra, A. Cassinese, L.R.M. Vicari, "Matrix-Assisted Pulsed Laser Thin Film Deposition by Using Nd:YAG Laser," *Journal of Nanomaterials* 395436 (2012)

[53] N.M. Bulgakova, R. Stoian, A. Rosenfeld, I.V. Hertel,"Continuum Models of Ultrashort Pulsed Laser Ablation," Springer Series in Materials Science **130**, 81-97 (2010)

[54] D.S. Ivanov and L.V. Zhigilei, "Combined atomistic-continuum modeling of short-pulse laser melting and disintegration of metal films," *Phys. Rev. B* **68**, 064114 (2003)

[55] D.S. Ivanov and L.V. Zhigilei, "Combined atomistic-continuum model for simulation of laser interaction with metals: application in the calculation of melting thresholds in Ni targets of varying thickness," *Appl. Phys. A* **79**, 977-981 (2004)

[56] A.M. Dongare, M. Neurock, and L.V. Zhigilei, "Angular-dependent embedded atom method potential for atomistic simulations*," Phys. Rev. B* **80**, 184106 (2009)

[57] Y. Dou, L.V. Zhigilei, N. Winograd, and B.J. Garrison, "Explosive Boiling of Water Films Adjacent to Heated Surfaces: A Microscopic Description," *J. Phys. Chem. A* **105**, 2748-2755 (2001)

[58] L.V. Zhigilei, P.B.S. Kodali, B.J. Garrison, "Molecular Dynamics Model for Laser Ablation and Desorption of Organic Solids," *J. Phys. Chem. B* **101**, 2028-2037 (1997)

[59] H.J.C. Berendsen, J.P.M. Postma, W.F. van Gunsteren, A. DiNola, and J.R. Haak, "Molecular dynamics with coupling to an external bath," *J. Chem. Phys.* **81**, 3684 (1984).

[60] C. Constantinescu, A. Matei, J. Schou, S. Canulescu, M. Dinescu, "Pulsed laser deposition of lysozyme: The dependence on shot numbers and the angular distribution," *Appl. Phys. B* **113**, 367-371 (2013)

[61] R. Cegielska-Radziejewska, G. Lesnierowski, J. Kizowski, "Properties and Application of Egg White Lysozyme and its Modified Preparations: a Review," *Pol. J. Food Nutr. Sci*, **58**, 5-10 (2008)

[62] B. Gavish, E. Gratton, and C.J. Hardy, "Adiabatic compressibility of globular proteins," *Biophysics: Proc. Natl. Acad. Sci. USA* **80** (1983)

[63] S. Speziale, F. Jiang, C. L. Caylor, S. Kriminski, C.-S. Zha, R. E. Thorne, and T. S. Duffy, "Sound Velocity and Elasticity of Tetragonal Lysozyme Crystals by Brillouin Spectroscopy," *Biophys. J.* **85**, 3202–3213 (2003)

[64] H.G. Nagendra, C. Sudarsanakumar and M. Vijayan, "Characterization of lysozyme crystals with unusually low solvent content," *Acta Cryst. D* **51**, 390-392 (1995)

[65] P. T. Underhill, P.S. Doyle, "On the coarse-graining of polymers into bead-spring chains," *J. Non-Newtonian Fluid Mech.* **122**, 3–31 (2004)

[66] M.S. Daw, S.M. Foiles, and M.I. Baskes, "The embedded-atom method: a review of theory and applications," *Mat. Sci. Rep.* **9**, 251 (1993)

[67] S.M. Foiles, "Embedded-atom and related methods for modeling metallic systems," *MRS Bulletin* **21**, 24-28 (1996)

[68] D.B. Chrisey, G.K. Hubler (eds.), *Pulsed Laser Deposition of Thin Films* (Wiley Interscience, New York, 1994)

[69] L.V. Zhigilei, Y.G. Yingling, T.E. Itina, T.A. Schoolcraft, and B.J. Garrison, "Molecular Dynamics Simulations of Matrix Assisted Laser Desorption – Connections to Experiment," *Int. J.Mass Spectrom.* **226**, 85-106 (2003)

[70] L.V. Zhigilei and B.J. Garrison, "Molecular dynamics simulation study of the fluence dependence of particle yield and plume composition in laser desorption and ablation of organic solids," *Appl. Phys. Lett.* **74**, 1341-1343 (1999)

[71] A.G. Zhidkov, L.V. Zhigilei, A. Sasaki, and T. Tajima, "Short-laser-pulse Driven Emission of Energetic Ions into a Solid Target from a Surface Layer Spalled by a Laser Prepulse," *Appl. Phys. A* **73**, 741-747 (2001)

[72] R.C. Smith and K.S. Baker, "Optical Properties of the clearest natural waters (200-800 nm)," *Appl. Opt.* **20**, 177-184 (1981)

[73] P.M. Morse, "Diatomic Molecules According to the Wave Mechanics. II. Vibrational Levels," *Phys. Rev.* **34**, 57-64 (1929)

[74] R.J. Abraham and R. Stolevik, "The morse curve as a non-bonded potential function," *Chem. Phys. Lett.* **58**, 622-624 (1978)

[75] Y.G. Yingling, L.V. Zhigilei, B.J. Garrison, "The role of the photochemical fragmentation in laser ablation: a molecular dynamics study," *J. Photochem. Photobiol., A: Chemistry* **145**, 173-181 (2001)

[76] A.R. Leach, *Molecular Modelling principles and applications* (Prentice Hall, 2001)

[77] W.G. Neubauer and L.R. Dragonette, "Experimental Determination of the Freefield Sound Speed in Water," *J. Acoust. Soc. Am.* **36**,1685-1690 (1964)

[78] J. Leblond and M. Hareng, "Physical properties of superheated water at one bar: a base to define the << normal >> components of expansivity and compressibility of stable water," *J. Physique* **45**, 373-381 (1984)

[79] H. J. Strauch and P. T. Cummings, "Comment on: Molecular simulation of water along the liquid-vapor coexistence curve from 25 ^{o}C to the critical point," *J. Chem. Phys.* **96**, 864 (1992)

[80] R. G. Fernandez, J. L. F. Abascal, and C. Vega, "The melting point of ice I_h for common water models calculated from direct coexistence of the solid-liquid interface," *J. Chem. Phys.* **124**, 144506 (2006)

[81] J. R. Morris and X. Song, "The melting lines of model systems calculated from coexistence simulations," *J. Chem. Phys.* **116**, 9352 (2002)

[82] D. R. Lide (ed.), *Handbook of Chemistry and Physics* (CRC Press, 79th ed., 1999)

[83] C.-W. Lin and J.P.M. Tusler, "The speed of sound and derived thermodynamic properties of pure water at temperatures between (253 and 473) K and at pressures up to 400 MPa," *J. Chem. Phys.* **136**, 094511 (2012)

[84] D.R. Lide (ed.), *CRC Handbook of Chemistry and Physics* (CRC Press, 77th ed., 1996).

[85] S.I. Stoliarov, P.R. Westmoreland, M.R. Nyden, G.P. Forney "A reactive molecular dynamics model of thermal decomposition in polymers: I. Poly(methyl methacrylate)," *Polymer* **44**, 883-894 (2003).

[86] J.D. Moore, S.T. Cui, H.D. Cochran, P.T. Cummings, A molecular dynamics study of a short-chain polyethylene melt.I. Steady-state shear, *J. Non-Newtonian Fluid Mech*. **93**, 83–99 (2000)

[87] M. Bastos, S.O. Nilsson; R. Da Silva, I. Wadso, "Thermodynamic properties of glycerol enthalpies of combustion and vaporization and the heat capacity at 298.15 K. Enthalpies of solution in water at 288 .15, 198.15, and 308.15 K," *J. Chem. Themodyn.* **20**, 1353-1359 (1998)

[88] M. V. Roux, M. Temprado, J.S. Chickos, Y. Nagano, "Critically Evaluated Thermochemical Properties of Polycyclic Aromatic Hydrocarbons," *J. Phys. Chem. Ref. Data* **37**, 1855 (2008).

[89] J. Lindner, P. Vohringer, M.S. Pshenichnikov, D. Cringus, D.A. Wiersma, M. Mostvoy, "Vibrational relaxation of pure liquid water," *Chem. Phys. Lett*. **421**, 329-333 (2006)

[90] D. Cringus, S. Yeremenko, M.S. Pshenichnikov, and D.A. Wiersma, "Hydrogen Bonding and Vibrational Energy Relaxation in Water-Acetonitrile Mixtures," *J. Phys. Chem. B* **108**, 10376-10387 (2004)

[91] K. Ohta, K. Tominga, "Vibrational population relaxation of hydrogen-bonded phenol complexes in solution: Investigation by ultrafast infrared pump-probe spectroscopy," *Chem. Phys*. **341**, 310-319 (2007)

[92] E. J. Heilweil, M.P. Casassa, R.R. Cavanagh, and J.C. Stephenson, "Population lifetimes of OH (v=1) and OD (v = 1) stretching vibrations of alcohols and silanols in dilute solution," *J. Chem. Phys*. **85**, 5004 (1986)

[93] H. Fujisaki, and J.E. Straub, "Vibrational energy relaxation in proteins," *PNAS* **102**, 6726-6731 (2005)

[94] L. Bu and J.E. Straub, "Simulating Vibrational Energy Flow in Proteins: Relaxation Rate and Mechanism for Heme Cooling in Cytochrome c," *J. Phys. Chem. B* **107**, 12339-12345 (2003)

[95] R. Diller, "Vibrational relaxation during the retinal isomerization in bacteriorhodopsin," *Chem. Phys. Lett*. **295**, 47-55 (1998)

[96] D. J. Phares and A.R. Srinivasa, "Molecular Dynamics with Molecular Temperature," *J. Phys. Chem. A* **108**, 6100-6108 (2004)

[97] J. Gomez, V.J. Hilser, D. Xie, E. Freire, "The Heat Capacity of Proteins," *PROTEINS: Structure, Function, and Genetics* **22**:4040-412 (1995)

[98] A. C. Skapski and M.L. Smart, "The Crystal Structure of Trimeric Palladium(II) Acetate," *Chemical Communications* 658-659 (1970)

[99] G. I. Zharkova, P.A. Stabnikov, S.A. Sysoev, I.K. Igumenov, "Volatility and crystal lattice energy of palladium(II) chelates," *J. Struct. Chem.* **46**, 320-327 (2005)

[100] P. K. Gallagher, M. E Gross, "The thermal decomposition of palladium acetate," *J. Thermal Anal.* **31**, 1231–1241 (1986)

[101] H. Schafer, C. Brendel, H. Rabeneck, E. Schibilla, "Gaseous acetates," *Z. Anorg. Allg. Chem.* **518**, 168 (1984)

[102] K. S. Sharma and C. M. Kachava, "Application of Morse potential to metals in the molecular-metallic-framework," *Indian J. Phys.* **45**, 425-431 (1979)

[103] M.L. Pusey, R.S. Snyder, R. Naumann, "Protein crystal growth. Growth kinetics or tetragonal lysozyme crystals," *J. Biol. Chem.* **261**, 6524-6529 (1986)

[104] C. Sauter, F. Otalora, J.A. Gavira, O. Vidal, R. Giege, J.M. Garcia-Ruiz, "Structure of tetragonal egg-white lysozyme at 0.94 Å from crystals grown by the counter-diffusion method," *Acta Crystallogr D Biol Crystallogr*. **57** 1119-1126 (2001)

[105] A. Nadarajah, M.L. Pusey, "Growth Mechanism and Morphology of Tetragonal Lysozyme Crystals," *Acta Cryst. D* **52**, 983-996 (1996)

[106] J. Hogle, S.T. Rao, M. Mallikarjunan, C. Beddell, R.K. McMullan, M. Sundaralingam, "Studies of Monoclinic Hen Egg White Lysozyme, I. Structure Solution at 4 Å Resolution and Molecular-Packing Comparisons with Tetragonal and Triclinic Lysozymes," *Acta Cryst. B* **37**, 591-597 (1981)

[107] D. M. Salunke, B. Veerapandian, R. Kodandapani and M. Vijayan, "Structural transformations in protein crystals caused by controlled Dehydration," *Proc. Int. Symp. Biomol. Struct. Interactions, Suppl. J. Biosci.***8**, 37–44 (1985)

[108] R.C. Smith and K.S. Baker, "Optical Properties of the clearest natural waters (200-800 nm)," *Appl. Opt*. **20**, 177-184 (1981).

[109] M. Zhang, J. Chen, Z. Che, J. Lu, Z. Zhong, L. Yang, H. Zhao, "Determination of Thermal Conductivities of Biological Tissue Protein," *3rd International Conference on Biomedical Engineering and Informatics* (BMEI 2010).

[110] T.A. Stephenson, S.M. Morehouse, A.R. Powell, J.P. Heffer, and G. Wilkinson, "Carboxylates of Palladium, Carboxylates of Palladium, Platinum, and Rhodium, and their Adducts," *J. Chem. Soc.* 3632-3640 (1965)

[111] Z. Geretovsky, I.W. Boyd, "Kinetic study of 222 nm excimerlamp induced decomposition of palladium-acetate films," *Appl. Surf. Sci.* **138-139**, 401-407 (1999)

[112] J-Y. Zhang, I.W. Boyd, "Investigations of photo-induced decomposition of palladium acetate for electroless copper plating," *Thin Solid Films* **318**, 234-238 (1998)

[113] J-Y. Zhang, H. Esrom, and I. W. Boyd, "Decomposition mechanisms of thin palladium acetate film with excimer UV radiation," *Appl. Surf. Sci.* **96-98**, 399-404 (1996)

[114] H. Esrom and U. Kogelschatz, "Investigation of the mechanism of the UV-induced palladium deposition process from thin solid palladium actetae films," *Appl. Surf. Sci.* **46**, 158 – 162 (1990)

[115] J-Y.Zhang, I.W. Boyd, "Photo-decomposition of thin palladium acetate films with 126 nm irradiation," *Appl. Phys. A* **65**, 379-382 (1997)

[116]   R.M. Mahfouz, S.M. Alshehri, M.A.S. Monshi, N.M. Abd El-Salam, "Isothermal Decomposition of γ-Irradiated palladium acetate," *Radiat. Eff. Defects Solids* **159**, 345-351 (2004)

[117] P.K. Gallagher, M. E Gross, "The thermal decomposition of palladium acetate," *J. Thermal Anal.* **31**, 1231–1241 (1986)

[118] E. Makino, T. Shibata, "Micromachining compatible metal patterning technique using localized decomposition of an organometallic compound by laser irradiation," *J. Micromech. Microeng.* **8**, 177-181 (1998)

[119]   H.T. Ng, V.H.T. Chew, M.F.C. Loh, K.L. Tan, L. Chan, S.F.Y. Li, "Thermal-Induced Chemical Modification of Palladium Acetate on the Submicrometer Scale by in Situ Scanning Thermal Microscopy," *Langmuir* **15**, 2425-2430 (1999)

[120] Q. Fang, G. He, W.P. Cai, J-Y. Zhang, I.W. Boyd, "Palladium nanoparticles on silicon by photo-reduction using 172 nm excimer lamps," *Appl. Surf. Sci.* **226**, 7-11 (2004)

[121] D.S. Ivanov and L.V. Zhigilei, "Kinetic limit of heterogeneous melting in metals," *Phys. Rev. Lett.* **98**, 195701 (2007)

[122] Z. Lin and L.V. Zhigilei, "Time-resolved diffraction profiles and atomic dynamics in short pulse laser induced structural transformations: Molecular dynamics study," *Phys. Rev. B* **73**, 184113 (2006)

[123] D.S. Ivanov and L.V. Zhigilei, "The effect of pressure relaxation on the mechanisms of short pulse laser melting," *Phys. Rev. Lett.* **91**, 105701 (2003)

[124] X.W. Zhou, H.N.G. Wadley, R.A. Johnson, D.J. Larson, N. Tabet, A. Cerezo, A.K. Petford-Long, G.D.W. Smith, P.H. Clifton, R.L. Martens, and T.F. Kelly, "Atomic scale structure of sputtered metal multilayers," *Acta. Mater.* **49**, 4005 (2001)

[125] H.J.C. Berendsen, J.P.M. Postma, W.F. van Gunsteren, J. Hermans, "Interaction models for water in relation to protein hydration," *Intermolecular Forces*, 331-342 (1981)

[126] Y. Guissani and B. Guillot, "A computer simulation study of the liquid-vapor coexistence curve of water," *J. Chem. Phys.* **98**, 8221-8235 (1993)

[127] R.S. Taylor, L.X. Dang, and B.C. Garrett, "Molecular dynamics simulations of the liquid/vapor interface of SPC/E water," *J. Phys. Chem. B* **100**, 11720-11725 (1996)

[128] S.L. Lee, P.G. Debenedetti, and J.R. Errington, "A computational study of hydration, solution structure, and dynamics in dilute carbohydrate solutions," *J. Chem. Phys.* **122**, 204511 (2005)

[129] K. Toukan and R. Rahman, "Molecular-dynamics study of atomic motions in water," *Phys. Rev. B* **31**, 2643-2648 (1985)

[130] J. Marti, J.A. Pedro, E. Guardia, "A molecular dynamics study of heavy water steam," *Mol. Phys.* **86**, 263-271, (1995)

[131] Y Dou, L.V. Zhigilei, Z. Postawa, N. Winograd, and B.J. Garrison, "Thickness effects of water overlayer on its explosive evaporation at heated metal surfaces," *Nucl. Instr. Meth. B* **180**, 105-111 (2001)

[132] Y. Dou, N. Winograd, B.J. Garrison, and L.V. Zhigilei, "Substrate-assisted laser-initiated ejection of proteins embedded in water films," *J. Phys. Chem. B* **107**, 2362-2365 (2003)

[133] E.L. Simmons, "The Photochemistry of Solid Layers. Reaction Rates", *J. Phys. Chem.* **75**, 588-590 (1971)

[134] T. Ozawa, "A New Method of Analyzing Thermogravimetric Data," *Bull. Chem. Soc. Jpn.* **38**, 1881-1886 (1965)

[135] J. Zsako and Cs. Varhelyi, "Kinetic Analysis of Thermogravimetric Data," *J. Therm. Anal.* **7**, 33-40 (1975)

[136] H.E. Kissinger, "Reaction Kinetics in Differential Thermal Analysis," *J. Anal. Chem*. **29**, 1702-1706 (1957)

[137] N. Bityurin, B.S. Luk'yanchuk, M.H. Hong, and T.C. Chong, "Models for Laser Ablation of Polymers," *Chem. Rev.* **103**, 519-552 (2003)

[138] B. Guillot, Y. Guissani, "How to build a better pair potential for water," *J. Chem. Phys.* **114** (15), 6720-6733 (2001)

[139] J.J. de Pablo, "Molecular simulation of water along the liquid-vapor coexistence curve from $25^{o}C$ to the critical point," *J. Chem. Phys*. **93** (10), 7355-7359 (1990)

[140] T.I. Mizan, P.E. Savage, and R.M. Ziff, "Molecular Dynamics of Supercritical Water Using a Flexible SPC Model," *J. Phys. Chem*. **98**, 13067-13076 (1994)

[141] E. M. Schulson, "The Structural and Mechanical Behavior of Ice," *JOM* **51**(2), 21-27 (1999)

[142] T. Bryk and A.D.J. Haymet, "The Ice/Water Interface: Density-Temperature Phase Diagram for the SPC/E Model of Liquid Water," *Mol. Simulat.* **30**: 2, 131 — 135 (2004)

[143] L. Pauling, "The Structure and Entropy of Ice and of other Crystals with Some other Randomness of Atomic Arrangement," *J. Am. Chem. Soc.* **57**, 2680-2684 (1935)

[144] J. D. Bernal and R.H. Fowler, "A Theory of Water and Ionic Solution, with Particular Reference to Hydrogen and Hydroxyl Ions", *J. Chem. Phys*. **1**, 515, (1933)

[145] M. Neumann, "The dielectric constant of water. Computer simulations with the MCY potential", *J. Chem. Phys.* **82**, 5663 (1985)

[146] F.H. Drake, G.W Pierce, and M.T. Dow, "Measurement of the Dielectric Constant and Index of Refraction of Water and Aqueous Solutions of KCl at High Frequencies," *Phys. Rev.* **35**, 613-622 (1930)

[147] M. Uematsu, E.U. Frank, "Static Dielectric Constant of Water and Steam," *J. Phys. Chem. Ref. Data* **9**, 1291-1306 (1980)

[148] B.J. Garrison, T.E. Itina, L.V. Zhigilei, "Limit of overheating and the threshold behavior in laser ablation," *Phys. Rev. E* **68**, 041501 (2003)

[149] W.L. Jorgensen, J. Chandrasekhar, J.D. Madura, R.W. Impey, M.L. Klein, "Comparison of simple potential functions for simulating liquid water," *J. Chem. Phys.* **79**, 926 (1983)

[150] H.J.C. Berendsen, J.R. Grigera, and T.P. Straatsma, "The Missing Term in Effective Pair Potentials," *J. Phys. Chem.* **91**, 6269-6271 (1987)

[151] K. Watanabe, M.L. Klein, "Effective pair potentials and the properties of water," *Chem. Phys.* **131**, 157-167 (1989)

[152] P.A. Thiel, T.E. Madey, "The interaction of water with solid surfaces: Fundamental aspects," *Surf. Sci. Rep.* **7**, 211-385 (1987)

[153] A. Michaelides, A. Alavi, D.A. King, "Insight into H_2O-ice adsorption and dissociation on metal surfaces from first-principles simulations," *Phys. Rev. B* **69**, 113404 (2004)

[154] V.A. Ranea, A. Michaelides, R. Ramirez, P.L. de Andres, J.A. Verges, D.A. King, "General Model for Water Monomer Adsorption on Close-Packed Transition and Noble Metal Surfaces," *Phys. Rev. Lett.* **90**, 216102 (2003)

[155] S. Meng, E.G. Wang, S. Gao, "Water adsorption on metal surfaces: A general picture from density functional theory studies," *Phys. Rev. B* **69** 195404 (2004)

[156] Y. Cao, Z.-X. Chen, "Theoretical studies on the adsorption and decomposition of H_2O on Pd(111) surface," *Surface Science* **600**, 4572-4583 (2006)

[157] C. Kittel, *Introduction to Solid State Physics* (Wiley-Interscience, New York 1996)

[158] C-M Lin, T-L Hung, Y-H Huang, K-T Wu, M-T Tang, C-H Lee, C.T. Chen, and Y.Y. Chen, "Size-dependent lattice structure of palladium studied by x-ray absorption spectroscopy," *Phys. Rev. B* **75**, 125426 (2007)

[159] H.C. Andersen, Rattle: "A "Velocity" Version of the Shake Algorithm Molecular Dynamics Calculations," *J. Comp. Phys.* **52**, 24-34 (1983)

[160] S. Koneshan, J.C.Rasaiah, R.M. Lynden-Bell, S.H. Lee, "Solvent Structure, Dynamics, and Ion Mobility in Aqueous Solutions at 25 ^{O}C," *J. Phys. Chem. B* **102**, 4193-4204 (1998)

[161] M. Yujing, A. Mellouki, "The near-UV absorption cross-sections for several ketones," *J. Photochem. Photobiol., A:* **134**, 31-36 (2000)

[162] M.A. Oehlschlager, D.F. Davidson, J.B. Jeffries, and R.K. Hanson, "Ultraviolet Absorption Cross-Sections of Hot Carbon Dioxide," *Chem. Phys. Lett*. **399**, 490-495 (2004)

[163] E.E. Finney, R.G. Finke, "Nanocluster nucleation and growth kinetic and mechanistic studies: A review emphasizing transition-metal nanoclusters," *J. Colloid Interf. Sci.* **317**, 351-374 (2008)

[164] D.H. Everett, *Basic Principles of Colloid Science* (Royal Society of Chemistry, London, 1988)

[165] B. Corain, G. Schmid and N. Toshima, *Metal Nanoclusters in Catalysis and Materials Science: The Issue of Size Control* (Elsevier, 2008)

[166] E. Roduner, "Size matters: why nanomaterials are different," *Chem. Soc. Rev.* **35**, 583–592 (2006)

[167] W. Thomson, "On the equilibrium of vapour at a curved surface of liquid," *Philos. Mag.* **42**, 448 (1871)

[168] H. Hirai, Y. Nakao, N. Toshima, "Preparation of Colloidal Transition Metals in Polymers by Reduction with Alcohols or Ethers," *J. Macromol. Sci. Chem. A* **13**, 727 (1979)

[169] H. Bönnemann, G. Braun, W. Brijoux, R. Brinkmann, A.S. Tilling, K. Seevogel, K. Siepen, "Nanoscale colloidal metals and alloys stabilized by solvents and surfactants. Preparation and use as catalyst precursors," *J. Organomet. Chem.* **520**, 143 (1996)

[170] Y. Xiong and Y. Xia, "Shape-Controlled Synthesis of Metal Nanostructures: The Case of Palladium," *Adv. Mater.* **19**, 3385-3391 (2007)

[171] J.G. Ulan, W.F. Maier, "Rational design of a heterogeneous palladium catalyst for the selective hydrogenation of alkynes," *J. Org. Chem.* **52**, 3132 (1987)

[172] W.H. Yang, G. C. Schatz, R. P. Van Duyne, "Discrete dipole approximation for calculating extinction and Raman intensities for small particles with arbitrary shapes," *J. Chem. Phys.* **103**, 869 (1995)

[173] J.M. Zhang, F. Ma, K. W. Xu, "Calculation of the surface energy of FCC metals with modified embedded-atom method," *Appl. Surf. Sci.* **229**, 34 (2004)

[174] A. Pimpinelli, J. Villain, *Physics of Crystal Growth* (Cambridge University Press, Cambridge, UK 1998)

[175] P. M. Ajayan, L. D. Marks, "Quasimelting and phases of small particles," *Phys. Rev. Lett.* **80**, 585 (1998)

[176] F. Baletto, R. Ferrando, "Structural properties of nanoclusters: Energetic, thermodynamic, and kinetic effects," *Rev. Mod. Phys.* **77**, 371 (2005)

[177] C. Cleveland, U. Landman, "The energetics and structure of nickel clusters: Size dependence," *J. Chem. Phys.* **94**, 7376 (1991)

[178] Y. Xiong, H. Cai, B. J. Wiley, J. Wang, M. J. Kim, Y. Xia, "Synthesis and Mechanistic Study of Palladium Nanobars and Nanorods," *J. Am. Chem. Soc.* **129**, 3665 (2007)

[179] Y. Xiong, J. M. McLellan, Y. Yin, Y. Xia, "Synthesis of Palladium Icosahedra with Twinned Structure by Blocking Oxidative Etching with Citric Acid or Citrate Ions," *Angew. Chem. Int. Ed.* **46**, 790 (2007)

[180] Y. Xiong, H. Cai, Y. Yin, Y. Xia, "Synthesis and characterization of fivefold twinned nanorods and right bipyramids of palladium," *Chem. Phys. Lett.* **440**, 273 (2007)

[181] Y. Xiong, I.Washio, J. Chen, H. Cai, Z.-Y. Li, Y. Xia, "Poly(vinyl pyrrolidone): A dual functional reductant and stabilizer for the facile synthesis of metal nanoplates in aqueous solutions," *Langmuir* **22**, 8563 (2006)

[182] V.K. LaMer, R.H. Dinegar, "Theory, Production and Mechanism of Formation of Monodispersed Hydrosols," *J. Am. Chem. Soc.* **72**, 4847 (1950)

[183] V.K. LaMer, 'Nucleation in Phase Transitions," *Ind. Eng. Chem.* **44**, 1270 (1952)

[184] E. Matijevic, "Preparation and properties of uniform size colloids," *Chem. Mater.* **5**, 412 (1993)

[185] M.A. Watzky, R.G. Finke, "Transition Metal Nanocluster Formation Kinetic and Mechanistic Studies. A New Mechanism When Hydrogen Is the Reductant: Slow, Continuous Nucleation and Fast Autocatalytic Surface Growth," *J. Am. Chem. Soc*. **119**, 10382-10400 (1997)

[186] G. Schmid (Ed.), *Clusters and Colloids: From Theory to Applications* (VHC, New York, 1994).

[187]   R.G. Finke, in: D.L. Feldheim, C.A. Foss Jr. (Eds.), *Metal Nanoparticles: Synthesis, Characterization, and Applications* (Marcel Dekker, Chapter 2, New York, 2001)

[188]   S. Papp, R. Patakfalvi, and I. Dekany, "Formation and Stabilization of Noble Metal Nanoparticles," *Croat. Chem. Acta* **80** (3-4) 493-502 (2007)

[189]   M.A. Watzky and R.G. Finke, "Nanocluster Size-Control and "Magic Number" Investigations. Experimental Test of the "Living-Metal Polymer" Concept and of Mechanism-Based Size-Control Predictions Leading to the Syntheses of Iridium(0) Nanoclusters Centering about Four Sequential Magic Numbers," *Chem. Mater.* **9**, 3083-3095 (1997)

[190] M. Cai, J. Chen, and J. Zhou, "Reduction and morphology of silver nanoparticles via liquid-liquid method," *Appl. Surf. Sci.* **226**, 422–426 (2004)

[191] D.N. Furlong, A. Launikonis, W. H. F. Sase and J. V. Sanders, "Colloidal Platinum Sols," *J. Chem.* Soc., *Faraday Trans. I* **80**, 571-588 (1984)

[192] R. Tausch-Treml, A. Henglein, and J. Lilie, "Reactivity of silver in aqueous solution-2. Pulse radiolysis study," *Ber. Bunsen-Ges. Phys. Chem.* **82**, 1335–1343 (1978)

[193] P.J. Thomas and G.U. Kulikarni, "From colloids to nanotechnology: Investigations on magic nuclearity palladium nanocrystals," *Curr. Sci.* **85**, 1760-1766 (2003)

[194] C.N.R. Rao, G.U. Kulkarni , P.J. Thomas and P.P. Edwards, "The Size-Induced Metal-Insulator Transition in Colloidal Gold," *Chem. Soc. Rev.* **29**, 27 (2000)

[195] G. Schmid, M. Bäumle and N. Beyer, "Ordered Two-Dimensional Monolayers of Au(55) Clusters," *Angew. Chem. Int. Ed. Engl.* **39**, 181-183 (2000)

[196] T.P. Martin, T. Bergmann, H. Göhlich and T. Lange, "Evidence for icosahedral shell structure in large magnesium clusters," *J. Phys. Chem.* **95**, 6421 (1991)

[197] M. Chen, J. Falkner, W-H Guo, J-Y Zhang, C. Sayes, V. L. Colvin, Synthesis and self-organization of soluble monodisperse palladium nanoclusters, *J. Colloid Interf. Sci.* **287**, 146-151 (2005)

[198] T. Teranishi, H. Hori, M. Miyake, "ESR Study on Palladium Nanoparticles," *J. Phys. Chem. B* **101**, 5774 (1997)

[199] T. Teranishi and M. Miyake, "Size Control of Palladium Nanoparticles and Their Crystal Structures," *Chem. Mater.* **10**, 594 (1998)

[200] P.J. Thomas, G.U. Kulkarni and C.N.R. Rao, "Magic nuclearity clusters of metal nanocrystals formed by mesoscale self-assembly," *J. Phys. Chem. B* **105**, 2515 (2001)

[201] P.J. Thomas, G.U. Kulkarni and C.N.R. Rao, "An investigation of two-dimensional arrays of thiolized Pd nanocrystals" *J. Phys. Chem. B* **104**, 8138 (2000)

[202] J.E. Martin, J.P. Wilcoxon, J. Odinek, P. Provencio, "Superlattices of Platinum and Palladium Nanoparticles," *J. Phys. Chem. B* **106**, 971 (2002)

[203] L. Motte, F. Billoudet, E. Lacaze, J. Douin, and M.P. Pileni, "Self-Organization into 2D and 3D Superlattices of Nanosized Particles Differing by Their Size," *J. Phys. Chem. B* **101**, 138-144 (1997)

[204] P.A. Namini, A.A. Babaluo, B.Bayati, "Palladium nanoparticles synthesis using polymeric matrix: poly(ethyleneglycol) molecular weight and palladium concentration effects," *IJNN* **3**, 37-43 (2007)

[205] S.W. Chen, K. Huang, J.A. Stearns, "Alkanethiolate-Protected Palladium Nanoparticles," *Chem. Mater.* **12**, 540 (2000)

[206] C.K. Yee, R. Jordan, A. Ulman, H. White, A. King, M. Rafailovich, J. Sokolov, "Novel one-phase synthesis of thiol-fuctionalized gold, palladium, and iridium nanoparticles using superhydride," *Langmuir* **15**, 3486 (1999)

[207] W. Hoogsteen and L. G. J. Fokkink, "Polymer-stabilized Pd sols : kinetics of sol formation and stabilization mechanism," *J. Colloid Interface Sci.* **175**, 12–26 (1995)

[208] K. Esumi, T. Itakura, and K. Torigoe, "Preparation of organo palladium sols from palladium complexes in various alcohols," *Colloids Surf. A* **82**, 111–113 (1994)

[209] J. Turkevich, P.C. Stevenson, J. Hillier, "A study of the nucleation and growth processes in the synthesis of colloidal gold," *Discuss. Faraday Soc.* **11**, 55-75 (1951)

[210] H. Hirai, Y. Nakao, N. Toshima, K. Adachi, "Colloidal rhodium in poly(vinyl alcohol) as a hydrogenation catalyst of olefins," *Chem. Lett.* **5**, 905 (1976)

[211] G. Schmid, R. Boese, R. Pfeil, F. Bandermann, S. Meyer, G.H.M. Calis, J.A.W. van der Velden, "$Au_{55}[P(C_6H_5)_3]12Cl_6$ − A gold cluster of an exceptional size," *Chem. Ber.* **114**, 3634 (1981)

[212] D. Astruc, F. Lu, J.R. Aranzaes, "Nanoparticles as recyclable catalysts: the frontier between homogeneous and heterogeneous catalysis," *Angew. Chem. Int. Ed.* **44**, 7852 (2005)

[213] H. Bonnemann, K. S. Nagabhushana, R.M. Richards, in: D. Astruc (ed.) *Nanoparticles and Catalysis,* Chapter 2 (Wiley-VCH, Weinheim, 2007)

[214] H. Bonnemann, W. Brijoux, "The preparation, characterization and application of organosols of early transition metals," *Nanostruct. Mater.* **5**, 135 (1995)

[215] R. Franke, J. Rothe, J. Pollmann, J. Hormes, H. Bonnemann, W. Brijoux, T. Hindenburg, " A Study of the Electronic and Geometric Structure of Colloida $Ti^0{\cdot}0.5THF$," *J. Am. Chem. Soc.* **118**, 12090 (1996).

[216] N. Toshima, M. Harada, T. Yonezawa, K. Kushihashi, K. Asakura, "Structural analysis of polymer-protected palladium/platinum bimetallic clusters as dispersed catalysts by using extended x-ray absorption fine structure spectroscopy," *J. Phys. Chem.* **95**, 7448 (1991)

[217] G. Schmid (ed.), *Nanoparticles: From Theory to Application* (Wiley-VCH, Weinheim, 2004)

[218] C.E. Briant, B.R.C.Theobald, J.W. White, C.K. Bell, D.M.P. Mingos, "Synthesis and *X*-ray structural characterization of the centred icosahedral gold cluster compound $[Au_{13}(PMe_2Ph)_{10}Cl_2](PF_6)_3$; the realization of a theoretical prediction," *Chem. Commun.* **20**, 201 (1981).

[219] H. Bonnemann, W. Brijoux, R. Brinkmann, E. Dinjus, T. Joussen B. Korall, "Electrochemical growth of superparamagnetic cobalt clusters," *Angew. Chem. Int. Ed.* **30**, 1312 (1991)

[220] M.T. Reetz, G. Lohmer, "Propylene carbonate stabilized nanostructured palladium clusters as catalysts in Heck reactions," *Chem. Commun.* (Cambridge) **16**, 1921 (1996)

[221] C. Kumar, *Metallic Nanomaterials* (WILEY-VCH, 2009)

[222] M. Ganesan, R.G. Freemantle and S.O. Obare, "Monodisperse thioether-stabilized palladium nanoparticles: synthesis, characterization, and reactivity," *Chem. Mater.* **19**, 3464 (2007)

[223] W. Ostwald, *Lehrbuck der Allgemeinen Chemie,* Vol. 2, Part 1, (Leipzig, Germany 1986)

[224] K. Aika, L. L. Ban, I. Okura, S. Namba and J. Turkevich, "Chemisorption and catalytic activity of a set of platinum catalysts," *J. Res. Inst. Catal. Hokkaido Univ*. **24**, 55 (1976)

[225] L.D. Rampino and F.F. Nord, "Preparation of Palladium and Platinum Synthetic High Polymer Catalysts and the Relationship betwenn Particle Size and Rate of Hydrogenation," *J. Am. Chem. Soc.* **63**, 2745 (1941)

[226] X.M. Lin, C.M. Sorenson, K.J. Klabunde, "Digestive Ripening, Nanophase Segregation and Superlattice Formation in Gold Nanocrystal Colloids," *J. Nanoparticle Res.* **2**, 157 (2000)

[227] S.I. Stoeva, B.LV. Prasad, S. Uma, P.K. Stoimenov, V. Zaikovski, C.M. Sorenson, K.J. Klabunde, "Face-centered cubic and hexagonal close-packed nanocrystal superlattices of gold nanoparticles prepared by different methods," *J. Phys. Chem. B.* **107**, 7441 (2003)

[228] B.LV. Prasad, S.I. Stoeva, C.M. Sorenson, K.J. Klabunde, "Digestive-ripening agents for gold nanoparticles: alternatives to thiols," *Chem. Mater.* **15**, 935 (2003)

[229] S.I. Stoeva, V. Zaikovski, B.LV. Prasad, P.K. Stoimenov, C.M. Sorenson, K.J. Klabunde, "Reversible transformations of gold nanoparticle morphology," *Langmuir* **21**, 10280 (2005)

[230] H.H. Smit, R.C. Thiel and L.J. de Jongh, "The thermal motion of gold atoms in metal cluster compounds as determined by Mössbauer and specific heat," *Z. Phys. D* **12**, 193 (1989)

[231] G. Schmid, B. Morun, J.O. Malm, Angew, "$Pt_{309}Phen_{36}^*O_{30\pm10}$, a four-shell platinum cluster," *Chem. Int. Ed. Engl.* **28**, 778 (1989)

[232] F.M. Mulder, T.A. Stegnik, R.C. Thiel, L.J. de Jongh, G. Schmid, "Metallic behaviour in a Pt_{309} cluster revealed by ^{197}Au Mössbauer spectroscopy," *Nature* **367**, 716 (1994)

[233] A. Bezryadin, C. Dekker, G. Schmid, "Electrostatic trapping of single conducting nanoparticles between nanoelectrodes," *Appl. Phys. Lett.* **71**, 279 (1997)

[234] H. van Kempen, J.G.A. Dubois, J.W. Gerritsen, G. Schmid, "Small metallic particles studied by scanning tunneling microscopy," *Physica B* **204**, 51 (1995)

[235] J.G.A. Dubois, J.W. Gerritsen, S.E. Shafranjuk, E.J.G. Boon, G. Schmid, H. van Kempen, "Coulomb staircases and quantum size effects in tunneling spectroscopy on ligand-stabilized metal clusters," *Europhys. Lett.* **33**, 279 (1996)

[236] C.P. Vinod, G.U. Kulkarni, and C.N.R. Rao, "Size dependent changes on the electronic structure of metal clusters as investigated by Scanning tunneling spectroscopy," *Chem. Phys. Lett.* **289**, 329 (1998)

[237] B.J. Berne, R. Pecora, *Dynamic Light Scattering with Applications to Chemistry, Biology, and Physics* (Dover Publications, New York, 2000)

[238] W. Brown (Ed.), *Dynamic Light Scattering: The Method and Some Applications*, (Oxford Univ. Press, Oxford, 1993)

[239] J.A. Creighton, D.G. Eadon, "Ultraviolet-visible absorption spectra of the colloidal metallic elements," *J. Chem. Soc. Faraday Trans*. **87**, 3881 (1991)

[240] A. Henglein, M. Giersig, "Reduction of Pt(II) by H_2: the effects of citrate and NaOH and reaction mechanism," *J. Phys. Chem. B* **104**, 6767 (2000)

[241] J. Wang, H.F.M. Boelens, M.B. Thathagar, G. Rothenberg, "In Situ Spectroscopic Analysis of Nanocluster Formation," *Phys. Chem. Chem. Phys.* **5**, 93 (2004)

[242] A.V. Gaikwad, G. Rothenberg, "In-situ UV-visible study of Pd nanocluster formation in solution," *Phys. Chem. Chem. Phys.* **8**, 31 (2006)

[243] M. Michaelis, A. Henglein, P. Mulvaney, "Composite Pd-Ag particles in aqueous solution," *J. Phys. Chem.* **98**, 6212 (1994)

[244] F.P. Zamborini, S.M. Gross, R.W. Murray, "Synthesis, characterization, reactivity, and electrochemistry of palladiummonolayer protected clusters," *Langmuir* **17**, 481 (2001)

[245] D.E. Cliffel, F.P. Zamborini, S.M. Gross, R.W. Murray, "Mercaptoammonium Monolayer-Protected, Water-Soluble Gold, Silver, and Palladium Clusters," *Langmuir* **16**, (2000) 9699.

[246] C.A. Jaska, I. Manners, "heterogeneous or homogeneous catalysis? Mechanistic studies of the rhodium-catalyzed dehydrocoupling of amine-borane and phosphine-borane adducts," *J. Am. Chem. Soc.* **126**, 9776 (2004)

[247] C.M. Hagen, J.A. Widegren, P.M. Maitlis, R.G. Finke, "Is it homogeneous or heterogeneous catalysis? Compelling evidence for both types of catalysts derived from [Rh(eta5-C5Me5)Cl2]2 as a function of temperature and hydrogen pressure," *J. Am. Chem. Soc.* **127**, (2005) 4423.

[248] G. Schmid, "Large clusters and colloids – metals in the embryonic state," *Chem. Rev.* **92**, 1709 (1992)

[249] V. Maurice, H.-H. Strehblow, P. Marcus, "In situ STM study of the initial stages of oxidation of Cu(111) in aqueous solution," Surf. Sci. **458**, 185 (2000)

[250] G. Margaritondo, *Elements of Synchrotron Light: For Biology, Chemistry, and Medical Research* (Oxford Univ. Press, Oxford, 2002)

[251] A.I. Frenkel, C.W. Hills, R.G. Nuzzo, "View from the inside: Complexity of the atomic scale ordering in metal nanoparticles," *J. Phys. Chem. B* **105**, 12689 (2001)

[252] Mohammed A.M. Shtaya-Suleiman, "Size-selective synthesis of nanometer-sized Palladium clusters and their hydrogen salvation behavior," Gottingen (2003)

[253] J. Zheng, P. R. Nicovich, R. M. Dickinson, Highly Fluorescent Noble Metal Quantum Dots, *Annu Rev Phys Chem.* **58**, 409–431 (2007)

[254] E. Cottancin, G. Celep, J. Lerme, M. Pellarin, J.R. Huntzinger, J.L. Vialle, M. Broyer, Optical properties of noble metal clusters as a function of the size : comparison between experiments and a semi-quantal theory, *Theor. Chem. Acc.* **116**, 514-523 (2006)

[255] G. Mattei, P. Mazzoldi and H. Bernas, *Metal Nanoclusters for Optical Properties* (Springer-Verlag Berlin Heidelberg, 2010)

[256] A. Pinchuk, G. von Plessen and U. Kreibig, ''Influence of interband electronic transitions on the optical absorption in metallic nanoparticles,'' *J. Phys. D : Appl. Phys.* **37**, 3133-3139 (2004)

257 P. B. Johnson and R. W. Christy, ''Optical constants of the noble metals'', *Phys. Rev. B* **6**, 4370 (1972).

258 S. Baset, H. Akbari, H. Zeynali, M. Shafie, ''Size measurement of metal and semiconductor nanoparticles via UV-vis absorption spectra,'' *Dig. J. Nanomater. Bios*. **6**, 709-716 (2011)

259 J. Lafait, F. Abeles, M. L. Theye and G Vuye, ''Determination of the infrared optical constants of highly reflecting materials by means of surface plasmon excitation—application to Pd,'' *J. Phys. F : Metal Phys.* **8** (1978)

260 B. T. Sullivan, ''Optical properties of palladium in the visible and near spectral regions,'' *Appl. Optics* **29**, 1964 (1990)

261 H.L. Xu, Z.W. Sun, Z.W. Dai, Z.K. Jiang, P. Palmeri, P. Quinet, and E. Biemont, ''Radiative lifetimes, branching fractions and oscillator strengths in Pd I and the solar palladium abundance,'' *A&A* **452**, 357-362 (2006)

262 E. J. van Duijn, S. Witte, R. Zinkstok, and W. Hogervorst, ''Hyperfine structure and isotope shift measurements on $4d^{10}\,^1S_0 \rightarrow 4d^9\,5p\,J = 1$ transitions in Pd I using deep-UV cw laser spectroscopy,'' *Eur. Phys. J. D* **19**, 25-29 (2002)

263 Robert C. Hilborn, ''Einstein coefficients, cross sections, f values, dipole moments, and all that,'' *Am. J. Phys.* **50**(11), (1982)

264 Timothy R. Gosnell, *Fundamentals of Spectroscopy and Laser Physics* (2002)

265 D.M. Mann and H.P. Broida, ''Ultraviolet Absorption Spectra of Transition Metal Atoms in Rare Gas Matrices,'' *J. Chem. Phys.* **55**, 84 (1971)

266 W. Schrittenlacher, H.H. Rotermund, and D.M. Kolb, ''Optical spectra of matrix isolated palladium atoms,'' *J. Chem. Phys.* **83**, 6145 (1985)

[267] P.H. Sydenham, N.H. Hancock and R. Thorn, *Introduction to Measurement Science and Engineering* (Wiley-Interscience, 1989)

[268] I.F. Hughes and T.P.A. Hase, *Measurements and their Uncertainties: A practical guide to modern error analysis* (Oxford University Press, 2009)